Dissertation zur Erlangung des Doktorgrades

der Fakultät für Chemie und Pharmazie

Der Ludwig-Maximilians-Universität München

Mechanistic Insights into Superoxide Dismutase (SOD) Mimicry by Metal Complexes with Redox-Active Ligands: Advancements in High-Pressure Kinetic Methodologies

Julian Edgar Oppelt

aus

Bamberg, Deutschland

2025

Erklärung

Diese Dissertation wurde im Sinne von § 7 der Promotionsordnung vom 28. November 2011 von Frau Prof. Dr. Ivana Ivanović-Burmazović betreut.

Eidesstattliche Versicherung

Diese Dissertation wurde eigenständig und ohne unerlaubte Hilfe erarbeitet.

München, 19.02.2025

_____

Julian Oppelt

Dissertation eingereicht am: 19.02.2025

1. Gutachterin/Gutachter: Prof. Dr. Ivana Ivanović-Burmazović

2. Gutachterin/Gutachter: Prof. Dr. Lena Daumann

Mündliche Prüfung am 27.03.2025

Diese Arbeit wurde in der Zeit von November 2020 bis Dezember 2024 am Department für Chemie der Ludwig-Maximilians-Universität München unter Anleitung von Frau Prof. Dr. Ivana Ivanović-Burmazović durchgeführt.

FÜR MEINE ELTERN

Danksagung

Zu Beginn möchte ich mich bei meiner Betreuerin und Doktormutter Prof. Dr. Ivana Ivanović-Burmazović bedanken. Ich danke dir für den perfekten Mix aus Freiheit, um kreativ zu arbeiten und mich zu entwickeln und der nötigen Führug und den Support um geplante Ziele zu erreichen. Vielen Dank für die unglaublich lehrreiche Zeit und die Möglichkeit die Gruppe in München mit aufzubauen.

Ebenfalls möchte ich mich bei Prof. Dr. Lena Daumann bedanken für die Übernahme des Zweigutachtens und der Möglichkeit sich auch neben der Forschung persönlich weiter zu entwickeln.

Danke an Prof. Dr. Hans-Christian Böttcher, Prof. Dr. Thomas M. Klapötke, Prof. Dr. Oliver Trapp und Prof. Dr. Silvija Markic für das Mitwirken in meiner Prüfungskommission und der Teilnahme an meiner mündlichen Prüfung.

Ein Dank geht ebenfalls an meinen langjährigen Kollaborationspartner Christian Goldsmith, welcher durch das Mitwirken an zahlreichen Projekten und mit Input Forschung vorangetrieben hat, Thanks Christian!

Danke an Annette Rogge, die stets und ermüdlich mit Rat und Tat zur Seite stand, damit man sich im schier endlosen Bürokratie-Dschungel zurecht finden konnte.

Danke an Sebastian und Ina dafür, dass im Laboralltag immer alles reibungslos ablief und die ein oder andere Masse, die gemessen wurde. Danke an Philipp für das Instandhalten der Technik und vor allem für den guten Start, den wir parallel in München haben durften.

Danke an mein Labor, welches immer für ordentlich Unterhaltung sorgte, egal ob mit neuen Memes, Game Nights von Valentin, die ich nie vergessen werde oder verrückten Geschichten von Fengsen.

谢谢朋友.

Natürlich darf die Sorbet Bande auch nicht fehlen, danke Christian, Peter, Sebi, Joel und natürlich das neuste Mitglied Rahel! Danke für jedes einzelne Mittagessen, die komplette Gesprächsbandbreite von fragwürdig bis hochkomplex, die unendlichen Stunden gefüllt mit Spaß, Lachen und Freude und sämtliche Aktivitäten, die wir zusammen erlebt haben. Ihr habt die Zeit defintiv um einiges bereichert.

Last but most important möchte ich meinen Freunden, meiner Familie und vor allem meinen Eltern danken. Worte können nicht im Ansatz beschreiben, wie dankbar ich für euch bin. Ihr seid immer da, wenn man euch braucht, es gibt keinen Weg der zu weit ist, keine Aufgabe die euch zu schwer erscheint oder Probleme, die man nicht lösen kann. Hauptsache man macht es gemeinsam mit Menschen, denen man vertrauen und auf die man sich verlassen kann. Diese unglaublich wichtige Lektion habe ich von euch gelernt und ich danke euch für jeden einzelnen Tag, den ich mit euch verbringen darf!

Table of Contents

List of Figures

Abbreviations

ABTS	2,2'-azinobis(3-ethylbenzthiazolin-6-sulfonic acid
atm	Atmospheres
ATP	Adenosine 5'-triphosphate
bTAML	Biuret tetraamido macrocyclic ligand
CYP450	Cytochrome P450 enzyme family
Cyt c	Cytochrome C
DMF	Dimethylformamide
DMSO	Dimethylsulfoxide
DPPH	2,2-diphenyl-1-picrylhydrazyl
DQA	2-n-decyl-quinazolin-4-ylamine
Ethylenediaminetetraacetic acid	EDTA
eq.	Equation
et al.	lat. et alia; and Others
(m)ETC	(mitochondrial) Electron Transport Chain
FMN	Flavin Mononucleotide
FMNH	Reduced form of FMN
HAA	Hydrogen Atom Abstraction
k	Rate constant
L	Liter(s)
M	Molar concentration [mol/L]
m-CPBA	*Meta*-chloroperoxybenzoic acid
MeCN	Acetonitrile
NAD+	Oxidized form of NADH
NADH	Nicotinamide Adenine Dinucleotide
NADP+	Oxidized form of NADPH
NADPH	Nicotinamide Adenine Dinucleotide Phosphate
NBT	Nitro Blue Tetrazolium
NHE	Normal Hydrogen Electrode
NOX	NADPH Oxidase(s)
p	para
PCET	Proton-Coupeld-Electron-Transfer

pH	Negative decadic logarithm of proton concentration
pKa	Acid dissociation constant
PUFA	Poly-Unsaturated Fatty Acid
RET	Reverse electron transfer
RNS	Reactive Nitrogen Species
ROS	Reactive Oxygen Species
s	Second(s)
XO	Xanthine Oxidase

1 Introduction

1.1 The superoxide anion

The accumulation of oxygen in Earth's atmosphere approximately 3.5 billion years ago was a pivotal event in the evolution of complex organisms and higher life forms establishing it as one of the most important elements in the periodic table. Atmospheric molecular oxygen eventually stabilized at a concentration of 21%, which remains constant today. In its ground state (triplet) molecular oxygen possesses two unpaired electrons of the same spin in the two different π^* orbitals. Formal one electron reduction of O_2 (eq. 1) produces the superoxide anion radical $O_2^{\bullet-}$ which, unlike molecular, is significantly more reactive towards organic substrates and serves as precursor for a variety of even more reactive species.[1,2]

$$O_2 + e^- \longrightarrow O_2^{\bullet-} \quad E^o = -160 \text{ mV vs. NHE} \quad (1)$$

$$O_2^{\bullet-} + 2H^+ + e^- \longrightarrow H_2O_2 \quad E^o = +890 \text{ mV vs. NHE} \quad (2)$$

The redox potentials for superoxide/oxygen redox couple are reported between -160 mV and-180 mV vs normal hydrogen electrode (NHE) and for the superoxide/hydrogen peroxide between 890 mV and 910 mV vs. NHE (eq. 2) depending on the surrounding environment.[3] Although superoxide can react with itself however this reaction tends to be relatively slow for a radical species due to electronic repulsion of the negatively charged ion. In contrary to the self-dismutation in aqueous solutions the superoxide anion radical exhibits the characteristics of a nucleophile and a strong Brønsted base deprotonating water fast in a disproportionation process (eq. 3).[4,5]

$$2O_2^{\bullet-} + H_2O \longrightarrow HOO^- + O_2 + OH^- \quad (3)$$

In proton-rich environments another reaction involves the superoxide anion radical reacting with its protonated form, the hydroperoxyl (eq. 4). With a pK_a of 4.8, hydroperoxyl acts as a weak acid, which play a minor role in role in aqueous solutions at physiological pH.

$$HO_2^{\bullet} + O_2^{\bullet-} \xrightarrow{[H^+]} O_2 + H_2O_2 \quad (4)$$

Nevertheless, the disproportionation is the fastest at pH = pK_a due to fact that protonated superoxide's concentration equals the concentration of deprotonated superoxide at these conditions. In Figure 1 the pH dependence of superoxide disproportionation by Bielski *et al*.[6] is illustrated which gives a great insight into suiting conditions when it comes to superoxide-based measurements.

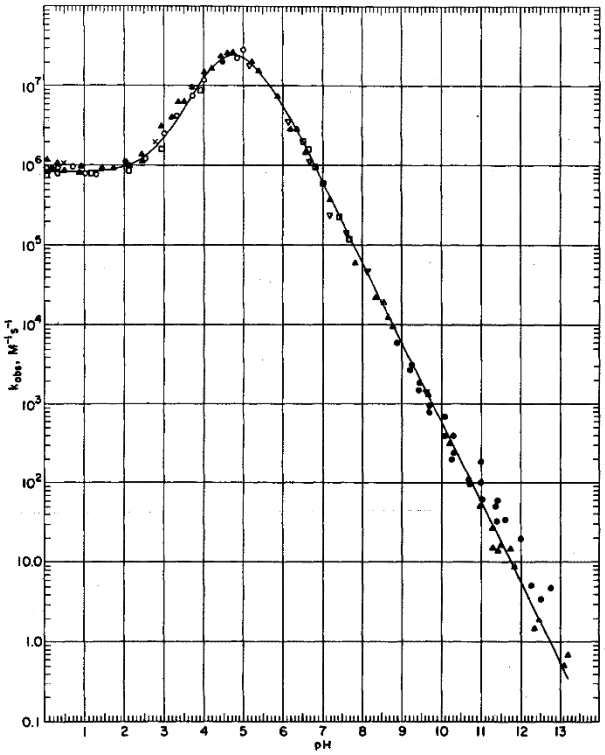

Figure 1: Second-order rate constant k_{obs} for the decay of HO_2/O_2^- plotted against the pH by Bielski *et al.*[6]

At higher pH, the contribution of protonated superoxide decreases, which slows down decomposition processes. This is due to the near absence of reactions between equally chared superoxide anions. Considering the above-mentioned disproportionation processes of superoxide in protic solvents the usage of $O_2^{\bullet-}$ in research is commonly focused on aprotic solvents as dimethyl sulfoxide (DMSO), dimethylformamide (DMF) and acetonitrile (MeCN). In such solvents, commercially available potassium superoxide KO_2 can be dissolved to ensure minimal loss of superoxide before the intended application. Superoxide in solution absorbs light with a maximum at around 250 nm, which makes it suitable for direct monitoring by UV/Vis. The role of superoxide in the human body is widely discussed field with many different research topics from the analysis of corresponding enzymes and their mimetics to the more recent role in biochemical redox signaling processes.[7]

1.2 Sources of superoxide

1.2.1 The mitochondrial electron transport chain

In general, superoxide and reactive oxygen species (ROS), along with reactive nitrogen species (RNS), can originate from both internal biochemical processes and external factors. The inherent complexity of intact cellular compartments represents a significant challenge to assign the production site precisely. Various experimental approaches have yielded different results depending on the designs of the study, yet there is an overall consensus that the primary source of superoxide in aerobic organisms is complex I of the mitochondrial electron transport chain (mETC).[8,9] The complex' fundamental function is the production of the universal energy storage unit adenosine 5'-triphosphate (ATP) via complex V (ATP synthase) while at complex IV (cytochrome c oxidase) oxygen is reduced to water (Figure 2). Ultimately superoxide will be transferred into the mitochondrial and subsequently cytosol where specialized enzymes decompose the radical species.

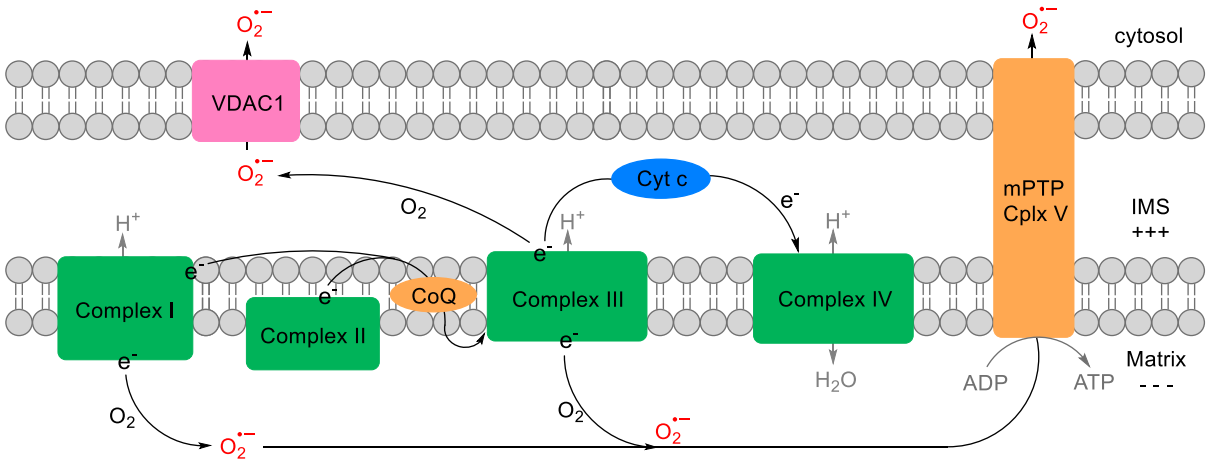

Figure 2: Schematic display of the mitochondrial electron transport chain, with possible superoxide expression sites highlighted in red adapted and reworked from Herb and Schramm.[10]

The ETC operates through a series of enzymatic complexes and cofactors that increase the potential difference between the intermembrane space and the mitochondrial matrix, generating a proton motive force that drives ATP synthesis at complex V. Complex I, primarily responsible for superoxide production within the mitochondrial matrix, transfers electrons via seven Fe-S clusters through the flavin mononucleotide (FMN) cofactor to the quinone cofactor (CoQ). In this cascade of redox reactions, a small portion of oxygen molecules (0.5-3 %)[11] is reduced to superoxide instead of being fully reduced to water. Given that Complex I contains at least 40 subunits, it is the most complex component of the electron transport chain (ETC). This complexity makes it particularly challenging to pinpoint the exact location where superoxide is produced. To date, the specific part of complex I, where ROS are generated, remains uncertain, though modern approaches and improving spectroscopic possibilities suggest two different possible pathways.

The first proposed pathway involves electron buildup in the Fe-S clusters, caused by inhibitors like rotenone or DQA. In presence of sufficient NADH at the FMN/$FMNH_2$ couple, which is likely under physiological conditions, superoxide production is highly probable, following the reaction displayed in Figure 3b). Thermodynamical calculations and numerous experimental investigations strongly support the flavin site being the main contributor to $O_2^{\bullet-}$ formation.[9,12]

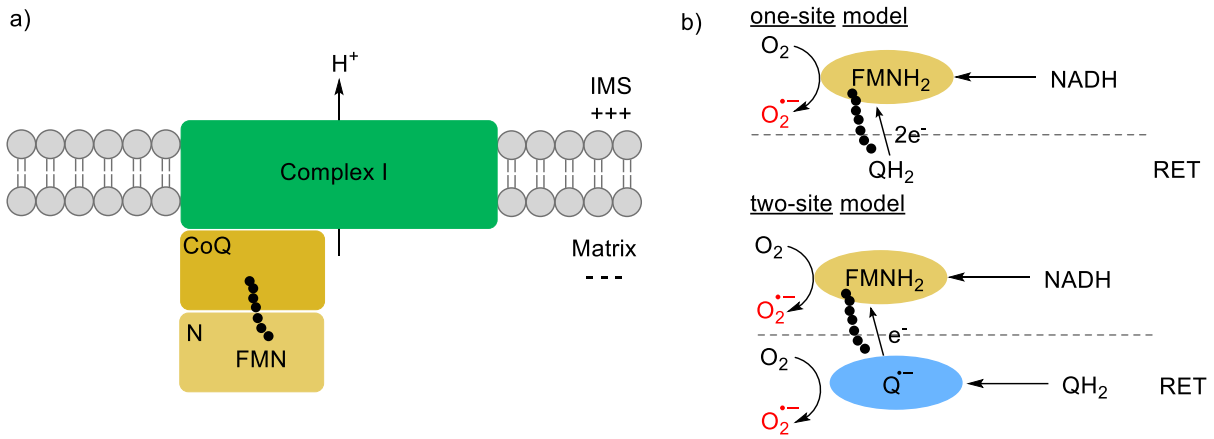

Figure 3: Superoxide production by complex I of the mETC. a) displays a detailed structure of complex I and cofactors b) the two possible mechanism which lead to superoxide adapted from Dröse *et al.*[13]

The second pathway is known as reverse electron transfer (RET), in which electrons will be transferred from complex II onto complex I. It has to be noted that for this pathway a high electrochemical membrane potential plus a proton motive force is fundamental to enable the possibility of superoxide production. For this route clarity about the exact formation site still stands out.[8,14] Due to backward electron transport, the Q-binding site of Complex I (NADH:ubiquinone oxidoreductase) becomes a critical region. Here, the semiquinone radical could potentially act as a redox partner for oxygen, facilitating the reduction of oxygen to superoxide. Latest works show that this pathway seems to be tissue-specific leaving an ongoing debate about its relevance.[13,15]

In addition to its indirect role in the RET, complex II is capable of producing superoxide independently, though this plays a rather minor role in overall ROS formation and therefore the exact mechanism was no matter of scientific interest yet.

In contrast to complexes I and II, complex III (cytochrome bc_1) releases superoxide not exclusively into the matrix but on both sides of the membrane. Complex III contains various subgroups and cofactors, which can vary depending on the organism. However, only three key proteins (cytochrome c1, cytochrome b and the Rieske iron-sulfur protein) are essential for its core functionality in the electron transport chain.[16,17] The catalytic processes in complex III involves two coupled steps (Figure 4). First, an electron is transferred from the ubiquinol (QH_2) cofactor via the binuclear iron-sulfur subunit of the Rieske protein onto cytochrome c_1 which ultimately passes it to complex IV of the ETC. Simultaneously two protons are transferred into the intermembrane space leaving the ubisemiquinone radical ($Q^{\bullet}$) as

the product at the ubiquinol oxidation site (Q_o). The remaining electron of $Q^{\bullet}$ takes an alternate path to the cytochrome b, which subsequently reduces a nearby ubiquinone (Q) at the ubiquinone reduction spot (Q_i) yielding another ubisemiquinone radical. The cycle is completed when a second ubiquinol is oxidized to ubiquinone, transferring two more protons into the intermembrane space and one electron enters the Rieske path towards complex IV. Finally, the second electron reduces the semiquinone radical ($Q^{\bullet}$) at the Qi site, with the addition of two protons from the mitochondrial matrix, resulting in the formation of ubiquinol (QH_2). The sequence of oxidation/reduction of ubiquinol/ubiquinone (Figure 5) is called the Q-Cycle and is the centerpiece of complex III. Together with the three aforementioned proteins, complex III plays a crucial role in the respiratory chain by facilitating electron transfer and contributing to the proton gradient necessary for ATP synthesis.

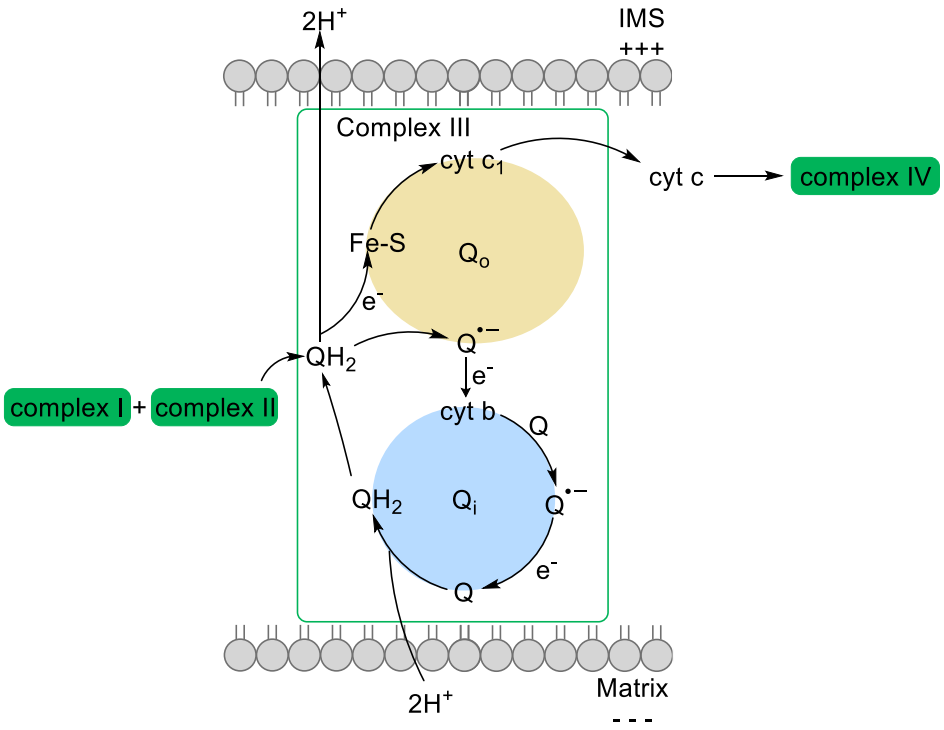

Figure 4: Schematic structure of the protonmotive Q-cycle based on the model from Guillaud *et al.*[18]

The concept of the Q-Cycle was first published in the pioneering work of Peter Mitchell in 1975[19] and since then it has been polished and refined. Even though it has been known for a long time the specific superoxide production mechanism has not been resolved yet. Experimental studies point to the Q_O site as the primary superoxide production site, but the structural details of this process are still unclear.

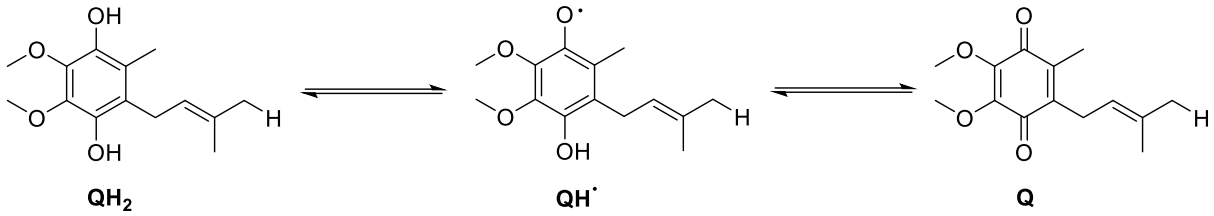

Figure 5: Redox cycling of ubiquinol to ubiquinone with the seminquinone radical intermediate.

As described above a potential intermediate in the catalytic mechanism of complex III is the ubisemiquinone radical, which has an unpaired electron and thus the chemical properties to reduce oxygen and form superoxide.[16,20] This pathway is widely accepted and the fact that a free radical is moving unhindered tends to be a logical explanation, even though there are other concepts which exclude a direct reaction between $Q^{\bullet}$ and molecular oxygen. In these hypotheses ubiquinone might act as redox mediator between cytochrome b and oxygen resulting in superoxide.[21]

1.2.2 Additional enzymes

Although mitochondria are the primary site of superoxide production, other enzymes also generate reactive oxygen species and contribute to oxidative stress. Among these the Cytochrome P450 (CYP450) enzymes are particularly noteworthy. The CYP450 family is a superfamily of heme-thiolate monooxygenase enzymes, which detoxify drugs and xenobiotics, but are also relevant for synthesis and metabolism of a wide range of biological active compounds, making it a versatile catalyst.[21,22] Nevertheless, the main reaction promoted by CYP450 is the oxidation of substrates (R in Figure 6) consuming present molecular oxygen. Highlighted are two possible uncoupled steps, which unintended can generate ROS (Figure 6).

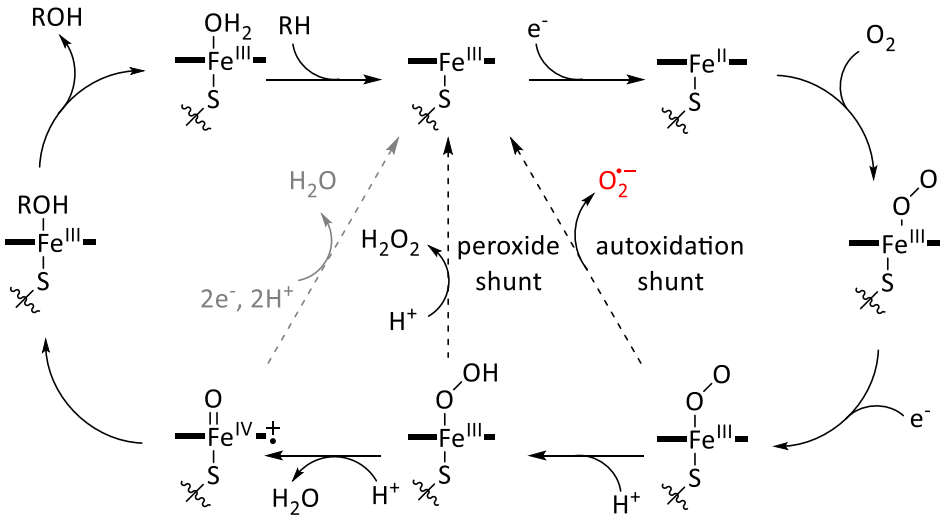

Figure 6: Simple catalytic cycle of the CYP450 family with potential superoxide production paths adapted from Denisov *et al.*[23] and Zagar *et al.*[24]

The “autoxidation shunt” pathway releases superoxide, which most likely will be transformed to hydrogen peroxide, while via the “peroxide shunt” hydrogen peroxide will be formed, both resulting in free ROS and the Fe(III) form of the enzyme. Even with sufficient substrate present, the cytochrome P450 enzyme can still produce reactive oxygen species (ROS). Its expression and activity, however, are influenced by various factors such as pH, oxygen availability, and the type of substrate present. These factors can modulate the enzyme's efficiency and the extent of ROS generation.[25,26]

Another significant enzyme responsible for superoxide production is the xanthine oxidase (XO), which catalyzes the sequential oxidation of hypoxanthine to xanthine and then further to uric acid (Figure 7).[27] During the oxidation, molecular oxygen is reduced to superoxide and expressed into the cytosol, the main cell compartment in which XO is present. The superoxide production of the xanthine/xanthine oxidase is well-studied and due to its reliable and steady production of superoxide, the XO system is frequently used in superoxide dismutase (SOD) assays, as discussed in chapter 1.6.1.[28,29]

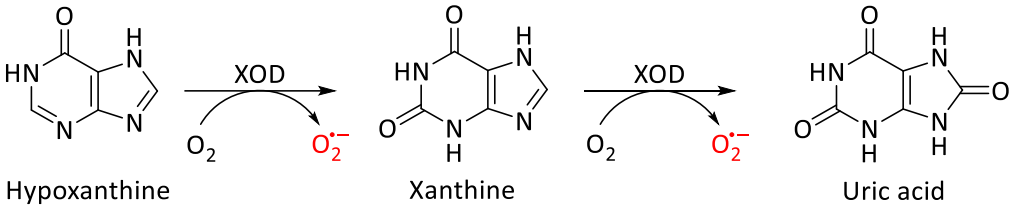

Figure 7: Superoxide production by the hypoxanthine/xanthine oxidase enzyme.

Unlike other enzymatic sources, where ROS is a byproduct, the NAPDH oxidase (NOX) family specifically generates ROS as part of its primary function. This family of transmembrane enzymes passes electrons from the nicotinamide adenine dinucleotide phosphate (NADPH) cofactor onto molecular oxygen, subsequently forming superoxide (Figure 8).

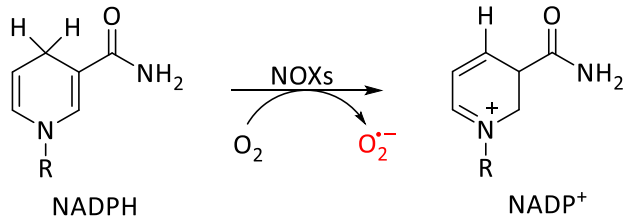

Figure 8: ROS generation by the NOX family.

This process is initially described in neutrophils, as essential group in immune defense mechanisms that can produce ROS.[30] Especially the second member of the enzyme family, NOX2, plays an important role in antimicrobial host defense by stimulating neutrophils when bacteria or various pathogens enter the human body.[31] The output of reactive oxygen species (ROS) by phagocytic cells is known as the "respiratory burst." During this process, ROS are released into the extracellular space, where they damage lipids and disrupt the cellular integrity of pathogens. This oxidative damage ultimately leads

to the destruction of the pathogens, allowing for their consumption by macrophages and contributing to effective immune protection.[32] Nevertheless, the superoxide and related highly reactive compounds produced during the respiratory burst do not specifically target pathogens. Instead, they can attack any nearby component, including host tissues, lipids and proteins, potentially leading to collateral damage in the surrounding environment. This makes the regulation of ROS production crucial to prevent excessive damage to host cells while ensuring effective pathogen destruction.

Apart from the main enzymatic sources of ROS mentioned above, additional, less prominent enzymes, such as those found in peroxisomes, lipoxygenases and certain components of the endoplasmic reticulum, can also generate superoxide. These represent additional endogenous sources of ROS within the cell, contributing to the overall pool of reactive oxygen species.[33]

1.2.3 External Sources of superoxide

While endogenous sources of superoxide dominate in biological systems, the increasing relevance of external sources needs to be addressed. Hand in hand with the increasing pollution of the natural environment and the rising levels of greenhouse gases, not only do we face climate change and global warming, but also the accumulation of ROS in the atmosphere. Especially fine particles, emitted by industrial facilities, car traffic and mineral dust from natural sources,[34] can be chemically transformed into long-living radicals as soon as they reach the atmosphere.[35] Reactants like ozone will alter the structure of these particles so they can cause oxidative damage to the respiratory tract of humans.[36,37] Connected to these fine particles is cigarette smoke, which also contains numerous deleterious chemicals, even free radicals and pro-oxidant species that can directly interact with tissue in lungs, causing pulmonary diseases and cancer.[38] But apart from cigarette smoke, nearly every emission from burning various compounds, e.g., firewood or plastic waste, contains free radicals.[39]

Besides the chemical alteration of pollutants in the atmosphere, radiation emitted by the sun might induce radical formation by photochemical processes.[40,41] UV light is known to have negative effects when overdosed, but it also plays an important role in the generation of ROS, leading to an increased concentration of harmful molecules in the air.[42] Additionally radiated light, especially exposure to UVB (290–320 nm) can damage human skin tissue and introduce radical species because of its deeper penetration through dermal layers.[41,43] Exposure to X-rays is less likely, but nonetheless, the interaction between human cells and this high-energy radiation can cause the production of ROS through water radiolysis. (Discussed in chapter 1.6.2)

Furthermore, consumption of food and the effects of malnutrition in formation of ROS gain more relevance in latest research. The impact on generation of superoxide is less due to direct radical-producing reactions and more related to the modulation of some of the above-mentioned enzymes, leading to an increased expression of pro-oxidant moieties.[44] Different components may cause various effects but especially (red) meat is connected to oxidative stress.[45] One possible explanation might be

the high level of ferrous ions contained by meat, which can further react and promote formation of ROS.[46] The second explanation is based on the oxidative decomposition products of lipids, which enhance development of harmful compounds and ultimately stimulate the NADPH oxidase to produce superoxide.[47] Also carbohydrates and unsaturated fatty acids, which are also a big part of western nutrition, seem to be associated with oxidative stress and enhance superoxide production.[45,48] The last relevant aspect that needs to be addressed is the deleterious effects of ethanol, generally referred to as alcohol, in terms of ROS production. It is well known that alcohol and its decomposition products are neurotoxins that damage neuronal connections and are therefore linked to various diseases.[49] Additionally, alcohol can trigger a member of the CYP450 family during digestion, which metabolizes alcohol and subsequently leads to increased superoxide production. It may also enhance the activity of xanthine oxidase, further contributing to oxidative stress.[50]

1.3 Reactive oxygen/nitrogen species (ROS/RNS)

Even though it is connected to many different pathological and harmful processes, superoxide itself is not highly reactive, but it can react with many precursor molecules to form a bouquet of reactive moieties, both ROS and RNS. Due to their deleterious effects in the human body, these compounds are involved into development and/or exacerbation of various diseases, including amyotrophic lateral sclerosis (ALS), Alzheimer's disease, Parkinson's disease, cancer and ultimately even the aging process. The term "ROS/RNS" is an umbrella term that does not provide information which exact chemical species of the many possible is involved in the damaging processes. In Figure 9 a rough overview of ROS and RNS formation under physiological conditions is displayed and the potential target molecules will be discussed further. Apart from their role in evolution of various pathological conditions, these radical species gain more and more importance in signaling processes and seem to play a much bigger role in aerobic organisms than indicated in former research.[51,52]

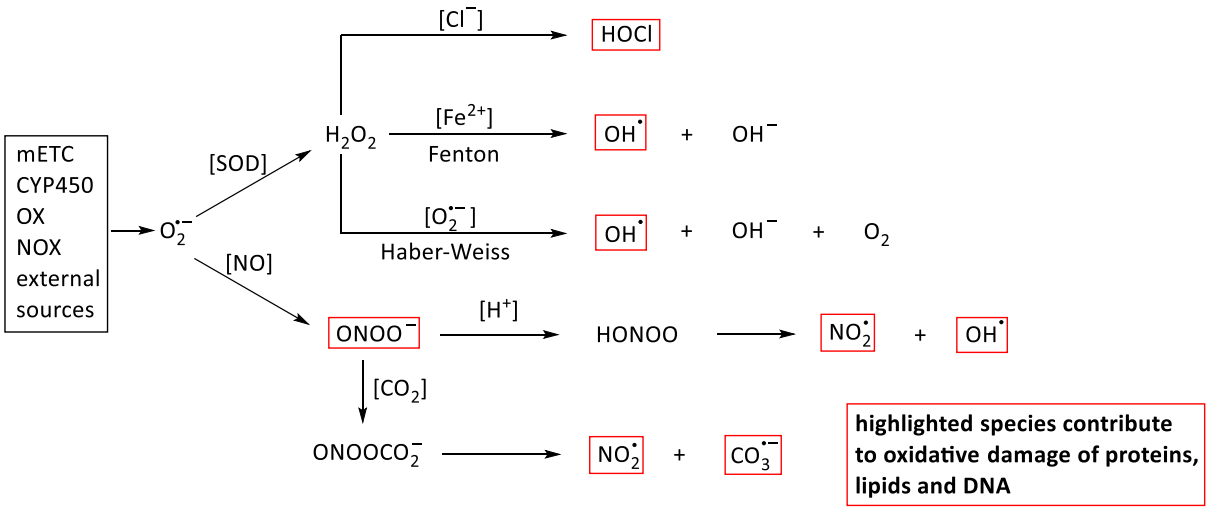

Figure 9: ROS/RNS generation with sources and highly potent agents highlighted in red.

Starting with a major ROS, hydrogen peroxide (H_2O_2), which is the product of the dismutation of superoxide, it can further react to form even more potent reactive species. In the presence of unbound iron(II) ions, the catalytic so-called Fenton-reaction leads to the hydroxyl radical ($OH^{\bullet}$).[53] Copper ions are also able to catalyze a similar reaction, with the same product which is among the most potent oxidizing agent. The highly reactive hydroxyl radical non-specifically oxidizes every adjacent biological matter near the diffusion limit (rate: $k \sim 10^9\ M^{-1}\ s^{-1}$). The Haber-Weiss reaction also yields $OH^{\bullet}$ through the interaction between superoxide and hydrogen peroxide.[54] Hydrogen peroxide also reacts with ubiquitous chloride ions (analogue with bromide) to form hypochlorous acid (HOCl), a potent oxidizing agent itself, which can again be converted into the hydroxyl radical.[55]

Another major pathway involves superoxide reacting with nitric oxide ($NO^{\bullet}$), a redox signaling molecule and vascular messenger produced by nitric oxide synthase, to form peroxynitrite ($ONOO^{-}$). This reactive nitrogen species is a versatile oxidant capable of attacking various biomolecules. However, even more significant are the decomposition products of protonated peroxynitrite. Once again, the highly reactive hydroxyl radical ($OH^{\bullet}$) is formed, along with the nitrogen dioxide radical ($NO_2^{\bullet}$), an atmospheric pollutant known for its harmful effects on the human respiratory system.[41] Alternatively, peroxynitrite can react with carbon dioxide (CO_2), leading to the formation of $NO_2^{\bullet}$ and the carbonate radical ($CO_3^{\bullet -}$), which also possesses pro-oxidative properties.

Lipid Peroxidation

The first potential target of these reactive radical species are polyunsaturated fatty acids (PUFAs). As a main part of cell membranes and due to their omnipresence in the environment of produced ROS/RNS, the double bonds of PUFAs can easily be attacked by corresponding oxidants. The resulting non-enzymatic series of radical reactions is referred to as lipid peroxidation (Figure 10), starting with a radical oxidation of a fatty acid (L) leading to a resonance stabilized alkyl radical ($L^{\bullet}$). This species reacts with oxygen to form fatty acid peroxyl radical ($LOO^{\bullet}$), which drives the chain reaction by subsequently converting a fatty acid into an alkyl radical and restarting the process. The second product of this reaction is the lipid hydroperoxide (LOOH) that decomposes into another peroxyl radical and various mobile electrophilic aldehydes, which can carry the attack to other parts of the cell or be toxic by themselves like e.g. malonaldehyde.[56-59]

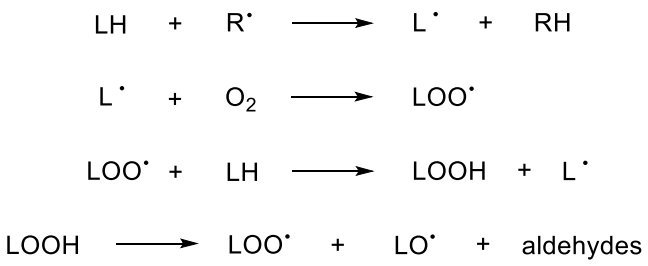

Figure 10: Lipid peroxidation by ROS and resulting radical cascade reaction adapted from Nimse *et al*.[60]

Another typical breakdown product of lipid peroxidation is 4-hydroxynonenal, which is known to be highly deleterious. It has been found in the brain cells of Alzheimer's disease patients, where it contributes to oxidative stress and neurodegeneration.[61,62] The resulting modifications of fatty acids are also connected to atherosclerosis, compromising the integrity of cell membranes and potentially leading to cell death.[63]

Protein Oxidation

The next relevant biological target species are proteins. They constitute around 70% of the dry mass of cells and tissues, making them omnipresent and highly susceptible to attack by ROS/RNS. Since the

structural differences in proteins are much more variable than in fatty acids, countless products are possible, which are nicely summarized in the literature.[64,65] But prominent interaction sites for oxidative modifications are the carbonyl side chains of proteins. Their alteration can lead to misfolding and aggregation, resulting in insoluble complexes or inactivation of enzymes.[66-68] The consequences of these changes are connected to cardiovascular and neurological diseases, as well as apoptosis.[69]

DNA and RNA Damage

The last biological relevant set of compounds that are decomposed and modified by oxidative stress are DNA and RNA. Mitochondrial DNA is much more likely to be targeted by ROS/RNS due to its proximity to the reactive radicals. Same as for proteins, the potential reactions between DNA and ROS are various, but can be broken down to a few relevant biochemical processes. The backbone sugars can be oxidized starting with proton abstraction by e.g. hydroxyl radical, resulting in structural disruption by strand breaking, hindering transcription and making replication impossible.[70,71]

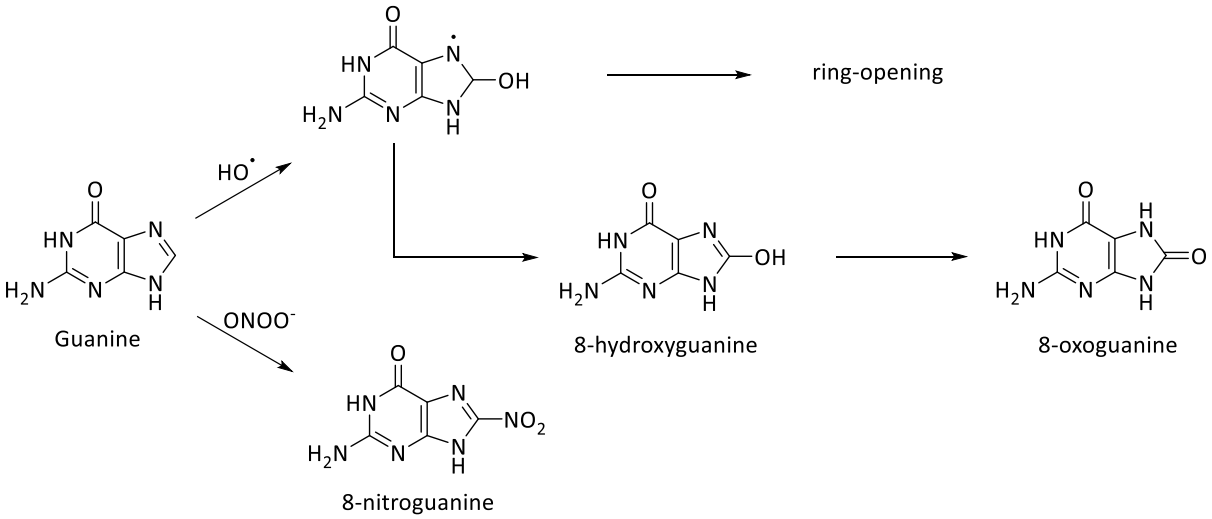

Figure 11: Oxidative modification of Guanine resulting in DNA damage based on the work from Juan *et al.*[66]

The hydroxyl radical can also react with nucleic bases like guanine, altering their chemical structure (Figure 11). The mechanism of oxidative damage at guanine is well-studied due to the fact that the modified product 8-oxo-7,8-dihydroguanine (8-oxoG), which is tautomer of 8-hydroxyguanine, is widely used as biomarker to indicate oxidative stress.[72] Attack site for $OH^{\bullet}$ is the double bond at C_8-position, converting the connected nitrogen (N_7) into a radical species and inserting the hydroxy group at the carbon atom. Reduction of this unstable intermediate results in 8-hydroxyguanine or via another pathway, in ring-opened moieties. 8-oxoG alteration of DNA cannot only force strand breaking, but also mispairing of base pairs resulting in mutagenic DNA species.[73] The second potential reaction is induced by peroxynitrite and leads to nitration at the C_8-position of guanine.[74] Usually these DNA alterations would cause repairing processes or decomposition of the modified strands, but the nitrated molecule is inert towards repair mechanisms, making it highly mutagenic. Eventually, the accumulation

of unrepaired DNA damage will lead to apoptosis or cancer and is also connected to the aging process.[75,76]

The presented harmful impacts of excessively generated ROS on biological organisms are commonly known as oxidative stress. The involvement of this phenomenon in various pathological conditions and even the aging process is widely accepted and remains an ongoing subject of current research. However, it is important to note that while ROS may be implicated in these diseases, they are not necessarily the fundamental cause of them.

1.4 Native Superoxide Dismutase Enzymes

The complex and widespread deleterious effects of superoxide and its follow-up reactive oxygen species made it crucial for aerobic organisms to develop defense tools to protect their cells from oxidative damage. The group of metalloenzymes responsible for controlling and catalytically degrading superoxide in a two-step reaction are called superoxide dismutase (SOD). This enzyme family can be divided into four subgroups based on the transition metal center. These subgroups include copper/zinc-containing (Cu/Zn-SOD), manganese-containing (Mn-SOD), iron-containing (Fe-SOD) and nickel-containing (Ni-SOD) enzymes. Depending on their localization in mammalian organisms, SOD enzymes can be further categorized into the cytosolic Cu/Zn enzyme (SOD1) and a special Cu/Zn isoform, only present in the extracellular space (SOD3 or EcSOD). Additionally, the most important SOD enzyme in humans, the Mn-SOD (SOD2), is located only in mitochondrial matrix, the main accumulation site of ROS. Fe-SOD are present in bacteria and plants and Ni-SOD can be found exclusively in prokaryotic organisms. Since superoxide penetrates membrane very poorly, it is necessary to interfere in the respective compartment of the cell to prevent further damage. Regardless of the specific metal center, each enzyme in this family has a redox potential (~ +0.300 mV vs. NHE)[77] that falls approximately between the reduction potential for the oxygen/superoxide (-0.160 mV vs. NHE) and superoxide/hydrogen-peroxide redox couples (+0.890 mV vs. NHE), making them ideal catalysts for both redox reaction steps.

$$M^{n+} + O_2^{\bullet -} + H^+ \longrightarrow M^{(n-1)+}(H^+) + O_2 \quad (5)$$

$$M^{(n-1)+}(H^+) + O_2^{\bullet -} + H^+ \longrightarrow M^{n+} + H_2O_2 \quad (6)$$

Native SOD enzymes follow a redox cycle shown in eq. 5 and eq. 6, that can be defined as “ping pong” mechanism. The metal center is either oxidized or reduced, while superoxide undergoes the opposite process, allowing it to remain constantly ready to react with additional present radicals. To prevent further formation of ROS, SOD alone is not sufficient, since one of the decomposition products is hydrogen peroxide, which can break down into the highly reactive hydroxyl radical. Therefore, SOD activity is closely linked to catalase activity, as catalase converts hydrogen peroxide into water and oxygen (eq. 7), thereby minimizing the potential for further oxidative damage.

$$2H_2O_2 \xrightarrow{\text{Catalase}} O_2 + 2H_2O \quad (7)$$

The cofactors of each enzyme in the SOD family and the chemical structure of the proteins induce an ideal electrostatic guidance for superoxide radicals to reach the metal center. The combination of these factors allow SOD to neutralize $O_2^{\bullet -}$ only limited by diffusion ($k \sim 10^9\ M^{-1}\ s^{-1}$) and preserve cellular integrity. Nevertheless, not all isoforms follow the same mechanism due to different structural conformations and transition metals mediating the catalytic activity.

1.4.1 Cu/Zn-SOD (SOD1 & SOD3)

Originally isolated by Mann and Keilin in 1938 from bovine erythrocytes, the blue-colored copper-containing protein was named haemocuprein.[78] Irwin Fridovich and McCord isolated and identified the human analogue enzyme responsible for the dismutation of superoxide in the human body, which they named superoxide dismutase (SOD).[79] These discoveries set the fundament for a broad and growing field of research in identification and characterization of the whole enzyme family. In 1982, the first resolved three-dimensional crystal structure of Mann and Keilin's bovine haemocuprein was discovered,[80] followed by the human Cu/Zn-SOD in 1992, unveiling the first deep details in protein architecture of this enzyme.[81]

SOD1 is a homodimer with both subunits containing a copper and a zinc ion, whereas the cuprous ion is the redox-active part, and the zinc ion is present to preserve the enzymatic structure and correct protein folding. Switching between the oxidation states Cu^{2+} and Cu^{+}, during the catalytic cycle, also results in changes in the coordination geometry at the metal center.[82] The copper ion is connected to four histidines (His46, His48, His63 and His120) and one solvent molecule (water) when it's in oxidation state 2+. His63 functions as bridging ligand to the zinc ion and when Cu^{2+} interacts with a superoxide radical, the connection to this residue will be lost and it rests completely at the Zn site. Apart from His63, there are two more histidine and one aspartic acid moiety connected to the zinc site.[83] Redox potential of SOD1 has been reported to be located in the range between +320 mV and +400 mV vs. NHE depending on origin and form, which is slightly higher than in other native enzymes of the family.[84,85] Nevertheless, it still remains in the region for optimal superoxide dismutation, except when an inhibitor molecule like the cyanide anion binds to the enzyme, changing the redox potential to -440 mV, which is then out of reach for SOD catalysis.[86]

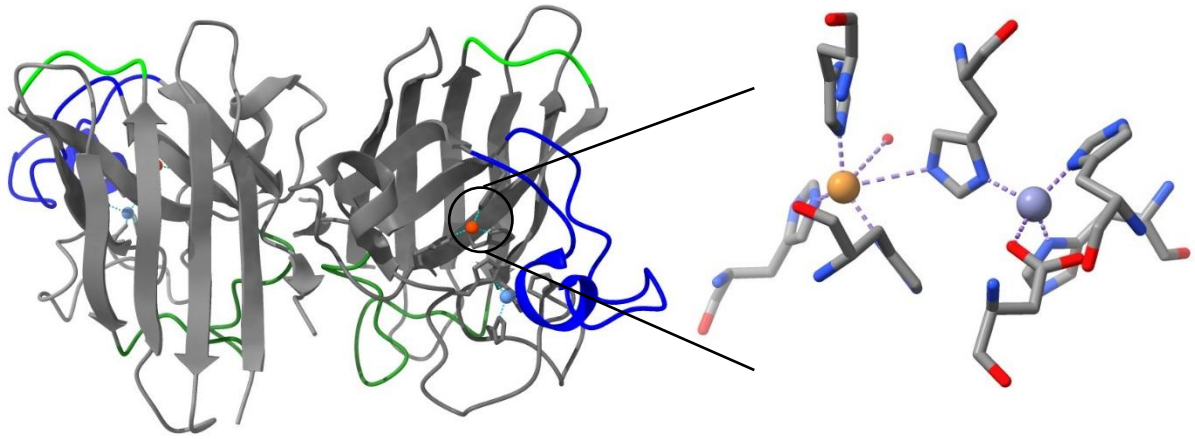

Figure 12: Stereo ribbon diagrams of dimeric human Cu/Zn-SOD (PDB code 1PU0[87]). Copper and zinc ions are highlighted, while proteins structures relevant for electrostatic guidance are shown in green and blue, adapted from Perry *et al.*[88] On the right side, a zoom into the enzymatic pocket is provided to illustrate coordination geometry. To display the crystal structure ChimeraX visualization program was used.[89]

Figure 12 depicts a stereo ribbon diagram of humas SOD1[87] that is present as homo dimer. Shown is the front view of the crystal structure, with Cu^{+} ions highlighted in red (with three-fold coordination characteristic for Cu^{+}) and Zn^{2+} ions highlighted in purple. Additionally, the important regions involved in the electrostatic guidance of superoxide towards the metal centers are color-coded for clarity. The so-called "electrostatic loop" is shown in dark blue, which has the main effect on substrate steering, consisting of charged and polar residues. In green are displayed the antiparallel β-strands forming Greek key connections, which also contribute to the electrostatic guidance of the superoxide radicals towards the metal centers.[88] In addition to the protein structures that leads $O_2^{\bullet-}$ directly to the redox-active metal center, making the dismutation of the radical effective and efficient, the enzymatic pocket provides space specifically suited for the size of superoxide. This selective binding prevents other negatively charged ions, such as phosphate, from entering and potentially blocking or inhibiting the activity near the copper ion. Especially the copper near arginine residue (Arg143) plays a major part in both synergic processes, by maintaining a positive charge that directs the superoxide anion towards the copper ion while simultaneously limiting the space in the enzymatic pocket. The crucial role of Arg143 has been demonstrated in experiments where SOD1's activity was reduced by 90% when the positively charged arginine was replaced by a neutral isoleucine residue, and approximately halved when replaced with a positively charged lysine residue.[90]

The first half of the catalytic cycle of Cu/Zn-SOD's (eq. 8), dismutation starts with a Cu^{2+} metal center, which is bound to the bridging His63. An arriving superoxide will be oxidized to molecular oxygen by the copper ion, leaving it in the reduced state. This is followed by bond cleavage with the bridging histidine residue, which becomes protonated, leading to the loss of the solvent molecule. Subsequently, the coordination sphere changes from a distorted pyramid in the Cu^{2+} state to a near trigonal planar structure. In the second half of the reaction (eq. 9), another $O_2^{\bullet-}$ reaches the now Cu^{+} metal center, where it is reduced. His63 then contributes its proton to the reaction, completing the dismutation process. Coordination of the deprotonated histidine will restore the initial coordination geometry and the reduced and protonated superoxide either leaves the pocket as HO_2^{-}, or it is further protonated by omnipresent protons resulting in hydrogen peroxide.[91] During the whole cycle, zinc remains in its four-fold coordination, preserving the enzyme's structural integrity and ensuring its activity.

$$\text{His63-Enzym}(Cu^{2+}) + O_2^{\bullet-} \xrightarrow{[H^+]} \text{His63-H} + \text{Enzym}(Cu^{+}) + O_2 \quad (8)$$

$$\text{His63-H} + \text{Enzym}(Cu^{+}) + O_2^{\bullet-} \xrightarrow{[H^+]} \text{His63-Enzym}(Cu^{2+}) + H_2O_2 \quad (9)$$

It should be noted that, apart from the defensive mechanisms performed by SOD1 and the associated protective effects against neurodegenerative diseases, studies indicate a link between mutated forms of SOD1 and amyotrophic lateral sclerosis (ALS), particularly familial amyotrophic lateral sclerosis (FALS). Abnormal accumulation of the respective mutant proteins in neuronal cells and even the wild

Cu/Zn-SOD itself can lead to pro-oxidative effects. [88,92,93] Therefore the enzyme's function is regulated by a co-enzyme, the copper chaperone CSS, which is responsible for incorporating the metal into the enzyme.[94] Nevertheless, some mutated SOD1 proteins are released into the intermembrane space or function independently of the copper chaperone CSS, and in both cases, the protein may still aggregate.[83]

SOD1 is primarily located within the cell, limiting its ability to provide antioxidative protection against ROS outside the cell membrane. In contrast, a specialized form of SOD1, known as SOD3, also containing copper and zinc ions, is exclusively found in the extracellular space. This unique localization allows SOD3 to neutralize ROS in areas inaccessible to other SOD enzymes. The genetic similarities between the Cu/Zn-containing SOD1 and SOD3, but not with other SOD family members, suggest that SOD3 evolved from SOD1 during an early phase of evolution.[95] Due to this fact it's not surprising that there are only a few structural differences between the protein folding of SOD1 and SOD3.

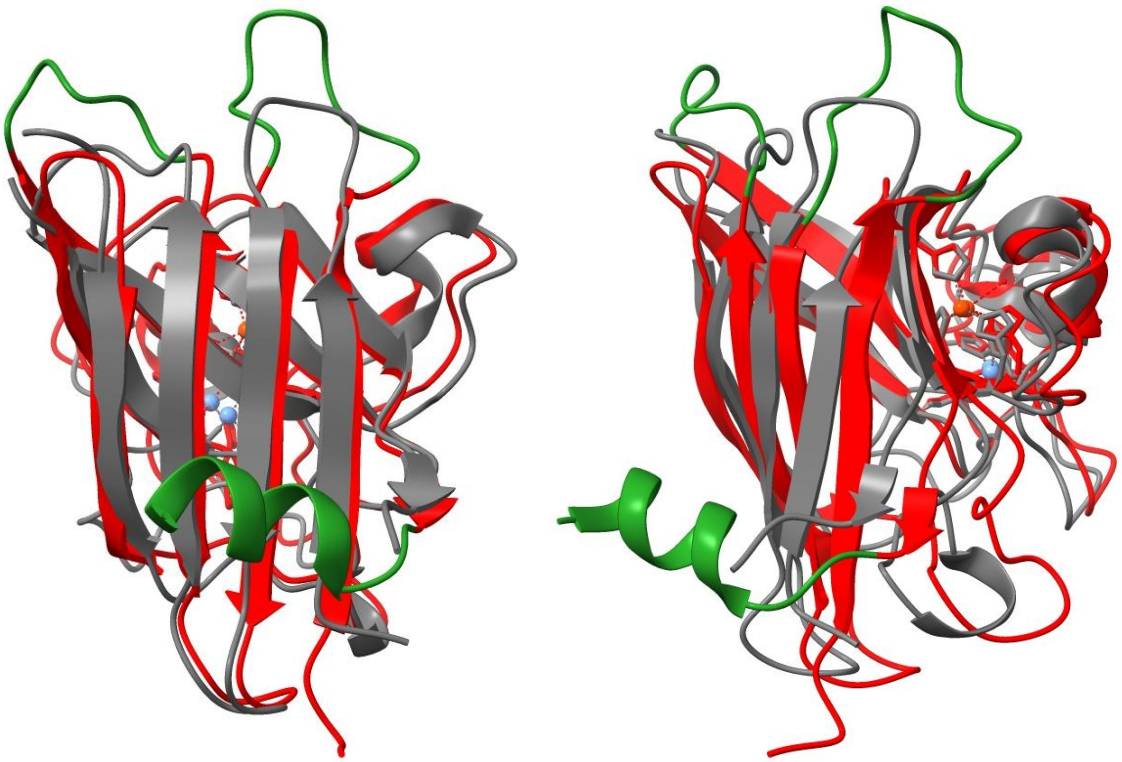

Figure 13: Overlay of SOD3 (in red; PDB code: 2JLP[96]) and SOD1 (PDB code: 1PU0[97]) stereo ribbon diagrams, a front (left) and a side view (right), to demonstrate structural differences. Relevant variations are highlighted in green based on the model of Antonyuk *et al*.[96] To display the crystal structure ChimeraX visualization program was used.[89]

Structural similarities are even more evident when both protein monomers are positioned above each other as in Figure 13, in which SOD3 is colored in red, and the most prominent differences are highlighted in green. Two different views, a front and a side view, are displayed in Figure 13, with copper ions shown in orange and zinc ions in light blue, similar to Figure 12 for SOD1. The two green

loops at the top, identified as Loop I and Loop III, play a crucial role in protein folding and appear elongated. Additionally, an extra residue is visible at the front, representing the C-terminus. Beyond these structural distinctions, an extra N-terminus unit and a disulfide bridge further reinforce the structural framework of the protein. Thus, the main parts relevant for efficient enzyme function remain in almost identical positions, including metal centers and the electrostatic loop. Therefore, it is not surprising, that both Cu/Zn-SODs can achieve the same turnover rates in decomposing superoxide.[97]

1.4.2 Fe-SOD

Another member of the SOD family contains iron as metal center and can be found mainly in prokaryotes, even though it is also present in many eukaryotes like plants. The first Fe-SOD was discovered in the year 1973 in escherichia coli bacteria, by Yord and Fridovich.[98] Since then, a variety of structurally similar enzymes have been identified in organisms such as bacteria, plants, and parasites. However, they appear to be absent in animals and fungi.[99-101] While dimeric Cu/Zn-SODs exclusively show an antiparallel β-strand Greek protein folding, the tetrameric Fe-SOD rather consist of α-strands and β-strands mixed. Since the Fe^{3+}/Fe^{2+}-pair has a redox potential of +770 mV (vs. NHE), that is already positioned between the two superoxide decomposition reactions, no significant redox tuning by the ligand environment is required. The iron center is coordinated by three histidine and an asparagine residue with an additional water molecule/hydroxy, which leads to a five-fold trigonal bipyramid (Figure 14). Like SOD1, the protein structure around the metal center provides an electrostatic guidance, which leads the substrate into the enzymatic pocket.[102]

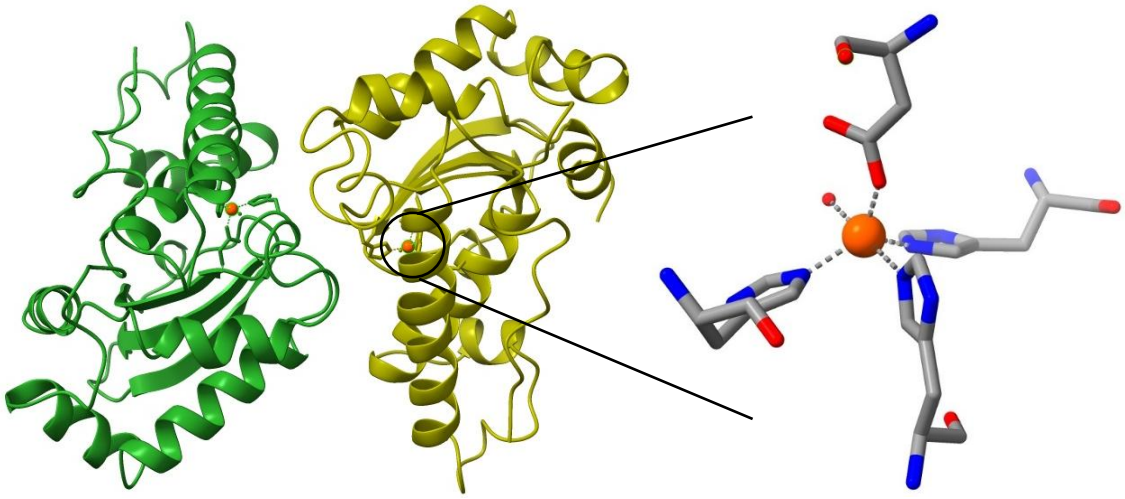

Figure 14: Stereo ribbon diagram of Fe-SOD (PDB code: 1ISB[103]) isolated from *E. coli* with a zoom into the coordination environment around the iron center on the right. The iron ion is highlighted in orange and coordinated water in red. To display the crystal structure ChimeraX visualization program was used.[89]

Mechanistic studies of iron containing SOD showed fundamental differences between the different enzymes. Unlike Cu/Zn-SOD, Fe-SOD does not undergo structural changes during the catalytic dismutation of superoxide. Instead, it maintains its five-fold coordination throughout the process.

Additionally, the bound water/hydroxy molecule which plays no role in redox cycling by SOD1, seems to be crucial for maintaining Fe-SOD's activity by donating a proton for the reduction of superoxide. Starting with the first half of the catalytic cycle, superoxide coordinates to the Fe^{3+} center following an inner-sphere mechanism, donating an electron and leaving the center as neutral molecular oxygen. Consequently Fe^{3+} gets reduced, and the coordinated hydroxy anion gets protonated by always present water. The exact process for the second half of the cycle is still not fully understood. Due to above-mentioned Fenton chemistry, which can be carried out by Fe^{2+} ions, it seems unlikely that superoxide will directly coordinate to the reduced metal center. A common method to determine whether the half-reactions of SODs follow an outer or inner-sphere mechanism is the integration of an azide anion (N_3^-), an ideal substitute for the labile and highly reactive superoxide anion radical. Detection of the bound azide indicates an inner-sphere mechanism, but for the second half, no coordination could be observed.[103] This leads to the assumption that superoxide reduction rather follows an outer-sphere process in which a proton-coupled-electron-transfer (PCET) from the coordinated water takes place together with an electron from the metal center. In contrary to SOD1, the required second proton does not come from a coordinated histidine residue. Its exact source is still in discussion. Since one tyrosine residue might participate in the redox cycle of a neighbored monomer, which can be brought near the now protonated hydroperoxyl species (HO_2), it is possible to consider it as proton source.[102]

1.4.3 Mn-SOD (SOD2)

The most important superoxide dismutase enzyme, according to many different knock-out experiments, is the manganese containing SOD or SOD2. Previous investigations have shown that the absence of Mn-SOD is a guarantee for the death of the respective organism.[104,105] SOD2 is especially fundamental for the human body as a defense mechanism against oxidative stress, as it is located specifically in the mitochondrial matrix, which is the primary site for superoxide production. The ligand environment of Mn-SOD is the same as it is for Fe-SOD, with three histidine residue, one asparagine residue and a water/hydroxy bound to the metal center. In general, both enzymes show so many similarities, that the concept of a shared evolutionary origin is widely accepted.[106] Experiments, in which rats were treated with an external inflammatory agent to generate inflammation and afterwards received and external supply of isolated human Mn-SOD showed a bell-shaped correlation between activity and dosage.[107] Hence, small concentrations of the native enzyme can conduct great activity towards superoxide up to a certain point (k_{cat} = 10^9 M^{-1} s^{-1}), from which the reactivity decreases again.[108]

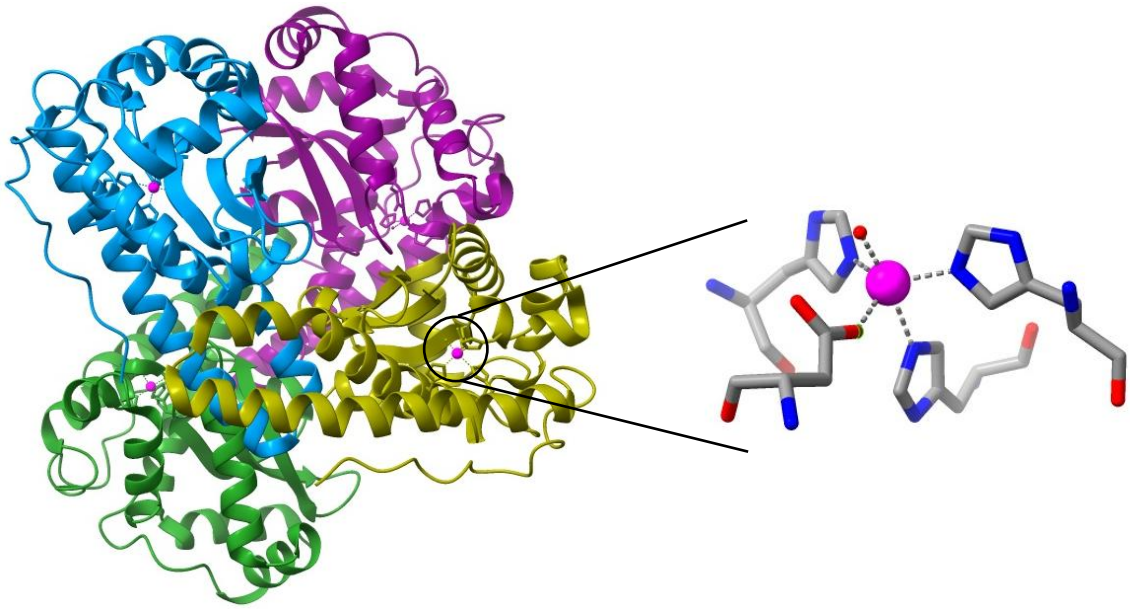

Figure 15: Stereo ribbon diagram of human Mn-SOD (PDB code: 1LUV[109]). Highlighted in purple is the manganese center of SOD2 and on the right a zoom into the enzymatic pocket is depicted. To display the crystal structure ChimeraX visualization program was used.[89]

The five-fold coordination might be disturbed during catalytic activity of SOD2. Although the discovery of the Mn-SOD enzyme was nearly 60 years ago, there is still no consensus on the exact mechanism used during superoxide dismutation. Different approaches have led to three proposed mechanisms, each supported by its own experimental data. The most common and widely accepted reaction path is called the 5-6-5 mechanism, related to the change in the coordination sphere when the superoxide anion reaches the active site.[103] Thus, the trigonal bipyramid dynamically shifts towards an octahedral coordination, which will then be restored after completed substrate decomposition. Closely related is

the associative displacement mechanism from Whittaker and Whittaker,[110,111] which suggests an inner-sphere mechanism as well, but instead of a changed geometry, the active site remains in its five-fold coordination with superoxide replacing a bound ligand, most likely the water molecule. The third mechanism relies on DFT calculations, which contradict the theory of an associative mechanism and rather propose the dismutation via an outer-sphere process.[112] Superoxide could be brought near the metal center via electrostatic guidance but instead of directly binding to the manganese ion, it remains in proximity due to hydrogen bond interactions and will be converted there. The DFT calculations were supported by NMR studies, which could not detect azide coordination to the metal center for *E. coli* Fe-SOD.[113]

Due to the structural similarities and the equivalent amino acids coordinated to the metal center, certain enzymes in specific organisms can integrate either manganese or iron as the metal center without losing their activity towards superoxide. These so-called cambialistic SODs are quite rare in biology, often found in anaerobic organisms and the preservation of activity displays an unusual behavior, since metal exchange normally results in diminishing or even complete inhibition of enzyme function. Figure 16 depicts a Fe-SOD in purple and an iron-substituted Mn-SOD in yellow, highlighting the structural similarities and the comparable ligand environment.[106]

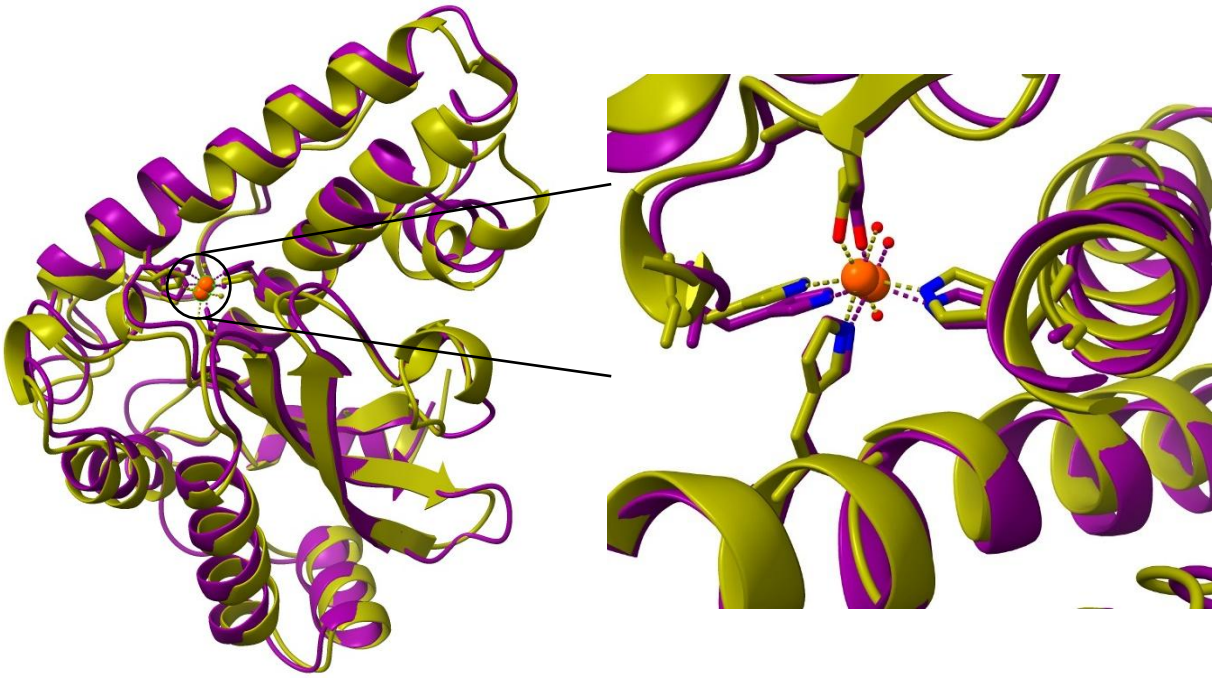

Figure 16: Overlay of Fe-SOD in purple (PDB code: 1ISB[103]) and Fe substituted Mn-SOD in yellow (PDB code: 1MMM[114]) of *E coli*. which demonstrate the structural similarities. Iron centers are highlighted in orange, with a zoomed-in view on the right showing the overlapping structure, adapted from Miller.[105] To display the crystal structure ChimeraX visualization program was used.[89]

1.4.4 Ni-SOD

The most recently discovered member of the SOD family is the nickel containing enzyme, found in streptomyces bacteria in 1996.[115,116] Since then, other organisms, almost exclusively bacteria, possessing this protein have been identified, with the majority found in oceans. None of the different Ni-SODs shares genetic sequence homology to the other SODs, indicating this subgroup evolved independently.[117] The fact that nickel is not commonly known to activate oxygen, and that most enzymes, not just SODs, typically possess zinc, iron, or copper as metal centers, makes Ni-SOD an interesting specimen.[118] Even though Ni-SOD definitely differs from the other SODs, it also shares many similarities and exhibits analogous behavior. Ni-SOD is a homohexamer, as depicted in Figure 17, and always contains a mixture of oxidized and reduced forms of nickel at the center of each respective monomer.[82] The extraordinary high redox potential of the Ni^{2+}/Ni^{3+} pair in aqueous solution, which exceeds +2.0 V (vs. NHE), places it beyond the typical range for SOD dismutation and thus makes it far out of reach for the usual catalytic processes involved in superoxide dismutation.[119,120] Therefore, a strong redox tuning ligand field is necessary to push the enzyme's potential into the catalytic active region. Compared to other SODs, Ni-SOD has an unusual protein environment, with two cysteines binding to the metal center. One cysteine, Cys6, coordinates to the nickel via an electron-rich thiolate, while the other, Cys2, binds through both thiolate and amide groups. Additionally, only one histidine (His1) is coordinated to the nickel, with its amino and imidazolate groups involved in coordination. The imidazolate is coordinated in an axial position, but this axial coordination is lost when the enzyme is in the Ni(II) reduced state. The amino acids are orientated in a way, which can be structurally described as hook-like shape, delivering the name for this section.

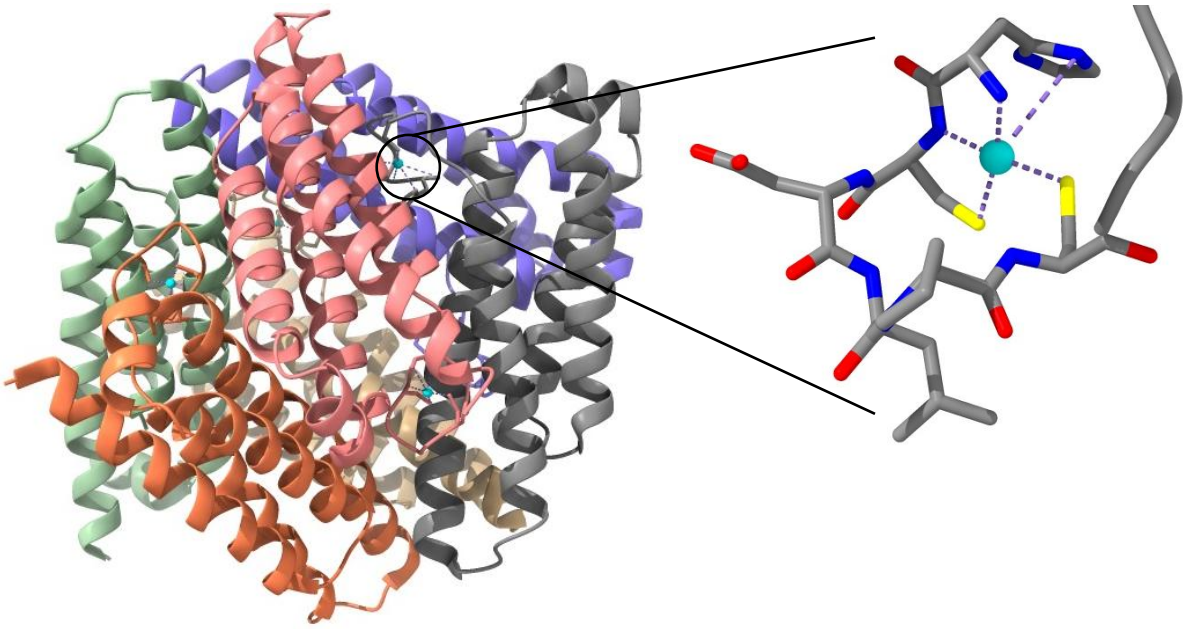

Figure 17: Stereo ribbon diagram of hexameric Ni-SOD (PDB code: 1T6U[121]) isolated from *S. coelicolor*. The nickel center is highlighted in cyan and on the right the Ni-hook motif is presented. To display the crystal structure ChimeraX visualization program was used.[89]

The "Ni-hook" motif, along with the related coordination environment shown on the right side of Figure 17, help to alter the redox potential of Ni-SOD to 290 mV (vs. NHE), bringing it into the desired range for catalytic activity.[122] Additionally, it plays a crucial role in holding the nickel ion in place within the enzyme, ensuring its stabilization. The motif can also provide electrostatic guidance for the substrate into the enzymatic pocket, as has been described for Cu/Zn-SOD. Even though positively charged residues can help guide superoxide into the active site of Ni-SOD, different ion-dependent assays have concluded that this electrostatic guidance plays a minor or negligible role in the catalytic activity of the enzyme.[123] Varying the ion concentration had almost no influence on the high dismutation rate, at the diffusion limit, of the nickel containing enzyme. The Ni-hook is not only fundamental for the SOD catalysis of the enzyme but also protects the oxidative labile thiolate residues of the cysteines., ensuring the stability against oxidative modifications and ultimately inactivation of Ni-SOD.

Ni-SOD also undergoes structural changes during redox cycling. Starting with a planar quadratic N_2S_2 coordination sphere in the reduced Ni^{2+} form, Ni-SOD features two cysteines that bind to the metal center via their thiolates and one amide group and a histidine residue bound through its terminal amine. Upon oxidation to Ni^{3+} the imidazole of this histidine additionally coordinates to the metal center in axial position, leading to a five-fold quadratic pyramidal structure. Apart from the general understanding, the exact mechanism of the catalytic cycle remains under discussion and is the subject of ongoing research. For other SODs, N_3^- coordination has been detected, but Ni-SOD shows only a weak affinity for the anion, suggesting that outer-sphere mechanisms are more likely involved.[124] Synthetic structural mimics of Ni-SOD with peptide ligands tend to favor an inner-sphere mechanism[125,126] Together with the free coordination site in the Ni^{3+} enzyme, the active channel topology of Ni-SOD seems to support the inner-sphere theory according to Barondeau *et al*,[127] even though they also detected no coordination of azide at the metal center. Nevertheless, there are still computational studies and some experiments that suggest an outer-sphere mechanism is more likely. This ongoing debate leaves the exact mechanism unclear, with no definitive conclusion reached yet.[128-130] Another key aspect of superoxide dismutation by Ni-SOD that is actively discussed is the source of protons for the reduction of superoxide in the overall mechanism. In Cu/Zn-SOD, the protonated histidine seems to be crucial for catalysis, but in the nickel enzyme the His1 residue is on the opposite site from the substrate coordination site, making it impossible to influence the reaction. Therefore, the bound sulfur atom of Cys2 seems to take the role of proton delivery during PCET-like reduction of superoxide to hydrogen peroxide.[131] Even though the specific mechanism is not fully understood, Ni-SOD found it's very own way of efficient superoxide dismutation providing protection for mainly bacteria.

1.5 Superoxide Dismutase mimics

In conditions of excessive superoxide production and the related overextension of protective mechanism, such as those provided by the native SODs, the oxidative stress has an even greater impact on tissues and the entire organism. Therefore, an adequate definition of oxidative stress is not simply the overaccumulation of ROS (as discussed in Chapter 1.3), but rather a disbalance between the overwhelming production of superoxide and the capacity of natural defense mechanisms to neutralize it, leading to the subsequent damage caused by these highly reactive species. Especially in terms of diseases or pathological conditions as inflammation, oxidative stress plays a crucial role. To support the organism's own protective enzymes during this disbalance, the idea of designing redox active molecules with similar superoxide-neutralizing properties gained momentum. The enzymes themselves, due to their large molar mass, which limits cell permeability, and the potential to trigger antigenicity , were found to be unsuitable as potent therapeutics. To overcome these challenges low molecular mass compounds were designed, which are expected to combine the best of both worlds.

This group of superoxide dismutase mimics (SODm) need to unite several demands in their chemical properties to serve as ideal mimics and to be considered as effective therapeutic agents. In general, the presence of metal center (mostly Fe and Mn) tends to be fundamental to ensure redox activity, even though in recent research the trend towards purely organic antioxidants, due to their ubiquitous biological presence, has started to attract increasing attention. The most fundamental chemical behavior for these molecules is their efficacy against superoxide. Consequently, similar to the native enzymes, the redox potential of SODm needs to be positioned between the oxidation potential of superoxide at -160 mV (vs. NHE) and its reduction potential at +890 mV (vs. NHE). Ideally, the redox potential should be around +300 mV (vs. NHE) to ensure optimal catalytic redox cycling during superoxide decomposition. The ligand framework is usually responsible for tuning these properties but can also be modified in a way that allows electrostatic guidance for the substrate towards the active site, similar as in the SOD enzymes and integrate a well-defined bulkiness as well to ensure a selectivity towards superoxide.

Other points might not directly influence the experimental activity of SODm against superoxide but will have a relevant impact on the application as therapeutic agents. Strongly connected to the ligand framework is the overall stability of the metal complex, since free metal ions can express prooxidative effects or even be cell toxic, e.g. Fe^{2+} or Cu^{2+}. Finally, the antioxidants need to maintain amphiphilicity by balancing sufficient lipophilicity to penetrate membranes and reach the mitochondria within the cell, while also preserving hydrophilicity to remain soluble in aqueous buffered solutions, which represent physiological conditions. Based on these desired characteristics, many different approaches towards SOD mimics have been developed, some built on the foundation of biological models.

1.5.1 Classic approaches

Copper containing SODm

Copper-containing SODm compounds were among the first developed mimetics due to copper's natural role in the Cu/Zn enzyme. One of the main drawbacks of Cu^{2+} is the cytotoxicity of free copper ions due to the fact that there are able to perform Fenton chemistry, similar to free iron ions.[132] Additionally, cuprous ions in aqueous and buffered solutions have proven themselves to be great SOD mimetics with rates close to the native Cu/Zn-SOD enzyme, without coordination to any ligand system.[133-135] Consequently, it was needed to achieve a thermodynamically stable complex to ensure only minor metal release, while preserving, or only slightly diminishing, the existing SOD activity of copper.[136] Nevertheless, many metal complexes that combined the desired characteristics emerged following different approaches with decent k_{cat} values.

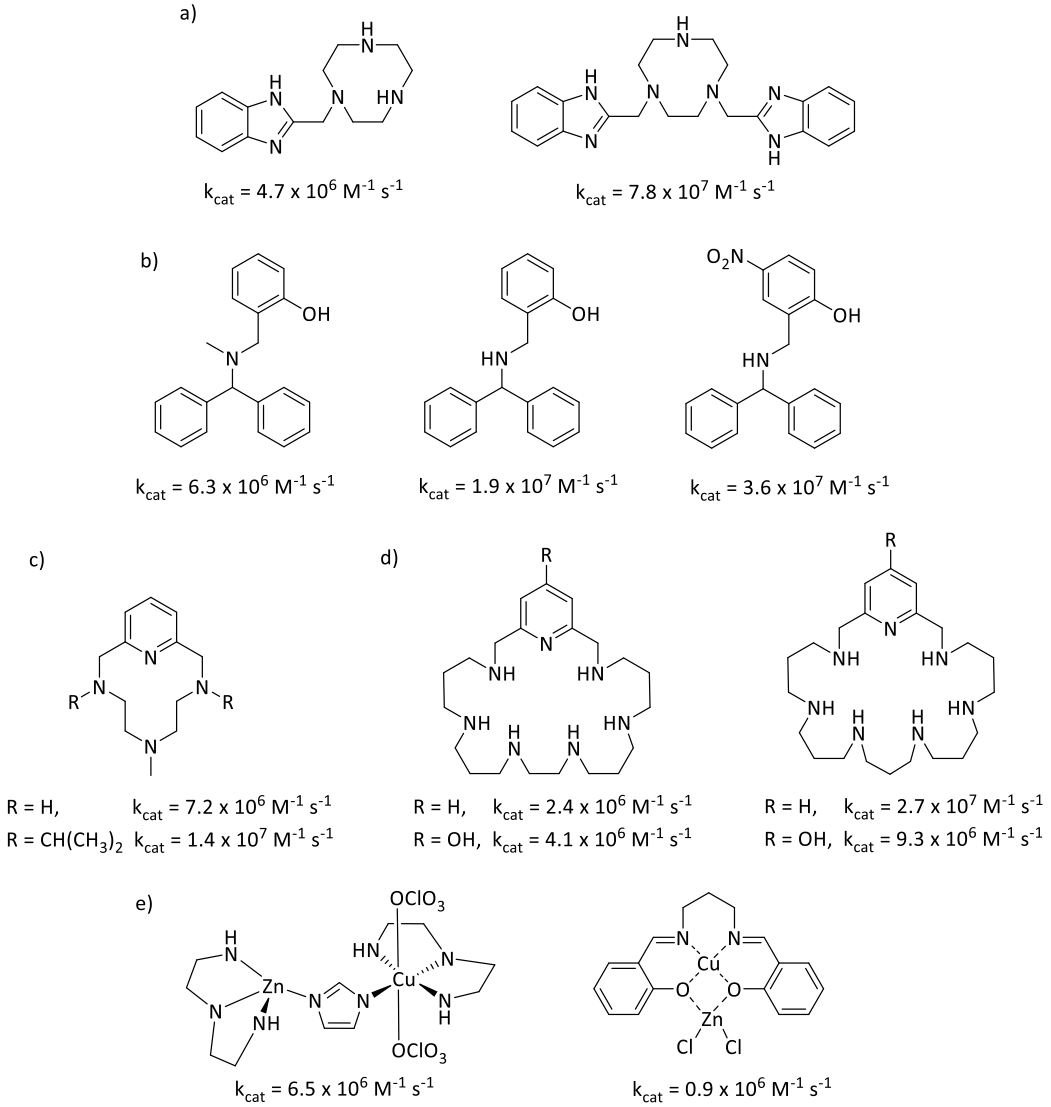

Figure 18: Excerpt of SOD-active copper complexes and/or applied ligand systems, designed and synthesized by various groups. a) by Li *et al.*[137], b) by Squarcina *et al.*[138], c&d) by Martinez-Camarena *et al.*[139,140], e) by Daier *et al.*[141]

Figure 18 illustrates several copper-based complexes with the ability to degrade superoxide. Some of the complexes as the poly-aza-macrocycles shown for d) develop binuclear complexes with k_{cat} values of 4.1 x 10^6 M^{-1} s^{-1}, that are more effective than the mononuclear complex possessing a k_{cat} of 2.5 x 10^6 M^{-1} s^{-1}.[140] Daier *et al*.[141] even reported different Cu/Zn containing hetero binuclear complexes (e) which represent the metals of wild type SOD1 with an SOD activity of 6.51 x 10^6 M^{-1} s^{-1} for the bridging imidazole complex. As seen from the values for k_{cat} given in Figure 18, the reported SOD activity of these synthetic systems is significantly lower than that of natural enzymes and free copper ions. Several other molecules have been designed and generated, using nanoparticle structures, naturally occurring molecules or even small peptide chains to form copper containing complexes.[142-144] But in the end the necessity to ensure stability of complex without metal release while keeping a satisfying SOD activity led to a more intense focus on other transition metals for the use of SODm.

Peptide-based complexes

Studies to understand the native (Ni-)SOD enzymes' mechanisms in detail, is not exclusively the benefit of peptide complexes that mime the protein coordination sphere of the respective metal center. Due to the high redox potential of the Ni^{2+}/Ni^{3+} pair, a strong electron-donating ligand system is required to make superoxide dismutation possible. The N_2S_2 coordination, provided by peptide-based ligands, is expected to deliver this necessary support in the case of Ni-SODm. But, the approach to rebuild nature's model is also reasonable and lead to a group of Ni-SODm compounds of which some are depicted in Figure 19. Some authors investigate the influence of donor atoms to the metal center by recreating and modifying the N_2S_2 environment of Ni-SODm, while examining effects on catalytic behavior.[145]

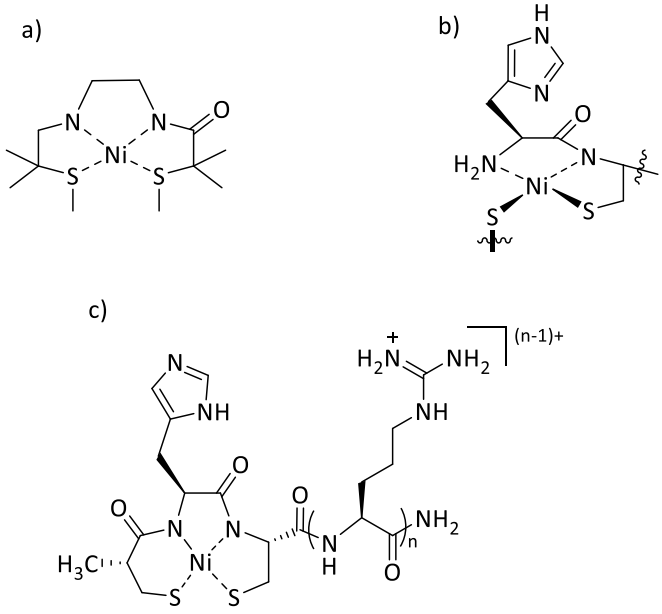

Figure 19: Molecular structures of Ni-based SODm from Naka *et al.*[149] (a) and enzyme-based peptide SODm from Guinard *et al.*[147] and Shearer[131] (b&c).

It needs to be mentioned that peptide-based superoxide dismutase mimetics predominantly contain nickel or copper. Nevertheless, manganese complexes with peptide strains consisting of arginine and glycine have been reported by Ching *et al*.,[148] with SOD activity from 4.2 to 6.6 x 10^6 M^{-1} s^{-1} depending on chain length and residue.

Salen complexes

Manganese N,N'-bis(salicylidene)ethylenediamine (Salen) complexes are of interest since 1993, when Jacobsen published a complex meant for the use of epoxidation, which showed SOD like activity.[149] Shortly after discovery Eukarion Inc. submitted a patent for EUK-8, the first member of the Salen SODm family with a k_{cat} of about 6.0 x 10^5 M^{-1} s^{-1}.[150] Due to the low SOD activity, further modifications and investigations have been made leading to additional members of that family, EUK-134 and EUK-184,

which not only decompose superoxide but can also mimic catalase enzymes.[151] EUK-134 and EUK-184 demonstrate IC_{50} values of 1.3 and 1.4 µM, respectively. However, while studying the SOD activity of the Salen family, a major issue arose.[152] When EDTA as a chelating agent is added to solutions, the activity was diminished, as it would be expected for present free metal ions.[149] To overcome this challenge another Salen complex was synthesized. In EUK-207 a crown-ether residue was introduced into the ligand framework aimed at increasing the stability in solution, which indeed was successful based on the higher accumulated plasma levels.[153] Nevertheless, Mn-Salen complexes do not play an important role in the field of SODm anymore, due to earlier issues and the limited space for chemical modification.

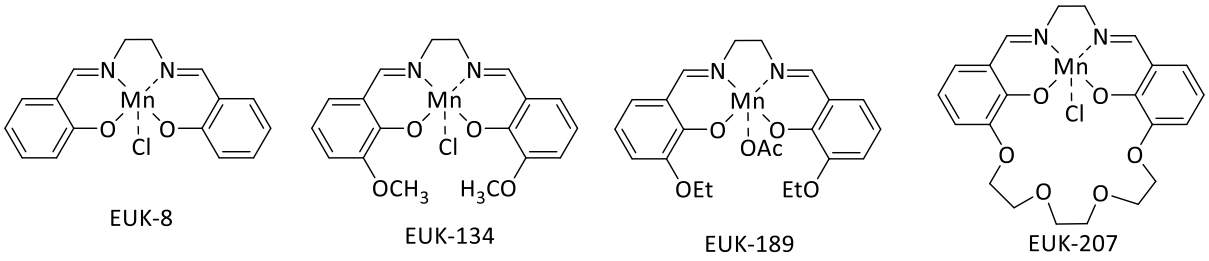

Figure 20: Manganese containing salene complexes.

Cyclic polyamines

More promising and even more potent superoxide dismutase mimetics are found in the family of cyclic polyamines. The main pioneering work has been done by Riley, developing seven coordinate Mn complexes which mime the activity of SOD enzymes.[154,155] Deriving from the parent $Mn([15]aneN_5)Cl_2$ complex, which performs SOD catalysis at rates of $4.13 \times 10^7\ M^{-1}\ s^{-1}$ at physiological pH, a great variety of related compounds was designed, using computational methods, and synthesized (Figure 21).[156,157]

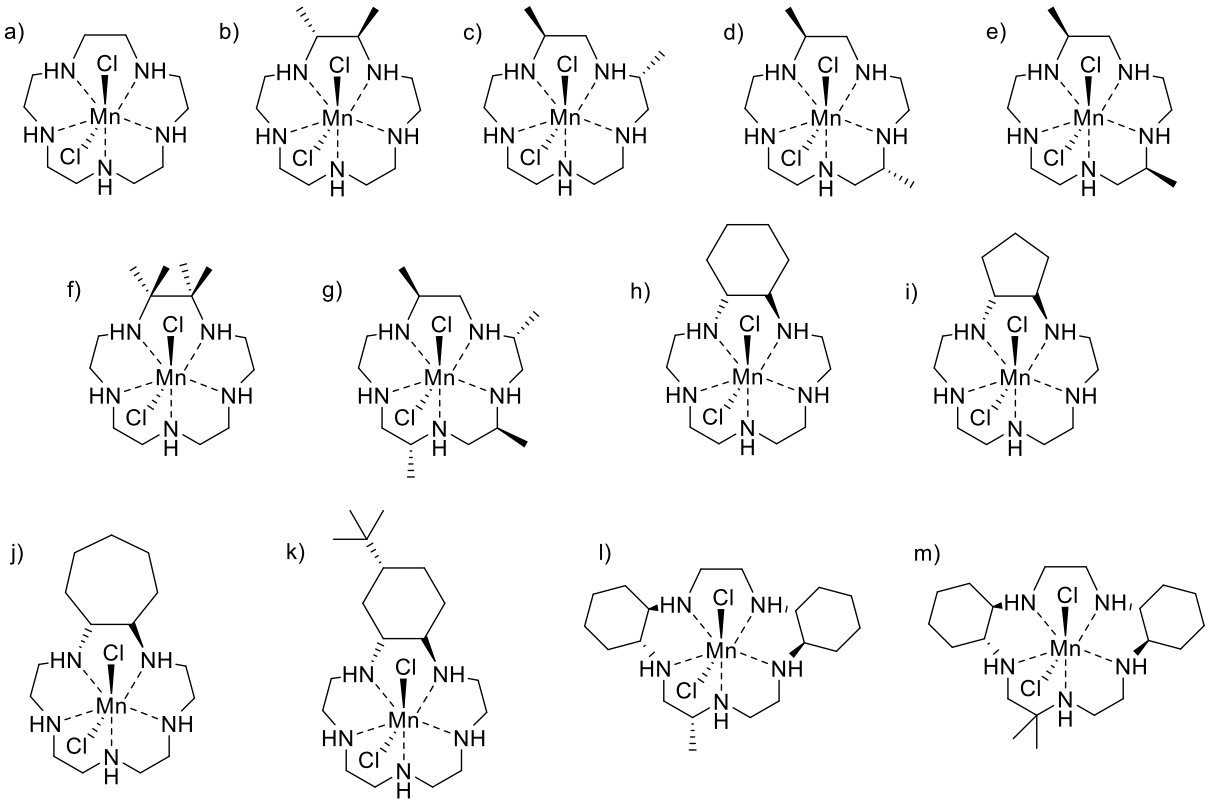

Figure 21: Cyclic polyamines with SODm properties designed and synthesized with the help of computational methods by Riley *et al*. [156,157]

Table 1: SOD catalytic rates (k_{cat}) of selected cyclic polyamines at pH 7.4.

Compound	k_{cat}: (x 10^7 M^{-1} s^{-1} for pH 7.4)	Ref
a)	4.13	156
b)	8.84	156
c)	5.52	156
d)	2.20	156
e)	5.37	156
f)	inactive	156
g)	inactive	156
h)	9.09	156
i)	1.37	156
j)	5.05	156
k)	7.23	156
l)	15.0	157
m)	0.3	157

The resulting complexes dismutate superoxide with a ranges of k_{cat} = 0.3 – 15.0 x 10^7 M^{-1} s^{-1} even maintaining their activity after treatment with EDTA.[156-158] Together with the comparably high catalytic rates and the chemical properties of high stability and solubility, the cyclic polyamines family represents a promising class of SOD mimetics. It needs to be mentioned, that Fe-SODm are permanently in consideration to be designed, but in general iron is avoided because of its cytotoxicity

and possibility to perform Fenton chemistry, leading to even more deleterious ROS. Nevertheless, some members of the pentaazamacrocyclic SOD family contained iron, but showed SOD activity one to two orders of magnitude lower than their manganese analogues.[159]

Building on the previously discussed Mn([15]aneN5) complexes, another closely related family emerged: the 1,4,7,10,13-pentaazacyclopentadecane complexes. This group began with the prototype M40403 and represents an additional family of macrocyclic compounds with extraordinarily high potential (Figure 22).[160]

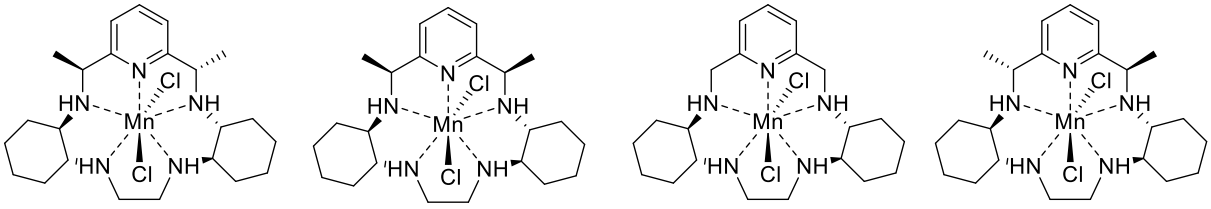

Figure 22: Structures of the M4040X family.[160-162]

Although structurally very similar, these complexes differ strongly in their catalytic behavior. With both M40402 and M40403 being satisfying SOD mimetics with rates in the 1.60 x 10^7 M^{-1} s^{-1} range, M40404 surprisingly shows no superoxide degradation at all. The S,S-dimethyl derivative M40401 exceeds both active compounds by the factor of 100, reaching k_{cat} = 1.6 x 10^9 M^{-1} s^{-1}, which represents the absolute peak of catalytic active SOD-mimicking compounds. Nevertheless, it remains unexpected that M40404 possess not activity towards superoxide at all, especially since the redox potentials for the whole M4040X family are fairly the same with $E_{1/2}$ = +462 mV for M40401, $E_{1/2}$ = +525 mV for M40403 and $E_{1/2}$ = +452 mV for M40404.[162] Thus, the reason for the big difference needs to be located elsewhere. Aston *et al*.[161] provide a reasonable explanation regarding a structure-activity correlation, based on molecular mechanistic studies. Accordingly, since the resting oxidation state of manganese in these cyclic polyamines is 2+, in contrary to the native enzyme, the rate determining step of the catalytic cycle will be the oxidation to Mn(III). This takes place either by pH-independent inner-sphere superoxide binding towards an axial coordination space of the Mn(II) center, or by an pH-dependent outer-sphere mechanism, in which the Mn(II)-complex possesses a coordination geometry close to oxidation product. In this case the metal center would undergo modification to fold into a pseudo-octahedral structure via an amine of the fifteen-membered ring, which will fill the axial position. Due to steric and electronic repulsive interactions, M40404 is strictly fixed into its planar geometry (right side in Figure 23) and therefore cannot be forced into the required 6-fold structure., which subsequently leads to no activity. For M40401, the exact opposite is the case. The Mn(II) complex can readily adjust its coordination sphere to facilitate catalytic dismutation, adopting the necessary structure (left side in Figure 23).[161]

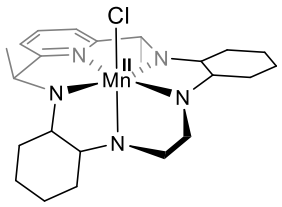

pseudo-octahedral structure for M40401

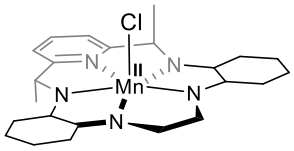

strictly planar structure for M40404

Figure 23: Structural intermediates during catalytic cycle for M40401 and M40404.[161]

Even though these theoretical mechanistic studies have provided a conclusive explanation for the unusual behavior of M40404, Maroz *et al*.[162] have a different explanation with an alternative route, which does not completely exclude previous investigations. The suggested mechanism is depicted in Figure 24 and it proposes not the oxidative addition to be the rate determining step but the oxidation of superoxide to be limiting. Starting with the same resting Mn(II) here, oxidative addition is depicted as fast reaction, which yields a $[Mn(III)LO_2]^+$ moiety. The next step would be the slower oxidation of another superoxide by the intermediate, a reaction greatly influenced by the three-dimensional structure of the metal complex. Therefore, the pseudo-octahedral geometry still plays a crucial role but not in the previously suggested manner. After an electron transfer occurred, reduced $[Mn(II)LO_2]$ remains and the peroxide coordinated to Mn(II) can be more easily released than from Mn(III), assisted by protonation, leading back to starting reagent. Experimental and theoretical data tend to support this mechanism and together with the data provided by Aston, the explanation for the great difference within in the M4040X family seems to be reliable.[161,162]

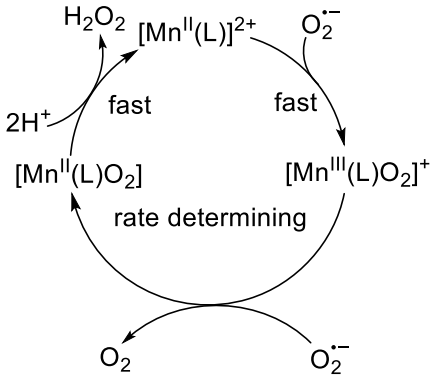

Figure 24: Alternative mechanism for superoxide decomposition catalyzed by the M4040X family.[162]

Another approach has been developed for the modification of SODm based on M4040X. The [*trans*-2,13-dimethyl-3,6,9,12,18-pentaazabicyclo-[12.3.1]octadeca-1(18),14,16-triene], or simply "Pyane" ligand, consist of an easy modifiable backbone, which can be readily altered by using different 4-subsituted pyridines as precursors. With two acetyl groups in the 2- and 6-position of the corresponding pyridine, reductive complexation yields the prototype $[Mn(Pyane)]Cl_2$ complex (Figure 25). Additionally, the ligand framework preserves a necessary stability to prevent the metal center release, but allows substrate molecules to reach the active site. These properties and the straight-

forward template synthesis of the related complexes make it ideal for design of SODm. The group of Ivanović-Burmazović designed different manganese containing compounds based on the model of the prototype [Mn(Pyane)]Cl_2, focusing on combining the desired structural and chemical characteristics mentioned in Chapter 1.5. Figure 25 depicts examples of the various possibilities, starting with the prototype complex followed by integration of long alkyl chains of different size to tune lipophilicity of the complex, resulting in catalytic rates around 1.50 x 10^7 M^{-1} s^{-1} at pH 7.4.[163] Thus, accumulation in cells and the associated physiological benefits, such as reaching mitochondria, the main contributor to oxidative stress, are enhanced. Taking this a step further, by modifying the complex of Kelso *et al.*[164] and adapting its structure to Pyane complexes, a triphenyl-phosphonium-anchored compound was developed. This modification introduces an extra positive charge, allowing the complex to specifically target mitochondria due to the negative potential of the mitochondrial matrix. Even the synthesis of a dinuclear complex with k_{cat} = 4.7 x 10^7 M^{-1} s^{-1} at physiological pH could be achieved.[165]

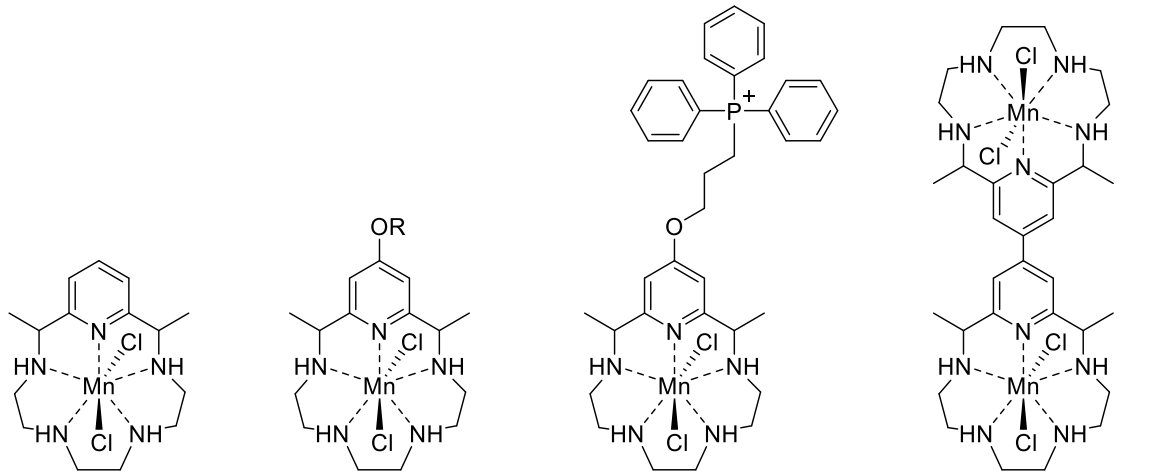

1: R = $C_{12}H_{25}$; **2**: R = $C_{16}H_{35}$; **3**: R = $C_{22}H_{45}$; **4**: R = $CH(CH_2OC_{12}H_{25})_2$; **5**: R = $CH(CH_2OC_{16}H_{33})_2$

Figure 25: MnPyane complexes designed by the group of Ivana Ivanovic-Burmazovic.[163,165]

Regarding biological effects, the cyclic pentaamine Mn complexes have demonstrated cell-protective properties in cases of inflammatory cascades and ischemia-reperfusion injury.[166-168] However, the elementary reactions underlying the biologically protective mechanisms of this class of SOD mimics (SODm) remain unclear. Although these complexes have been reported to be strictly selective for superoxide and do not interact with other ROS/RNS, research by the Ivanović-Burmazović group has shown that, in the case of [Mn(Pyane)]Cl_2, some of them can interfere with NO by dismutating it through a mechanism analogous to that of superoxide dismutation.[169,170] This process generates other nitrogen species, such as nitroxyl (HNO) and nitrosonium (NO^+), with the latter subsequently being converted to nitrite.

Porphyrins

The probably biggest group of superoxide dismutase mimetics are porphyrianto complexes. The biological relevance and physiological omnipresence of porphyrin-based molecules, such as those found in the cytochrome P450 enzyme family, along with their structural versatility, made them the first choice for developing enzyme mimics to replicate the function of native SOD enzymes. In 1979 the first reported SOD mimetic based on the tetrapyrrolic macrocycle was the (tetrakis-4-*N*-methylpyridyl)porphyrin)), $[FeTM\text{-}4\text{-}PyP]^{5+}$, by Pasternack *et al*. using iron active site.[171,172] In contrary to previous compounds which bear the reduced metal form as resting state, porphyrins tend to stabilize the oxidized M^{3+} form. $[FeTM\text{-}4\text{-}PyP]^{5+}$, which demonstrated only moderate SOD activity and showed toxicity towards E. coli, led to further modifications aimed at improving its properties. This resulted in the development of the TM-2-PyP ligand system.[173]

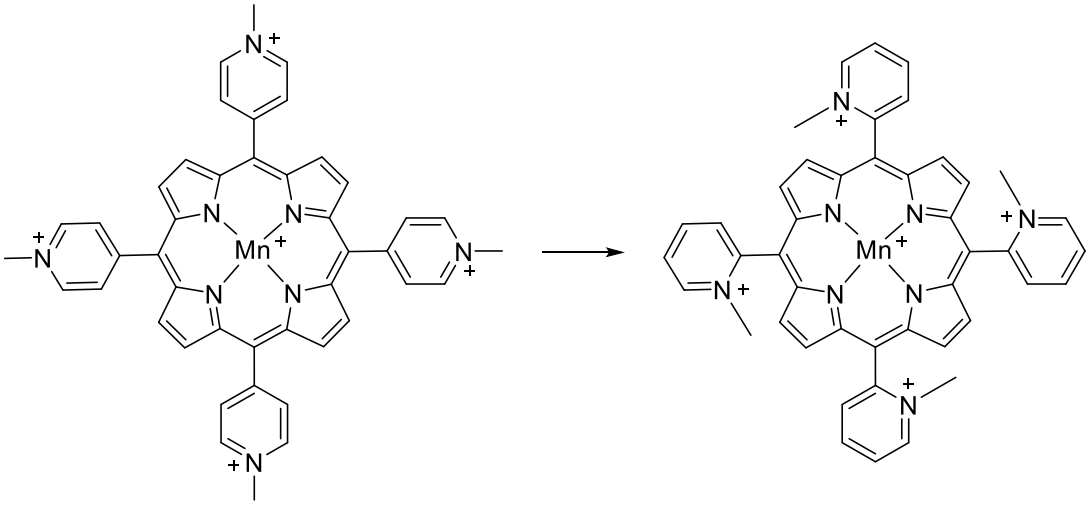

Figure 26: First modifications of Mn(Porphyrins) to decrease electron density at the metal center.[173]

Similar considerations to those made for cyclic polyamines must be applied when designing porphyrins to mimic native SOD enzymes, starting with the metal choice. In most cases iron and manganese are in the active site of the complex, since incorporation of different metals, such as zinc, lead to complete loss of activity for corresponding Fe-porphyrins.[174] Even though the iron was used at the beginning, further investigations and utilization of new compounds lead to manganese being identified as the desired redox active entity. Upon reduction during catalytic processes, both the Mn(II) and Fe(II) are more likely to be released from the complex, leading to cell toxic effects, especially in the case of ferrous ions. Furthermore, Fe(II) even in a coordinated form seems to own the ability to perform Fenton-like chemistry, making it unsuitable for further applications.[175] However, iron porphyrins have been demonstrated to conduct protective effects in cells by dismutation of not only superoxide but also hydrogen peroxide.[176,177] In Figure 27 different selected porphyrin complexes are depicted to demonstrate the structure-activity relationship, with their respective k_{cat} values in Table 2.

Table 2: Catalytic rates of selected MnPorphyrinato complexes at pH 7.8.

Compound	k_{cat} (x 10^6 M^{-1} s^{-1}) for pH 7.8	Ref
MnTM-2-PyP^{5+}	62	183
MnTnHex-2-PyP^{5+}	30	183
MnTnMOHex-2-PyP^{5+}	6	183
MnTnBuOE-2-PyP^{5+}	68	183

Starting with [MnTM-4-PyP]$^{5+}$ as the foundation for modification, this complex exhibited moderate SOD activity and a redox potential of +60 mV (vs. NHE), which is significantly lower than the desired value of approximately +300 mV for optimal catalytic efficiency in superoxide dismutation. Therefore, the *para* positioned positive charge was place into *ortho* position, creating a stronger electron withdrawing effect and subsequently raising the $E_{1/2}$ value to 220 mV for the [MnTM-2-PyP]$^{5+}$. Furthermore, the fact that the positive charge is now placed closer to the metal center resulted in an enhanced electrostatic guidance and a 16-fold increased SOD activity (Table 2). The fundamental importance of this positive charge became evident when lesser-charged complexes, such as [MnT-2-PyP]$^{+}$ or even negatively charged [MnTSPP]$^{3-}$, were investigated for their SOD activity. These complexes showed results indistinguishable from the self-decay of superoxide, highlighting the necessity of a positive charge for effective catalytic activity.[178,179] By introducing bromide residues at the β-pyrrolic positions of [MnTM-2-PyP]$^{5+}$ the electron density at the metal center was even more decreased thus, the synthesized compound possessed a great k_{cat}. However, the stability of this compound was diminished, making it unappealing for further research. Since [MnTM-2-PyP]$^{5+}$occupies a nearly planar structure, its interaction with RNA/DNA might have a negative impact on *in vivo* activity of the complex, leaving the promising SOD activity without further benefit. Thus, the methyl groups were replaced by ethyl groups which resulted in a candidate for clinical trials.[180] While already possessing a huge positive charge, the uptake into cells was still an ongoing challenge. To achieve increased bioavailability a similar approach as for the pyane complex has been made, by increasing the length of the alkyl-chain to six carbon atoms. The resulting [MnTnHex-2-PyP]$^{5+}$ indeed showed enhanced lipophilic properties, but the micellar toxicity was impaired as well. To overcome this issue, incorporation of an oxygen atom into the aliphatic chain was supposed to maintain the lipophilic character, while quenching the toxic characteristics. Hence, [MnTMOHex-2-PyP]$^{5+}$ was designed and synthesized which was followed by [MnTnBuOE-2-PyP]$^{5+}$, another candidate for clinical trial.[181,182] This concise demonstration of structure-activity relations by designing the ideal SODm candidate, from beginning to the [MnTnBuOE-2-PyP]$^{5+}$ complex, which took over 30 years, is depicted in Figure 27.

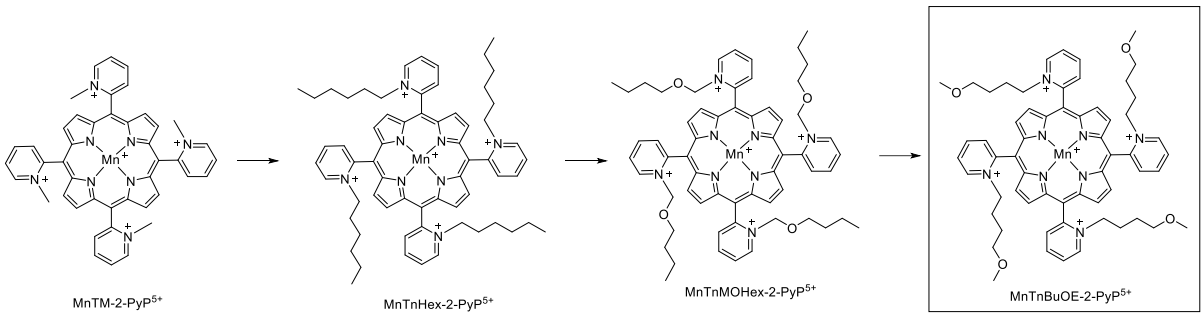

Figure 27: Route to a promising MnPorphyrinato clinical trial candidate adapted from Batinic-Haberle *et al*.[183]

This has been only a brief overview of the potential applications and capabilities of porphyrin-based superoxide dismutase mimetics. For more detailed insights, Batinić-Haberle has excellently reviewed the historical development and modern strategies, not only on porphyrinato-complexes, but also on the major groups of compounds that mimic the native SOD enzyme.[184]

1.5.2 Alternative strategies towards SODm

Traditional superoxide dismutase mimetics keep their relevance, since they have proven to be promising therapeutics, even reaching second stage clinical trials. Nevertheless, new approaches have been made to design alternative transition metal compounds, which may dismutate superoxide. Even the use of solely organic compounds gains more interest in recent research.

Nanoparticles

The widespread application field for nanoparticles also includes mimicking enzymes including SODs. To achieve potential effects, already known SODm can be loaded onto non-reactive materials, like silica or alumina of different size, or nanoparticles can be synthesized out of metal-based compounds.[185,186] It needs to be noted, that obtained enzyme like behavior can depend on particle shape and subsequently on the synthetic method. The SOD activity of nanoceria in the form of CeO_2 is directly linked to the Ce^{3+}/Ce^{4+} ratio, as demonstrated by numerous studies that vary the amount of cerium atoms. [187,188] Nanoceria particles with a size between 3 and 5 nm perform the best, exhibiting catalytic rates similar to those of the Cu/Zn-SOD enzyme. However, comparing nanoparticles with molecular SODm may not be straightforward. Both exceeding and falling below the optimal particle size range resulted in a loss of activity, highlighting the importance of precise size control for maintaining catalytic efficiency.[189.190]

Two dinuclear Cu/Zn complexes discussed in section 1.5.1 were applied to silica nanoparticles of different sizes. In both cases, the incorporation of these complexes significantly enhanced SOD activity, increasing it by approximately one order of magnitude.[185,186] Even the promising compound for clinical trials, $[MnTnBuOE\text{-}2\text{-}PyP]^{5+}$, was loaded onto nano silica encapsulated by lipophilic membranes, planning to ensure a slow, steady release in cells.[191] Apart from the mentioned examples, the potential applications of nanostructures are vast and not limited to merely mimicking wild-type enzymes.

Accordingly, the group of potential nanoparticles is huge, including OsO_4 with the Os^{VIII}/Os^{VII} redox couple[192], ferrite NPS like MFe_2O_4 (with M = Mn, Co, Cu),[193] Pt-based compounds,[194,195] metal-organic frameworks (MOFs) like the CuTCPP nanodots,[196] fullerene frameworks[197-199] and manganese oxides.[200,201]

Natural antioxidants

Research into the broad group of natural molecules with potential antioxidative capabilities has been ongoing since the early 21st century.[202] In particular the role of polyphenolic compounds has gained significant relevance, not only in scientific studies but also for practical daily life applications. These compounds are increasingly recognized for their beneficial effects in health, nutrition, and even skincare.[203] Several studies on different natural antioxidants have been performed and published, identifying a huge variety of compounds with protective characteristics against oxidative modifications. A prominent subgroup contains of coloring molecules, vitamins and tannins which are commonly found in everyday foods such as berries, grapes and other groceries.[204] Several thousand polyphenols have been isolated and characterized to date, which can be categorized based on their structural backbones respectively.[205,206] A selection of basic polyphenolic molecules is depicted in Figure 28, including benzoic acid derivates, stilbenes and particularly flavonoids, along with the related anthocyanidins, that three big members of the polyphenol family.

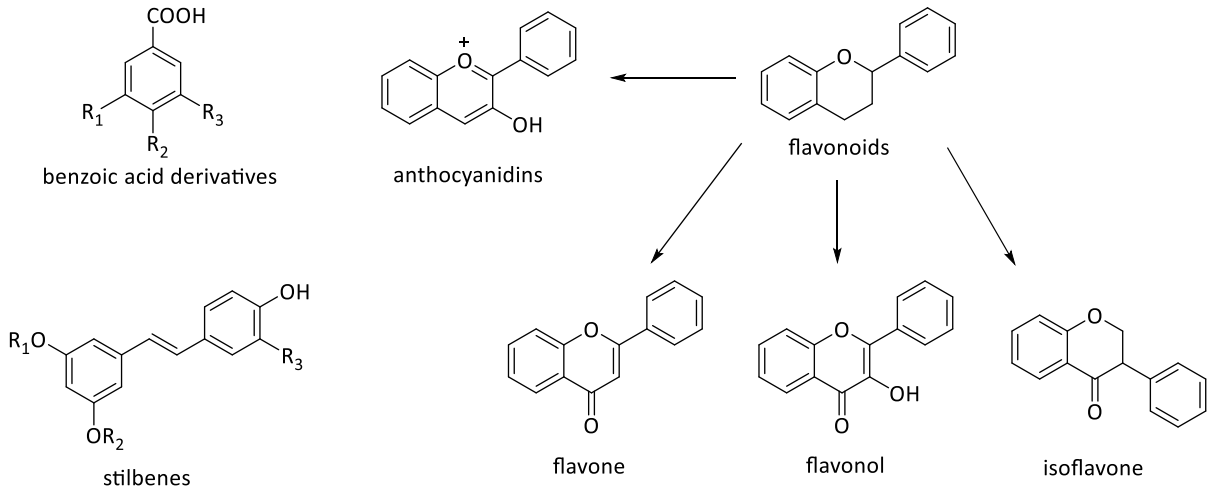

Figure 28: Main subgroups forming antioxidative compounds in the polyphenol family.

In general, the antioxidative properties of polyphenols are related to nutrition studies, due to their numerous occurrences in food. Honokiol[207,208], genistein[209] or the often discussed curcumin[210,211] represent examples for organic compounds capable of decomposing superoxide. Due to the huge number of molecules in this family and the structural differences, one underlying mechanism behind their reaction with $O_2^{\bullet-}$ could not be determined. Nevertheless, different approaches have been proposed trying to explain how polyphenols interact with superoxide. The easiest and widely accepted

mechanism would be direct radical scavenging, which could result in reduction of ROS. In this case the hydroxyl group would be transformed into a radical species itself, which is less potent than superoxide. This radical can now further react with other radical species, deactivating more potentially damaging compounds. Studies indicate that for optimal superoxide dismutation a π-π interaction between ROS and another corresponding polyphenol molecule is enhancing.[212,213] The fact, that *ortho*-substituted compounds demonstrate the best activity compared to their related *para*-substituted analogues and the necessity to transfer a proton during the reaction, suggest the involvement of a hydrogen abstraction process in form of a PCET meachnism.[214-216] Both possible reaction paths do not exclude each other, but rather could both be integrated into a final mechanistic explanation in the future. Another approach is based on the fact, that polyphenols are known to be redox mediator molecules, which can transfer an electron from one reaction partner to another.[217,218] Since iron, manganese and copper ions in solution already hold the potential to dismutate superoxide and polyphenolic molecules are known to possess chelating potential,[219] the latter could simply enhance these properties by serving as electron shuttling compounds between the metal ion and ROS. Furthermore, the metal chelation could provide protection against oxidative damage via another path, by inhibiting Fenton reactions. Finally, it needs to be noted that the SODm studies so far mainly have not been conducted *in vivo* and deeper insights into the metabolism of polyphenols in the human body point to a diminished bioavailability.[220] If ROS scavenging occurs at all, the most likely site would be in the gastrointestinal tract, where lipid peroxidation could be prevented by polyphenols.

The group of Christian R Goldsmith designed quinol-containing ligand systems, which form metal complexes, that apparently combine the antioxidative properties of both components. Together with the group of Ivana Ivanović-Burmazović the N-(2-hydroxy-5-methylbenzyl)-N,N',N'-tris(2-pyridinylmethyl)-1,2-ethanediamine ligand (L^{OH}) and the corresponding Mn(II) complex was tested for its SOD mimicking characteristics.[221] With considerably low k_{cat} values in the 10^6 region, improvement of the ligand system was necessary, which was achieved by replacing the methyl-group by another hydroxy residue. The new H_2qp1 ligand and furthermore the refined H_4qp2 ligand, with two quinol units enhanced the reactivity towards superoxide for the corresponding Mn(H_4qp2) and Mn(H_2qp1) complexes, reaching catalytic activity in Hepes buffer at pH 7.4 that exceeds those of the clinically tested $[MnTnBuOE\text{-}2\text{-}PyP]^{5+}$.[222]

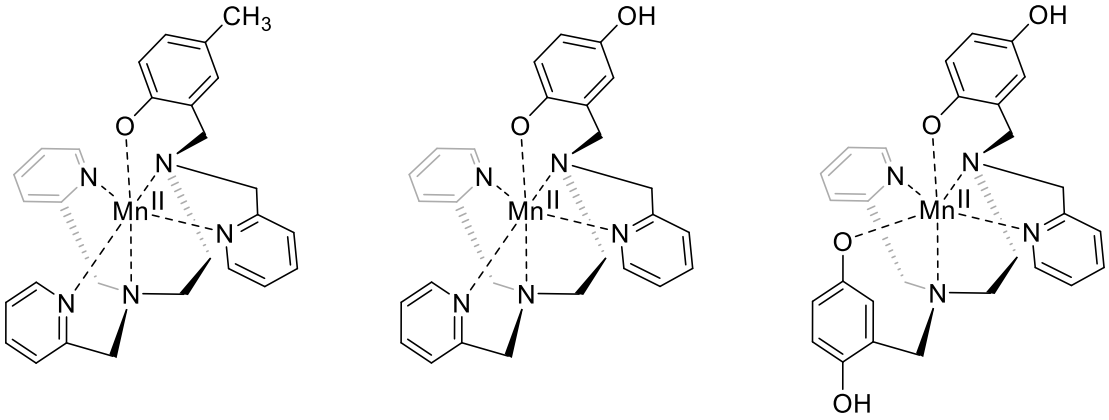

Mn(L^{OH}) Mn(H_2qp1) Mn(H_4qp2)

Figure 29: Mn(L^{OH}) by Kenkel *et al*.[221], Mn(H_2qp1) and Mn(H_4qp2) by Senft *et al*.[222]

Not only did the optimization of incorporating more hydroxy groups enhance the SOD activity, but it was also possible to form a corresponding Zn(H_2qp1) complex, further improving the catalytic properties. Even though zinc is a redox-innocent metal, [Zn(H_2qp1)OTf]OTf features catalytic activity towards superoxide that is higher than that of the manganese containing L^{OH} complex (Table 3). Low-temperature mass spectrometry experiments and EPR indicate that a semiquinone radical species is involved in the mechanism of superoxide dismutation, which supports the idea, that quinol containing molecules can act as electron shuttling moieties during redox reactions. Interestingly, the zinc complex depicts highest SOD activity in phosphate buffered solution, which is unusual, since phosphate is commonly known to bind free coordination sites at the metal center, blocking them and inhibiting electron transfer to substrate molecules.[223] Accordingly, this leads to the mechanism proposed by Ward *et al*.,[224] which implement the phosphate as relevant reaction partner by delivering protons to dismutate superoxide.

Table 3: Catalytic rates of ligand systems by Goldsmith group.

Compound	**k_{cat} [x 10^5 M^{-1} s^{-1}] (HEPES pH 7.4)**	**k_{cat} [x 10^5 M^{-1} s^{-1}] (HEPES pH 8.1)**	**k_{cat} [x 10^5 M^{-1} s^{-1}] (Phosphate pH 7.4)**	**Ref**
[Mn(L^{OH})]	36	6.2	11	221
[Mn(H_2qp1)]	970	220	80	222
[Mn(H_4qp2)]	120	96	100	222
[Zn(H_2qp1)]	34	47	190	224

1.6 Different approaches to determine SOD activity

Determination of SOD activity is crucial to compare different SOD mimicking compounds (SODm) and bring them in relation to each other. Since many different methods developed, which can provide k_{cat}, a comparison and classification is necessary to assess their scientific significance and ensure that the results are consistent and meaningful across different studies. The general idea is to track superoxide and compare the decomposition in presence of potential SODm, either by directly following superoxide's decay at around 250 nm or indirectly via indicator molecules, which are influenced by radical species. For all applications the compulsive necessity of buffered solutions is important due to the strong pH dependent self-dismutation of superoxide, which was depicted in Figure 1.

1.6.1 Indirect assays

The initial efforts to categorize SOD active compounds were pioneered by Fridovich and McCord, resulting in the first assay able to determine the antioxidative properties of compounds.[79] In general, indirect methods consist of a superoxide producing reagent, mainly the xanthine/xanthine oxidase system, which releases a steady state concentration of $O_2^{\bullet -}$, and a spectroscopic active substance that can be followed e.g. by UV/Vis. One example is the cytochrome c assay, where the Fe(III) band at 550 nm is followed, which in presence of superoxide would increase due to reduction of the Fe(III) to Fe(II) form.[225] Introducing a SOD mimic into the system inhibits the reduction of the cytochrome c. However, the decomposition product hydrogen peroxide could cause problems by reacting with still present superoxide in Haber-Weiss reaction creating the hydroxyl radical. [55] Other well-established reporter molecules (Figure 30), which have been used as indicators of SOD activity are b) nitroblue tetrazolium (NBT)[226], c) lucigenin, d) luminol and two more assays that directly determine the radical scavenging properties of antioxidants, with DPPH and ABTS as colorful detector molecules.[227]

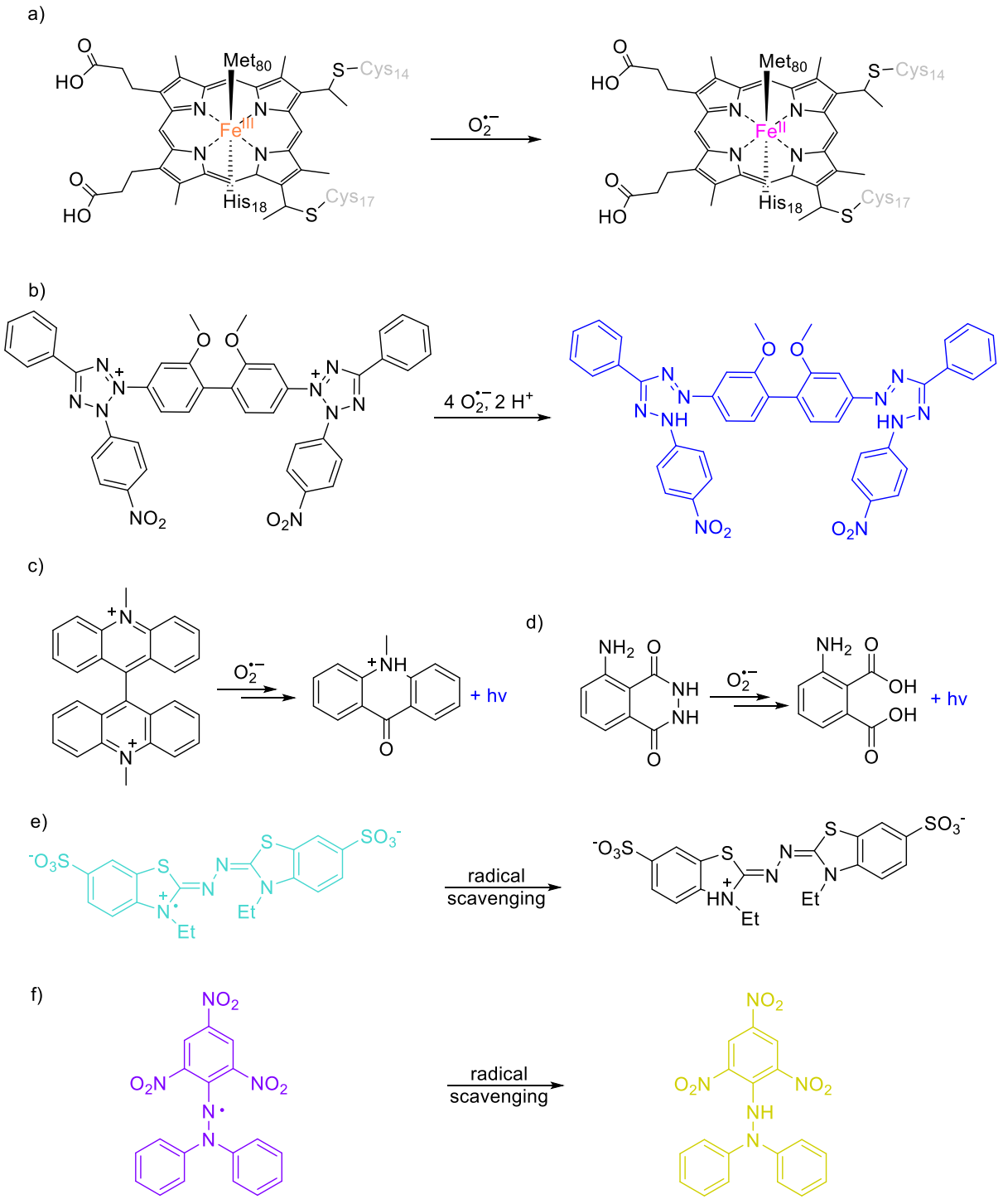

Figure 30: Chemical structure of reporter molecules (indicators) for indirect SOD activtiy assays. Colors indicate the exhibtited color. a) cytochome c, b) nitroblue tetrazolium (NBT), c) lucigenin, d) luminol, e) ABTS, f) DPPH

1.6.2 Direct methods

Pulse radiolysis

The critical difference between previously described assays and the direct methods for SOD activity evaluation is the spectroscopically followed dismutation of $O_2^{\bullet-}$ at 250 nm. The two commonly used methods using the absorption of superoxide are the pulse radiolysis[228,229] and stopped-flow technique, allowing a precise measurement of SOD activity by following superoxide decay spectrophotometrically. As described in section 1.1, the formal one-electron reduction of oxygen generates superoxide. This reaction is used in pulse radiolysis to generate a defined amount of superoxide in an oxygen enriched solvent, which will be irradiated by a high intensity light beam. However, radical formation during pulse radiolysis does not produce a superoxide exclusively but a mixture of radical species, such as $H^{\bullet}$ and $OH^{\bullet}$, thus it is necessary to add a $OH^{\bullet}$ scavenger. Formate reacts with the hydroxyl radical, ultimately generating superoxide, similar to how hydrogen atoms react with solvated oxygen to form the conjugate acid (Figure 31).[230,231] Even though radical generation in the pulse radiolysis technique is not specific, it is possible to follow the decay of superoxide, making it a powerful direct method to determine SOD activity

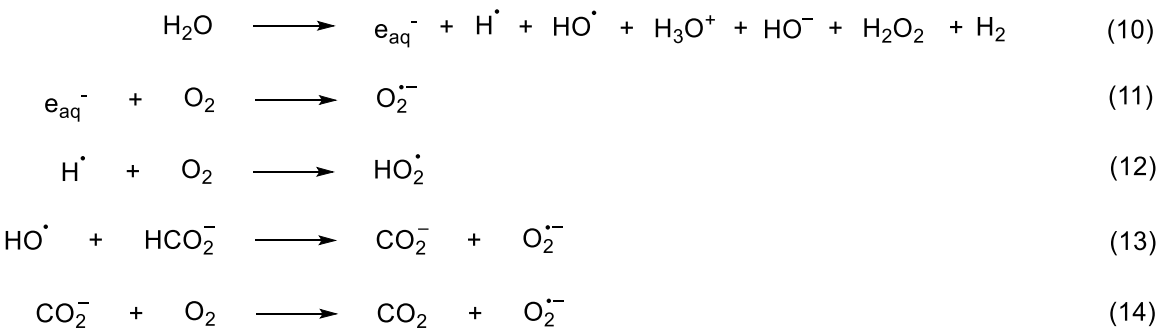

Figure 31: Radical reactions induced by the high intensity beam during pulse radiolysis. Equation 13 displays hydroxyl scavenging by added formate.

Nevertheless, the unconventional instruments necessary to realize pulse radiolysis make it unattractive compared to the indirect assays, which are easy to apply. Additionally, the lack of isolated superoxide generation can cause problems through degradation or oxidative inactivation of chosen SODm. In the following section, the stopped-flow technique addresses these problems by directly dissolving the potassium superoxide salt, allowing for more controlled and reliable analysis.

Stopped-Flow technique

Pulse radiolysis relies on the steady-state generation of superoxide in low concentrations, which can present disadvantages similar to those encountered with indirect methods. In contrast the stopped flow technique overcomes these limitations, providing a more precise means of studying superoxide dismutation. First demonstrated by McClune and Fee[232] the potassium superoxide salt was suspended in DMSO with an appropriate amount of 18-crown-6 to ensure dissolving, with subsequent

spectroscopical monitoring of superoxide decay. Due to technical limitations, the dead time of the instrument was long, resulting in the self-decay of superoxide being a relevant opposing process, which limited the investigations by McClune and Fee to high pH. Riely *et al*. [233] improved the technique via rapid mixing, with a dead time between 1-2 ms, allowing monitoring of superoxide's decay under physiological conditions. The group of Ivana Ivanović-Burmazović further refined the method reaching superoxide concentrations of around 200 µM, which assures first order conditions to determine a true catalytic activity.[224] In Figure 32 the schematic setup of Biologic's SFM-400 stopped-flow device is shown, with a Berger-ball mixer that allows an efficient mixing of DMSO and a buffered solution. On the right side, an example of kinetic curves is displayed, which were fitted to a first-order decay model. The obtained values were then plotted against the catalyst concentration to calculate the second-order rate constant (k_{cat}), as shown in the inset of Figure 32.

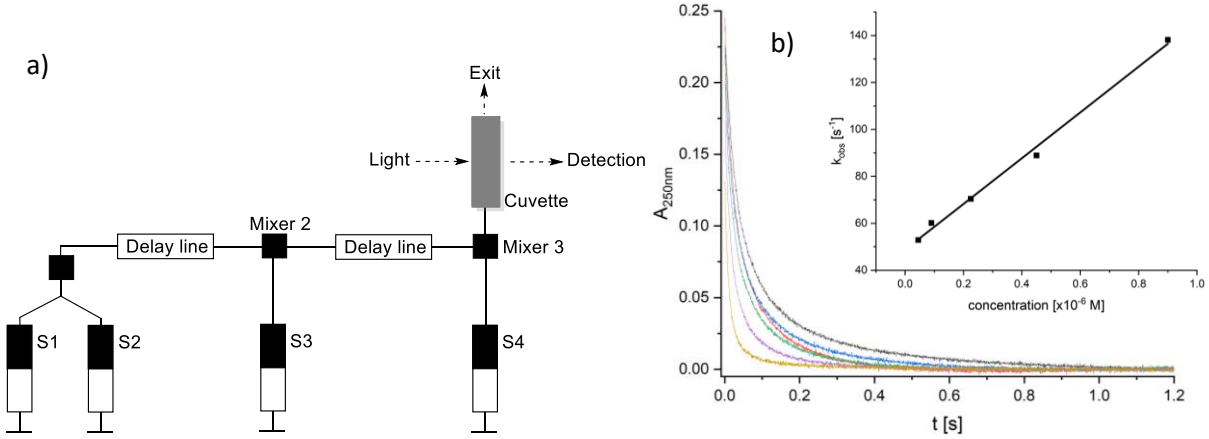

Figure 32: a) Schematic structure of the SFM-400 instrument by Biologic, replicated from the manual. b) exemplary kinetic traces of superoxide decay followed at 250 nm by stopped flow technique. Inset: k_{obs} values plotted against catalyst concentration for determination of the second order catalytic rate constant.

1.6.3 Critical comparison of both methods

All described methods for investigating SOD activity have been established for specific purposes and are widely accepted. Nevertheless, some techniques offer distinct advantages, making them more reliable when it comes to accurate comparison of catalytic rates. Indirect assays are cost-effective and easy to apply, making them suitable for use in any laboratory. Despite their practicality, the results obtained from indirect assays must be interpreted cautiously as numerous side reactions can occur during SOD catalysis.[234] One significant limitation is the potential interaction of SODm with the used reporter molecule, which may bypass superoxide entirely. Either direct oxidation or reduction of the indicator can lead to overestimation or underestimation of the compound, respectively, making it very difficult to distinguish the actual antioxidative properties of the applied SODm. Additionally, a possible suppression of the xanthine/xanthine oxidase system has been reported,[235,236] which leads to a

misinterpretation of SOD activity as well. Another disadvantage that affects the reliability of direct pulse radiolysis is that the generated steady-state superoxide concentration may be significantly low at the beginning of the reaction. This could favor the detection of a stoichiometric reaction rather than real catalytic activity, a limitation that does not apply to the stopped-flow technique. Finally, the lack of consistency in results across assays shows a major issue that might occur while exclusively relying on indirect methods. Nevertheless, their easy and cheap application and the fact, that direct methods like stopped-flow are limited to detect activities above $5x10^5$ M^{-1} s^{-1}, sustain the relevance of some of indirect SOD assays.[237]

Based on the principle of stopped-flow instruments further developments have been made over the time, including the possibility to decrease the experimental temperature. This allows detection of labile reaction intermediates, which gives further insight into reaction mechanisms and determination of the reaction pathways. Combining time-resolved UV/Vis detection with low-temperature stopped-flow systems enhances the characterization of reactive intermediates throughout the catalytic cycle, improving the relevance and reliability for assigning the underlying mechanisms. Even better comprehension can be gained, when pressure is applied during the experiment with the stopped-flow instrument, resulting in high-pressure stopped-flow technique. Even though this advanced system is rarely used, its ability to study reactions in greater detail—especially in characterizing the transition state and understanding the activation process—provides unprecedented insights.

2 Aims and Summary of Results

2.1 Aims

The suppression of deleterious effects induced by the overproduction of reactive oxygen species (ROS) is a critical aspect in the prevention and treatment of various neurodegenerative and cardiovascular diseases. This work focuses on the design, synthesis, and characterization of bioactive transition metal complexes with antioxidant properties, particularly superoxide dismutase mimetics (SODm). Moving beyond conventional ligand systems commonly reported in the literature, we explored novel redox-active organic functionalities inspired by biological settings, such as hydroquinones. Our approach not only introduced acyclic and macrocyclic ligand frameworks but also strategically increased the number of redox-active moieties by incorporating a second hydroquinone entity. Additionally, we investigated the potential of diverse metal centers, including Mn, Fe, Zn, and Ni, which are naturally utilized in SOD enzymes, to achieve synergistic antioxidative activity when combined with these redox-active ligands.

A key objective of this work was to elucidate the mechanistic intricacies of these SOD mimetics, determining whether the interplay between the ligand and metal center can be fine-tuned to maximize catalytic efficiency while ensuring the overall stability of the complex under catalytic conditions. One of the major challenges in the development of efficient SOD mimetics lies in deciphering mechanistic details, particularly through the characterization of reaction intermediates along the catalytic cycle. Given that the catalytic process operates at exceptionally high rate constants, exceeding 10^8 $M^{-1}s^{-1}$, traditional indirect methods fail to provide reliable kinetic data. To address this, a central aim of this study was the application of a direct stopped-flow technique to accurately determine catalytic rate constants for superoxide dismutation, thereby offering precise and reliable SOD activity values. Furthermore, by integrating (cryo)-stopped-flow spectroscopy with cryo spray mass spectrometry, we aimed to identify transient catalytic intermediates and establish a comprehensive mechanistic framework for these systems.

This work not only provides fundamental insights into the role of metal-ligand interactions in tuning redox activity but also demonstrates the potential of a new class of biomimetic antioxidants based on redox-active ligand components. Our unique methodological approach has yielded novel mechanistic perspectives and paves the way for future investigations incorporating other biologically inspired redox-active organic moieties. Ultimately, these findings contribute to the rational design of next-generation SOD mimetics with optimized performance, stability, and therapeutic potential.

An additional key objective of this work was to advance kinetic studies of bioinorganic reaction mechanisms by developing a high-pressure stopped-flow setup capable of operating at lower temperatures while allowing the mixing of three solutions under high pressure instead of the conventional two. Coupled with a time-resolved UV/Vis detection unit, this setup enabled a more detailed investigation of complex reactions by determining activation volumes as a crucial kinetic

parameter for characterizing transition states, thereby providing deeper insights into reaction mechanisms.

2.2 Summary of Results

2.2.1 Insights into the SOD Mechanisms of Complexes Featuring Redox-Active Hydroquinone-Containing Ligands

Comprehensive kinetic and mechanistic studies were conducted on Zn, Ni, Mn, and Fe complexes featuring acyclic or macrocyclic redox-active ligands containing one or two hydroquinone groups, respectively. The resulting SOD activities are summarized in Table 4. Importantly, our investigations identified key factors influencing the catalytic performance of these complexes, providing valuable experimental guidance for the tunable design of SOD mimetics based on redox-noninnocent ligand frameworks.

Table 4: Catalytic rates of quinol-containing metal complexes relevant for this work.

Compound	Catalytic rates (k_{cat}) in buffered solutions.		Ref
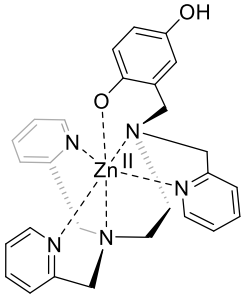 $Zn(H_2qp1)$	HEPES, 7.4	3.4×10^6 M^{-1} s^{-1}	224
	HEPES, 8.1	4.7×10^6 M^{-1} s^{-1}	
	Phosphate, 7.4	1.9×10^7 M^{-1} s^{-1}	
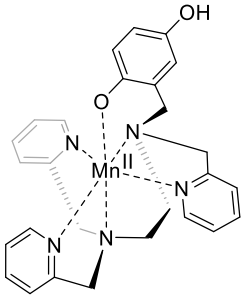 $Mn(H_2qp1)$	HEPES, 7.4	9.7×10^7 M^{-1} s^{-1}	222
	HEPES, 8.1	2.2×10^7 M^{-1} s^{-1}	
	Phosphate, 7.4	8.0×10^6 M^{-1} s^{-1}	
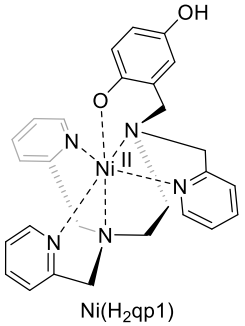 $Ni(H_2qp1)$	MOPS, 7.4	1.8×10^7 M^{-1} s^{-1}	**Publication 3** from this work
	MOPS, 7.8	1.2×10^7 M^{-1} s^{-1}	
	Phosphate, 7.4	1.1×10^7 M^{-1} s^{-1}	

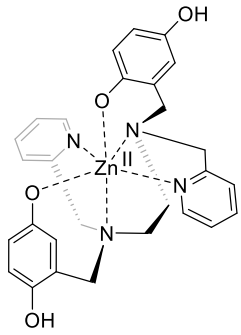 Zn(H_4qp2)	MOPS, 7.4	1.6 x 10^7 M^{-1} s^{-1}	**Publication 1** from this work
	MOPS, 7.8	4.9 x 10^7 M^{-1} s^{-1}	
	Phosphate, 7.4	2.5 x 10^7 M^{-1} s^{-1}	
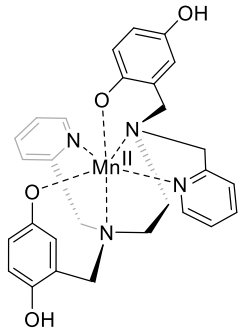 Mn(H_4qp2)	HEPES, 7.4	1.2 x 10^7 M^{-1} s^{-1}	222
	HEPES, 8.1	9.6 x 10^6 M^{-1} s^{-1}	
	Phosphate, 7.4	1.0 x 10^7 M^{-1} s^{-1}	
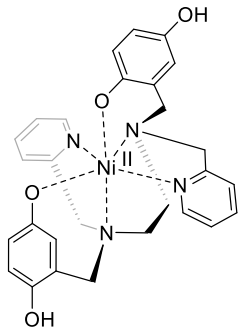 Ni(H_4qp2)	MOPS, 7.4	1.3 x 10^8 M^{-1} s^{-1}	**Publication 3** from this work
	MOPS, 7.8	9.7 x 10^7 M^{-1} s^{-1}	
	Phosphate, 7.4	6.2 x 10^7 M^{-1} s^{-1}	
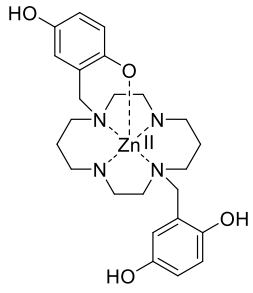 Zn(H_3qp4)	inactive		**Publication 4** from this work
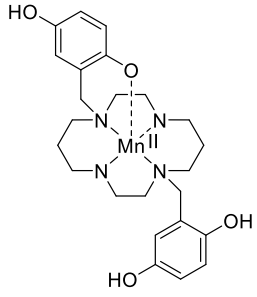 Mn(H_3qp4)	MOPS, 7.4	6.0 x 10^6 M^{-1} s^{-1}	**Publication 4** from this work
	MOPS, 7.8	4.5 x 10^6 M^{-1} s^{-1}	
	Phosphate, 7.4	2.9 x 10^6 M^{-1} s^{-1}	

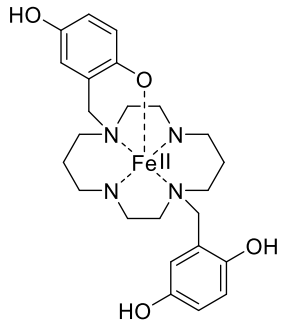 Fe(H_3qp4)	inactive	**Publication 4** from this work

2.2.1.1 Systems with acyclic ligands

In **Publication 1** from this work, the synthesis and the low-temperature stopped-flow UV/Vis time resolved analysis, as well as cryo MS studies of the novel Zn(H_4qp2) complex (Figure 33), featuring the acyclic H_4qp2 ligand with two hydroquinone moieties, towards superoxide were reported. This second-generation compound, incorporating redox-innocent zinc(II), exhibited excellent SOD activity compared to the Zn complex with a single hydroquinone unit, Zn(H_2qp1) (Figure 33 and Figure 34), which displayed lower activity (Table 4). Additionally, the macrocyclic complex Zn(H_4qp4) (Figure 36), despite containing two hydroquinone moieties, showed no SOD activity (Table 4). Importantly, such catalytic performance of Zn(H_4qp2) towards superoxide decomposition, as well as activity of all other studded complexes, was demonstrated by direct stopped-flow measurements.

Interestingly, Zn(H_4qp2) emerged as a superior SOD mimetic compared to its Mn(H_4qp2) analogue, despite the redox-inert nature of the zinc center. Notably, its activity remained high even in phosphate buffer, which is not the case for manganese complexes, being of physiologically relevance.

The full dependence of the catalytic cycle on the redox-active ligand system was confirmed through cryo mass spectrometry and low-temperature stopped-flow kinetic studies, which provided mechanistic insights. The detection of a semiquinone radical (SQ) during superoxide dismutation strongly supported the involvement of the ligand in the SOD catalytic cycle. The proposed mechanism (Figure 33) suggests that one hydroquinone unit undergoes redox cycling, while the other contributes to complex stability and modulates coordination dynamics. Through protonation/deprotonation and corresponding dechelation/chelation equilibria, the ligand tunes the number of accessible coordination sites while remaining a good chelator throughout the catalytic turnover, ultimately enabling efficient SOD activity.

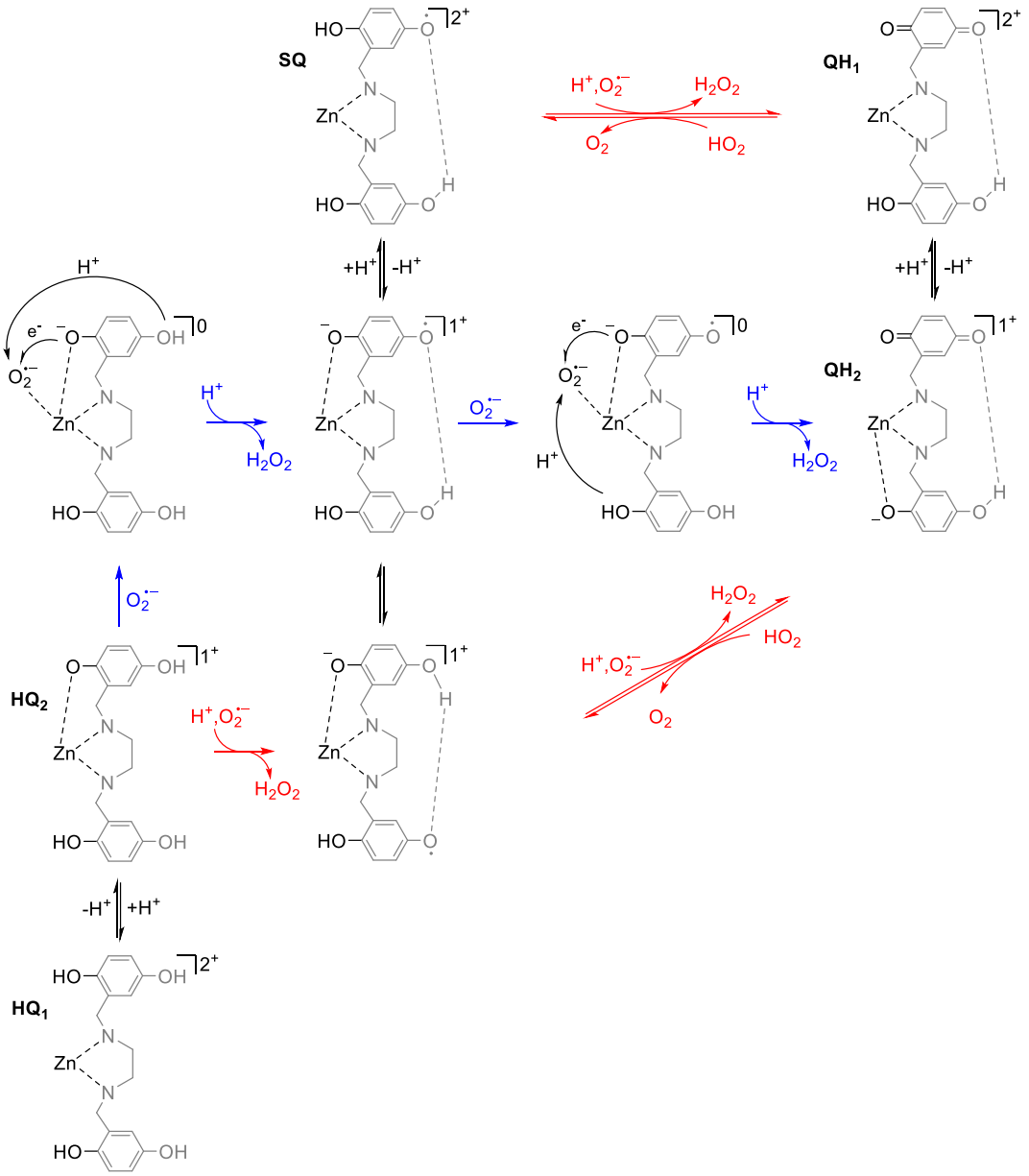

Figure 33: Proposed catalytic mechanism for dismutation of superoxide by the Zn(H4qp2) complex. The assigned species are described as **HQ1** for the protonated diquinol species, **HQ2** for the deprotonated diquionol species, **SQ** for the semiquinone radical species, **QH1** for the protonated mono-*para*-quinone (also referred to as quinhydrone) species and **QH2** for the deprotonated quinhydrone species.

In **Publication 2**, further mechanistic insights into the SOD catalysis by Zn(Hqp1) were gained through computational analysis. Our findings demonstrated that the SOD activity of Zn(Hqp1) is highly dependent on its ability to operate via an inner-sphere mechanism, which requires efficient superoxide binding to the metal center. For this mechanism to be effective, the coordination sphere geometry (influenced by the ligand's chelating ability, conformational flexibility, and steric properties) must allow

superoxide to bind *cis* to the coordinated quinolate upon pyridine displacement (Figure 34) Density Functional Theory (DFT) calculations predicted that designing a ligand system that favors the meridional (*mer*) conformer (left molecule in Figure 34) inherently promotes *cis* binding of the superoxide anion upon pyridin ring opening, thereby enhancing superoxide affinity. This finding reinforces the critical role of ligand structural and chelating properties in SOD activity, consistent with our observations for Zn(H_4qp2). Another key feature of the ligand system is the presence of a second nonmetal-bound -OH group on the hydroquinone moiety, whose deprotonation lowers its redox potential, facilitating its oxidation by the coordinated superoxide. This was further validated experimentally: an analogous complex, where the quinol unit was replaced with phenol (lacking the second -OH), was synthesized and found to be SOD-inactive.

This study thus underscores the importance of a ligand design, where both steric control of the coordination sphere and tunable redox properties dictate the catalytic efficiency of Zn-based SOD mimetics.

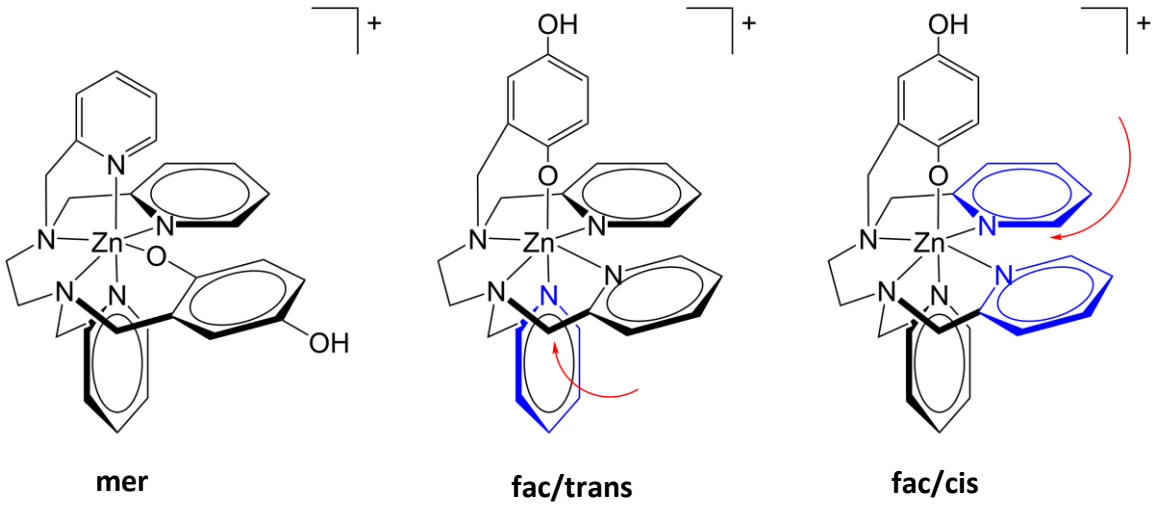

Figure 34: ZnII(Hqp1) complex forming the mer-conformer (left) that inevitably binds superoxide cis to the quinol moiety, resulting (based on theoretical calculations) in the intermediates with lower free energy.

Publication 3 explores the potential of the nickel(II) center, a relatively underutilized metal in SOD mimetic design, in combination with H_2qp1 and H_4qp2 ligands to support SOD catalysis. Our study revealed that both Ni(H_2qp1) and Ni(H_4qp2) (Figure 35) function as potent SOD mimetics, with Ni(H_4qp2) emerging as the most efficient catalyst in the series, surpassing all corresponding transition metal complexes with the same ligand systems (Table 4).

Like for the Zn analogue, cryo-spray mass spectrometry confirmed the participation of a semiquinone radical species, reinforcing the critical role of the ligand-based redox cycle in catalysis. Our investigations demonstrated that the catalytic cycle relies exclusively on ligand redox transformations,

while Ni(II) (despite its potential redox activity) functions analogously to Zn(II) as a superoxide binding center. It modulates both superoxide reactivity and hydroquinone redox properties through coordination and deprotonation of the -OH functionality, emphasizing the significance of an inner-sphere electron transfer mechanism in redox catalysis.

A key distinguishing feature of Ni(H_4qp2) is its resistance to oxidative modifications by superoxide, ensuring greater complex stability under operando catalytic conditions. This stability likely contributes to its superior SOD activity compared to related complexes. We demonstrated this enhanced stability through time-resolved cryo-MS analysis of reaction mixtures and by measuring the catalytic rate constant of pre-reacted Ni(H_4qp2) solutions after exposure to superoxide, confirming its sustained catalytic efficiency.

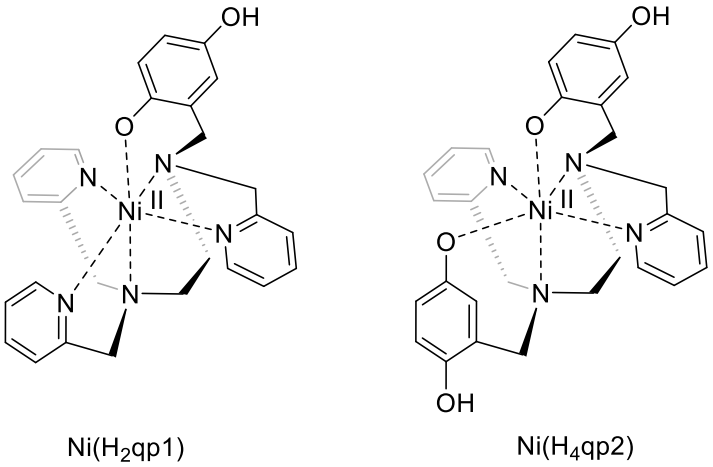

Ni(H_2qp1) Ni(H_4qp2)

Figure 35: Nickel complexes with ligand systems H2qp1 and H4qp2.

2.2.1.2 Systems with macrocyclic ligand

In **Publication 4**, we investigated the combined catalase- and SOD-mimicking properties of Mn, Zn, and Fe complexes featuring the redox-active macrocyclic ligand H_4qp4, which contains two hydroquinone groups (Figure 36). Interestingly, while all three complexes exhibit prominent catalase activity, ranking among the most active small-molecule catalase mimics reported to date, only the manganese complex demonstrated both catalase and SOD activity.

However, the catalytic rate constant for superoxide decomposition by Mn(H_4qp4) is at least an order of magnitude lower than that of the corresponding acyclic ligand complexes, Mn(H_2qp1) and Mn(H_4qp2) (Table 4). This suggests that the more rigid and conformationally restricted macrocyclic ligand framework does not effectively support the SOD catalytic cycle of its metal complexes.

Despite this limitation, all three compounds proved to be highly efficient catalase mimetics. Notably, while the Mn and Fe complexes decompose hydrogen peroxide via high-valent oxo species, the Zn analogue appears to follow a ligand-centered redox mechanism, highlighting distinct mechanistic pathways for catalase activity among these complexes.

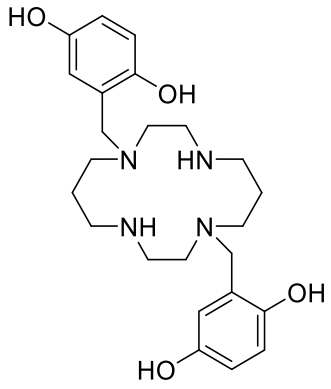

[M(H$_3$qp4)]OTf

M = Mn^{II}, Fe^{II}, Zn^{II}

Figure 36: Transition metal complexes based on the H4qp4 ligand system.

2.2.3 Conclusion

Our studies highlight the critical role of ligand design and flexibility in modulating the SOD and catalase activities of Zn, Ni, Mn, and Fe complexes. Acyclic ligands with redox-active hydroquinone functionalities and greater conformational flexibility facilitate efficient SOD activity via inner-sphere electron transfer through semiquinone intermediates, independent of metal redox properties. Notably, Ni(H$_4$qp2) exhibits exceptional oxidative stability, achieving SOD activity only one order of magnitude lower than native enzymes.

In contrast, the rigid macrocyclic ligand restricts the conformational adaptability needed for the SOD catalytic cycle but enables outstanding catalase activity, placing these complexes among the most potent small-molecule catalase mimetics. The Mn and Fe complexes operate through high-valent oxo species, whereas the Zn analogue follows a ligand-centered redox mechanism for H_2O_2 decomposition.

These findings provide a blueprint for the rational design of next-generation biomimetic antioxidants, emphasizing the crucial role of ligand flexibility in enabling and fine-tuning redox cycling of metal complexes. They also inspire further exploration of metal center interactions with diverse redox-active organic motifs from biological systems, paving the way for the development of potent bioinspired antioxidants.

2.2.4 Advancing High-Pressure Stopped-Flow Techniques for Mechanistic Investigations

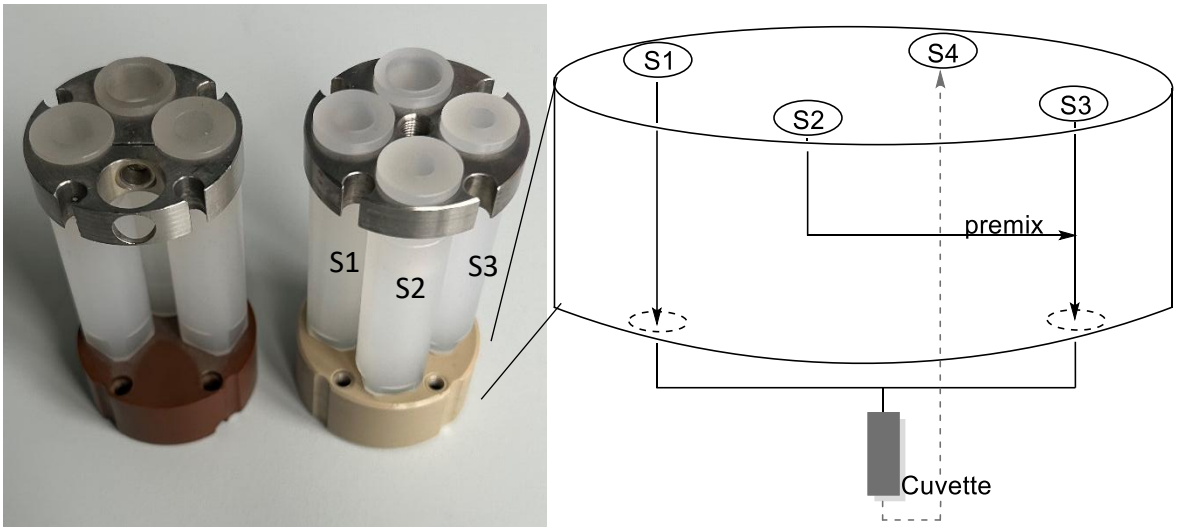

Figure 37: Picture of syringe components for high-pressure stopped-flow systems. Two-syringe-mixing system and the new developed three-syringe-mixing system are shown in the left picture. On the right: a schematic construction plan of the operating principle of the three-syringe-mixing system with S1 and S2 undergoing a pre-mixing.

Building on the principles of stopped-flow instrumentation, significant advancements have been made over time to enable experiments at lower temperatures. This innovation has been important for detecting labile reaction intermediates, thereby providing deeper insights into reaction mechanisms and elucidating reaction pathways. The findings presented in this thesis further highlight the importance of low-temperature kinetic studies, particularly in the context of SOD catalytic mechanisms, reinforcing their relevance in the broader field of reaction kinetics and catalysis.

To achieve an even deeper mechanistic understanding of catalytic processes, applying high-pressure conditions while measuring kinetic rate constants is a powerful yet underutilized approach. Despite its potential to reveal crucial mechanistic details, the application of high-pressure stopped-flow techniques remains rare in the literature. Until now, scientific studies employing this method have been limited to two-syringe-mixing systems (Figure 37, left), which allow for the combination of only two solutions during kinetic investigations.[238-241]

To overcome this limitation, this work presents the development of an innovative three-syringe-mixing high-pressure stopped-flow system, designed to enable the mixing of three solutions while maintaining the same experimental parameters as previous setups. The schematic overview (Figure 37, right) illustrates the novel design, where solutions flow within a closed system, with S4 collecting waste after data acquisition. A key innovation of this setup is its ability to premix solutions in S2 and S3, effectively mimicking the functionality of a delay line found in commercial stopped-flow instruments. This feature

allows the controlled premixing of two reactants with a defined delay before introducing a third compound, significantly enhancing the flexibility of kinetic studies.

This advancement enables, for example, the rapid formation of a high-valent iron-oxo species by combining a precursor iron complex with an oxidizing agent. The active species can then be mixed with a substrate molecule under high-pressure conditions to determine the catalytic substrate transformation rate at variable pressures. The efficient operation of this construct and its capability to deliver unique results have been demonstrated in preliminary experiments, where the kinetics of hydrogen atom abstraction (HAA) from xanthene by Fe(V)-oxo species, generated in situ by premixing [Fe(bTAML)] with *m*-CPBA, were studied at variable pressure (see 5. Supporting Information). This investigation resulted in the determination of the volume of activation for HAA, a crucial kinetic parameter for distinguishing between HAA and concerted proton-coupled electron transfer (PCET), which had remained unexplored in the literature due to experimental inaccessibility. These findings underscore the significance of this methodological advancement. Furthermore, this setup allows not only pressure-variable kinetic measurements but also real-time spectroscopic monitoring of reaction progress, providing a more detailed characterization of evolving intermediates throughout the reaction course.

In conclusion, this novel high-pressure stopped-flow system represents the first in the literature to facilitate the mixing of three different solutions under simultaneous low-temperature and high-pressure conditions, combined with rapid-scan detection. By overcoming previous technical constraints, this innovation significantly broadens the scope of kinetic investigations, particularly in catalytic processes where short-lived reactive species must be generated in situ from pre-catalysts. This methodological breakthrough is expected to open new research avenues in deciphering complex (bio)inorganic reaction mechanisms and advancing the field of reaction kinetics and catalysis.

3 Zusammenfassung

3.1 Ziel der Arbeit

Die Unterdrückung gesundheitsschädlicher Effekte, die durch die Überproduktion reaktiver Sauerstoffspezies (ROS) hervorgerufen werden, ist ein entscheidender Faktor bei der Prävention und Behandlung verschiedener neurodegenerativer und kardiovaskulärer Erkrankungen. Diese Arbeit konzentriert sich auf das Design, die Synthese und die Charakterisierung bioaktiver Übergangsmetallkomplexe mit antioxidativen Eigenschaften, insbesondere auf Superoxid-Dismutase-Mimetika (SODm). Über die in der Literatur weit verbreiteten konventionellen Ligandensysteme hinaus wurden neuartige redoxaktive organische Funktionalitäten untersucht, die von biologischen Systemen inspiriert sind, insbesondere Hydrochinone. Dieser Ansatz führte nicht nur zur Einführung azyklischer und makrocyclischer Liganden, sondern ermöglichte auch eine strategische Erhöhung der Anzahl redoxaktiver Gruppen durch die Integration einer zweiten Hydrochinon-Einheit. Darüber hinaus wurde das Potenzial verschiedener Metallzentren, darunter Mn, Fe, Zn und Ni, untersucht, die auch in natürlichen SOD-Enzymen vorkommen. Ziel war es, eine synergetische antioxidative Aktivität in Kombination mit diesen redoxaktiven Liganden zu erzielen.

Ein zentrales Ziel dieser Arbeit bestand darin, die mechanistischen Feinheiten dieser SOD-Mimetika aufzuklären und zu untersuchen, ob sich das Zusammenspiel zwischen Ligand und Metallzentrum gezielt optimieren lässt, um die katalytische Effizienz zu maximieren, während gleichzeitig die Stabilität des Komplexes unter katalytischen Bedingungen gewährleistet bleibt. Eine der größten Herausforderungen bei der Entwicklung effizienter SOD-Mimetika liegt in der Aufklärung mechanistischer Details, insbesondere durch die Charakterisierung von Reaktionsintermediaten entlang des katalytischen Zyklus. Da der katalytische Prozess mit außergewöhnlich hohen Geschwindigkeitskonstanten abläuft, die 10^8 $M^{-1}s^{-1}$ übersteigen, sind herkömmliche indirekte Methoden nicht in der Lage, zuverlässige kinetische Daten zu liefern. Daher bestand ein zentraler Fokus dieser Studie in der Anwendung einer direkten Stopped-Flow-Technik, um katalytische Geschwindigkeitskonstanten der Superoxiddismutation präzise zu bestimmen und damit zuverlässige Werte für die SOD-Aktivität zu erhalten.

Durch die Kombination von (Kryo)-Stopped-Flow-Spektroskopie mit Kryo-Spray-Massenspektrometrie wurde zudem angestrebt, transiente katalytische Intermediate zu identifizieren und eine umfassende mechanistische Beschreibung dieser Systeme zu erstellen.

Diese Arbeit liefert nicht nur grundlegende Einblicke in die Rolle von Metall-Ligand-Wechselwirkungen bei der Steuerung der Redoxaktivität, sondern zeigt auch das Potenzial einer neuen Klasse biomimetischer Antioxidantien, die auf redoxaktiven Ligandensystemen basieren. Der einzigartige methodische Ansatz hat neuartige mechanistische Erkenntnisse hervorgebracht und eröffnet neue Perspektiven für zukünftige Untersuchungen mit weiteren biologisch inspirierten redoxaktiven

organischen Einheiten. Letztlich tragen diese Ergebnisse zur gezielten Entwicklung nächster Generationen von SOD-Mimetika mit optimierter katalytischer Leistung, Stabilität und therapeutischem Potenzial bei.

Ein weiteres zentrales Ziel dieser Arbeit war die Weiterentwicklung kinetischer Untersuchungen bioanorganischer Reaktionsmechanismen durch die Entwicklung eines Hochdruck-Stopped-Flow-Systems, das nicht nur bei niedrigen Temperaturen betrieben werden kann, sondern auch das Mischen dreier Lösungen unter Hochdruckbedingungen ermöglicht, anstelle der konventionellen Zwei-Spritzen-Techniken. In Kombination mit einer zeitaufgelösten UV/Vis-Detektion konnte dieses System eine detailliertere Untersuchung komplexer Reaktionen ermöglichen, indem Aktivierungsvolumina als entscheidender kinetischer Parameter zur Charakterisierung von Übergangszuständen bestimmt wurden, was wiederum tiefere Einblicke in die Reaktionsmechanismen lieferte.

3.2 Zusammenfassung der Ergebnisse

Umfassende kinetische und mechanistische Untersuchungen wurden an Zn-, Ni-, Mn- und Fe-Komplexen durchgeführt, die entweder azyklische oder makrocyclische redoxaktive Liganden mit einer oder zwei Hydrochinon-Gruppen enthalten. Die resultierenden SOD-Aktivitäten sind in TabelleTable 4 zusammengefasst. Unsere Untersuchungen identifizierten entscheidende Faktoren, die die katalytische Leistung dieser Komplexe beeinflussen, und lieferten wertvolle experimentelle Erkenntnisse für das gezielte Design von SOD-Mimetika auf Basis redox-noninnocenter Ligandensysteme.

In **Publikation 1** dieser Arbeit wurden die Synthese sowie die Tieftemperatur und zeitaufgelöste Stopped-Flow-UV/Vis-Analyse und kryo Massenspektrometrie (MS) des neuartigen Zn(H_4qp2)-Komplexes (Abbildung 33) untersucht, welcher auf dem azyklischen H_4qp2-Liganden mit zwei Hydrochinon-Einheiten basiert. Die zweite Generation dieses Komplexes, welches das redox-inerte Zink(II) enthält, zeigte im Vergleich zum Zn-Komplex mit nur einer Hydrochinon-Einheit, Zn(H_2qp1) (Abbildungen 33 und 34), eine signifikant höhere SOD-Aktivität (Tabelle 4). Im Gegensatz dazu wies der makrocyclische Komplex Zn(H_4qp4) (Abbildung 36) , trotz zweier Hydrochinon-Gruppen, keinerlei SOD-Aktivität auf (Tabelle 4). Die katalytische Aktivität von Zn(H_4qp2) in der Superoxiddismutation sowie die Aktivität aller untersuchten Komplexe wurden durch direkte Stopped-Flow-Messungen nachgewiesen.

Bemerkenswert ist, dass Zn(H_4qp2) eine überlegene SOD-Mimetik im Vergleich zu seinem Mn(H_4qp2)-Analog darstellt, obwohl das Zinkzentrum redox-inert ist. Zudem bleibt die Aktivität selbst in Phosphatpuffer hoch, während dies für Mangan-Komplexe nich zutrifft, was physiologisch äußerst relevant ist.

Die Abhängigkeit des katalytischen Zyklus von dem redoxaktiven Ligandensystem wurde durch kryo Massenspektrometrie und Tieftemperatur Stopped-Flow Experimente bestätigt, die mechanistische Einblicke lieferten. Der Nachweis eines Semichinon-Radikals (SQ) während der Superoxiddismutation unterstützt maßgeblich die Beteiligung des Liganden am SOD-Katalysezyklus. Der vorgeschlagene Mechanismus (Abbildung 33) legt nahe, dass eine der Hydrochinon-Einheiten einem Redox-Zyklus unterliegt, während die andere zur Stabilität des Komplexes beiträgt und die Koordination sichert. Durch Protonierung/Deprotonierung sowie korrespondierende Dechelatisierungs-/Chelatisierungs-Gleichgewichte reguliert der Ligand die Anzahl der zugänglichen Koordinationsstellen, bleibt jedoch während des gesamten katalytischen Zyklus ein effektiver Chelator, was letztlich eine effiziente SOD-Aktivität ermöglicht.

In **Publikation 2** wurden weitergehende mechanistische Einblicke in die SOD-Katalyse von Zn(Hqp1) durch computergestützte Analysen gewonnen. Unsere Ergebnisse zeigen, dass die SOD-Aktivität von Zn(Hqp1) stark von seiner Fähigkeit abhängt, über einen “inner-sphere-Mechanismus“ zu arbeiten, der eine effiziente Superoxid-Bindung an das Metallzentrum erfordert. Damit dieser Mechanismus funktioniert, muss die Geometrie der Koordinationssphäre, beeinflusst durch die Chelatfähigkeit, konformationelle Flexibilität und sterische Eigenschaften des Liganden es ermöglichen, dass Superoxid cis zur koordinierten Chinolat-Einheit bindet, nachdem eine Pyridin-Dissoziation erfolgt ist (Abbildung Figure 34).

Berechnung mithilfe der Dichtefunktionaltheorie (DFT) prognostizierten, dass das Design eines Ligandensystems, das den meridionalen (mer) Konformer begünstigt (linke Molekülstruktur in Abbildung 34), eine cis-Bindung des Superoxid-Anions erleichtert und somit dessen Affinität steigert. Diese Erkenntnis unterstreicht die entscheidende Rolle der strukturellen und chelatisierenden Eigenschaften des Liganden für die SOD-Aktivität, im Einklang mit unseren Beobachtungen für Zn(H_4qp2). Eine weitere zentrale Eigenschaft des Ligandensystems ist die zweite, nicht metallgebundene -OH-Gruppe der Hydrochinon-Einheit, deren Deprotonierung das Redoxpotenzial senkt und somit ihre Oxidation durch koordiniertes Superoxid erleichtert. Dies wurde experimentell bestätigt: Ein analoger Komplex, in dem die Chinol-Einheit durch eine Phenol-Gruppe (ohne die zweite -OH-Funktion) ersetzt wurde, erwies sich als SOD-inaktiv.

Diese Untersuchung hebt die Bedeutung eines Ligandendesigns hervor, bei dem sowohl die sterische Kontrolle der Koordinationssphäre als auch die einstellbaren Redox-Eigenschaften die katalytische Effizienz von Zn-basierten SOD-Mimetika bestimmen.

In **Publikation 3** wurde das Potenzial von Nickel(II) als bislang wenig untersuchtes Metallzentrum für SOD-Mimetika in Kombination mit den H_2qp1- und H_4qp2-Liganden untersucht. Unsere Studie zeigte, dass sowohl Ni(H_2qp1) als auch Ni(H_4qp2) (Abbildung 35) als leistungsstarke SOD-Mimetika fungieren, wobei Ni(H_4qp2) der effizienteste Katalysator der Serie ist und alle entsprechenden Übergangsmetallkomplexe mit denselben Ligandensystemen übertrifft (Tabelle 4).

Wie bei den Zink-Analogen bestätigte die kryo-spray-Massenspektrometrie die Beteiligung eines Semichinon-Radikals, wodurch die zentrale Rolle des ligandbasierten Redox-Zyklus in der Katalyse untermauert wurde. Die Untersuchungen zeigten, dass der katalytische Zyklus ausschließlich auf Ligand-Redox-Transformationen basiert, während Ni(II), trotz seiner potenziellen Redox-Aktivität, analog zu Zn(II) als Superoxid-Bindungszentrum fungiert.

Eine Schlüsselfunktion von Ni(H_4qp2) ist seine hohe oxidative Stabilität gegenüber Superoxid, was eine größere Komplexstabilität unter operando-katalytischen Bedingungen gewährleistet. Diese Stabilität trägt maßgeblich zu seiner überlegenen SOD-Aktivität bei.

In **Publikation 4** wurden die kombinierten Katalase- und SOD-mimetischen Eigenschaften von Mn-, Zn- und Fe-Komplexen mit dem makrocyclischen, redoxaktiven H_4qp4-Liganden untersucht (Abbildung 36). Während alle drei Komplexe eine herausragende Katalase-Aktivität zeigten, erwies sich nur der Mn-Komplex als dual-aktiv. Dennoch war seine katalytische Konstante für Superoxiddismutation mindestens eine Größenordnung niedriger als die der entsprechenden azyklischen Ligandenkomplexe Mn(H_2qp1) und Mn(H_4qp2) (Tabelle 4), was auf eine limitierende sterische Hinderung des makrocyclischen Liganden zurückzuführen ist.

3.3 Fazit

Unsere Studien unterstreichen die entscheidende Rolle des Ligandendesigns und der Flexibilität bei der Modulation der SOD- und Katalase-Aktivitäten von Zn-, Ni-, Mn- und Fe-Komplexen. Azyklische Liganden mit redoxaktiven Hydrochinon-Funktionalitäten und hoher konformationeller Flexibilität ermöglichen eine effiziente SOD-Aktivität durch inner-sphere-Elektronentransfer über Semichinon-Intermediate, unabhängig von den Redoxeigenschaften des Metallzentrums. Bemerkenswerterweise weist Ni(H_4qp2) eine außergewöhnliche oxidative Stabilität auf und erreicht eine SOD-Aktivität, die lediglich eine Größenordnung niedriger als die nativer Enzyme liegt.

Im Gegensatz dazu beschränkt der sterisch gehinderte, makrocyclische Ligand die notwendige Anpassungsfähigkeit für den SOD-Katalysezyklus, ermöglicht jedoch eine hervorragende Katalase-Aktivität. Dadurch zählen diese Komplexe zu den leistungsstärksten niedermolekularen Katalase-Mimetika. Während die Mn- und Fe-Komplexe über hochvalente Oxo-Spezies agieren, folgt das Zn-Analogon einem ligandenzentrierten Redoxmechanismus für die H_2O_2-Zersetzung.

Diese Erkenntnisse liefern eine strategische Grundlage für das Design der nächsten Generation biomimetischer Antioxidantien und betonen die zentrale Bedeutung der Ligandenflexibilität, um das Redox-Cycling von Metallkomplexen zu ermöglichen und gezielt zu steuern. Darüber hinaus regen sie zur weiteren Erforschung von Wechselwirkungen zwischen Metallzentren und vielfältigen redoxaktiven organischen Motiven biologischer Systeme an und ebnen damit den Weg für die Entwicklung leistungsstarker bioinspirierter Antioxidantien.

3.4 Weiterentwicklungen der Hochdruck-Stopped-Flow Technik für mechanistische Untersuchungen

Aufbauend auf den Prinzipien der Stopped-Flow-Technik wurden im Laufe der Zeit erhebliche Fortschritte erzielt, die Experimente bei sehr niedrigen Temperaturen ermöglichen. Diese Innovation ist von besonderer Bedeutung für die Detektion labiler Reaktionsintermediate, wodurch tiefere Einblicke in Reaktionsmechanismen gewonnen und Reaktionswege aufgeklärt werden können. Die in dieser Arbeit vorgestellten Ergebnisse unterstreichen die Relevanz tieftemperaturgestützter kinetischer Studien, insbesondere im Kontext von SOD-Katalysemechanismen, und verdeutlichen ihre Bedeutung für das breitere Forschungsfeld der Reaktionskinetik und Katalyse.

Um ein noch detaillierteres mechanistisches Verständnis katalytischer Prozesse zu gewinnen, stellt die Anwendung von Hochdruckbedingungen bei der Messung kinetischer Geschwindigkeitskonstanten eine leistungsstarke, jedoch bisher selten genutzte Methode dar. Trotz ihres Potenzials, entscheidende mechanistische Erkenntnisse zu liefern, bleibt der Einsatz von Hochdruck-Stopped-Flow-Techniken in der wissenschaftlichen Literatur bislang eine Seltenheit. Bisherige Studien, die diese Methode nutzen, waren auf Zwei-Spritzen-Mischsysteme beschränkt (Abbildung 37, links), die lediglich die Kombination zweier Lösungen während kinetischer Untersuchungen ermöglichen.[238–241]

Um diese Einschränkung zu überwinden, wird in dieser Arbeit die Entwicklung eines innovativen Drei-Spritzen-Hochdruck-Stopped-Flow-Systems vorgestellt, das die Mischung dreier Lösungen erlaubt, während die experimentellen Parameter der bisherigen Systeme erhalten bleiben. Die schematische Darstellung (Abbildung 37, rechts) veranschaulicht das neuartige Design, bei dem die Lösungen in einem geschlossenen System fließen und S4 das Abfallprodukt nach der Datenerfassung sammelt. Eine Schlüsselinnovation dieses Aufbaus ist die Möglichkeit, die Lösungen in S2 und S3 vorzumischen, wodurch die Funktion einer „delay line“ (Verzögerung) nachgeahmt wird, wie sie in kommerziellen Stopped-Flow-Instrumenten eingesetzt wird. Dies erlaubt eine kontrollierte Vormischung zweier Reaktanden mit einer definierten Verzögerung, bevor eine dritte Verbindung hinzugefügt wird, was die Flexibilität kinetischer Studien erheblich erweitert.

Diese Weiterentwicklung ermöglicht es beispielsweise, eine hochvalente Eisen-Oxo-Spezies schnell zu erzeugen, indem eine Vorstufe des jeweiligen Eisen-oxo-Komplex mit einem Oxidationsmittel kombiniert wird. Die gebildete aktive Spezies kann anschließend unter Hochdruckbedingungen mit einem Substratmolekül umgesetzt werden, um die katalytische Umwandlungsrate unter variablen Druckbedingungen zu bestimmen. Die Effizienz dieses Systems sowie seine Fähigkeit, neue experimentelle Erkenntnisse zu liefern, wurden in ersten Untersuchungen nachgewiesen. Dabei wurde die Kinetik der Wasserstoff-Transfer-Reaktion (HAA) von Xanthen durch eine Fe(V)-Oxo-Spezies, die in situ durch Vormischen von [Fe(bTAML)] mit m-CPBA erzeugt wurde, unter variablen Druckbedingungen untersucht (siehe 5. Supporting Information). Diese Studie führte zur Bestimmung des Aktivierungsvolumens für HAA, eines entscheidenden kinetischen Parameters zur Unterscheidung

zwischen HAA-Mechanismen und konzertierten protonengekoppelten Elektronentransfer-Reaktionen (PCET). Da diese Messungen aufgrund experimenteller Einschränkungen bislang nicht zugänglich waren, stellt dieses Ergebnis einen bedeutenden Fortschritt dar. Darüber hinaus ermöglicht das entwickelte System nicht nur druckvariable kinetische Messungen, sondern auch spektroskopische Überwachung des Reaktionsverlaufs in Echtzeit. Dies erlaubt eine detailliertere Charakterisierung der entstehenden Intermediate während der gesamten Reaktion.

Zusammenfassend stellt dieses neuartige Hochdruck-Stopped-Flow-System das erste in der Literatur dokumentierte System dar, das die Mischung dreier unterschiedlicher Lösungen unter gleichzeitigen Niedrigtemperatur- und Hochdruckbedingungen ermöglicht und mit schneller spektraler Detektion kombiniert ist. Durch die Überwindung vorheriger technischer Einschränkungen erweitert diese Innovation das Spektrum kinetischer Untersuchungen erheblich, insbesondere bei katalytischen Prozessen, in denen kurzlebige reaktive Spezies in situ aus Vorstufen erzeugt werden müssen. Dieser methodische Durchbruch eröffnet neue Forschungsansätze zur Aufklärung komplexer (bio)anorganischer Reaktionsmechanismen und trägt zur Weiterentwicklung der Reaktionskinetik und Katalyse bei.

4 Peer-Reviewed Publications

Publication 1: Diquinol Functionality Boosts the Superoxide Dismutase Mimicry of a Zn(II) Complex with a Redox-Active Ligand while Maintaining Catalyst Stability and Enhanced Activity in Phosphate Solution

J.L. Moore, J. Oppelt, L. Senft, A. Franke, A. Scheitler, M. W. Dukes, H. B. Alix, A. C. Saunders, S. Karbalaei, D. D. Schwartz, I. Ivanović-Burmazović and C. R. Goldsmith

Inorganic Chemistry, **2022**, *61*, 19983-19997.

Summary: In this publication the use of a redox-active organic ligand that becomes activated by coordinating a redox innocent metal center was demonstrated in a collaboration between Goldsmith and Ivanović-Burmazović groups. The synthesis of the acyclic hexadentate H_4qp2 and pentadentate H_2qp3 ligands and following the metal incorporation was performed by Jamonica L. Moore, resulting in a novel second-generation SOD active Zn(II) complex. With two quinol arms in its ligand framework, Zn(H_4qp2) has been shown to efficiently catalyze superoxide dismutation, whereas the closely related Zn(H_3qp2), which contains only one quinol group and one fewer donor atom than H_4qp2, exhibited no activity toward the superoxide anion radical. Further experimental studies monitoring reaction of superoxide with the complex via cryo spray mass spectrometry and low-temperature stopped-flow to resolve the catalytic mechanism indicate the presence of a semiquinone radical. The characterized intermediates are integrated into the postulated mechanism, highlighting the crucial role of the redox-active ligand system and its coordination dynamics in enable superoxide dismutation.

Contribution: Kinetic studies were performed by JO using stopped-flow technique to observe time-resolved decay of the superoxide anion radical in presence of the Zn(H_4qp2) complex. The resulting k_{cat} values, along with data from cryo-spray mass spectrometry and low-temperature stopped-flow experiments, were analyzed, interpreted, and integrated into the proposed overall mechanism by JO, under the mentorship of IIB. The observed involvement of a semiquinone radical species strongly supported a metal centered redox mechanism that together with coordination variability of the H_4qp_2 ligand explains the catalytic performance of [Zn(H_4qp2)](OTf)$_2$. JO shares first authorship with Jamonica L. Moore on this publication.

Inorganic Chemistry

pubs.acs.org/IC Article

Diquinol Functionality Boosts the Superoxide Dismutase Mimicry of a Zn(II) Complex with a Redox-Active Ligand while Maintaining Catalyst Stability and Enhanced Activity in Phosphate Solution

Jamonica L. Moore,[⊥] Julian Oppelt,[⊥] Laura Senft, Alicja Franke, Andreas Scheitler, Meghan W. Dukes, Haley B. Alix, Alexander C. Saunders, Sana Karbalaei, Dean D. Schwartz, Ivana Ivanović-Burmazović,* and Christian R. Goldsmith*

Cite This: *Inorg. Chem.* 2022, 61, 19983−19997 Read Online

ACCESS | Metrics & More | Article Recommendations | Supporting Information

ABSTRACT: In the current work, we demonstrate ligand design concepts that significantly improve the superoxide dismutase (SOD) activity of a zinc complex; the catalysis is enhanced when two quinol groups are present in the polydentate ligand. We investigate the mechanism through which the quinols influence the catalysis and determine the impact of entirely removing a chelating group from the original hexadentate ligand. Our results suggest that SOD mimicry with these compounds requires a ligand that coordinates Zn(II) strongly in both its oxidized and reduced forms and that the activity proceeds through Zn(II)-semiquinone complexes. The complex with two quinols displays greatly enhanced catalytic ability, with the activity improving by as much as 450% over a related complex with a single quinol. In the reduced form of the diquinol complex, one quinol appears to coordinate to the zinc much more weakly than the other. We believe that superoxide can more readily displace this portion of the ligand, facilitating its coordination to the metal center and thereby hastening the SOD reactivity. Despite the presence of two redox-active groups that may communicate through intramolecular hydrogen bonding and redox tautomerism, only one quinol undergoes two-electron oxidation to a *para*-quinone during the catalysis. After the formation of the *para*-quinone, the remaining quinol deprotonates and binds tightly to the metal, ensuring that the complex remains intact in its oxidized state, thereby maintaining its catalytic ability. The Zn(II) complex with the diquinol ligand is highly unusual for a SOD mimic in that it performs more efficiently in phosphate solution.

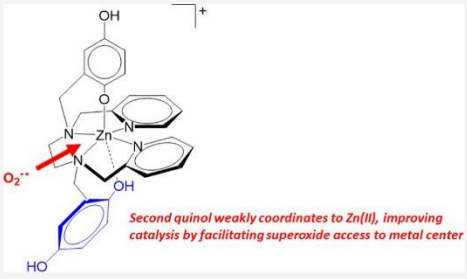

INTRODUCTION

The over-production of reactive oxygen species (ROS), such as superoxide ($O_2^{\cdot-}$) and hydrogen peroxide (H_2O_2), has been associated with a wide array of health conditions.[1−7] Although the exact contributions of ROS to these disorders remain unresolved, the development of antioxidants capable of correcting aberrant oxidative activity within the body would greatly benefit modern medicine.[8] One attractive antioxidant design strategy is to synthesize small molecules that resemble the enzymes that the body itself uses to regulate ROS concentrations. A small dose of such an antioxidant would alleviate oxidative stress by catalytically degrading one or more sorts of ROS. Investigated antioxidants include functional mimics of superoxide dismutases (SODs), which are manganese-, iron-, nickel-, or copper-containing enzymes that catalyze the degradation of $O_2^{\cdot-}$ to O_2 and H_2O_2 (eq 1).[9−17] In these enzymes, the metal cycles between two oxidation states, with the oxidized form oxidizing $O_2^{\cdot-}$ to O_2 and the reduced partner reducing $O_2^{\cdot-}$ to H_2O_2. The copper-containing SODs usually, but not always,[18] contain a Zn(II) ion in the active site. The role of the Zn(II) appears to be to stabilize the enzyme and facilitate release of the H_2O_2 product, but some catalysis is retained if the zinc is removed.[19,20]

$$2O_2^{\cdot-} + 2H^+ \rightarrow O_2 + H_2O_2 \quad (1)$$

Our laboratory has recently found that three Mn(II)-containing magnetic resonance imaging contrast agent sensors for H_2O_2 can also serve as catalysts for $O_2^{\cdot-}$ degradation.[21−25] The organic ligands of two of these probes contain quinol (hydroquinone, HQ) groups, which reversibly oxidize to *para*-quinones upon reaction with excess $O_2^{\cdot-}$ or H_2O_2 (Scheme

Received: September 13, 2022
Published: November 29, 2022

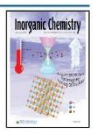

https://doi.org/10.1021/acs.inorgchem.2c03256
Inorg. Chem. 2022, 61, 19983−19997

1).[22,23,25] These catalysts differ from other SOD mimics in that the organic ligand can potentially serve as a redox partner for

Scheme 1

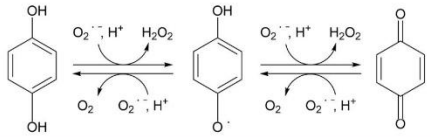

the oxidation and reduction of $O_2^{\cdot-}$; normally, the transition metal is the sole oxidant and reductant. Although metal-free *N*-(2,5-dihydroxybenzyl)-*N*,*N*′,*N*′-*tris*(2-pyridinylmethyl)-1,2-ethanediamine (H_2qp1, Scheme 2) cannot catalyze superoxide degradation by itself, $[Zn(H_2qp1)(OTf)]^+$ (**1**) is a viable catalyst, with activity comparable to those of manganese-containing SOD mimics.[26] The activity is further notable because it is amplified in phosphate buffer; phosphate anions competitively inhibit most manganese-containing SOD mimics.[24,27,28] Because Zn(II) cannot readily change oxidation states, the H_2qp1 ligand was proposed to be the relevant redox partner for $O_2^{\cdot-}$ and cycle through three different forms, containing either a quinol (HQ), a quinoxyl radical (semiquinone, SQ), or a *para*-quinone (Scheme 1). The catalytic activity of this compound demonstrates that the dual roles of the transition metal ion in traditional SOD mimicry—electrostatically attracting $O_2^{\cdot-}$ and transferring electrons to or from the substrate—can instead be fulfilled by a complex consisting of a redox-inactive metal ion and a redox-active ligand.

There are many benefits to such an approach. First, it allows innocuous metal ions to be used in the place of more toxic redox-active transition metals, such as iron and manganese. Second, Zn(II) complexes tend to be more stable than their Mn(II) and Fe(II) analogues,[29,30] which should prolong catalysis. Due to these first two factors, the study of manganese-containing SOD mimics has been heavily centered around complexes with macrocyclic ligands, which can be difficult to synthesize and modify. Even with these measures, these compounds tend to have limited stability in aqueous solutions.[31−33] A third, and unanticipated, benefit is the aforementioned enhanced activity of **1** in phosphate solution. This is a significant advantage because mammalian cells contain high levels of phosphate.[34,35]

The development of additional complexes is essential to determine how the molecular structure can impact function, for even subtle changes to the ligand may substantially alter the activity. The H_2qp1 ligand is hexadentate and is capable of fully coordinating the Zn(II) by itself.[26] Previously obtained mass spectrometry data suggest that **1** reacts with $O_2^{\cdot-}$ through an inner-sphere mechanism. Replacing H_2qp1 with a pentadentate ligand or replacing one of the nitrogen atoms with a weaker oxygen atom donor could potentially improve the activity by introducing a more accessible site for superoxide coordination. The structural and potentiometric pH titration data that we have previously obtained for Mn(II) and Zn(II) complexes suggest that quinols are poor ligands but that deprotonation to the quinolate form markedly improves their metal-binding affinity.[22,26] The installation of a second redox-active quinol into the ligand may improve the activity either by better ensuring that a quinol remains bound to the Zn(II) at all times or by providing a donor atom that is easier to displace if one of the quinols remains protonated. Furthermore, the additional quinol may serve to protect the catalyst from inadvertent oxidation and deactivation by ROS by providing a sacrificial reductant; **1** was found to degrade when the concentration of H_2O_2 became too high.[26] In order to develop structure−function relationships for this new class of SOD mimic, we have therefore prepared Zn(II) complexes with *N*,*N*′-(2,5-dihydroxybenzyl)-*N*,*N*′-*bis*(2-pyridinylmethyl)-1,2-ethanediamine (H_4qp2) and *N*-(2,5-dihydroxybenzyl)-*N*,*N*′-*bis*(2-pyridinylmethyl)-1,2-ethanediamine (H_2qp3, Scheme 2). The former ligand was previously used in a redox-responsive MRI contrast agent, whereas the potentially pentadentate H_2qp3 was the immediate precursor in its synthesis.[22]

The complex with two quinols, $[Zn(H_4qp2)]^{2+}$ (**2**), is more active than **1** and likewise performs better as a catalyst in phosphate buffer, whereas $[Zn(H_2qp3)(H_2O)]^{2+}$ (**3**) does not noticeably hasten $O_2^{\cdot-}$ degradation beyond the uncatalyzed reaction. Simply mixing zinc salts and quinols together is therefore not sufficient to achieve SOD mimicry. The relative activities of the three Zn(II)-quinol complexes can be rationalized by the speciation of the complexes in water and the observed end-products of oxidation by $O_2^{\cdot-}$. Complex **2** also differs from **1** in that it can react with O_2; this represents a rare instance of a redox-inactive metal activating dioxygen.[36]

■ EXPERIMENTAL SECTION

Materials. All chemicals and solvents were purchased from Sigma-Aldrich and used as received unless otherwise noted. 2,2-Diphenyl-1-picryl-hydrazyl hydrate (DPPH) was supplied by EMD Millipore. All deuterated solvents were bought from Cambridge Isotopes. Diethyl ether (ether) and methanol (MeOH) were bought from Fisher. Methylene chloride (CH_2Cl_2) was purchased from Mallinckrodt Baker. *N*,*N*′-*Bis*(2,5-dihydroxybenzyl)-*N*,*N*′-*bis*(2-pyridinylmethyl)-1,2-ethanediamine (H_4qp2) and *N*-(2,5-dihydroxybenzyl)-*N*,*N*′-*bis*(2-pyridinylmethyl)-1,2-ethanediamine (H_2qp3) were previously prepared.[22]

Instrumentation. All ^1H and ^{13}C NMR spectra were recorded on a 400 MHz or 600 mHz AV Bruker NMR spectrometer. In each spectrum, the reported NMR resonance peak frequencies were

Scheme 2

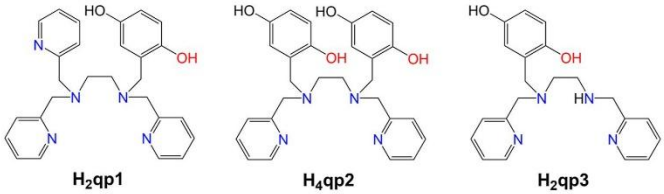

https://doi.org/10.1021/acs.inorgchem.2c03256
Inorg. Chem. 2022, 61, 19983−19997

referenced to internal standards, such as solvent resonances. A Bruker EMX-6/1 X-band electron paramagnetic resonance (EPR) spectrometer operated in the perpendicular mode was used to collect EPR data, which were subsequently analyzed with the program EasySpin. All EPR samples were run as frozen solutions in quartz tubes. Optical data were collected on a Varian Cary 50 spectrophotometer and analyzed using software from the WinUV Analysis Suite. High-resolution mass spectrometry data were obtained at the Mass Spectrometer Center at Auburn University on a Bruker microflex LT MALDI-TOF mass spectrometer via direct probe analysis operated in the positive ion mode. Infrared spectroscopy (IR) data were obtained with a Shimadzu IR Prestige-21 FT-IR spectrophotometer. Cyclic voltammetry (CV) was performed under N_2 at 294 K using an Epsilon electrochemistry workstation (Bioanalytical System, Inc.), a gold working electrode, a platinum wire auxiliary electrode, and a silver/silver (I) chloride reference electrode. All elemental analyses (C, H, and N) were performed by Atlantic Microlabs (Norcross, GA); crystalline samples were dried under vacuum and placed under a N_2 atmosphere prior to shipment.

X-ray Crystallography. Structural data on single crystals were collected using a Bruker D8 VENTURE κ-geometry diffractometer system equipped with an Incoatec IμS 3.0 microfocus sealed tube (Mo Kα, λ = 0.71073 Å) and a multilayer mirror monochromator. SMART (v 5.624) was used to determine the preliminary cell constants and control data acquisition. The Bruker SAINT software package was used to determine integrated intensities; the data were corrected for absorption effects using the multi-scan method (SADABS). The structure was solved and refined using the Bruker SHELXTL software package. All non-hydrogen atoms were refined anisotropically. Hydrogen atoms were included at idealized positions 0.95 Å from their parent atoms prior to the final refinement. Further details regarding the data acquisition and analysis are included in the Supporting Information as well as Table 1.

Table 1. Selected Crystallographic Data for 2 and 3[a]

parameter	$[Zn(H_4qp2)](OTf)_2$ (2)	$[Zn(H_2qp3)(H_2O)](OTf)_2$ (3)
formula	$C_{30}H_{30}F_6N_4O_{10}S_2Zn$	$C_{23}H_{27}F_6N_4O_{10}S_2Zn$
MW	850.07	762.97
crystal system	triclinic	monoclinic
space group	$P\bar{1}$	$P121/n1$
a (Å)	11.5601(4)	11.5256(4)
b (Å)	11.9171(4)	12.4789(4)
c (Å)	13.8096(5)	21.6728(7)
α (°)	100.936(2)	90
β (°)	105.707(2)	90.4010(10)
γ (°)	105.978(2)	90
V (Å^3)	1687.37(10)	317.05(18)
Z	2	4
crystal color	colorless	colorless
T (K)	100(2)	110(2)
reflns collected	57,040	93,868
unique reflns	16,337	16,779
$R1$ (F, $I > 2\sigma(I)$)	0.0517	0.0454
$wR2$ (F^2, all data)	0.1375	0.1256

[a] $R1 = \Sigma||F_o| - |F_c||/\Sigma|F_o|$; $wR2 = [\Sigma w(F_o^2 - F_c^2)^2/\Sigma w(F_o^2)^2]^{1/2}$.

Potentiometric Titrations. The speciation chemistry of the Zn(II) complexes in water was assessed using a METROHM 765 Dosimat with a jacketed, airtight glass titration vessel. A Fisher Scientific Accumet Research AR15 pH meter was used to determine the pH of the sample solutions during the titrations. The electrode was calibrated before each titration using commercially available standard solutions buffered to pH 4.0, 7.0, and 10.0. All samples were purged with argon prior to analysis and subsequently analyzed under an argon atmosphere at 25 °C. All solution samples were prepared in solutions of 100 mM KCl in deionized Millipore water. The titrations investigating metal−ligand speciation were run with solutions that contained a 1:1 molar mixture of the ligand and $Zn(OTf)_2$. Carbonate-free solutions of 0.10 M KOH and 0.10 M HCl were prepared using argon-saturated deionized Millipore water. Initially, we estimated pK_a values through visual inspection of the data plotted in KaleidaGraph v. 4.0. We subsequently attempted to analyze and fit the data to speciation models using the Hyperquad2006 program.[37]

Analysis of the Antioxidant Properties of the Coordination Complexes. We previously screened the abilities of other coordination complexes to catalytically degrade superoxide using the xanthine oxidase/hypoxanthine/lucigenin assay.[22,23,38] The superoxide was generated in situ from a reaction between xanthine and xanthine oxidase. A subsequent reaction between O_2^- and lucigenin provides a spectroscopic signal that can be used to quantify an antioxidant's ability to degrade O_2^-. The copper/zinc superoxide dismutase isolated from bovine erythrocytes (0.001−100 U/mL, Calbiochem) served as a positive control. Each assay was carried out in a total volume of 1 mL containing 50 mM Tris (pH 8.0), hypoxanthine (50 μM), xanthine oxidase (0.005 U/mL, Calbiochem), and dark-adapted lucigenin (5 μM) in the presence of either the studied Zn(II) complex (0.1 nM−10 μM) or its vehicle. Reactions were carried out at room temperature and were initiated by the addition of xanthine oxidase to the hypoxanthine-containing solution. Luminescence was measured using a TD-20/20 (Turner Designs) luminometer and expressed as relative light units (RLUs). Luminescence was measured for four 10 s integrations after an initial delay of 3 s. The four RLU values were averaged, and each concentration was expressed as a percent of that produced in the presence of vehicle. Duplicates of each data point were collected, and the entire assay was performed three times.

We also assessed the antioxidant activities of the Zn(II) complexes through the DPPH assay (DPPH = 2,2-diphenyl-1-picrylhydrazyl radical hydrate).[39−41] In this assay, potential antioxidants are tested for their abilities to donate hydrogen atoms to the radical to generate the corresponding hydrazine. Aqueous solutions of either **2**, **3**, or ascorbic acid were added to a solution of 0.10 mM DPPH in MeOH, such that the final reaction volume was 0.2 mL. Samples were incubated in the dark for 30 min at room temperature before being spectrophotometrically analyzed on a Molecular Devices Spectramax Plus. The absorbance at 517 nm, the λ_{max} of the hydrazine product, was recorded. Experiments were performed in triplicate.

Determination of In Vitro SOD Activity via Stopped-Flow Kinetics. The abilities of the Zn(II) complexes to catalytically degrade superoxide were more thoroughly tested by a direct method using stopped-flow techniques that have been more fully described in prior work from one of our laboratories.[27] Stopped-flow measurements were performed on a Biologic SFM-400 four syringe stopped-flow system using only the first three syringes and a Berger Ball mixer to minimize mixing effects between aqueous buffered solutions and DMSO solutions of KO_2. A J&M TIDAS S MMS UV/VIS diode array detector (integration time 0.5 ms, 180−720 nm wavelength) and an Energetiq LDLS ENQ EQ-99-FC laser-driven light source were used.

Superoxide solutions were prepared by suspending 220−240 mg KO_2 in 20 mL of dry DMSO. The suspension was stirred for at least 30 min under an inert atmosphere before the suspension was filtered through a PTFE syringe filter (Ø = 0.45 μm) to give a saturated KO_2 solution, which was transferred to the stopped flow setup. The potential SOD mimics (SODm) were dissolved in aqueous solutions buffered to either pH 7.4 or 8.1. The buffers were prepared from Millipore water and either 4-morpholinepropanesulfonic acid (MOPS) or sodium dihydrogen phosphate. The concentration of the buffer was 60 mM, and the ionic strength was adjusted to 150 mM for each solution through the addition of NaCl. All of the buffered solutions were treated with Chelex 100 sodium exchange resin for at least 24 h before use in order to remove adventitious metal ions. Stock solutions containing 0.10 mM of each tested SODm were prepared in each buffer; if necessary, the stock solution contained 10% DMSO to ensure that the complexes dissolved fully. The stock solutions were

https://doi.org/10.1021/acs.inorgchem.2c03256
Inorg. Chem. 2022, 61, 19983−19997

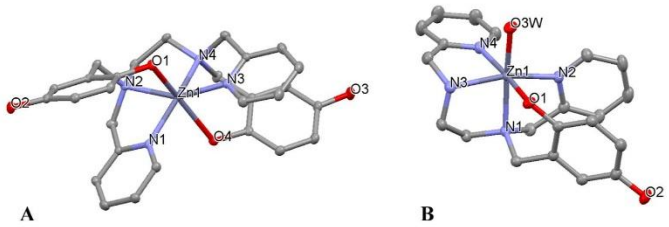

Figure 1. Thermal ellipsoid plots of (A) $[Zn(H_4qp2)]^{2+}$ and (B) $[Zn(H_2qp3)(H_2O)]^{2+}$. Ellipsoids set at 50% probability. All hydrogen atoms, triflate counteranions, and non-bound solvent molecules have been omitted for clarity.

diluted in buffer to give a series of SODm concentrations suitable for the stopped-flow experiments.

Kinetic measurements were performed adding a large excess of superoxide to the putative SOD mimetic: $[O_2^{\cdot-}]$ = 100−200 μM, [SODm] = 0.25−4.5 μM. The aqueous solution containing the studied Zn(II) complex was mixed in a 9:1 ratio with the superoxide solution in DMSO using a high-density mixer. In each experiment, the concentration of superoxide exceeded that of the zinc-containing catalyst by at least 10-fold to ensure catalytic conditions. The starting concentrations of superoxide were determined before each measurement from the absorbance at 250 nm—the characteristic λ_{max} for the superoxide band—and the documented molar extinction coefficient for $O_2^{\cdot-}$ at this wavelength (ε = 2257 M^{-1} cm^{-1} at pH 7.4 and 7.8 or ε = 2260 M^{-1} cm^{-1} for pH 8.1).[42] All kinetic data were fit with the program Biokine 32 V4.80. Each k_{obs} value represents an average of at least nine measurements. Each k_{cat} was determined from the slope of k_{obs} versus [SODm]. All measurements were performed at 21 °C.

Cryospray-Ionization Mass Spectrometry. Cryospray-ionization mass spectrometry (CSI-MS) measurements were performed on a UHR-TOF Bruker Daltonik maXis Plus, an ESI-quadrupole time-of-flight (qToF) mass spectrometer capable of a resolution of at least 60.000 (FWHM), which was coupled to a Bruker Daltonik Cryospray unit. The detector was run in the positive ion mode with a source voltage of 3.5 kV and a flow rate of 240 μL/h. The temperatures of the N_2 spray gas and the dry gas used for solvent removal were −40 and −35 °C for superoxide experiments and 0 and 0 °C for hydrogen peroxide experiments, respectively. The mass spectrometer was calibrated prior to each experiment via direct infusion of an Agilent ESI-TOF low concentration tuning mixture, which provided a m/z range of singly charged peaks up to 2700 Da in both ion modes. For the reactions with $O_2^{\cdot-}$, 1 × 10^{-5} M solutions of each compound in MeCN were cooled to −40 °C and mixed with excess solid KO_2. For the reactions with H_2O_2, 1 × 10^{-5} M solutions of each coordination complex in MeCN were cooled to 0 °C and mixed with the given amount of H_2O_2. Aliquots from the resultant mixtures were then injected into the mass spectrometer. To ensure the survival of metastable reaction species generated at low temperatures, the injection syringe and the tubing of the mass spectrometer were precooled with tempered solvent (0 °C or −40 °C, respectively). After tempering, the reaction solutions were injected as quickly as possible, with the recording of mass spectrometry data commencing immediately afterward. Multiple samples were collected and analyzed over time to determine whether the product distribution was changing during the course of the reaction. Aliquots were also analyzed after the reactions warmed to room temperature. The solvents were not rigorously dried in order to ensure a source of protons. The measured data were processed and analyzed with Bruker Data Analysis 5.2.

Syntheses. *[N,N′-Bis(2,5-Dihydroxybenzyl)-N,N′-bis(2-pyridinylmethyl)-1,2-ethanediamine]zinc (II) Triflate {[Zn(H$_4$qp2)](OTf)$_2$, 2}.* The H_4qp2 ligand (213 mg, 0.434 mmol) and $Zn(OTf)_2$ (159 mg, 0.434 mmol) were dissolved in 3 mL of acetonitrile (MeCN) under N_2. The solution was stirred for 16 h at 60 °C. After the solution was cooled to room temperature (RT), ether was gradually added to precipitate the product as a white powder (264 mg, 71%). CH_2Cl_2 was gradually added to a saturated solution of the product in MeOH to yield crystals suitable for single-crystal X-ray diffraction. ^{1}H NMR (400 MHz, CD_3CN, 293 K): δ 8.73 (d, J = 5.4 Hz, 2H), 7.92−8.03 (m, 3H), 7.54 (t, J = 6.4 Hz, 2 H), 7.32−7.45 (m, 5H), 4.39 (d, J = 16.4 Hz, 2H), 4.09−4.27 (m, 1H), 3.72−3.91 (m, 6H), 3.43 (d, J = 13.6 Hz, 2H), 3.22 (s, 1H), 2.75 (d, J = 10.9 Hz, 2H), 2.60 (d, J = 11.1 Hz, 2H). ^{13}C NMR (100 MHz, CD_3CN, 293 K): δ 155.11, 150.56, 147.86, 147.83, 141.11, 132.30, 131.29, 128.73, 125.01, 124.94, 57.38, 52.87. Optical spectroscopy (MeCN, 293 K): 298 nm (ε = 2400 M^{-1} cm^{-1}), 262 nm (ε = 2500 M^{-1} cm^{-1}). IR (KBr, cm^{-1}): 3406 (m), 3144 (m), 1653 (w), 1612 (m), 1576 (w), 1508 (w), 1458 (w), 1400 (s), 1385 (s), 1252 (m), 1157 (m), 1101 (w), 1032 (s), 943 (w), 920 (w), 878 (w), 824 (m), 766 (s), 638 (s), 577 (m), 517 (s), 419 (m). MS (ESI): Calcd for $[Zn(H_3qp2)]^+$, 549.1481, $[Zn(H_4qp2)(OTf)]^+$, 699.1079; Found, 549.1415, 699.1237. Elemental analysis: Calcd for $C_{30}H_{30}N_4F_6O_{10}S_2Zn{\cdot}H_2O$: C, 41.51%; H, 3.72%; N, 6.45%. Found: 41.30%; H, 3.37%; N, 6.32%.

Aqua[N-(2,5-Dihydroxybenzyl)-N,N′-bis(2-pyridinylmethyl)-1,2-ethanediamine]zinc (II) Triflate {[Zn(H$_2$qp3)(H$_2$O)](OTf)$_2$, 3}. The H_2qp3 ligand (166 mg, 0.456 mmol) and $Zn(OTf)_2$ (166 mg, 0.456 mmol) were dissolved in 3 mL of MeCN under N_2. The solution was stirred for 16 h at 60 °C. Ether was added to the solution as it cooled to RT to deposit the product as a white crystalline powder (267 mg, 78% yield). Gradually adding ether to a saturated MeCN solution resulted in crystals that were suitable for single-crystal X-ray diffraction. ^{1}H NMR (400 MHz, CD_3CN, 293 K): δ 8.84 (d, J = 4.8 Hz, 1H) 8.56 (d, J = 4.4 Hz, 1H), 8.39−7.98 (m, 4 H), 7.64−7.35 (m, 6H), 4.54−4.48 (m, 2H), 4.28 (d, J = 16.4 Hz, 2H), 3.73 (t, J = 13.2 Hz, 2H), 3.54 (d, J = 13.3 Hz, 2H), 3.08−3.04 (m, 2H), 2.95 (d, J = 13.2 Hz, 1H). ^{13}C NMR (100 MHz, CD_3CN, 293 K): δ 154.86, 151.18, 147.31, 140.66, 124.42, 121.22, 79.42, 52.97. Optical spectroscopy (MeCN): 295.9 nm (ε = 908 M^{-1} cm^{-1}), 262 nm (ε = 2094 M^{-1} cm^{-1}). IR (KBr, cm^{-1}): 3507 (w), 3134 (m), 1686 (w), 1611 (w), 1508 (w), 1400 (s), 1385 (s), 1260 (m), 1179 (m), 1096 (w), 1032 (s) 876 (w), 860 (w), 820 (w) 800 (w), 766 (m), 727 (w), 646 (s), 581 (m), 521 (s), 415 (m). MS (ESI): Calcd for $[Zn(Hqp3)]^+$, 427.1113, $[Zn(H_2qp3)(OTf)]^+$, 577.0711; found, 427.1127, 577.0742. Elemental analysis (crystals): Calcd for $C_{23}H_{24}N_4F_6O_8S_2Zn{\cdot}2H_2O$: C, 36.16%; H, 3.69%; N, 7.33%. Found: C, 36.12%; H, 3.74%; N, 7.11%.

RESULTS

Synthesis. In a prior publication from our laboratory, we reported the synthesis of both the H_4qp2 and H_2qp3 ligands and the chemistry of a Mn(II) complex with H_4qp2.[22] The triflic acid salt of the H_2qp3 ligand, which was the immediate precursor to H_4qp2, was structurally characterized in that report.

Zn(II) complexes with the H_2qp2 and H_2qp3 ligands can be prepared by dissolving a 1:1 mixture of the ligand and $Zn(OTf)_2$ in hot MeCN. Adding diethyl ether to these solutions precipitates $[Zn(H_4qp2)](OTf)_2$ (**2**) and $[Zn(H_2qp3)(H_2O)](OTf)_2$ (**3**) in high yields (>70%) and purities. The compositions were established by both

https://doi.org/10.1021/acs.inorgchem.2c03256
Inorg. Chem. 2022, 61, 19983−19997

crystallography and elemental analysis. The only challenging aspect about the syntheses is that $Zn(OTf)_2$ is poorly soluble in MeCN, necessitating both the elevated temperature (60 °C) and the lengthy reaction time (16 h). The 1:1 stoichiometry must be strictly observed because any excess $Zn(OTf)_2$ will also precipitate under the isolation conditions and contaminate the desired products. As anticipated, the products are diamagnetic and colorless. The ^{1}H NMR spectra of crystalline samples of both Zn(II) complexes in CD_3CN (Figures S1 and S5) contain more features than anticipated from the crystal structures, and each complex appears to exist as a mixture of conformers and/or coordination isomers in solution. Similarly complicated speciation in solution was also noted for $[Zn(H_2qp1)(OTf)](OTf)$ (**1**).[26]

Structural Characterization. The complexes can be crystallized from either $MeOH/CH_2Cl_2$ or MeCN/ether solutions (Figure 1). The structures differ substantially from the two Zn(II) complexes crystallized from **1**, $[Zn(H_2qp1)(MeCN)](OTf)_2$ and $[Zn(H_2qp1)(OTf)](OTf)$, in that the quinols are bound directly to the metal center.[26] Both of the new structures feature a 2:1 ratio of triflates to Zn(II)-ligand subunits, suggesting that all of the quinols remain protonated. The C−O bonds range from 1.36 to 1.39 Å, confirming both that the quinols have not been inadvertently oxidized and that each of the O−H groups remains protonated.[22,23,43]

In the structure of **2**, the H_4qp2 ligand binds in a hexadentate fashion, accounting for all six of the donor atoms in the coordination sphere of the metal ion. Overall, the Zn(II) is chelated in a highly distorted octahedral geometry, with the two quinols *trans* to each other and the two pyridines approximately *cis* to each other. There are two significant distortions from octahedral geometry. First, the bond angle between the two pyridine N-donors, N(1)-Zn(1)-N(3), is 122°; the larger space between the pyridines makes the structure somewhat resemble a pentagonal bipyramid with a missing equatorial vertex. The quinols shift slightly from their ideal octahedral positions toward the gap between the pyridine rings, resulting in a 163° O−Zn(II)−O bond angle. Second, one of the quinols is bound much more weakly than the other, with Zn−O(1) and Zn−O(4) having bond lengths of 2.196 and 2.364 Å, respectively. Each quinol appears to be hydrogen bonded to two triflates. The extensive hydrogen bonding network results in a relatively dense crystal (1.673 g/cm^3). Each quinol is approximately parallel to a pyridine ring, which may suggest aromatic interactions between these groups. The centroids of the aromatic rings are 3.73 and 3.89 Å apart, with the pyridine-containing N(3) and the quinol-containing O(4) being slightly closer together.

The structure of **3** likewise features the quinol-containing ligand coordinating the metal ion to its maximum extent. The Zn(II) center is coordinated in a distorted octahedral geometry by five atoms from H_2qp3 and an oxygen atom from a water molecule. The bond angles around the Zn(II) center do not deviate from the ideal octahedral values as much as they do for **2**. The pyridine rings from the ligand are *cis* to each other, whereas the bound H_2O is *trans* to one of the amines. As with **2**, the components within the asymmetric unit hydrogen bond extensively with each other, resulting in another dense crystal (1.626 g/cm^3). The non-coordinated OH group in the quinol donates a hydrogen bond to a triflate, while the metal-bound OH hydrogen bonds to an outer-sphere molecule of H_2O. The Zn(II)-bound H_2O hydrogen bonds to the second triflate, which is disordered over two positions. The quinol appears to aromatically interact with one of the pyridine rings; the centroids of the quinol and the pyridine ring containing N(2) are 3.59 Å apart.

Aqueous Solution Characterization. Neither of the solid-state structures of the Zn(II) complexes with H_2qp1 was found to be maintained in water, and the predominant aqueous species for **1** above pH 7 is $[Zn(Hqp1)]^+$, which features a metal-coordinated quinolate.[26] Because **2** and **3** are intended to be used as catalysts for the decomposition of superoxide in aqueous solutions, understanding their behavior in water is essential. We therefore determined the speciation of **2** and **3** in water using potentiometric and spectrophotometric pH titrations (Figures S9−S11).

The acid/base chemistry of the H_4qp2 ligand in water was previously described during our characterization of its complex with Mn(II).[22] The Zn(II) complex displays two clear ionization events as the pH increases from 2.5 to 10. These are consistent with pK_a values of 5.3 and 8.5, which we assign to the deprotonation of the two Zn(II)-bound quinols. The major species between pH 7.0 and 7.4 would therefore be $[Zn(H_3qp2)]^+$, where H_3qp2^- is the singly deprotonated form of the ligand. Unfortunately, we could not use these data to obtain stability constants for $[Zn(H_3qp2)]^+$ and $[Zn(H_2qp2)]$. The log(β) values for these species do not converge to stable numbers even after extensive attempts to fit the data to a wide variety of models using the speciation program Hyperquad. We had encountered similar difficulties modeling the data for $[Zn(H_2qp1)(OTf)]^+$.[26] The ability to calculate these values requires a substantial amount of the metal to dissociate from the ligand under acidic conditions; this does not appear to happen for either the H_2qp1 or H_4qp2 systems. Complex **2** is therefore more stable in water than its Mn(II) analogue, which does dissociate under similar treatment.[22]

The H_2qp3 ligand undergoes four ionization events as the pH is increased from 2.5 to 10 (Table 2 and Figure 2A). We have assigned these to four sequential deprotonations of H_5qp3^{3+}. The first three ionization events are associated with pK_a values of 3.5, 5.13, and 8.19 and likely correspond to the removal of protons from pyridinium and ammonium groups. The 10.2 pK_a value associated with the last ionization event is consistent with the deprotonation of a phenolic OH group, which would convert H_2qp3 into $Hqp3^-$. The error for this value is higher because the $Hqp3^-$ species did not fully form during the titration.

The Zn(II) complex with H_2qp3 appears to be stable above pH 5 (Figure 2B), and the pZn calculated for 1.0 mM ligand and 1.0 mM Zn(II) at pH 7.4 is 7.54. Below pH 5, the Zn(II) complex displays two ionization events. The first is assigned to the association/dissociation of Zn(II). We believe that the second ionization event observed with the increase in pH corresponds to the deprotonation of $[Zn(H_3qp3)]^{3+}$ to $[Zn(H_2qp3)]^{2+}$. The protonation of the ligand at low pH likely facilitates the loss of the metal ion under acidic conditions. The complex is further deprotonated as the pH rises past 5. The 5.57 pK_a value associated with the third ionization event is consistent with the deprotonation of a Zn(II)-bound quinol.[26] At pH 7 and above, the Zn(II) mostly exists as $[Zn(Hqp3)]^+$.

Electrochemistry. The redox behavior of **2** and **3** in aqueous phosphate solutions buffered to pH 7.0 was analyzed by CV. The CV for each complex displays a single feature. For complex **2**, the redox event has $E_{1/2}$ = 195 mV versus Ag/AgCl, with ΔE = 208 mV at a 100 mV/s scan rate (Figure S11).

https://doi.org/10.1021/acs.inorgchem.2c03256
Inorg. Chem. 2022, 61, 19983−19997

Table 2. Stability Constants and pK_a Values for the H_4qp2 and H_2qp3 Ligands and Their Zn(II) Complexes as Determined by Potentiometric Titration at 25 °C

H_4qp2		**Zn−H_4qp2**	
pK_{L1}[a]	7.18 (±0.03)	pK_{a1}[b]	5.3 (±0.3)
pK_{L2}[a]	4.47 (±0.08)	pK_{a2}[b]	8.5 (±0.3)
H_2qp3		**Zn−H_2qp3**	
pK_{L1}[a]	10.2 (±0.3)	pK_{a1}[b]	5.57 (±0.10)
pK_{L2}[a]	8.19 (±0.05)	pK_{a2}[b]	2.98 (±0.15)
pK_{L3}[a]	5.13 (±0.05)	log K(ZnHqp3)[c]	15.75
pK_{L4}[a]	3.5 (±0.3)	log K(ZnH_2qp3)[c]	11.14
		log K(ZnH_3qp3)	5.93

[a]Ligand pK_a values correspond to the following equilibrium constants:

H_4qp2
$K_{L1} = [(H_4qp2)][H^+]/[(H_5qp2)^+]$, from reference.
$K_{L2} = [(H_3qp2)^+][H^+]/[(H_4qp2)^{2+}]$, from reference.

H_2qp3
$K_{L1} = [(Hqp3)^-][H^+]/[(H_2qp3)]$, $pK_{L1} = \log\beta_{010} - \log\beta_{-110}$.
$K_{L2} = [(H_2qp3)][H^+]/[(H_3qp3)^+]$, $pK_{L2} = \log\beta_{110} - \log\beta_{010}$.
$K_{L3} = [(H_3qp3)^+][H^+]/[(H_4qp3)^{2+}]$, $pK_{L3} = \log\beta_{210} - \log\beta_{110}$.
$K_{L4} = [(H_4qp3)]^{2+}[H^+]/[(H_5qp3)^{3+}]$, $pK_{L4} = \log\beta_{310} - \log\beta_{210}$.

[b]Metal complex pK_a values correspond to the following equilibrium constants:

Zn-H_4qp2
$K_{a1} = [[Zn(H_3qp2)]^+][H^+]/[[Zn(H_4qp2)]^{2+}]$.
$K_{a2} = [[Zn(H_2qp2)]][H^+]/[[Zn(H_3qp2)]^+]$.

Zn-H_2qp3
$K_{a1} = [[Zn(Hqp3)]^+][H^+]/[[Zn(H_2qp3)]^{2+}]$, $pK_{a1} = \log\beta_{011} - \log\beta_{-111}$.
$K_{a2} = [[Zn(H_2qp3)]^{2-}][H^+]/[[Zn(H_3qp3)^{3+}]]$, $pK_{a12} = \log\beta_{111} - \log\beta_{011}$.

[c]Metal complex stability constants correspond to the following equilibrium constants:

$K(ZnHqp3) = [[Zn(Hqp3)]^+]/[Zn^{2+}][Hqp3^-]$
$K(ZnH_2qp3) = [[Zn(H_2qp3)]^{2-}]/[Zn^{2+}][H_2qp3]$
$K(ZnH_3qp3) = [[Zn(H_3qp3)^{3-}]]/[Zn^{2+}][H_3qp3^-]$

Complex **3** gives rise to a more reversible redox feature with $E_{1/2}$ = 150 mV versus Ag/AgCl and ΔE = 166 mV at a 100 mV/s scan rate (Figure S12). The peak-to-peak separations for both compounds become larger with faster scan rates, consistent with irreversible redox processes. The peak-to-peak separations increase more markedly for **2**, consistent with the redox for this complex being less reversible. Because the metal center is essentially redox-inactive, these features correspond to the oxidation of the quinols in the ligand to *para*-quinones and their subsequent reduction back to their original state.

Antioxidant Activity. Both **2** and **3** were initially screened using the xanthine oxidase/hypoxathine/lucigenin assay[22,23,38,44] and display above-baseline activity (Figure 3). The IC_{50} values for the elimination of the lucigenin sensing reaction were found to be within error of each other: 24 (±1) nM for **2** and 27 (±17) nM for **3**. The assay likewise does not meaningfully distinguish the antioxidant activities of **2** and **3** from those of the related complexes $[Mn(H_4qp2)Br_2]$ (IC_{50} = 18 nM)[22] and **1** (IC_{50} = 17 nM).[26]

Complexes **2** and **3** were also analyzed with the DPPH assay (Figure 4), which tests the abilities of compounds to donate hydrogen atoms to 2,2-diphenyl-1-picrylhydrazyl radical hydrate.[39−41,45] In this assay, the production of the hydrazine is confirmed and followed by UV/vis. The IC_{50} values for **2** and **3** were measured to be 8.7 and 17.2 μM, respectively, with the H_4qp2 complex being substantially better as an antioxidant. The ascorbic acid standard had an IC_{50} value of 24.2 μM under the same conditions. Other divalent metal complexes with the H_2qp1 and H_4qp2 ligands likewise outperformed ascorbic acid in these measurements by approximately the same extent.[22,23,26]

The aforementioned assays, unfortunately, often provide misleading accounts of the actual reactivity with superoxide due to competing side-reactions between the various components in the reaction mixtures.[12,27,46−49] Consequently, the SOD mimicry was more thoroughly assessed by analyzing the direct reactions between the compounds and KO_2 (Figure 5 and Table 3). Complex **2** reacts directly with $O_2^{\cdot-}$ and accelerates its decomposition, but compound **3** is not a competent catalyst for superoxide disproportionation (Figure S13). The catalytic rate constants for **1** and **2** in various aqueous solutions are provided on Table 3. The activity improves when the solution is made more basic or the buffer is changed from a sulfonate derivative (HEPES, MOPS) to phosphate.

Mechanistic Analysis. When mixtures of **3** and KO_2 are analyzed by mass spectrometry, we find m/z features consistent with Zn(II)-free oxidized ligand but not any that are consistent with Zn(II) complexes with either H_2qp3 or its *para*-quinone counterpart qp3 (Figure S16). The data suggest that the initial oxidation of **3** by KO_2 to $[Zn(qp3)]^{2+}$ weakens the binding affinity of the ligand enough to destabilize the qp3 complex. Our control experiments indicate that free H_2qp3 by itself cannot catalyze superoxide degradation; consequently, we believe that the dissociation of the Zn(II) from the oxidized H_2qp3 ligand (qp3) halts catalysis.

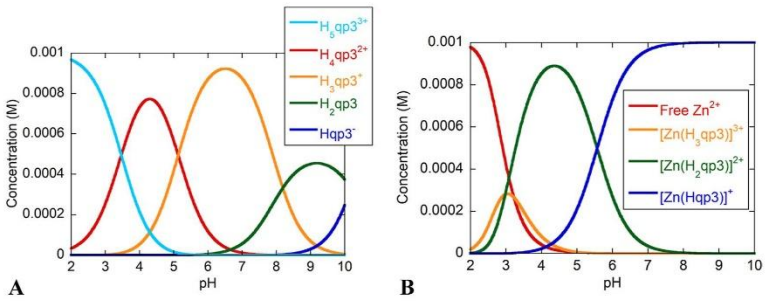

Figure 2. Predicted speciation as a function of pH for (A) 1.0 mM H_2qp3 and (B) a mixture of 1.0 mM H_2qp3 and 1.0 mM $ZnCl_2$ in 100 mM KCl solution.

https://doi.org/10.1021/acs.inorgchem.2c03256
Inorg. Chem. 2022, 61, 19983−19997

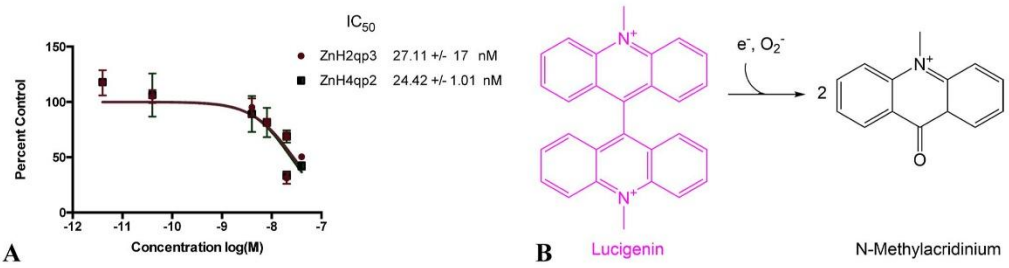

Figure 3. (A) Superoxide scavenging effects of **2** and **3**. Superoxide was generated using a hypoxanthine-xanthine oxidase reaction and detected using the chemiluminescent probe lucigenin. Reactions were carried out in 50 mM Tris−HCl (pH 8.0). Data for the various concentrations of Zn(II) complexes are expressed as a percentage of luminescence in the presence of vehicle. (B) Illustration of the fundamental reaction between lucigenin and superoxide. The depletion of lucigenin eliminates the observed chemiluminescence. The added SOD mimic competes with lucigenin for the superoxide.

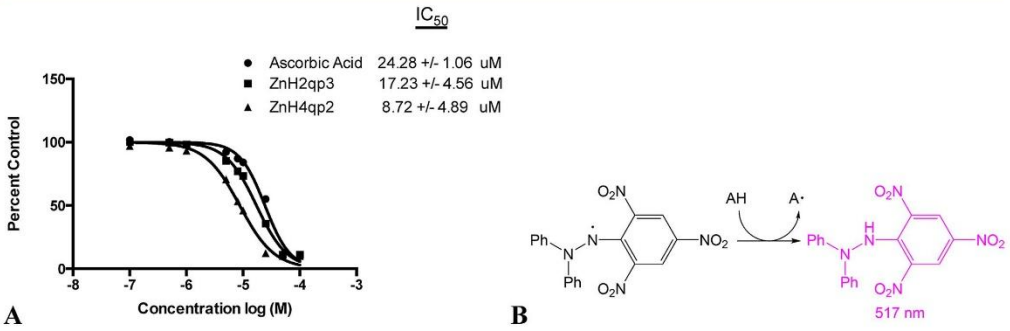

Figure 4. (A) DPPH free radical scavenging assay of **2**, **3**, and ascorbic acid. The antioxidants were added to DPPH and incubated in the dark for 30 min at 298 K. Spectroscopic measurements were performed at 517 nm. The data were normalized to the absorbance in the presence of vehicle. All experiments were performed in triplicate. (B) Illustration of the underlying chemical reaction between DPPH and an antioxidant (AH). H atom transfer from AH to the DPPH radical generates the visible hydrazine species.

We analyzed the reaction between the catalytically active **2** and KO_2 in MeCN by CSI-MS (Figure 6); all identified species are depicted on Scheme 3. $[Zn(H_4qp2)]^{2+}$ (HQ_1) and its conjugate base $[Zn(H_3qp2)]^{+}$ (HQ_2) are found under all conditions. When KO_2 is present, we observe m/z peaks consistent with oxidation to $[Zn(H_2qp2)]^{2+}$ (QH_1) and its subsequent deprotonation to $[Zn(Hqp2)]^{+}$ (QH_2). Although the ligand could conceivably be further oxidized to the di-*para*-quinone compound qp2, we do not detect any traces of either free qp2 or its complex with Zn(II) at either −40 °C or 0 °C. At 0 °C, we do find evidence for the oxidation of the benzylic or picolylic carbons on the ligand framework with both quinolate/quinol (HQ_{2ox}) and quinolate/*para*-quinone (QH_{2ox}) groups (Figure 7). We do not, however, observe any degradation products that would result from either N−C bond cleavage or dechelation (Figure 7).

Unexpectedly, we find traces of a Zn(II) complex with the mono-*para*-quinone form of the ligand (H_2qp2) in the absence of the superoxide. Aerobic solutions of metal-free H_4qp2 do not give rise to either the m/z peaks associated with H_2qp2.

When 0.10 mM **2** is mixed with excess KO_2 in MeCN at −40 °C and monitored by UV/vis, bands at 422 and 448 nm develop over 300 s (Figure 8). These features are characteristic of semiquinone (SQ) radicals.[50,51] Over longer periods of time (600 s), an additional band appears at 520 nm. The energy of this feature is reminiscent of the charge transfer complex quinhydrone (QH), which consists of a reduced hydroquinone interacting with an oxidized *para*-quinone.[52−54] Bands with almost exactly the same energies were observed for a Mn(II) complex with H_4qp2.[25] The intensities of all three features noticeably decrease by 1200 s.

We were able to independently generate a Zn(II)-ligand radical by reacting **2** with a base and a one-electron oxidant in MeCN. When 1.0 mM **2** reacts with 2.4 mM $Ag(SbF_6)$ and 235 mM Et_3N at 25 °C, we observe a strong signal at $g = 2.0$ (Figure S17) at 30 s; the g value is consistent with an organic radical. By 45 min, the feature decreases in intensity by approximately 50%. When we subjected **1** to similar treatment, we likewise observed a transient radical species, but the data differ from those for **2** in that the radical has almost completely vanished by 45 min. We also observed evidence of the generation of a semiquinone radical (SQ, Scheme 3) in the CSI-MS data shown in Figure 6B, where all three possible oxidation forms of the redox active ligand moiety, that is, hydroquinone, semiquinone, and *para*-quinone (quinhydrone), were detected in their protonated forms in the reaction mixture under catalytic conditions. Furthermore, the semiquinone species was detected by CSI-MS in the reaction between **2** and a 10-fold excess of H_2O_2. The reaction with H_2O_2 is orders of magnitude slower than the one with superoxide at 0 °C

https://doi.org/10.1021/acs.inorgchem.2c03256
Inorg. Chem. 2022, 61, 19983−19997

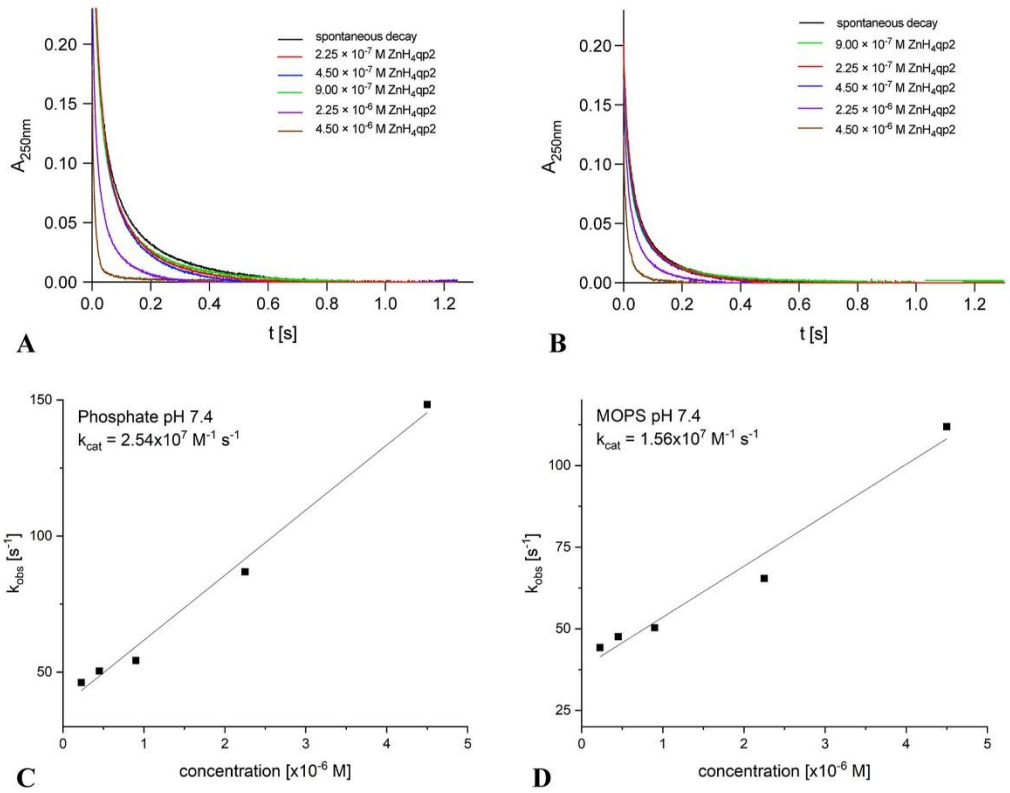

Figure 5. Kinetic traces of superoxide decomposition at 250 nm by **2**. (A) Data taken in 50 mM phosphate buffer, pH 7.4, ionic strength of 150 mM. The starting concentration of superoxide is 1.5×10^{-4} M. (B) Data taken in 60 mM MOPS buffer, pH 7.4, ionic strength of 150 mM. The starting concentration of superoxide is 9×10^{-5} M. (C) Plot of k_{obs} vs [**2**] for the pH 7.4 phosphate data. The k_{obs} values are calculated from the traces in panel A. (D) Plot of k_{obs} vs [**2**] for the pH 7.4 MOPS data. The k_{obs} values are calculated from the traces in panel B.

Table 3. Catalytic Rate Constants, k_{cat} (M^{-1} s^{-1}), Measured by Stopped-Flow Kinetics for the Direct Reactions of 1, 2, and 3 with Superoxide

buffer, pH	1[a]	2	3
60 mM HEPES/MOPS, 7.4	3.4×10^6	1.56×10^7	N.A.
60 mM MOPS, 7.8	N.D.	4.94×10^7	N.A.
60 mM HEPES, 8.1	4.7×10^6	N.D.	N.A.
50 mM phosphate, 7.4	1.9×10^7	2.54×10^7	N.A.

[a]Data from ref 26.

(Figure S18) and does not proceed with a measurable rate at −40 °C. Without the superoxide to serve as a reaction partner, the semiquinone intermediate undergoes self-decay, leading to almost complete degradation of the complex.

■ DISCUSSION

The recently characterized superoxide dismutase (SOD) mimic [Zn(H_2qp1)(OTf)](OTf) (**1**) is highly unusual in that it uses an organic component as the redox partner for the superoxide substrate and lacks a redox-active transition metal ion. Given the instability of most manganese-containing SOD mimics[31−33] and the potential toxicity of this metal in biological systems,[55] the absence of redox-active transition metal ions may make **1** and similar complexes attractive candidates for the clinical treatment of oxidative stress. In order to determine what structural features are required for functional SOD mimicry for this fundamentally new class of catalysts, we prepared Zn(II) complexes with the quinol-containing H_4qp2 and H_2qp3 ligands (Scheme 2). These molecules differ from H_2qp1 in that they either feature a second quinol in place of a pyridine (H_4qp2) or lack one pyridine altogether, being pentadentate rather than hexadentate (H_2qp3).

The syntheses of [Zn(H_4qp2)]$(OTf)_2$ (**2**) and [Zn(H_2qp3)-(H_2O)]$(OTf)_2$ (**3**) are relatively straightforward, and we can readily isolate crystalline samples of both complexes (Figure 1). The crystal structures of **2** and **3** differ from those of **1** in that the quinols bind directly to the Zn(II) center.[26] The structural data for **2** suggest that both quinols cannot coordinate tightly to the Zn(II) at the same time, for the Zn−O(4) bond length is much longer than a typical Zn−O bond.[56] Based on this and the other distortions from octahedral geometry, we speculate that the Zn(II) metal

https://doi.org/10.1021/acs.inorgchem.2c03256
Inorg. Chem. 2022, 61, 19983−19997

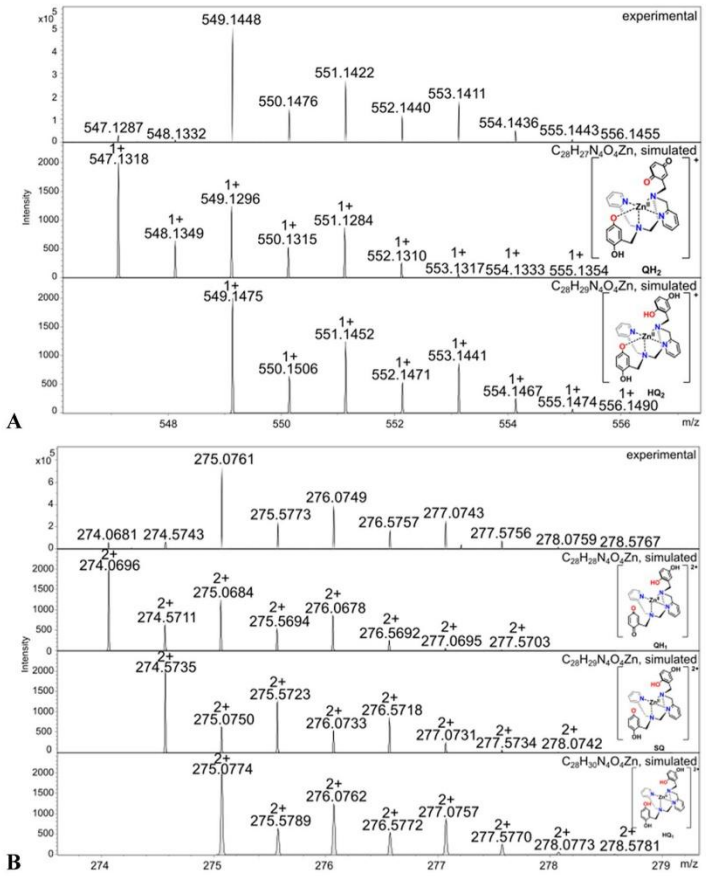

Figure 6. CSI-MS spectrometry of **2** upon reaction with KO_2. The graphics depict possible structures; we cannot preclude other modes of ligand coordination. The m/z = 556.1455 feature in **A** is assigned to $[Zn(H_3qp2)]^+$ (HQ_2, Scheme 3), the deprotonated form of the diquinol species $[Zn(H_4qp2)]^{2+}$ (HQ_1 in Scheme 3) which itself is assigned to the m/z = 275.0761 feature in **B**. The m/z = 547.1287 feature in **A** is assigned to $[Zn(Hqp2)]^+$ (QH_2, Scheme 3), the deprotonated form of the mono-*para*-quinone (existing as quinhydrone, *vide infra*) species $[Zn(H_2qp2)]^{2+}$ (QH_1, Scheme 3) which itself is assigned to the m/z = 274.0696 feature in **B**. The m/z = 274.5743 feature in **B** is assigned to a semiquinone radical species $[Zn(H_3qp2)]^{\cdot 2+}$ (SQ_1 Scheme 3). Experimental conditions: 1 mM solutions of **2** in MeCN (1% DMF) were cooled to −40 °C and then mixed with an excess of solid KO_2. After 6 min, the mixture was diluted in a pre-cooled syringe with pre-cooled MeCN to approximately 1×10^{-5} M and quickly injected into the mass spectrometer. The full range of data is shown in Figure S15.

center may be too small to be fully chelated by the H_4qp2 ligand. The NMR data for all three complexes are consistent with more than one conformer or coordination isomer existing in solution, suggesting that metal coordination by H_2qp1, H_4qp2, and H_2qp3 is both flexible and dynamic.

The weaker association of the second quinol with the Zn(II) appears to be maintained when **2** is dissolved in water. The first pK_a is consistent with a phenol ligated to a divalent metal (Table 2),[22,26,57] but the second measured pK_a value of 8.5 is much higher than anticipated and approaches the value of 10 expected for a non-metal-bound phenol. Both **2** and **3** appear to be stable in water, and the major species between pH 7.0 and 7.4 are Zn(II) complexes with singly deprotonated H_3qp2^- and $Hqp3^-$ ligands: $[Zn(H_3qp2)]^+$ and $[Zn(Hqp3)]^+$ (Figure 2).

Complex **2**, much like **1**, is particularly stable in water, with no metal dissociation observed even at low pH values.[26] The aqueous stabilities of both Zn(II) complexes compare highly favorably to those of the most active small molecule SOD mimics. The Mn(II) porphyrin complex $Mn^{II}Br_8TM\text{-}4\text{-}PyP^{4+}$, for instance, has been documented to be unstable at neutral pH, and the release of free manganese from the complex has hampered its path to clinical use.[31] Manganese complexes with pentaazamacrocycles represent the other major family of highly active SOD mimics. Arguably the best of these catalysts is M40401, which has a catalytic rate constant of approximately

https://doi.org/10.1021/acs.inorgchem.2c03256
Inorg. Chem. 2022, 61, 19983−19997

Scheme 3. Proposed Mechanism of Superoxide Dismutation Catalyzed by 2[a]

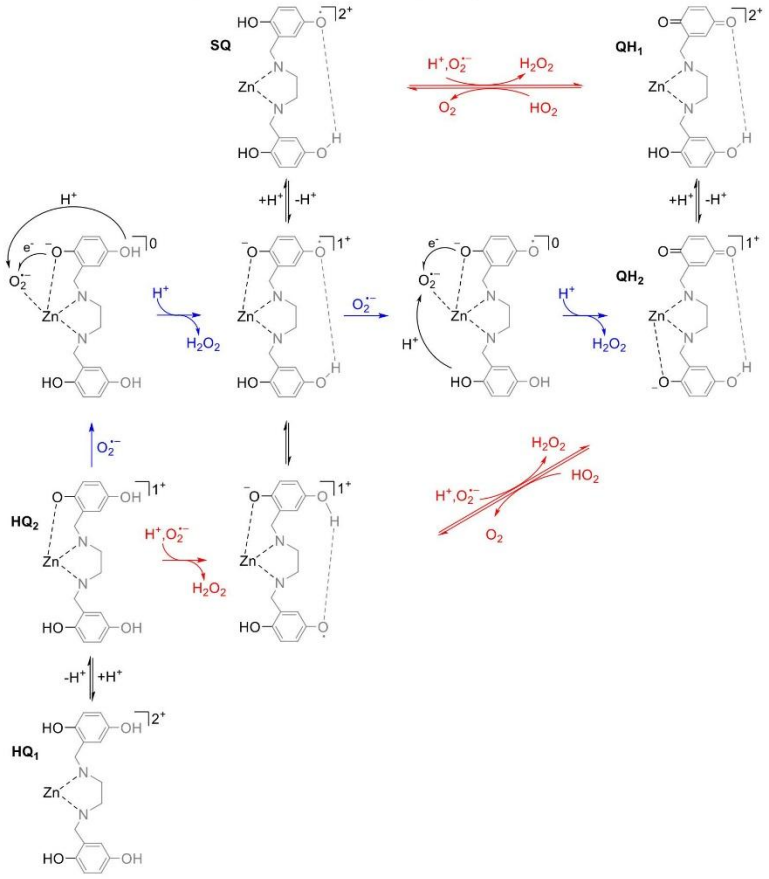

[a]Possible inner-sphere pathways are outlined in blue, whereas outer-sphere pathways are outlined in red. Hydroquinone and quinhydrone species HQ_1, HQ_2, QH_1, and QH_2, respectively, were detected under conditions of catalytic reaction with superoxide by CSI-MS, whereas a semiquinone species SQ was detected within an order of magnitude slower reaction with H_2O_2.

1.5×10^9 M^{-1} s^{-1}, but this compound likewise has limited conditional stability in water.[32,33]

Electrochemically, complexes **2** and **3** resemble **1** in that only a single reduction/oxidation couple is observed by CV (Figures S11 and S12).[26] The ligand structure, however, markedly impacts both $E_{1/2}$ and ΔE. The removal of a pyridine ring from the coordination environment increases $E_{1/2}$ from 312 mV versus NHE (**1**) to 347 mV versus NHE (**3**). This structural change also worsens the reversibility, with ΔE increasing from 95 mV (**1**) to 166 mV (**3**) with a 100 mV/s scan rate. The inclusion of another quinol in the coordination sphere raises $E_{1/2}$ further to 397 mV versus NHE (**2**), and this redox feature is the least reversible of the three observed for the Zn(II)-quinol complexes, with a ΔE of 208 mV with a 100 mV/s scan rate. The H_4qp2 ligand likewise gave rise to a much less reversible redox event than H_2qp1 when ligated to Mn(II), and the CV features observed for $[Mn(H_4qp2)Br_2]$ in water would be considered irreversible by most.[22,23] The ligand-derived redox couple seen for $[Mn(H_4qp2)Br_2]$, however, has an $E_{1/2}$ that is less positive than that of $[Mn(H_2qp1)(MeCN)]^{2+}$. Unlike **2**, both of the H_4qp2 quinols appear to tightly coordinate to the larger Mn(II) center in solution, providing an explanation for why the same decrease in $E_{1/2}$ is not observed for the Zn(II) complexes when the H_2qp1 ligand is replaced by H_4qp2.[22] In both **2** and **3**, the $E_{1/2}$ shifts away from the ~300 mV ideal for SOD activity; these shifts and the lesser reversibility could potentially worsen the catalysis of $O_2^{\bullet-}$ degradation by an outer-sphere mechanism. That **2** is more catalytically active than **1**, despite the less reversible redox feature, suggests that the superoxide dismutation instead proceeds through a more efficient inner-sphere path.

Both **2** and **3** initially appeared to be competent SOD mimics when analyzed via the xanthine oxidase/hypoxanthine/lucigenin[38] and DPPH assays.[39−41,45] The IC_{50} values from

https://doi.org/10.1021/acs.inorgchem.2c03256
Inorg. Chem. 2022, 61, 19983−19997

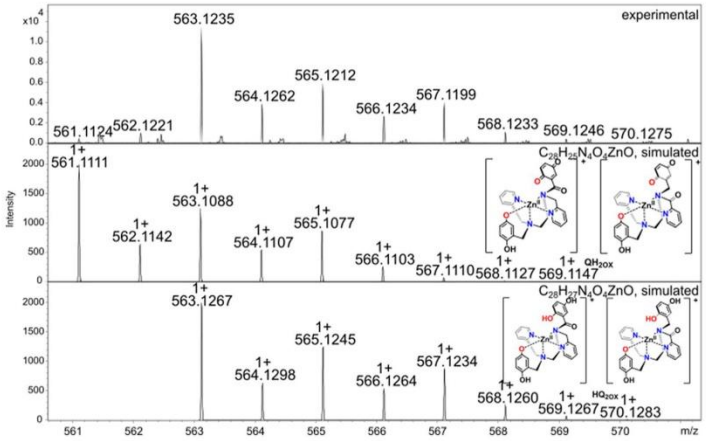

Figure 7. CSI-MS spectrometry of **2** upon a 6 min reaction with KO_2. The graphics depict possible structures; we cannot preclude other modes of ligand coordination. The m/z = 561.1124 feature is assigned to a Zn(II) complex with an oxidized *para*-quinone ligand (QH_{2ox}). Other m/z features are more consistent with Zn(II) complexes with oxidized forms of the quinol ligand (HQ_{2ox}). Experimental conditions: 1 mM solutions of **2** in MeCN (1% DMF) were cooled to −40 °C and then mixed with an excess of solid KO_2. After 6 min, the mixture was diluted in a pre-cooled syringe with pre-cooled MeCN to approximately 1×10^{-5} M and quickly injected into the mass spectrometer. The full range of data is shown in Figure S15.

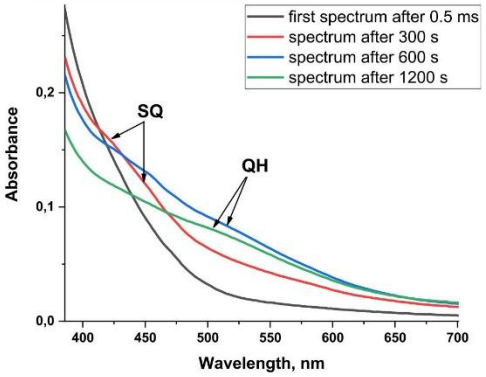

Figure 8. UV/vis data for the reaction between 0.10 mM **2** and excess KO_2 in MeCN at −40 °C.

these measurements (Figures 2 and 3) suggested that their abilities to behave as antioxidants were either comparable or only slightly inferior to those of the related compounds [Mn(H_4qp2)Br_2] and **1**.[22,26] The assay results, however, are misleading. When the direct reactions between the Zn(II) complexes and KO_2 are studied by stopped-flow kinetics methods, the data reveal that **2** is a markedly better catalyst than **1**, whereas **3** is not active enough to measurably increase the rate of $O_2^{\cdot-}$ disproportionation above that of the uncatalyzed reaction (Table 3).

Complex **2** is approximately fivefold more active in MOPS buffer than **1** in the comparable HEPES buffer. As with **1**, the catalysis of **2** proceeds more quickly in phosphate solution. The activities of **1** and **2** are more similar in phosphate buffered to pH 7.4, with **2** being 20% more active than **1**. Complexes **1** and **2** are unique among SOD mimics in that their activities are enhanced, rather than diminished in phosphate buffers.[24,27,28] Given the high prevalence of phosphate in mammalian cells, this represents a substantial advantage.[34,35] That the activity of **2** improves in phosphate buffer suggests that this is a replicable and trademark feature of Zn(II)-quinol SOD mimics that is not just limited to compound **1**. The improved activity in phosphate likely results from the substantially different speciations of the buffer components between pH 7 and 8. MOPS exists as a mixture of a neutral and a monoanionic species, whereas phosphate is a mixture of a monoanionic and a dianionic species. The greater overall negative charge on the phosphate-derived species facilitates their ability to interact with and transfer protons to and from the positively charged Zn(II) species on the mechanistic proton-coupled electron transfer cycle.

Curiously, replacing H_2qp1 with H_4qp2 worsens the SOD mimicry of manganese-containing complexes. Mn(II) is larger than Zn(II),[56] allowing H_4qp2 to fully coordinate the metal center. This in turn allows both quinols to approach the Mn(II) close enough to form strong Mn−O bonds, weakening the associated O−H bonds. With the manganese species, the ability of H_4qp2 to deprotonate to a dianionic form (H_2qp2^{2-}) renders its complexes with Mn(II) and Mn(III) less positive than the analogous complexes with Hqp1$^-$. The lesser overall positive charge hinders the ability of the Mn−H_4qp2 compounds to attract and bind $O_2^{\cdot-}$, thereby decreasing the rate of $O_2^{\cdot-}$ decomposition. The Zn(II)−H_4qp2 system differs from the Mn−H_4qp2 one in that the second quinol cannot approach the metal center as closely (Figure 1) which weakens the influence of the metal center on the acid/base properties of the quinol. The Zn(II)-for-Mn(II) substitution thereby raises the pK_a of the second quinol in the coordination complexes from 7.14 [Mn(II)][22] to 8.5 [Zn(II), Table 2]. The major species for **2** in water at pH 7.4 is consequently cationic [Zn(H_3qp2)]$^+$ rather than [Zn(H_2qp2)]. The Zn(II)-for-

https://doi.org/10.1021/acs.inorgchem.2c03256
Inorg. Chem. 2022, 61, 19983−19997

Mn(II) substitution also doubles the catalytic activity in pH 7.4 phosphate buffer.

The charge of the major species for **1** in pH 7.4 water, $[Zn(Hqp1)]^+$, is likewise +1, yet **1** is a less active catalyst, particularly in solutions using sulfonic acid-based buffers.[26] We speculate that the weak interaction between the second H_4qp2 quinol and the Zn(II) makes that particular coordination site on the metal center more accessible to exogenous ligands, such as $O_2^{\cdot-}$. Although H_4qp2 is hexadentate, the inability of the second quinol to attach firmly to Zn(II) gives the ligand some pentadentate character. All of the donor atoms from H_2qp1, conversely, coordinate strongly to the metal center, and this ligand is more strongly hexadentate as a consequence. With the relatively small size of the Zn(II) ion, the H_2qp1 ligand more efficiently blocks the access of $O_2^{\cdot-}$ to the metal center than H_4qp2. The more ready accessibility of the Zn(II) center in **2** leads to faster $O_2^{\cdot-}$ degradation.

The greater accessibility of the metal center in **2** relative to that in **1** may also explain why O_2 reactivity, albeit slight, is observed for the H_4qp2 complex. Recently, it has been found that O_2 coordination to Zn(II) could activate this oxidant toward reactivity with HS^-, promoting the formation of $H_2S_2^{\cdot-}$ and $O_2^{\cdot-}$ radicals and thereby the persulfidation of proteins containing Zn(II) cofactors.[36] Subsequently, it was demonstrated that a dinuclear zinc complex with labile coordination sites can bind $O_2^{\cdot-}$ and activate it toward the oxidation of an appended phenolate ligand to the corresponding phenoxyl radical.[58] The Zn(II) is essential to the reaction; the free phenolic ligand and superoxide do not react in bulk solution. The Zn(II) in **2** may similarly mediate electron transfer between dioxygen and the coordinated quinolate. Our findings represent another rather unusual instance of Zn(II) modulating redox processes via an inner-sphere metal-coupled/mediated electron transfer mechanism. Given the heavy prevalence of zinc in biology, it seems likely that the roles that this metal ion plays in regulating physiological redox processes have yet to be fully elucidated.

The lack of activity for **3** is proposed to result from the dissociation of the ligand from the Zn(II) after its initial oxidation by $O_2^{\cdot-}$. The H_2qp3 ligand essentially becomes tetradentate upon two-electron oxidation of the quinolate to a *para*-quinone (qp3). The loss of the strongly coordinating quinolate allows the anions from the MOPS and phosphate buffers to strip the metal ion from the polydentate ligand; the resultant Zn(II) salts then precipitate from the solution. MS analysis of the reaction mixtures confirms that the reaction with KO_2 produces metal-free oxidized ligand as the major product (Figure S16). The results suggest that this quinol-containing ligand, similar to H_2qp1,[26] needs to remain tightly bound to the Zn(II) in order for catalysis to proceed. The observation of oxidized ligand demonstrates that **3** can initially react with $O_2^{\cdot-}$, but the stopped-flow kinetics data suggest that the catalyst does not survive enough turnovers to noticeably impact the rate of $O_2^{\cdot-}$ disproportionation.

Unlike **3**, complex **2** maintains its catalysis after the initial round of oxidation. In addition to providing a readily accessible coordination site for $O_2^{\cdot-}$, the second quinol also serves as a replacement anionic ligand when the first quinol is oxidized to a *para*-quinone. The resultant complex, $[Zn(Hqp2)]^+$, where $Hqp2^-$ is a quinolate/*para*-quinone ligand (QH_2, Scheme 3), is stable enough to persist in water and continue to participate in catalysis, accounting for its higher activity. The second quinol in the ligand, similar to that in the related $[Mn(H_4qp2)Br_2]$, appears to resist oxidation.[25]

Although the higher activity of **2** relative to **1** may be consistent with an inner-sphere pathway, the MS and low-temperature UV/vis data cannot preclude outer-sphere reactions with $O_2^{\cdot-}$. Aside from Zn(II)−OOH species, the two pathways would yield the same intermediates (Scheme 3). Unlike **1**, we do not observe any m/z features that could correspond to Zn(II)−OOH species in reactions between **2** and KO_2.[26] The second quinol can potentially protonate putative Zn(II)−OOH species, and the concomitant coordination of the resultant quinolate may hasten H_2O_2 release enough to preclude detection of the short-lived hydroperoxo intermediate. The UV/vis data for these reactions are consistent with the formation of semiquinone (SQ) radical anions and quinhydrone (QH) species. The latter consists of the *para*-quinone interacting with the remaining quinol/quinolate. The semiquinone radical anions may also be stabilized through similar interactions.

Although **2** possesses two quinols, all of our data are consistent with only one of these serving as a redox partner for $O_2^{\cdot-}$ during catalysis. This said, the second quinol is essential to the observed activity for two reasons. First, its ability to deprotonate to an anionic quinolate helps to keep the oxidized ligand anchored to the Zn(II), preventing the initial oxidation of the ligand from halting catalysis as it does for **3**. Second, the UV/vis signatures suggest that the quinol/quinolate can hydrogen bond to and stabilize the radical species in the catalytic cycle.

■ CONCLUSIONS

The reactivity of the Zn(II)−H_4qp2 complex **2** demonstrates that the design strategy for SOD mimicry used for the Zn(II)−H_2qp1 complex **1**—using a redox-active ligand in place of a redox-active metal—is generally applicable and is not limited to a single catalyst. Low-temperature UV/vis provides evidence for the intermediacy of Zn(II)-semiquinone radicals, which were speculated but not directly observed in the catalysis performed by **1**. Although there are two redox-active organic groups in **2**, only one appears to participate as a redox partner for $O_2^{\cdot-}$ in the SOD mimicry. The replacement of one of the H_2qp1 pyridines with a quinol improves the activity in aqueous solutions buffered with sulfonic acids fivefold, likely by improving the accessibility of the metal center to $O_2^{\cdot-}$, facilitating the efficient release of H_2O_2 through a proton delivery associated with coordination of resulted quinolate, and assuring stability of the complex upon oxidation of the first quinol. Complex **2**, similar to **1**, functions better in phosphate buffer, differentiating these catalysts from manganese-containing SOD mimics and potentially making them more suitable for treating oxidative stress in vivo. Complex **3**, conversely, is not a successful SOD mimic due to the lesser stability of its oxidized form $[Zn(qp3)]^{2+}$. The inability of **3** to noticeably impact the rate of superoxide disproportionation demonstrates that merely having a mixture of a Zn(II) salt and a quinol/*para*-quinone compound is not sufficient for catalysis; the redox-active organic component needs to be closely associated with, if not covalently tethered to, the metal center for these reactions to succeed.

https://doi.org/10.1021/acs.inorgchem.2c03256
Inorg. Chem. 2022, 61, 19983−19997

■ ASSOCIATED CONTENT

Supporting Information

The Supporting Information is available free of charge at https://pubs.acs.org/doi/10.1021/acs.inorgchem.2c03256.

NMR spectra, MS spectra, IR spectra, pH titration data, and CV data for **2** and **3** (PDF)

Accession Codes

CCDC 1899770 and 1909028 contain the supplementary crystallographic data for this paper. These data can be obtained free of charge via www.ccdc.cam.ac.uk/data_request/cif, or by emailing data_request@ccdc.cam.ac.uk, or by contacting The Cambridge Crystallographic Data Centre, 12 Union Road, Cambridge CB2 1EZ, UK; fax: +44 1223 336033.

■ AUTHOR INFORMATION

Corresponding Authors

Ivana Ivanović-Burmazović − *Department Chemie, Ludwig-Maximilians Universität (LMU) München, München 81377, Germany*; Email: ivivch@cup.lmu.de

Christian R. Goldsmith − *Department of Chemistry and Biochemistry, Auburn University, Auburn, Alabama 36849, United States*; orcid.org/0000-0001-7293-1267; Email: crgoldsmith@auburn.edu

Authors

Jamonica L. Moore − *Department of Chemistry and Biochemistry, Auburn University, Auburn, Alabama 36849, United States*

Julian Oppelt − *Department Chemie, Ludwig- Maximilians Universität (LMU) München, München 81377, Germany*

Laura Senft − *Department Chemie, Ludwig- Maximilians Universität (LMU) München, München 81377, Germany*

Alicja Franke − *Department Chemie, Ludwig- Maximilians Universität (LMU) München, München 81377, Germany*

Andreas Scheitler − *Department of Chemistry and Pharmacy, University of Erlangen-Nürnberg, Erlangen 91508, Germany*

Meghan W. Dukes − *Department of Chemistry and Biochemistry, Auburn University, Auburn, Alabama 36849, United States*

Haley B. Alix − *Department of Chemistry and Biochemistry, Auburn University, Auburn, Alabama 36849, United States*

Alexander C. Saunders − *Department of Chemistry and Biochemistry, Auburn University, Auburn, Alabama 36849, United States*

Sana Karbalaei − *Department of Chemistry and Biochemistry, Auburn University, Auburn, Alabama 36849, United States*

Dean D. Schwartz − *Department of Anatomy, Physiology, and Pharmacology, College of Veterinary Medicine, Auburn University, Auburn, Alabama 36849, United States*

Complete contact information is available at: https://pubs.acs.org/10.1021/acs.inorgchem.2c03256

Author Contributions

⊥J.L.M. and J.O. contributed equally to this work.

Notes

The authors declare no competing financial interest.

■ ACKNOWLEDGMENTS

We thank Auburn University and the National Science Foundation (NSF-CHE-1662875 and NSF-CHE-1954336) for financially supporting this work. We also thank Ludwig-Maximilians University and the Bayerisches Staatsministerium für Wissenschaft und Kunst.

■ REFERENCES

(1) Ahmed, M. I.; Gladden, J. D.; Litovsky, S. H.; Lloyd, S. G.; Gupta, H.; Inusah, S.; Denney, T., Jr.; Powell, P.; McGiffin, D. C.; Dell'Italia, L. J. Increased Oxidative Stress and Cardiomyocyte Myofibrillar Degeneration in Patients with Chronic Isolated Mitral Regurgitation and Ejection Fraction >60. *J. Am. Coll. Cardiol.* **2010**, *55*, 671−679.

(2) Fearon, I. M.; Faux, S. P. Oxidative Stress and Cardiovascular Disease: Novel Tools Give (Free) Radical Insight. *J. Mol. Cell. Cardiol.* **2009**, *47*, 372−381.

(3) Eskici, G.; Axelsen, P. H. Copper and Oxidative Stress in the Pathogenesis of Alzheimer's Disease. *Biochemistry* **2012**, *51*, 6289−6311.

(4) Kinnula, V. L. Production and Degradation of Oxygen Metabolites During Inflammatory States in the Human Lung. *Curr. Drug Targets - Inflamm. Allergy* **2005**, *4*, 465−470.

(5) AbdulSalam, S. F.; Thowfeik, F. S.; Merino, E. J. Excessive Reactive Oxygen Species and Exotic DNA Lesions as an Exploitable Liability. *Biochemistry* **2016**, *55*, 5341−5352.

(6) Mosley, R. L.; Benner, E. J.; Kadiu, I.; Thomas, M.; Boska, M. D.; Hasan, K.; Laurie, C.; Gendelman, H. E. Neuroinflammation, Oxidative Stress, and the Pathogenesis of Parkinson's Disease. *Clin. Neurosci. Res.* **2006**, *6*, 261−281.

(7) Laforge, M.; Elbim, C.; Frère, C.; Hémadi, M.; Massaad, C.; Nuss, P.; Benoliel, J.-J.; Becker, C. Tissue Damage from Neutrophil-Induced Oxidative Stress in COVID-19. *Nat. Rev. Immunol.* **2020**, *20*, 515−516.

(8) Abouhashem, A. S.; Singh, K.; Azzazy, H. M. E.; Sen, C. K. Is Low Alveolar Type II Cell SOD3 in the Lungs of Elderly Linked to the Observed Severity of COVID-19? *Antioxid. Redox Signaling* **2020**, *33*, 59−65.

(9) Riley, D. P.; Weiss, R. H. Manganese Macrocyclic Ligand Complexes as Mimics of Superoxide Dismutase. *J. Am. Chem. Soc.* **1994**, *116*, 387−388.

(10) Riley, D. P.; Schall, O. F. Structure−Activity Studies and the Design of Synthetic Superoxide Dismutase (SOD) Mimetics as Therapeutics. *Adv. Inorg. Chem.* **2006**, *59*, 233−263.

(11) Riley, D. P.; Lennon, P. J.; Neumann, W. L.; Weiss, R. H. Toward the Rational Design of Superoxide Dismutase Mimics: Mechanistic Studies for the Elucidation of Substituent Effects on the Catalytic Activity of Macrocyclic Manganese(II) Complexes. *J. Am. Chem. Soc.* **1997**, *119*, 6522−6528.

(12) Riley, D. P. Functional Mimics of Superoxide Dismutase Enzymes as Therapeutic Agents. *Chem. Rev.* **1999**, *99*, 2573−2588.

(13) Tovmasyan, A.; Carballal, S.; Ghazaryan, R.; Melikyan, L.; Weitner, T.; Maia, C. G. C.; Reboucas, J. S.; Radi, R.; Spasojevic, I.; Benov, L.; Batinic-Haberle, I. Rational Design of Superoxide Dismutase (SOD) Mimics: The Evaluation of the Therapeutic Potential of New Cationic Mn Porphyrins with Linear and Cyclic Substituents. *Inorg. Chem.* **2014**, *53*, 11467−11483.

(14) Batinic-Haberle, I.; Reboucas, J. S.; Spasojevic, I. Superoxide Dismutase Mimics: Chemistry, Pharmacology, and Therapeutic Potential. *Antioxid. Redox Signaling* **2010**, *13*, 877−918.

(15) Batinic-Haberle, I.; Rajic, Z.; Tovmasyan, A.; Reboucas, J. S.; Ye, X.; Leong, K. W.; Dewhirst, M. W.; Vujaskovic, Z.; Benov, L.; Spasojevic, I. Diverse Functions of Cationic Mn(III) N-substituted Pyridylporphyrins, Recognized as SOD Mimics. *Free Rad. Biol. Med.* **2011**, *51*, 1035−1053.

(16) Abreu, I. A.; Cabelli, D. E. Superoxide Dismutases- A Review of the Metal-Associated Mechanistic Variations. *Biochim. Biophys. Acta* **2010**, *1804*, 263−274.

(17) Policar, C.; Bouvet, J.; Bertrand, H. C.; Delsuc, N. SOD Mimics: From the Tool Box of the Chemists to Cellular Studies. *Curr. Opin. Chem. Biol.* **2022**, *67*, 102109.

(18) Robinett, N. G.; Peterson, R. L.; Culotta, V. C. Eukaryotic Copper-Only Superoxide Dismutases (SODs): A New Class of SOD

Enzymes and SOD-Like Protein Domains. *J. Biol. Chem.* **2018**, *293*, 4636−4643.
(19) Potter, S. Z.; Zhu, H.; Shaw, B. F.; Rodriguez, J. A.; Doucette, P. A.; Sohn, S. H.; Durazo, A.; Faull, K. F.; Gralla, E. B.; Nersissian, A. M.; Valentine, J. S. Binding of a Single Zinc Ion to One Subunit of Copper−Zinc Superoxide Dismutase Apoprotein Substantially Influences the Structure and Stability of the Entire Homodimeric Protein. *J. Am. Chem. Soc.* **2007**, *129*, 4575−4583.
(20) Ellerby, L. M.; Cabelli, D. E.; Graden, J. A.; Valentine, J. S. Copper−Zinc Superoxide Dismutase: Why Not pH-Dependent? *J. Am. Chem. Soc.* **1996**, *118*, 6556−6561.
(21) Yu, M.; Beyers, R. J.; Gorden, J. D.; Cross, J. N.; Goldsmith, C. R. A Magnetic Resonance Imaging Contrast Agent Capable of Detecting Hydrogen Peroxide. *Inorg. Chem.* **2012**, *51*, 9153−9155.
(22) Yu, M.; Ward, M. B.; Franke, A.; Ambrose, S. L.; Whaley, Z. L.; Bradford, T. M.; Gorden, J. D.; Beyers, R. J.; Cattley, R. C.; Ivanović-Burmazović, I.; Schwartz, D. D.; Goldsmith, C. R. Adding a Second Quinol to a Redox-Responsive MRI Contrast Agent Improves Its Relaxivity Response to H_2O_2. *Inorg. Chem.* **2017**, *56*, 2812−2826.
(23) Yu, M.; Ambrose, S. L.; Whaley, Z. L.; Fan, S.; Gorden, J. D.; Beyers, R. J.; Schwartz, D. D.; Goldsmith, C. R. A Mononuclear Manganese(II) Complex Demonstrates a Strategy to Simultaneously Image and Treat Oxidative Stress. *J. Am. Chem. Soc.* **2014**, *136*, 12836−12839.
(24) Kenkel, I.; Franke, A.; Dürr, M.; Zahl, A.; Dücker-Benfer, C.; Langer, J.; Filipović, M. R.; Yu, M.; Puchta, R.; Fiedler, S. R.; Shores, M. P.; Goldsmith, C. R.; Ivanović-Burmazović, I. Switching between Inner- and Outer-Sphere PCET Mechanisms of Small Molecule Activation: Superoxide Dismutation and Oxygen/Superoxide Reduction Reactivity Deriving from the Same Manganese Complex. *J. Am. Chem. Soc.* **2017**, *139*, 1472−1484.
(25) Senft, L.; Moore, J. L.; Franke, A.; Fisher, K. R.; Scheitler, A.; Zahl, A.; Puchta, R.; Fehn, D.; Ison, S.; Sader, S.; Ivanović-Burmazović, I.; Goldsmith, C. R. Quinol-Containing Ligands Enable High Superoxide Dismutase Activity by Modulating Coordination Number, Charge, Oxidation States and Stability of Manganese Complexes throughout Redox Cycling. *Chem. Sci.* **2021**, *12*, 10483−10500.
(26) Ward, M. B.; Scheitler, A.; Yu, M.; Senft, L.; Zillmann, A. S.; Gorden, J. D.; Schwartz, D. D.; Ivanović-Burmazović, I.; Goldsmith, C. R. Superoxide Dismutase Activity Enabled by a Redox-Active Ligand rather than a Metal. *Nat. Chem.* **2018**, *10*, 1207−1212.
(27) Friedel, F. C.; Lieb, D.; Ivanović-Burmazović, I. Comparative Studies on Manganese-Based SOD Mimetics, Including the Phosphate Effect, by Using Global Spectral Analysis. *J. Inorg. Biochem.* **2012**, *109*, 26−32.
(28) Lieb, D.; Friedel, F. C.; Yawer, M.; Zahl, A.; Khusniyarov, M. M.; Heinemann, F. W.; Ivanović-Burmazović, I. Dinuclear Seven-Coordinate Mn(II) Complexes: Effect of Manganese(II)-Hydroxo Species on Water Exchange and Superoxide Dismutase Activity. *Inorg. Chem.* **2013**, *52*, 222−236.
(29) Irving, H.; Williams, R. J. P. 637. The Stability of Transition-Metal Complexes. *J. Chem. Soc.* **1953**, 3192−3210.
(30) Martell, A. E.*Critical Stability Constants*; Plenum Press: New York, NY, 1974.
(31) Batinic-Haberle, I.; Spasojevic, I. 25 Years of Development of Mn Porphyrins — from Mimics of Superoxide Dismutase Enzymes to Thiol Signaling to Clinical Trials: The Story of Our Life in the USA. *J. Porphyr. Phthalocyanines* **2019**, *23*, 1326−1335.
(32) Salvemini, D.; Wang, Z.-Q.; Zweier, J. L.; Samouilov, A.; Macarthur, H.; Misko, T. P.; Currie, M. G.; Cuzzocrea, S.; Sikorski, J. A.; Riley, D. P. A Nonpeptidyl Mimic of Superoxide Dismutase with Therapeutic Activity in Rats. *Science* **1999**, *286*, 304−306.
(33) Aston, K.; Rath, N.; Naik, A.; Slomczynska, U.; Schall, O. F.; Riley, D. P. Computer-Aided Design (CAD) of Mn(II) Complexes: Superoxide Dismutase Mimetics with Catalytic Activity Exceeding the Native Enzyme. *Inorg. Chem.* **2001**, *40*, 1779−1789.
(34) Bergwitz, C.; Jüppner, H. Phosphate Sensing. *Adv. Chron. Kidney Dis.* **2011**, *18*, 132−144.
(35) Bevington, A.; Mundy, K. I.; Yates, A. J. P.; Kanis, J. A.; Russell, R. G. G.; Taylor, D. J.; Rajagopalan, B.; Radda, G. K. A Study of Intracellular Orthophosphate Concentration in Human Muscle and Erythrocytes by ^{31}P Nuclear Magnetic Resonance Spectroscopy and Selective Chemical Assay. *Clin. Sci.* **1986**, *71*, 729−735.
(36) Lange, M.; Ok, K.; Shimberg, G. D.; Bursac, B.; Markó, L.; Ivanović-Burmazović, I.; Michel, S. L. J.; Filipovic, M. R. Direct Zinc Finger Protein Persulfidation by H_2S Is Facilitated by Zn^{2+}. *Angew. Chem., Int. Ed.* **2019**, *58*, 7997−8001.
(37) Gans, P.; Sabatini, A.; Vacca, A. Investigation of equilibria in solution. Determination of equilibrium constants with the HYPERQUAD suite of programs. *Talanta* **1996**, *43*, 1739−1753.
(38) McCord, J. M.; Fridovich, I. Superoxide Dismutase: An Enzymic Function for Erythrocuprein (Hemocuprein). *J. Biol. Chem.* **1969**, *244*, 6049−6055.
(39) Kedare, S. B.; Singh, R. P. Genesis and Development of DPPH Method of Antioxidant Assay. *J. Food Sci. Technol.* **2011**, *48*, 412−422.
(40) Blois, M. S. Antioxidant Determinations by Use of a Stable Free Radical. *Nature* **1958**, *181*, 1199−1200.
(41) Milaeva, E. R.; Shpakovsky, D. B.; Gracheva, Y. A.; Orlova, S. I.; Maduar, V. V.; Tarasevich, B. N.; Meleshonkova, N. N.; Dubova, L. G.; Shevtsova, E. F. Metal Complexes with Functionalised 2,2′-Dipicolylamine Ligand Containing an Antioxidant 2,6-Di-*tert*-butylphenol Moiety: Synthesis and Biological Studies. *Dalton Trans.* **2013**, *42*, 6817−6828.
(42) Bielski, B. H. J.; Cabelli, D. E.; Arudi, R. L.; Ross, A. B. Reactivity of HO_2/O_2^- Radicals in Aqueous Solution. *J. Phys. Chem. Ref. Data* **1985**, *14*, 1041−1100.
(43) Chan, T.-L.; Mak, T. C. W. X-Ray Crystallographic Study of Guest-Molecule Orientations in the *β*-Hydroquinone Clathrates of Acetonitrile and Methyl Isocyanide. *J. Chem. Soc., Perkin Trans.* **1983**, *2*, 777−781.
(44) Iranzo, O. Manganese Complexes Displaying Superoxide Dismutase Activity: A Balance between Different Factors. *Bioorg. Chem.* **2011**, *39*, 73−87.
(45) Ancerewicz, J.; Migliavacca, E.; Carrupt, P.-A.; Testa, B.; Brée, F.; Zini, R.; Tillement, J.-P.; Labidalle, S.; Guyot, D.; Chauvet-Monges, A.-M.; Crevat, A.; Le Ridant, A. Structure-Property Relationships of Trimetazidine Derivatives and Model Compounds as Potential Antioxidants. *Free Rad. Biol. Med.* **1998**, *25*, 113−120.
(46) Fridovich, I. Superoxide Anion Radical (O_2^-), Superoxide Dismutases, and Related Matters. *J. Biol. Chem.* **1997**, *272*, 18515−18517.
(47) Liochev, S. I. Superoxide Dismutase Mimics, Other Mimics, Antioxidants, Prooxidants, and Related Matters. *Chem. Res. Toxicol.* **2013**, *26*, 1312−1319.
(48) Riley, D. P.; Rivers, W. J.; Weiss, R. H. Stopped-Flow Kinetic Analysis for Monitoring Superoxide Decay in Aqueous Systems. *Anal. Biochem.* **1991**, *196*, 344−349.
(49) Liochev, S. I.; Fridovich, I. Lucigenin (Bis-N-methylacridinium) as a Mediator of Superoxide Anion Production. *Arch. Biochem. Biophys.* **1997**, *337*, 115−120.
(50) Swallow, A. J.Physical Chemistry of Semiquinones. In *Functions of Quinones in Energy Converting Systems*; Trumpower, B. L., Ed.; Elsevier, Inc.: New York, NY, 1982, pp 59−72.
(51) Zhao, X.; Imahori, H.; Zhan, C.-G.; Sakata, Y.; Iwata, S.; Kitagawa, T. Resonance Raman and FTIR Spectra of Isotope-Labeled Reduced 1,4-Benzoquinone and Its Protonated Forms in Solutions. *J. Phys. Chem. A* **1997**, *101*, 622−631.
(52) Slifkin, M. A.*Charge Transfer Interactions of Biomolecules*; Academic Press: London, 1971.
(53) González Moa, M. J.; Mandado, M.; Mosquera, R. A. A Computational Study on the Stacking Interaction in Quinhydrone. *J. Phys. Chem. A* **2007**, *111*, 1998−2001.
(54) Regeimbal, J.; Gleiter, S.; Trumpower, B. L.; Yu, C.-A.; Diwakar, M.; Ballou, D. P.; Bardwell, J. C. A. Disulfide Bond Formation Involves a Quinhydrone-Type Charge−Transfer Complex. *Proc. Natl. Acad. Sci. U.S.A.* **2003**, *100*, 13779−13784.

https://doi.org/10.1021/acs.inorgchem.2c03256
Inorg. Chem. 2022, 61, 19983−19997

(55) Chen, P.; Chakraborty, S.; Mukhopadhyay, S.; Lee, E.; Paoliello, M. M. B.; Bowman, A. B.; Aschner, M. Manganese Homeostasis in the Nervous System. *J. Neurochem.* **2015**, *134*, 601−610.
(56) Shannon, R. D. Revised Effective Ionic Radii and Systematic Studies of Interatomic Distances in Halides and Chalcogenides. *Acta Crystallogr.* **1976**, *32*, 751−767.
(57) Gale, E. M.; Mukherjee, S.; Liu, C.; Loving, G. S.; Caravan, P. Structure-Redox-Relaxivity Relationships for Redox Responsive Manganese-Based Magnetic Resonance Imaging Probes. *Inorg. Chem.* **2014**, *53*, 10748−10761.
(58) Squarcina, A.; Fehn, D.; Senft, L.; Langer, J.; Ivanović-Burmazović, I. Dinuclear Zn Complex: Phenoxyl Radical Formation Driven by Superoxide Coordination. *Z. Anorg. Allg. Chem.* **2021**, *647*, 809−814.

https://doi.org/10.1021/acs.inorgchem.2c03256
Inorg. Chem. 2022, 61, 19983−19997

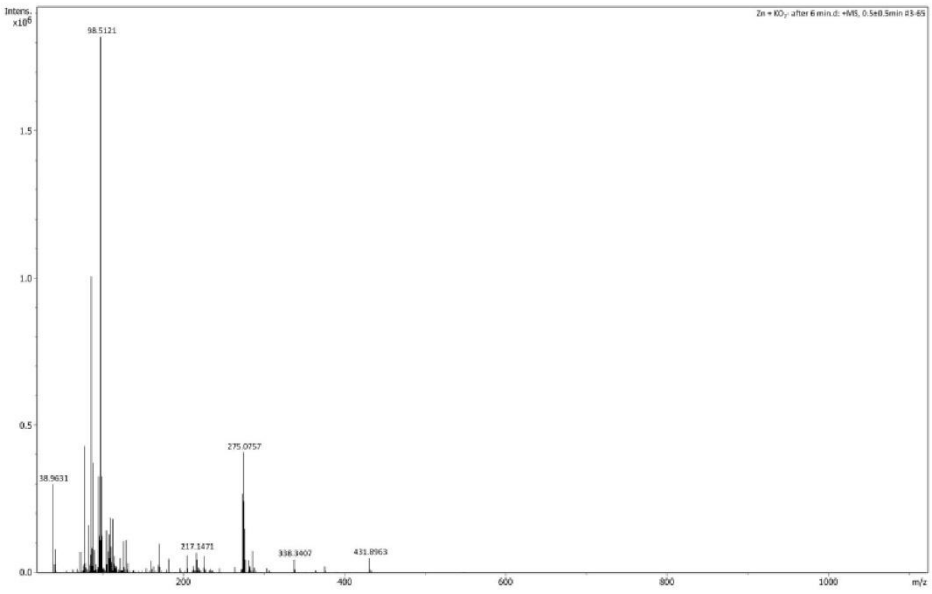

Figure S15. CSI-MS spectrometry of **2** upon with KO_2. Experimental conditions: 1 mM solutions of **2** in MeCN (1% DMF) were cooled to -40 °C and then mixed with an excess of solid KO_2. After 6 min, the mixture was diluted in a pre-cooled syringe with pre-cooled MeCN to approximately 1 × 10^{-5} M and quickly injected into the mass spectrometer. Portions of these data are presented in **Figure 6** and **Figure 7**.

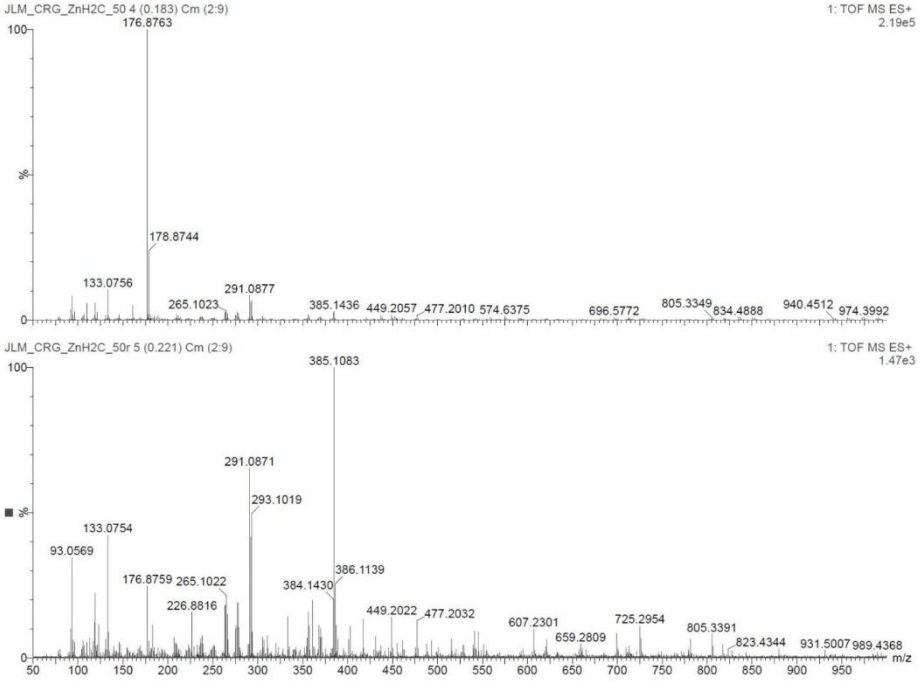

Figure S16. Mass spectrometry analysis of the reaction between **3** and 50 equiv. of KO_2 in carbonate-buffered water (pH 8.1). The 385.1083 m/z peak is assigned to the sodium salt of the oxidized *para*-quinone form of the ligand (qp3): $[Na(qp3)]^+$. Note the absence of the 427.1194 m/z peak associated with $[Zn(Hqp3)]^+$ and a peak at 213.0517 that would be associated with $[Zn(qp3)]^+$.

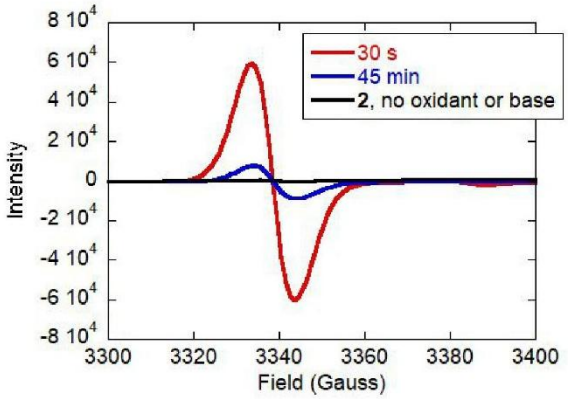

Figure S17. X-band EPR data for the reaction between 1.0 mM **2**, 2.4 mM $Ag(SbF_6)$, and 235 mM Et_3N in water. At the given time points, aliquots were taken from solution and frozen at 77 K.

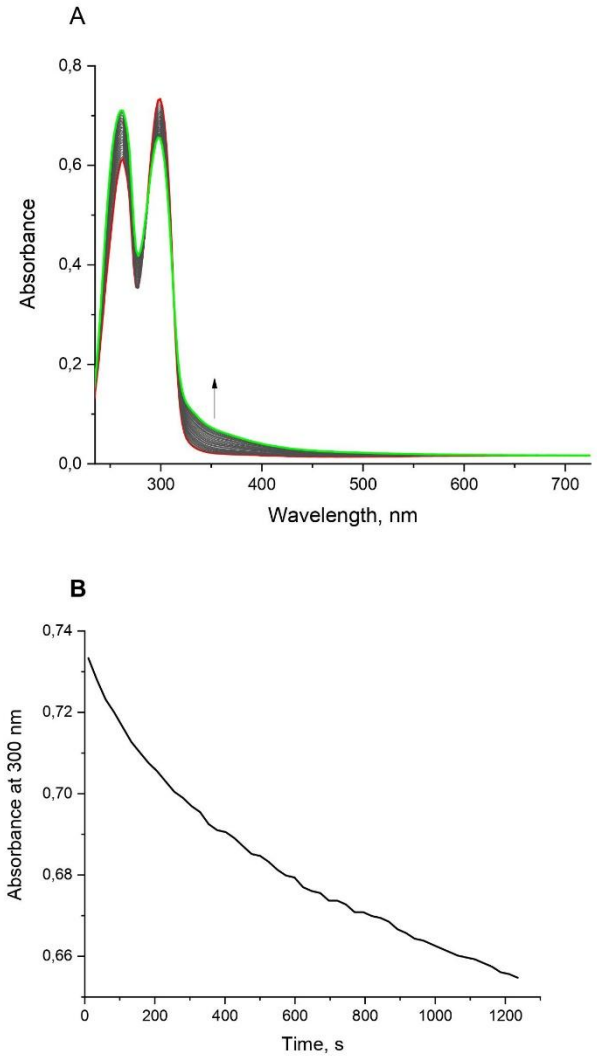

Figure S18. A) UV/vis spectral changes recorded within 1200 s after rapid mixing 0.1 M **2** with a 20-fold excess of H_2O_2 in MeCN at 0 °C. The red and green spectra were recorded at 10 s and 1200 s, respectively. B) Corresponding kinetic trace recorded at 300 nm.

Supporting Information for

Diquinol Functionality Boosts the Superoxide Dismutase Mimicry of a Zn(II) Complex with a Redox-Active Ligand while Maintaining Catalyst Stability and Enhanced Activity in Phosphate Solution

Jamonica L. Moore,[†,δ] Julian Oppelt,[‡,δ] Laura Senft,[‡] Alicja Franke,[‡] Andreas Scheitler,[§] Meghan W. Dukes,[†] Haley B. Alix,[†] Alexander C. Saunders,[†] Sana Karbalaei,[†] Dean D. Schwartz,[¥] Ivana Ivanović-Burmazović,[‡,*] and Christian R. Goldsmith[†,*]

[†]Department of Chemistry and Biochemistry, Auburn University, Auburn, AL 36849, United States (USA)

[¥]Department of Anatomy, Physiology, and Pharmacology, College of Veterinary Medicine, Auburn University, Auburn, AL 36849, USA

[‡]Department Chemie, Ludwig- Maximilians Universität (LMU) München, 81377 München, Germany

[§]Department of Chemistry and Pharmacy, University of Erlangen-Nürnberg, Egerlandstr. 1, 91508 Erlangen, Germany

[δ]J.L.M. and J.O. contributed equally to this work.

*Corresponding author email addresses: ivivch@cup.lmu.de, crgoldsmith@auburn.edu

Contents

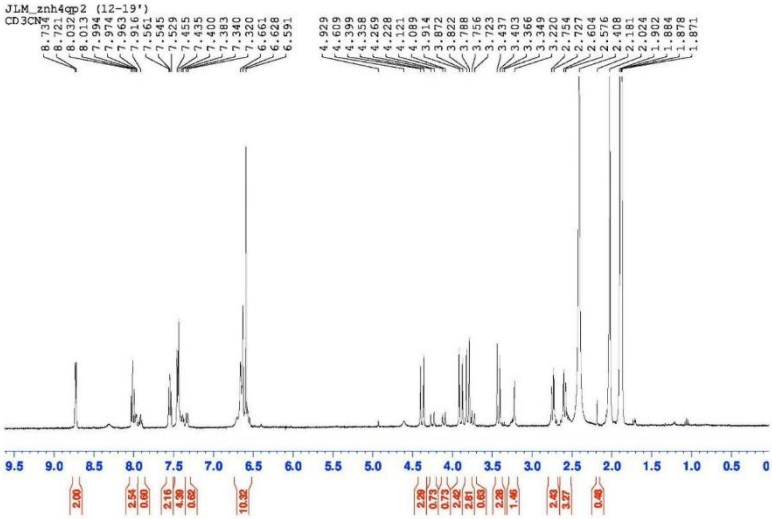

Figure S1. ^{1}H NMR spectrum of a crystalline sample of $[Zn(H_4qp2)](OTf)_2$ (**2**) in CD_3CN (400 MHz, 293 K). Solvent peaks from diethyl ether (1.21, 3.82), water (2.02) and MeCN (1.88) are present.

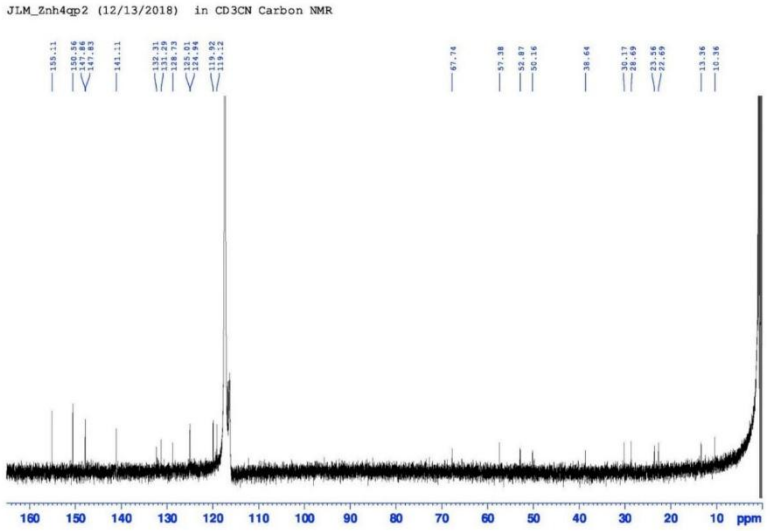

Figure S2. ^{13}C NMR spectrum of a crystalline sample of **2** in CD_3CN (100 MHz, 293 K). Solvent peaks from diethyl ether (13.36, 67.74), MeOH (50.16), and MeCN (117.35) are present.

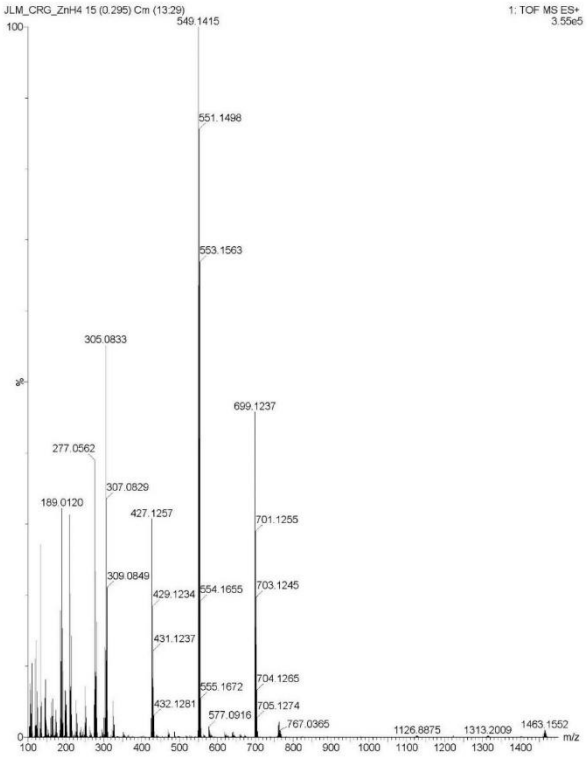

Figure S3. Mass spectrometry (ESI) for $[Zn(H_4qp2)(OTf)](OTf)$ (**2**) in MeCN. The m/z feature at 549.1415 is assigned to $[Zn(H_3qp2)]^+$ (calculated m/z = 549.1481). The feature at 699.1237 is assigned to $[Zn(H_4qp2)(OTf)]^+$ (calculated m/z = 699.1079).

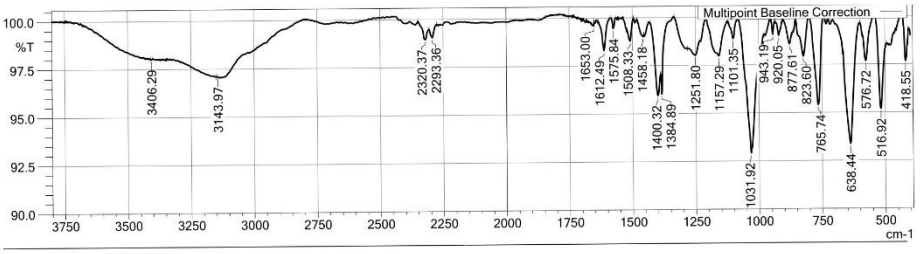

Figure S4. IR spectrum of **2** (KBr).

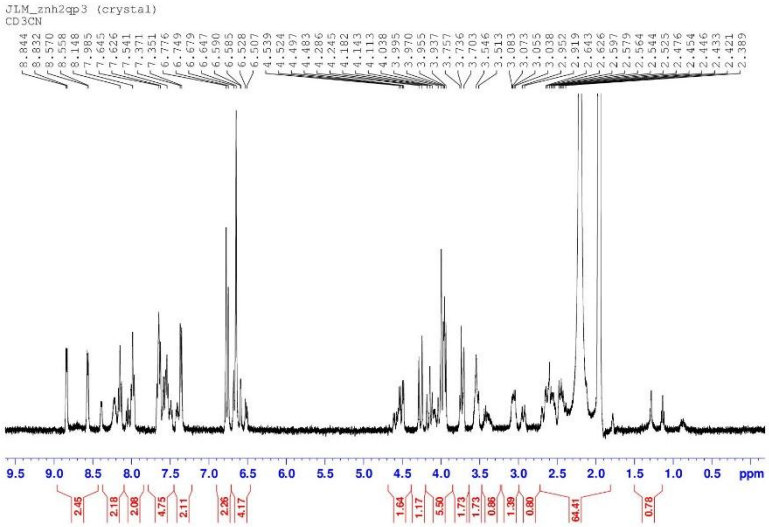

Figure S5. ^{1}H NMR spectrum of a crystalline sample of [Zn(H_2qp3)(H_2O)](OTf)$_2$ (**3**) in CD_3CN (400 MHz, 293 K). Solvent peaks from diethyl ether (1.29, 3.97), water (2.21), and MeCN (1.95) are present.

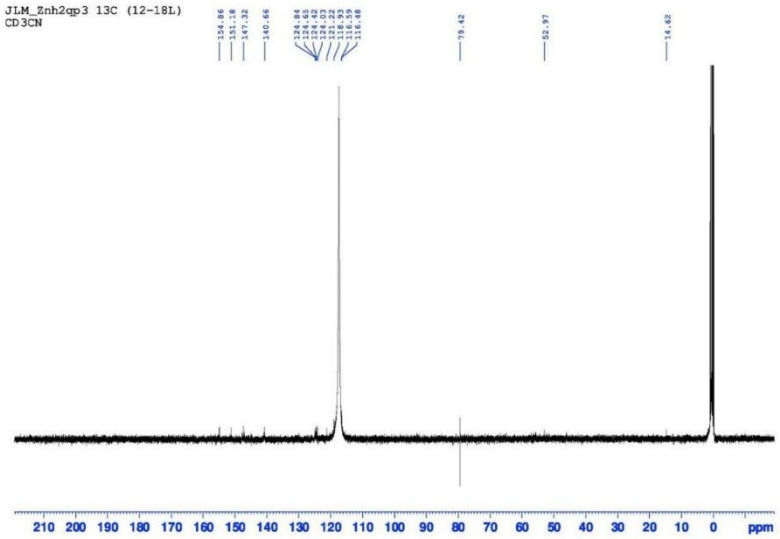

Figure S6. ^{13}C NMR spectrum of a crystalline sample of **3** in CD_3CN (100 MHz, 293 K). Solvent peaks from diethyl ether (79.42, 14.62) and MeCN (118.93) are present.

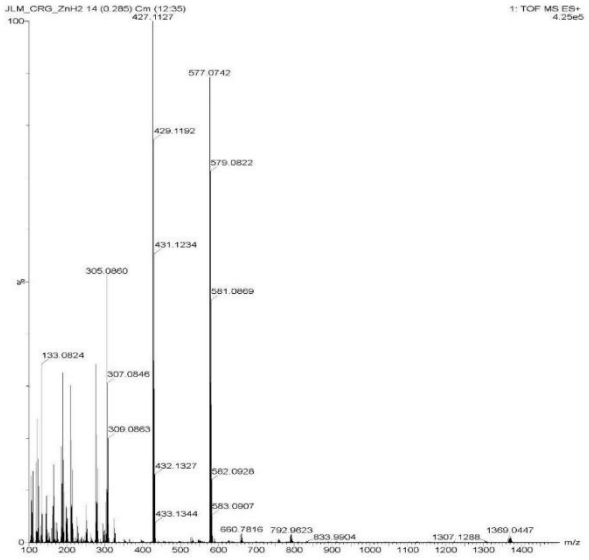

Figure S7. Mass spectrometry (ESI) for **3** in MeCN. The m/z feature at 427.1127 is assigned to $[Zn(Hqp3)]^+$ (calculated m/z = 427.1113). The feature at 577.0742 is assigned to $[Zn(H2qp3)(OTf)]^+$ (calculated m/z = 577.0711).

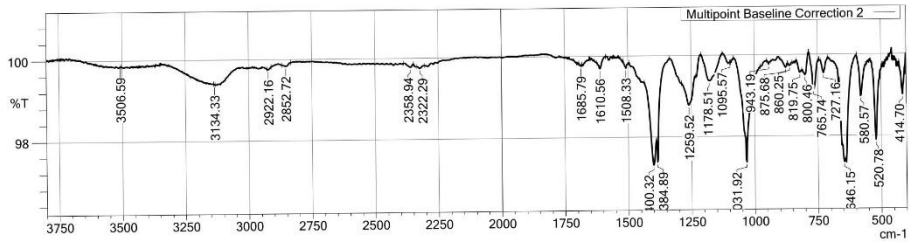

Figure S8. IR spectrum of **3** (KBr).

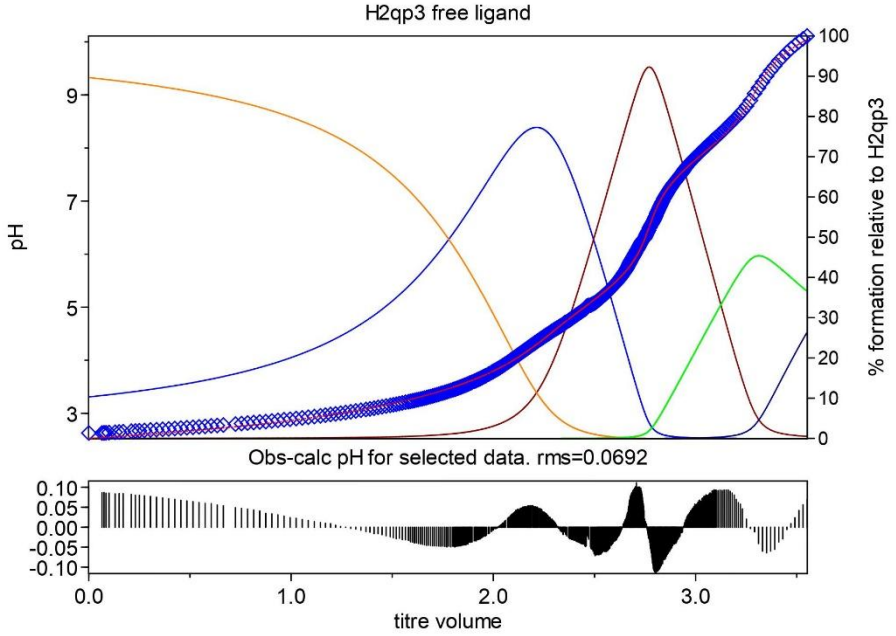

Figure S9. Hyperquad model (red line) overlaid on the experimental data from a potentiometric pH titration (blue) of the H_2qp3 ligand in water. For the titration, 0.1 M KOH was added to an acidic aqueous solution containing 0.1 M KCl and 1.0 mM H_2qp3 at 25 °C under an Ar atmosphere. The residuals for the fit are provided below. The curves represent the formation of $[H_5qp3]^{3+}$ (orange), $[H_4qp3]^{2+}$ (blue), $[H_3qp3]^{+}$ (purple), $[H_2qp3]$ (green), and $[Hqp3]^{-}$ (indigo).

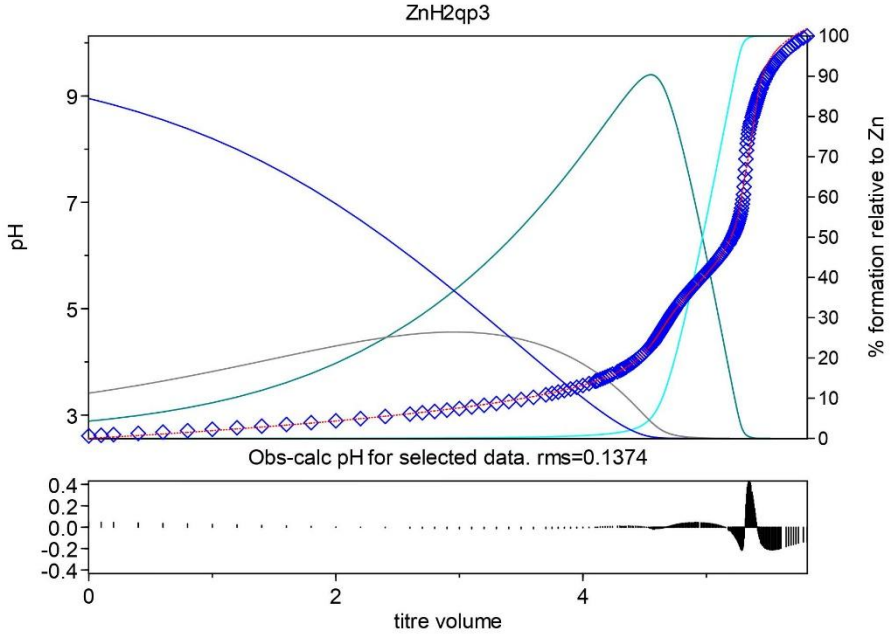

Figure S10. Hyperquad model (red line) overlaid on the experimental data from a potentiometric pH titration (blue) of a 1:1 mixture of $ZnCl_2$ H_2qp3 ligand in water. For the titration, 0.1 M KOH was added to an acidic aqueous solution containing 0.1 M KCl, 1.0 mM $ZnCl_2$, and 1.0 mM H_2qp3 at 25 °C under an Ar atmosphere. The residuals for the fit are provided below. The curves represent the formation of free Zn(II) (blue), $[Zn(H_3qp3)]^{3+}$ (gray), $[Zn(H_2qp3)]^{2+}$ (pine green), and $[Zn(Hqp3)]^{+}$ (light blue).

Table S1: Parameters for the Hyperquad models used in **Figures S9** and **S10**.

Species	H^+	(H_2qp3)	Zn^{2+}	log(β)	Derived Values
$(Hqp3)^-$	-1	1	0	-10.182 (±0.3)	
(H_2qp3)	0	1	0	0.00	pK_{L1} = 10.2 (±0.3)[a]
$(H_3qp3)^+$	1	1	0	8.1908 (±0.05)	pK_{L2} = 8.19 (±0.05)[a]
$(H_4qp3)^{2+}$	2	1	0	13.3226 (±0.05)	pK_{L3} = 5.13 (±0.05)[a]
$(H_5qp3)^{3+}$	3	1	0	16.7886 (±0.3)	pK_{L4} = 3.5 (±0.3)[a]
$[Zn(Hqp3)]^+$	-1	1	1	5.5659 (±0.05)	log K(ZnHqp3) = 15.75[b]
$[Zn(H_2qp3)]^{2+}$	0	1	1	11.1351 (±0.05)	pK_{a1} = 5.57 (±0.10)[c], log K(ZnH_2qp3) = 11.14[b]
$[Zn(H_3qp3)]^{3+}$	1	1	1	14.1158 (±0.1)	pK_{a2} = 2.98 (±0.15)[c] log K(ZnH_3qp3) = 5.93[b]

[a]Ligand pK_a values correspond to the following equilibrium constants:

$K_{L1} = [(Hqp3)^-][H^+]/[(H_2qp3)]$, $pK_{L1} = \log\beta_{010} - \log\beta_{-110}$.

$K_{L2} = |(H_2qp3)||H^+|/|(H_3qp3)^+|$, $pK_{L2} = \log\beta_{110} - \log\beta_{010}$.

$K_{L3} = |(H_3qp3)^+||H^-|/|(H_4qp3)^{2+}|$, $pK_{L3} = \log\beta_{210} - \log\beta_{110}$.

$K_{L4} = [(H_4qp3)]^{2+}[H^+]/|(H_5qp3)^{3+}|$, $pK_{L4} = \log\beta_{310} - \log\beta_{210}$.

[b]Metal complex stability constants correspond to the following equilibrium constants:

$K(ZnHqp3) = [[Zn(Hqp3)]^+]/[Zn^{2+}][Hqp3^-]$

$K(ZnH_2qp3) = [[Zn(H_2qp3)]^{2+}]/[Zn^{2+}][H_2qp3]$

$K(ZnH_3qp3) = [[Zn(H_3qp3)^{3+}]]/[Zn^{2+}][H_3qp3^-]$

[c]Metal complex pK_a values correspond to the following equilibrium constants:

$K_{a1} = [[Zn(Hqp3)]^+][H^+]/[[Zn(H_2qp3)]^{2+}]$, $pK_{a1} = \log\beta_{011} - \log\beta_{-111}$.

$K_{a2} = [[Zn(H_2qp3)]^{2+}][H^+]/[[Zn(H_3qp3)^{3+}]]$, $pK_{a12} = \log\beta_{111} - \log\beta_{011}$.

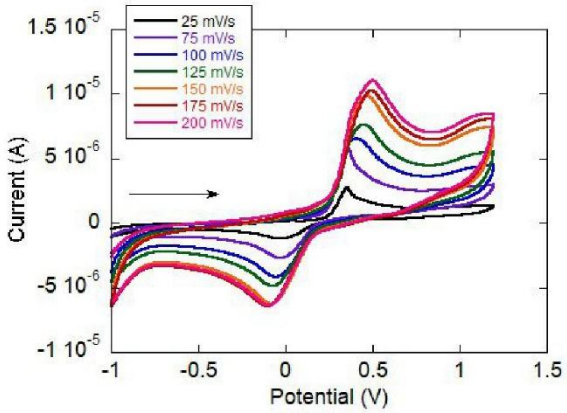

Figure S11. Cyclic voltammetry of 1.0 mM **2** in 0.10 M phosphate buffer (NaH_2PO_4/Na_2HPO_4, pH 7.0). The scan rate was varied from 25 to 200 mV/s. At 100 mV/s, $E_{1/2}$ = 195 mV vs. Ag/AgCl (saturated KCl) or 396 mV vs NHE, ΔE = 208 mV. The black arrow indicates the starting potential and the initial direction of the scan.

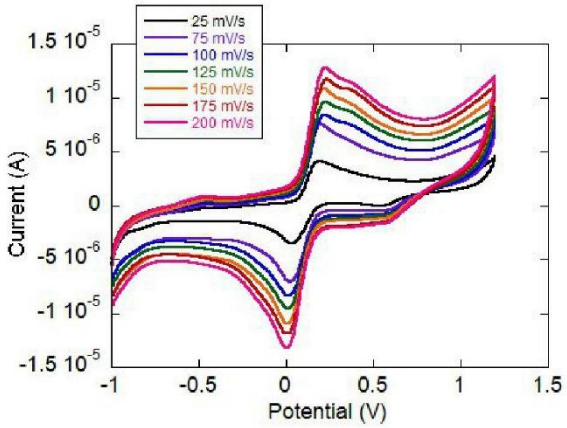

Figure S12. Cyclic voltammetry of 1.0 mM **3** in 0.10 M phosphate buffer (NaH_2PO_4/Na_2HPO_4, pH 7.0). The scan rate was varied from 25 to 200 mV/s. At 100 mV/s, $E_{1/2}$ = 150 mV vs. Ag/AgCl (saturated KCl) or 347 mV vs NHE, ΔE = 166 mV. The black arrow indicates the starting potential and the initial direction of the scan.

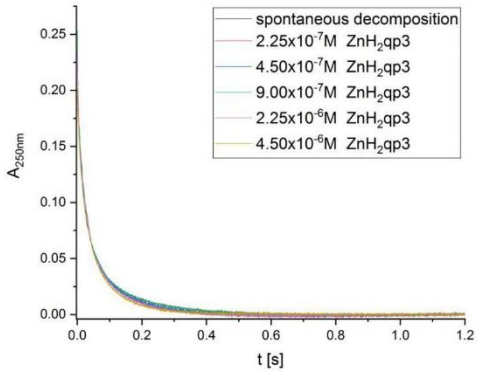

Figure S13. Kinetic traces of superoxide decomposition at 250 nm (60 mM MOPS buffer, pH 7.4 ionic strength of 150 mM) by **3**. The addition of **3** does not have a noticeable impact on the rate of superoxide decay.

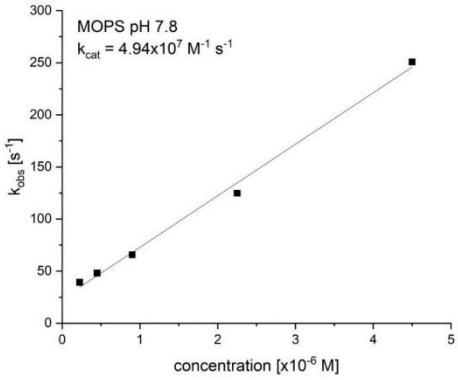

Figure S14. Plot of k_{obs} vs. [**2**] for superoxide dismutation reactions run in pH 7.8 MOPS. Data taken in 60 mM MOPS buffer, pH 7.8 ionic strength of 150 mM.

Publication 2: Computational Analysis of the Superoxide Dismutase Mimicry Exhibited by a Zinc(II) Complex with a Redox-Active Organic Ligand

E. Miliordos, J. L. Moore, S. V. Obisesan, J. Oppelt, I. Ivanović-Burmazović and C. R. Goldsmith

Journal of Physical Chemistry A, **2024**, *128*, 1491-1500.

Summary: Further studies on quinol-containing zinc-based complexes to understand the mechanism during SOD catalysis led to computational analysis of potential intermediates. The crucial role of the coordinated quinol residue and its respective coordination modes was presented using DFT calculations. Complete loss of SOD-activity for the $[Zn(Hpp1)](OTf)_2$ complex ([N-(2-Hydroxybenzyl)-N,N',N'-tris(2-pyridinylmethyl)-1,2-ethanediamine]zinc(II) Triflate), where one quinol was substituted by phenol, was proposed by the calculations.

Contribution: The postulated inactivity of $[Zn(Hpp1)](OTf)_2$ against the superoxide anion radical was demonstrated by JO using the stopped-flow technique by directly monitoring the decay of superoxide in buffered solutions. These experiments were crucial to support theoretical findings and provided deeper insight into the mechanism of this class of SOD mimetics, based on ligand redox, coordination and protolytic properties.

THE JOURNAL OF PHYSICAL CHEMISTRY A
A JOURNAL OF THE AMERICAN CHEMICAL SOCIETY

pubs.acs.org/JPCA Article

Computational Analysis of the Superoxide Dismutase Mimicry Exhibited by a Zinc(II) Complex with a Redox-Active Organic Ligand

Evangelos Miliordos,* Jamonica L. Moore, Segun V. Obisesan, Julian Oppelt, Ivana Ivanović-Burmazović, and Christian R. Goldsmith*

Cite This: *J. Phys. Chem. A* 2024, 128, 1491−1500 Read Online

ACCESS | Metrics & More | Article Recommendations | Supporting Information

ABSTRACT: Previously, we found that a Zn(II) complex with the redox-active ligand *N*-(2,5-dihydroxybenzyl)-*N*,*N*′,*N*′-tris(2-pyridinylmethyl)-1,2-ethanediamine (H_2qp1) was able to act as a functional mimic of superoxide dismutase, despite its lack of a redox-active transition metal. As the complex catalyzes the dismutation of superoxide to form O_2 and H_2O_2, the quinol in the ligand is believed to cycle between three oxidation states: quinol, quinoxyl radical, and *para*-quinone. Although the metal is not the redox partner, it nonetheless is essential to the reactivity since the free ligand by itself is inactive as a catalyst. In the present work, we primarily use calculations to probe the mechanism. The calculations support the inner-sphere decomposition of superoxide, suggest that the quinol/quinoxyl radical couple accounts for most of the catalysis, and elucidate the many roles that proton transfer between the zinc complexes and buffer has in the reactivity. Acid/base reactions involving the nonmetal-coordinating hydroxyl group on the quinol are predicted to be key to lowering the energy of the intermediates. We prepared a Zn(II) complex with *N*-(2-hydroxybenzyl)-*N*,*N*′,*N*′-tris(2-pyridinylmethyl)-1,2-ethanediamine (Hpp1) that lacks this functional group and found that it could not catalyze the dismutation of superoxide; this confirms the importance of the second, distal hydroxyl group of the quinol.

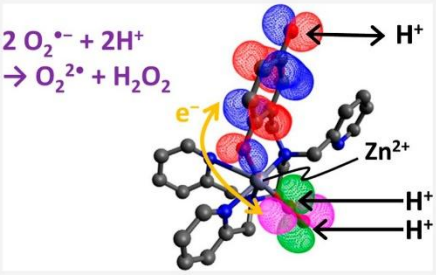

INTRODUCTION

Superoxide dismutases (SODs) are enzymes that catalyze the degradation of superoxide ($O_2^{\bullet-}$) to dioxygen (O_2) and hydrogen peroxide (H_2O_2, eq 1).

$$2O_2^{\bullet-} + 2H^+ \rightarrow O_2 + H_2O_2 \quad (1)$$

All known SODs employ a redox-active transition metal in the active site, containing either manganese, iron, nickel, or copper.[1,2] The metals act as redox partners for $O_2^{\bullet-}$. During catalysis, the metals cycle between two oxidation states, with the more highly oxidized metal ion oxidizing $O_2^{\bullet-}$ to O_2 and the more reduced metal ion reducing $O_2^{\bullet-}$ to peroxide, which gets protonated to H_2O_2.

The overproduction of $O_2^{\bullet-}$ and other reactive oxygen species (ROS) has been correlated to a diverse group of health conditions, including inflammatory, cardiovascular, and neurological disorders.[3−11] This has motivated us and other researchers to develop small-molecule mimics of SOD that could catalytically lower ROS levels in vivo. In turn, this could potentially alleviate the symptoms of these health conditions or even halt the progression of the diseases altogether.

Most functional mimics of SOD resemble the enzymes in that they contain redox-active metal ions.[1,12−34] The most active of these mimetics, as assessed by the k_{cat} rate constants for their in vitro reactions with superoxide, have been manganese complexes with either cationic porphyrinic or pentaazamacrocyclic ligands.[23−32] Certain classes of metal-free compounds, chiefly nitroxides and fullerene derivatives, have also been found to catalyze the degradation of $O_2^{\bullet-}$ but at rates that are much slower than those of both the enzymes and the best transition metal-containing SOD mimics.[23,27,35,36]

Recently, we reported functional SOD mimics that rely on a third strategy: complexing a redox-active organic molecule to a redox-inactive metal ion, specifically Zn(II).[37,38] The first two mimics use *N*-(2,5-dihydroxybenzyl)-*N*,*N*′,*N*′-tris(2-pyridinylmethyl)-1,2-ethanediamine (H_2qp1) and *N*,*N*′-bis(2,5-dihydroxybenzyl)-*N*,*N*′-bis(2-pyridinylmethyl)-1,2-ethanediamine (H_4qp2) as the ligands; the quinols in these molecules can be oxidized by two electrons to *para*-quinones.[39] Both [Zn(H_2qp1)(OTf)](OTf) (**1**) and [Zn(H_4qp2)](OTf)$_2$ (**2**) catalyze the dismutation of $O_2^{\bullet-}$ at rates that were both much faster than those of purely organic antioxidants and comparable to those of manganese-containing SOD

Received: November 8, 2023
Revised: January 26, 2024
Accepted: January 29, 2024
Published: February 14, 2024

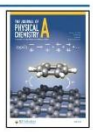

https://doi.org/10.1021/acs.jpca.3c07403
J. Phys. Chem. A 2024, 128, 1491−1500

Scheme 1. Structures of $[Zn(Hqp1)]^+$, Its Conjugate Base $[Zn(qp1)]$, Its Deprotonated and One-Electron Oxidized Form $[Zn(qp1)]^{\bullet+}$, and the Deprotonated/Two-Electron Oxidized Product $[Zn(qp1)]^{2+}$. The *para*-Quinone in $[Zn(qp1)]^{2+}$ May Bind Weakly to the Metal Center

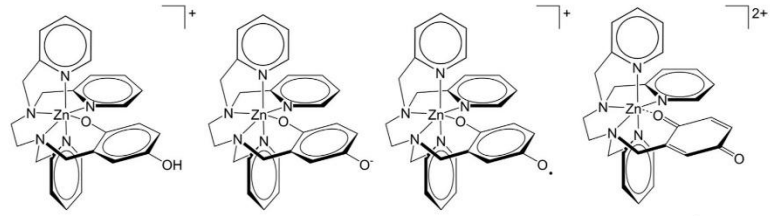

mimics.[37,38] Both complexes differ from all other small-molecule SOD mimics in that their activities are enhanced rather than inhibited in phosphate buffer. At physiological pH (pH ~ 7.4), **1** deprotonates to $[Zn(Hqp1)]^+$ (Scheme 1);[37] **2** similarly deprotonates to the monocationic $[Zn(H_3qp2)]^+$.[38]

The diamagnetism of Zn(II) limits our ability to spectroscopically monitor the stoichiometric and catalytic reactions between the zinc complexes and $O_2^{\bullet-}$. The observed UV/vis bands come exclusively from intraligand transitions and provide evidence for the oxidation of the quinol portion of H_2qp1 to a *para*-quinone (qp1); the oxidation of the Zn(II) compound to a mixture of the starting complex and the two-electron oxidized form $[Zn(qp1)]^{2+}$ is also supported by mass spectrometry.[37] Although it was not observed in the catalysis for the initial report, the chemistry was believed to proceed through the Zn(II) complex with the one-electron-oxidized ligand Hqp1$^{\bullet}$, which can deprotonate to qp1$^{\bullet-}$. With **2**, low-temperature UV/vis analysis suggested that semiquinone radicals were indeed produced.[38] Low-temperature mass spectrometry data for **1** are consistent with the formation of a Zn(II)−OOH species and an inner-sphere mechanism of superoxide dismutation,[37] but a similar species was not detectable for **2**.[38] Furthermore, the MS data for **1** could instead correspond to a Zn(II)−OH species with an oxygenated ligand. Regrettably, these complexes lack charge transfer bands that would enable us to confirm the bound OOH groups through resonance Raman spectroscopy.

Here, we test the viability of the proposed mechanism for superoxide degradation using density functional theory (DFT). We assess the structures and energies of various proposed intermediates derived from **1**; we selected this over **2** to avoid complications from the inclusion of a second redox-active quinol. Our chief interests are (1) probing the feasibilities of inner-sphere reduction and oxidation of $O_2^{\bullet-}$ with a redox-inactive metal, (2) determining whether the qp1$^{\bullet-}$/Hqp1$^-$ or qp1/qp1$^{\bullet-}$ redox couple features more prominently in the catalysis, (3) elucidating the electronic structure of the $[Zn(qp1^{\bullet-})]^+$ species, (4) understanding how acid/base chemistry with the solvent and/or buffer impacts the mechanistic cycle, and (5) predicting how activity could be improved through synthetic modifications to the catalyst. We also prepared a Zn(II) complex with *N*-(2-hydroxybenzyl)-*N*,*N*′,*N*′-tris(2-pyridinylmethyl)-1,2-ethanediamine (Hpp1, Scheme 2); this compound differs from the Zn(II)−H_2qp1 complex in that it lacks the distal, noncoordinating hydroxyl group. The Hpp1 complex was not a competent catalyst for superoxide dismutation.

Scheme 2. Structure of H_4qp2 and Hpp1 with Metal-Coordinating Atoms Highlighted

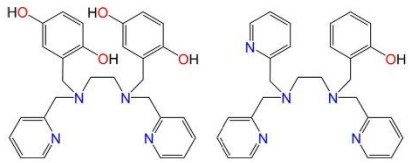

METHODS

Materials. Most chemicals and solvents were purchased from Sigma-Aldrich and used without further purification. Diethyl ether (ether) and methanol (MeOH) were purchased from Fisher. Deuterated methanol (CD_3OD) was purchased from Cambridge Isotopes. *N*-(2-Hydroxybenzyl)-*N*,*N*′,*N*′-tris-(2-pyridinylmethyl)-1,2-ethanediamine (Hpp1) was synthesized as previously described.[40]

Instrumentation. All nuclear magnetic resonance (NMR) data were collected on a 500 mHz AV Bruker NMR spectrometer. All NMR resonance peak frequencies were referenced to internal standards. UV/vis data were collected on a Varian Cary 50 spectrophotometer and analyzed using software from WinUV Analysis Suite. High-resolution mass spectrometry data were obtained at the Mass Spectrometer Center at Auburn University on a Bruker Microflex LT MALDI-TOF mass spectrometer via direct probe analysis operated in positive ion mode. Infrared (IR) data were obtained with a Shimadzu IR Prestige-21 Fourier transform infrared spectrophotometer. Elemental analysis (C, H, and N) was performed by Atlantic Microlab (Norcross, GA); the sample was dried under vacuum and placed under a N_2 atmosphere prior to shipment.

Kinetic Assessment of SOD Activity. The ability of the Hpp1 complex to catalytically degrade superoxide was tested by a direct method using stopped-flow techniques described in a previous publication from one of our laboratories.[41] Experiments were carried out using syringes 1, 2, and 3 on a Biologic SFM-400 instrument that was equipped with an Energetiq LDLS ENQ EQ-99-FC laser-driven light source and a J&M TIDAS diode array detector (integration time = 0.5 ms, λ = 180−724 nm). The source of superoxide was commercially available KO_2 dissolved in dry and nonbuffered dimethyl sulfoxide (DMSO) with $[O_2^{\bullet-}] \approx 1-2$ mM. The Zn(II)−

https://doi.org/10.1021/acs.jpca.3c07403
J. Phys. Chem. A 2024, 128, 1491−1500

Scheme 3. Illustration of the mer and fac Conformations of $[Zn(Hqp1)]^+$. For the mer Conformer, Superoxide Necessarily Coordinates *cis* to the Quinolate upon Displacement of a Pyridine. For the fac Conformer, Superoxide Can Coordinate Either *trans* (fac/trans) Or *cis* (fac/cis) to the Quinolate upon Displacement of a Pyridine Ring. The Red Arrows Show the Possible Trajectories of $O_2^{\bullet-}$, with the Potentially Displaced Pyridines Being Highlighted in Blue

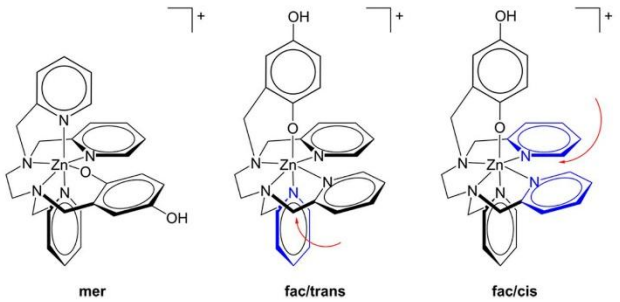

Hpp1 complex was tested at four different concentrations between 0.9 and 9 μM in aqueous solutions buffered with 3-(*N*-morpholino)propanesulfonic acid (MOPS) to pH 7.4. The ionic strength of all solutions was 150 mM. The aqueous solution containing the Zn(II) complex was mixed in a 9:1 ratio with the superoxide solution in DMSO using a high-density mixer. The initial concentration of the superoxide is determined from the intensity of the UV band at 250 nm as assessed immediately after stopped-flow mixing of the superoxide DMSO solution with the appropriate buffer. The 250 nm band is characteristic for superoxide and has well-known and -established molar extinction coefficients for each buffer and pH used.[42] In each experiment, the concentration of superoxide exceeded that of the metal-containing catalyst by at least 10-fold to ensure catalytic conditions. Millipore water was used for the preparation of the buffer solutions. All prepared buffers were treated with Chelex 100 sodium exchange resin for at least 12 h before use in order to remove adventitious metal ions. Data analysis was performed using BioKine V4.66 software.

Computational Details. The structures of possible intermediates were optimized by DFT. To obtain the calculated structures, we used the MN15 functional[43] combined with the 6-31g(d,p) basis set for all atoms except oxygen, which instead uses 6-31g+(d,p), which has an additional series of diffuse functions.[44−48] The addition of diffuse functions on oxygen was essential to reasonably predict the electron affinity of O_2 (0.55 eV vs the experimental value of 0.45 eV).[49] The chosen functional previously performed well for systems containing transition metals and systems bearing noncovalent interactions.[50,51] We applied the solvent model based on density (SMD) methodology to account for solvent (water) effects.[52] All structures were found to have only real vibrational harmonic frequencies. Free-energy corrections at 20 °C and 1.0 atm were calculated via the harmonic approximation, and all calculations were carried out with Gaussian16.[53]

Synthesis. *[N-(2-Hydroxybenzyl)-N,N′,N′-tris(2-pyridinylmethyl)-1,2-ethanediamine]zinc(II) Triflate {[Zn(Hpp1)](OTf)$_2$, **3**}.* Hpp1 (0.100 g, 0.228 mmol) and $Zn(OTf)_2$ (0.083 g, 0.228 mmol) were dissolved in 2 mL of MeOH under N_2 and stirred at room temperature. After 16 h, 2 mL of ether was added to the solution to precipitate the crude product. The solid was further purified by washing with MeOH/ether (1:5 v/v) and dried under N_2 to give the product as a white powder (0.100 g, 55% yield). ^{1}H NMR (500 MHz, CD_3OD, 293 K): δ 8.64 (d, J = 5.4 Hz, 2H), 8.34 (m, 1H), 8.17−8.21 (d, J = 6.4 Hz, 2H), 7.70−7.81 (d, J = 13.6 Hz, m, 7H), 6.90 (m, 2H), 6.78 (m, 2H), 4.66−4.73 (d, J = 16.4 Hz, 3H), 4.49 (m, 1H), 4.28−4.36 (m, 1H), 4.25 (m, 1H), 3.51 (m, 2H), 3.50 (m, 1H), 3.32 (m, 1H), 2.87 (d, J = 10.9 Hz, 2H), 2.23 (d, J = 11.1 Hz, 1H). ^{13}C NMR (125 MHz, CD_3OD, 293 K): δ 157, 155, 148, 147, 146, 141, 132, 125, 124, 121, 120, 119, 115, 65, 60, 55, 54, 52, 48, 47, 15. Optical spectroscopy (MeOH, 293 K): 239 nm (ε = 2000 M^{-1} cm^{-1}), 273 nm (ε = 1800 M^{-1} cm^{-1}). IR (cm^{-1}): 3331 (m), 1609 (s), 1574 (w), 1516 (m). 1487 (w), 1444 (s), 1275 (w), 1236 (w), 1221 (s), 1155 (s), 1107 (w), 1080 (m), 1056 (m), 1025 (s), 979 (w), 945 (w), 828 (m), 760 (s), 724 (w), 633 (s), 597 (w), 572 (m), 514 (s). MS (ESI): calcd for $[Zn^{II}(Hpp1)]^{2+}$, 251.5832; found, 251.5826, calcd for $[Zn^{II}(Hpp1)(HCOO^-)]^+$, 548.1612; found, 548.1642, calcd for $[Zn^{II}(Hpp1)(OTf)]^+$, 652.1124; found, 652.1170. Elemental analysis: calcd for $C_{29}H_{29}N_5ZnF_6O_7S_2{\cdot}2H_2O$: C, 41.29%; H, 3.94%; N, 8.30%; found, C, 40.98%; H, 3.92%; N, 8.12%.

■ RESULTS AND DISCUSSION

The Zn(II)−H_3qp1 complex (**1**) can potentially be oxidized by up to two electrons and is either singly or doubly deprotonated. At physiological pH, **1** spontaneously deprotonates to $[Zn(Hqp1)]^+$;[37] consequently, the metal-bound O atom from the quinol-derived portion of the ligand remains deprotonated in all investigated intermediates. The possible general reaction steps considered in this study for the degradation of superoxide to hydrogen peroxide (eq 1) facilitated by $[Zn(Hqp1)]^+$ in phosphate buffer are listed below

$$[Zn(Hqp1)]^+ + O_2^{\bullet-} \rightarrow [O_2Zn(Hqp1)]^{\bullet} \quad (A)$$

$$[O_2Zn(Hqp1)]^{\bullet} + H_2PO_4^- \rightarrow [HOOZn(Hqp1)]^{\bullet+} + HPO_4^{2-} \quad (B)$$

$$[HOOZn(Hqp1)]^{\bullet+} + H_2PO_4^- \rightarrow [H_2O_2Zn(Hqp1)]^{\bullet,2+} + HPO_4^{2-} \quad (C)$$

$$[H_2O_2Zn(Hqp1)]^{\bullet,2+} \rightarrow [Zn(Hqp1)]^{\bullet,2+} + H_2O_2 \quad (D)$$

https://doi.org/10.1021/acs.jpca.3c07403
J. Phys. Chem. A 2024, 128, 1491−1500

Table 1. Relative Free Energies (kcal/mol) for the Products of Reaction Steps A–F for the Various Conformations of the Zn(II) Complex with Respect to the Lowest-Energy IS

species	$[Zn(Hqp1)]^{+a}$	$[Zn(qp1)]^{a,b}$	$[Zn(qp1)]^{b,c}$	$[Zn(qp1)]^{b,d}$	$[Zn(qp1)]^{\bullet+a,e}$
(IS)[f] $[Zn(Hqp1)]^+/[Zn(qp1)]/[Zn(qp1)]^{\bullet+}$, $2H_2PO_4^-$, $2O_2^{\bullet-}$	0.0	15.5	18.4	18.4	99.3
(A) $[O_2Zn(Hqp1)]^{\bullet}/[O_2Zn(qp1)]^{\bullet-}/[O_2Zn(qp1)]^{2\bullet}(S = 0)$, $2H_2PO_4^-$, $O_2^{\bullet-}$	12.7	26.6	26.8	27.8	113.2
(B) $[HOOZn(Hqp1)]^{\bullet+}/[HOOZn(qp1)]^{\bullet}/[HOOZn(qp1)]^+$, $H_2PO_4^-$, HPO_4^{2-}, $O_2^{\bullet-}$	21.4	12.3	5.9	8.0	110.0
(C) $[H_2O_2Zn(Hqp1)]^{\bullet2+}/[H_2O_2Zn(qp1)]^{\bullet+}/[H_2O_2Zn(qp1)]^{2+}$, $2HPO_4^{2-}$, $O_2^{\bullet-}$	12.6	2.6	4.4	5.9	110.1
(D) $[Zn(Hqp1)]^{\bullet2+}/[Zn(qp1)]^{\bullet+}/[Zn(qp1)]^{2+}$ $2HPO_4^{2-}$, $O_2^{\bullet-}$, H_2O_2	6.0	−3.1	−1.7	−1.7	102.0
(E) $[O_2Zn(Hqp1)]^{2\bullet,+}(S = 1)$[g]$/[O_2Zn(qp1)]^{2\bullet}(S = 1)$[h]$/[O_2Zn(qp1)]^{\bullet+}$[i], $2HPO_4^{2-}$, H_2O_2	−0.2	10.8	8.8	6.7	100.2
(F) $[Zn(Hqp1)]^+/[Zn(qp1)]/[Zn(qp1)]^{\bullet+}$, $2HPO_4^{2-}$, $O_2^{2\bullet}(S = 1; X^3\Sigma_g^-)$, H_2O_2	−9.5	6.1	8.9	8.9	89.9

[a]Structure corresponds to the **mer** conformation in Scheme 3. [b]The free-energy difference between $[Zn(Hqp1)]^+$ and $[Zn(qp1)]$ is fixed at +15.5 kcal/mol to account for the acid/base free-energy difference in the solution; see text. [c]Structure corresponds to the **fac**/**cis** conformation and trajectory of superoxide binding in Scheme 3. [d]Structure corresponds to the **fac**/**trans** conformation and trajectory of superoxide binding in Scheme 3. [e]The $[Zn(qp1)]^{\bullet+}$ free energy is obtained as the $[Zn(qp1)]$ free energy plus the $[Zn(qp1)]^{\bullet+}/[Zn(qp1)]$ free energy difference. [f]Initial species. [g]$O_2^{2\bullet}(S = 1)$,$[Zn(Hqp1)]^+$ complex. [h]$S = 0$ is just 0.03 kcal/mol higher. [i]$O_2^{2\bullet}(S = 1)$,$[Zn(qp1)]^{\bullet+}$ complex.

$$[Zn(Hqp1)]^{\bullet,2+} + O_2^{\bullet-} \rightarrow [O_2Zn(Hqp1)]^{2\bullet,+} \quad (E)$$

$$[O_2Zn(Hqp1)]^{2\bullet,+} \rightarrow [Zn(Hqp1)]^+ + O_2^{2\bullet} \quad (F)$$

In step A, one pyridine group of the H_2qp1 ligand detaches from Zn(II) allowing $O_2^{\bullet-}$ to coordinate to the metal center. Our calculations show that the pentacoordinate complex with a detached pyridine is only ∼7 kcal/mol higher in energy than the hexacoordinate complex, suggesting that the two species may exchange and that a dissociative mechanism for ligand exchange is plausible. In reaction B, a proton is transferred from a dihydrogen phosphate from the buffer to the terminal oxygen atom of the coordinated superoxide while an electron is transferred from $Hqp1^-$ to the superoxide. This reduces and protonates superoxide ($O_2^{\bullet-}$) to hydroperoxide (OOH^-). In reaction C, a second proton is provided by another equiv of dihydrogen phosphate to form H_2O_2, which is subsequently released in step D. In step E, a second $O_2^{\bullet-}$ binds to Zn(II). The superoxide reduces the quinol-derived portion of the ligand as it oxidizes to O_2 in step (F). Analogous routes are studied for reactions starting from $[Zn(qp1)]$ and $[Zn(qp1)]^{\bullet+}$, which differ from $[Zn(Hqp1)]^+$ by the removal of a proton and a net hydrogen atom, respectively. The Supporting Information provides more details on reaction steps A–F starting from these two species.

Reaction Step A—Initial Coordination of Superoxide. The most stable $[Zn(Hqp1)]^+$ species adopts two structures that differ with respect to the coordinating position of the quinolate relative to those of the two tertiary amines. The **mer** and **fac** conformers are shown in Scheme 3, with the former being ∼5 kcal/mol more stable. In the **fac** case, $O_2^{\bullet-}$ can potentially bind either next to (**fac**/**cis**) or across from (**fac**/**trans**) the quinolate when it displaces a pyridine ring, as visualized by the red arrows in Scheme 3. In the **mer** conformation, an incoming $O_2^{\bullet-}$ necessarily occupies a position *cis* to the quinolate upon displacing one of the pyridines. Similar structures are possible for $[Zn(qp1)]$ and $[Zn(qp1)]^{\bullet+}$. Our calculations confirm our expectations that placing the two redox-active components, quinolate and $O_2^{\bullet-}$, closer together facilitates the electron transfer between these groups (see below) and that orienting these *cis* to each other will result in more rapid SOD mimicry.

The theoretically predicted low energy differences between the **mer** and **fac** structures are consistent with the previously obtained data. Again, these designations refer to the relative orientations of the quinolate and the two tertiary amines. ^1H NMR data for **1** suggest the existence of multiple species in solution,[37] and it is likely that both the **mer** and **fac** isomers are present and exchanging with each other. In our initial report,[37] however, we were unable to unambiguously identify, differentiate, and quantify these isomers. The hydroxy group in the quinolate could potentially be deprotonated, leading to $[Zn(qp1)]$. The latter is initially 15.5 kcal/mol higher in energy but becomes much more energetically feasible after the reaction with superoxide (see below). The energy difference of 15.5 kcal/mol between $[Zn(Hqp1)]^+$ and $[Zn(qp1)]$ is calculated with eq 2

$$\Delta G = 2.3\ R\ T\ pK_a \quad (2)$$

where the pK_a corresponds to $[Zn(Hqp1)]^+ \rightleftharpoons [Zn(qp1)] + H^+$ and has been estimated to be 11.6.[54] We were unable to directly measure this value due to precipitation of the complex above pH 9.0.[37] Computationally, the same energy difference can be estimated by comparing $[Zn(Hqp1)]^+ + HPO_4^{2-}$ and $[Zn(qp1)]^+ + H_2PO_4^-$; this provides an alternative value of 11.2 kcal/mol. We used the 15.5 kcal/mol value in the rest of our study, but the conclusions and predicted mechanism remained the same for either value.

The relative free energies for reaction step A using $H_2PO_4^-$ as a proton donor and $[Zn(Hqp1)]^+$, $[Zn(qp1)]$, or $[Zn(qp1)]^{\bullet+}$ as the acceptor are listed in Table 1, and the corresponding free energy diagrams (FEDs) are shown in Figure 1. All free energies are referenced to those of the lowest-energy reacting species: $[Zn(Hqp1)]^+$(**mer**) + $2H_2PO_4^-$ + $2O_2^{\bullet-}$. The **mer** conformers are our primary focus for all three starting species since they are the most stable, but the **fac** conformers for the redox-active $[Zn(qp1)]$ species are also considered with both the **cis** and **trans** trajectories for the coordinating superoxide. In all six steps (A–F), the mass, charge, and spin (number of unpaired electrons) are conserved. The FEDs for $[Zn(Hqp1)]^+$(**mer**) and $[Zn(qp1)]^{\bullet+}$(**mer**) are parallel, with the latter lying higher by +99.3 kcal/mol. Therefore, only the former is included in Figure 1. The high similarity of these species results from the fact that $[Zn(Hqp1)]^+$ and $[Zn(qp1)]^{\bullet+}$ only differ by a single $H^{\bullet}$; the formed "observer" O–H bond does not significantly impact the geometries. The enthalpy and entropy changes

https://doi.org/10.1021/acs.jpca.3c07403
J. Phys. Chem. A 2024, 128, 1491−1500

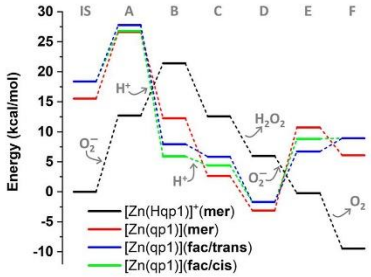

Figure 1. FEDs for the initial species (IS) and the intermediate species formed from steps A−F in Table 1 for superoxide dismutation catalyzed by $[Zn(Hqp1)]^+$ (**mer**) and $[Zn(Hqp1)]$ (**mer**, **fac**/**trans**, and **fac**/**cis**).

during the initial insertion of $O_2^{\bullet-}$ increase the free energy in all cases by as much as 11−14 kcal/mol. $O_2^{\bullet-}$ remains largely ionic with one localized unpaired electron in its π^* orbital (Figure 2).

Reaction Step B—Proton Transfers Facilitate Intramolecular Superoxide Reduction. In step B, the Zn(II)-bound superoxide abstracts a proton from the solution, as it accepts one electron from the quinol-derived portion of the H_2qp1 ligand via a concerted proton-coupled electron transfer (PCET). Our calculations show that the unpaired electron is delocalized throughout the oxidized quinolate (Figure 2). At this point in the reaction, the free energy for the $[Zn(Hqp1)]^+$-derived intermediate is substantially higher than that derived from $[Zn(qp1)]$. The PCET for the **mer** conformer of the $[Zn(qp1)]$-derived intermediate is favorable, with $\Delta G = -14.4$ kcal/mol; ΔG for the analogous PCET reactions starting from the **fac**/**cis** and **fac**/**trans** conformers, conversely, are −20.1 and −19.8 kcal/mol, respectively. As a result, the free energy of intermediate B, where the electron transfer has occurred, is lower for **fac**/**cis** than **fac**/**trans** (Figure 1). The $[HOOZn(qp1)]^{\bullet}$ product is lower in energy than its conjugate acid $[HOOZn(Hqp1)]^{\bullet+}$, and it is at this step that the two FEDs corresponding to the $[Zn(Hqp1)]^+$ and $[Zn(qp1)]$ starting materials cross each other. Initially deprotonating the OH group of the semiquinolate anion enables the subsequent PCET to proceed through lower-energy intermediates, facilitating the formation of OOH.

To understand why the deprotonation of the OH of the semiquinolate anion renders electron transfer more thermodynamically favorable, we calculated the ionization energies of $Hqp1^-$, $qp1^{2-}$, and $qp1^{\bullet-}$—the redox-active moieties of $[Zn(Hqp1)]^+$, $[Zn(qp1)]$, and $[Zn(qp1)]^{\bullet+}$—to see which species most readily relinquishes an electron. The $qp1^{2-}$ is the only one of the three to be stabilized upon ionization, with a negative ionization energy of −3.5 eV. Both $Hqp1^-$ and $qp1^{\bullet-}$, conversely, have positive ionization energies (1.7 and 1.9 eV), indicating that they prefer to accept an electron. The formation of $qp1^{2-}$ in solution from *para*-quinone-containing qp1 would require the provision of two electrons. Alternatively, the dianionic ligand can also be formed from H_2qp1 by removing two protons and stabilizing $qp1^{2-}$ over $qp1^-$. This second path is not feasible for the metal-free ligands since $qp1^-$ is more stable than $qp1^{2-}$ by 3.5 eV. Our calculations indicate that Zn(II) is crucial to forming and electrostatically stabilizing $qp1^{2-}$. One last note is that a change in the conformation at this reaction step is also possible since the $[Zn(Hpq1)]^+$ FED crosses with the FEDs of all three (**mer**, **fac**/**trans**, and **fac**/**cis**) conformations of $[Zn(qp1)]$ (Figure 1). Independently of the conformation adopted, the overall mechanism and process will remain the same since all three FEDs are "parallel" to each other and all cross again with the $[Zn(Hqp1)]^+$ FED at step E.

The importance of this deprotonation is corroborated by the previously obtained kinetic data. When the pH of the solution is raised from 7.4 to 8.1, the k_{cat} rate constant for superoxide dismutation by **1** increases by ∼40%.[37] The improved activity of the Zn(II)−H_2qp1 catalyst under basic conditions is unusual. Many other SOD mimics, including the manganese analog of **1**, often lose activity and become less effective catalysts under more basic conditions.[12−14,16,17,34,41,55−57]

Reaction Steps C and D—Protonation of Hydroperoxide and Release of Hydrogen Peroxide. After the intramolecular reduction and protonation of the superoxide,

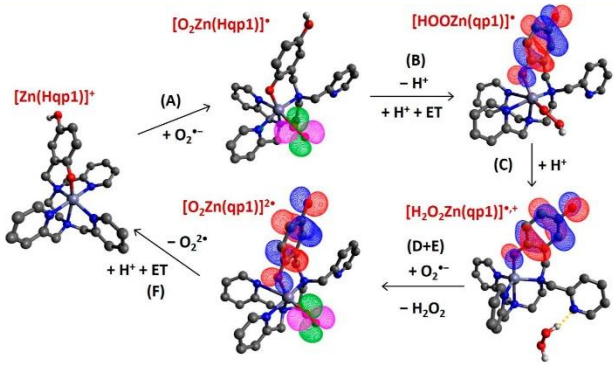

Figure 2. Molecular orbitals hosting the unpaired electrons of all species pertaining to the proposed dominant $[Zn(Hqp1)]^+/[Zn(qp1)]$ (**mer**) cycle. The reaction steps are listed in parentheses. The $[O_2Zn(qp1)]^{2\bullet}$ intermediate bears two unpaired electrons (open-shell singlet) and the related orbitals are depicted with different colors (blue/red vs green/purple). ET signifies electron transfer from either the ligand to the $O_2^{\bullet-}$ (step B) or the reverse direction (step F).

https://doi.org/10.1021/acs.jpca.3c07403
J. Phys. Chem. A 2024, 128, 1491−1500

the resultant HOO^- is further protonated by the phosphate buffer; as long as the **mer** conformation is maintained, reaction step C is exergonic by 9.6 kcal/mol (Table 1). This is followed by the exergonic release of the H_2O_2 ligand ($\Delta G = -5.7$ kcal/mol) in step D. The free energies of the intermediates for [Zn(qp1)] continue to be lower than those for [Zn(Hqp1)], indicating that the semiquinone anion continues to stabilize the intermediates.

Reaction Steps E and F—Coordination of the Second Equiv of Superoxide and Its Oxidation to Dioxygen. The coordination of the second equivalent of $O_2^{\bullet-}$ to $[Zn(qp1)]^{\bullet,+}$ resembles the other superoxide-binding event seen in step A in that it is endergonic for all **mer**, **fac**/**cis**, and **fac**/**trans** cases by 8−14 kcal/mol (Table 1 and Figure 1). The two unpaired electrons on $O_2^{\bullet-}$ and $qp_1^{\bullet-}$ can couple into an open-shell singlet or a triplet. The triplet density is always lower by 0.6−0.7 kcal/mol for all three species.

The coordination of $O_2^{\bullet-}$ to $[Zn(Hqp1)]^{\bullet 2+}$ was less straightforward. We were not able to find a stable $O_2^{\bullet-}$ + $[Zn(Hqp1)]^{\bullet 2+}$ coordination complex. Instead, when we started from the geometry of the stable $O_2^{\bullet-}$ + $[Zn(qp1)]^{\bullet,+}$ coordination complex $[O_2Zn(qp1)]^{2\bullet}$ ($S = 1$) and added a proton to the oxygen terminus of $qp1^{2-}$ to form $[O_2Zn(Hqp1)]^{2\bullet,+}$, we obtained a weakly bound complex of an O_2 molecule and $[Zn(Hqp1)]^+$. An analogous reaction occurs with $O_2^{\bullet-}$ + $[Zn(qp1)]^{2+}$, which creates a weakly bound complex of O_2 and $[Zn(qp1)]^{\bullet+}$. These observations agree with the electronic state of the semiquinone ligand in the three cases. The $qp1^{\bullet-}$ ligand of $[Zn(qp1)]^{\bullet,+}$ is less willing to accept an electron compared to qp1 and $Hqp1^{\bullet}$ of $[Zn(qp1)]^{2+}$ and $[Zn(Hqp1)]^{\bullet 2+}$, respectively (see above; reaction step B). Consequently, we believe that the oxidation of the $O_2^{\bullet-}$ occurs in an intramolecular fashion for $[Zn(qp1)]^{\bullet,+}$ but with rapid outer-sphere mechanisms for $[Zn(qp1)]^{2+}$ and $[Zn(Hqp1)]^{\bullet 2+}$.

The resulting $O_2^{2\bullet}$ ($S = 1$)−$[Zn(Hqp1)]^+$ molecular complex is lower in energy than $[O_2Zn(qp1)]^{2\bullet}$, and the black and red FEDs of Figure 1 cross at this point. Therefore, in solution, $[O_2Zn(qp1)]^{2\bullet}$ will get protonated and spontaneously eject a molecule of O_2. The $[Zn(Hqp1)]^+$ byproduct can relax back to its optimal structure, closing the catalytic cycle.

Overall, the acid/base chemistry of the quinol-derived portion of the H_2qp1 ligand plays important roles in the catalysis. The initial deprotonation of the nonmetal-bound hydroxyl group greatly facilitates the transfer of an electron from the quinolate to $O_2^{\bullet-}$, and its subsequent reprotonation is needed to complete the catalytic cycle. The highest-energy species intermediate on the proposed path, the product of step C with [Zn(qp1)], is 12.7 kcal/mol higher in energy than the initial reactants $[Zn(Hqp1)]^+$ (Figure 1, Table 1).

The molecular orbitals hosting one unpaired electron for the intermediates corresponding to the proposed lowest-energy path $[Zn(Hqp1)]^+$/[Zn(qp1)] (**mer**) route (black/red lines of Figure 1) are shown in Figure 2. The first $O_2^{\bullet-}$ initially keeps its electron in the π_{OO}^* orbital until the attachment of the first proton induces the migration of one electron from one delocalized π orbital of the quinolate (leaving it singly occupied) to O_2H. This step is facilitated by the deprotonation of the quinol. Upon reduction, the latter moiety becomes a basic HOO^- that can accept a second proton to yield H_2O_2. During the last step, the electron of the second $O_2^{\bullet-}$ (green/purple orbital) couples into a triplet with the electron localized on the semiquinolate anion (red/blue orbital). One of the two electrons of the doubly occupied π^* orbital of $O_2^{\bullet-}$ migrates to the same orbital of the quinol-derived portion of the ligand, yielding $O_2^{2\bullet}$ ($S = 1$) and a quinolate dianion. This last step is facilitated by protonation of the quinolate dianion.

The Mulliken charges and spin densities for all oxygen atoms are shown in Figure S3 of the SI and are in complete agreement with the molecular orbitals' picture. The charges of the oxygen atoms in the quinol remain practically unchanged throughout the process. For the structures with an unpaired electron in the quinol ring, half of the spin density belongs to the carbon atoms, with the two oxygen atoms sharing the other half of the electron in a ∼3:1 ratio. The distal oxygen has a higher spin density than the metal-bound oxygen. The charge and spin density on the O_2 moiety are about −0.6 and 1.0 when it is formally $O_2^{\bullet-}$, and the charge ranges from −0.85 to −0.89 when it is formally an OOH^- or HOOH.

The Zn(II) serves three roles. As mentioned previously, the first role of the metal ion is to stabilize $qp1^{2-}$. The second role is to coulombically attract and coordinate $O_2^{\bullet-}$. Manganese-containing SOD mimetics with higher positive charges tend to catalyze superoxide dismutation more efficiently.[16,25,26,29,31,58] The ability of Zn(II) to place superoxide in close proximity to $qp1^{2-}$ enables facile electron transfer from $qp1^{2-}$ to $O_2^{\bullet-}$. The third role is to hinder the coordination of other competitively binding anions, particularly phosphate. Phosphate inhibition has been found to decrease the activities of manganese-containing SOD mimics, as assessed by the k_{cat} values of the reactions between the compounds and superoxide,[17,41,55] but not those of zinc-quinol catalysts.[37,38] The ΔG for superoxide coordination remains practically the same when Mn(II) is substituted for Zn(II): 3.7 and 3.7 kcal/mol, respectively. With Mn(III), the more positive charge renders the free energy for superoxide coordination negative ($\Delta G = -0.5$ kcal/mol). However, Mn(III) also has a higher affinity for PO_4^{3-}. The ΔG values for the formation of the Zn(II)/PO_4^{3-}, Mn(II)/PO_4^{3-}, and Mn(III)/PO_4^{3-} species are −7.8, −7.1, and −11.8 kcal/mol, respectively. The phosphate inhibition observed for manganese-containing SOD mimics is correlated with the ability of manganese to access the +3 oxidation state. The inability of Zn(II) to be oxidized to a more positive metal ion discourages phosphate coordination, preventing phosphate from competitively inhibiting the coordination and activation of superoxide.

Formation and Possible Catalytic Roles of the *para*-Quinone Species. The quinol can potentially be doubly deprotonated and oxidized by two electrons to form a *para*-quinone group; the loss of two net H atoms yields the qp1 form of the ligand. The key intermediate for this reactivity is $[Zn(qp1)]^{\bullet,+}$, which is produced at reaction step D of the proposed mechanism; this is the lowest-energy intermediate of the FED for [Zn(qp1)] (**mer**) (Figure 1). When $O_2^{\bullet-}$ binds to $[Zn(qp1)]^{\bullet,+}$, there are two possible routes. First, an electron can be transferred from the superoxide to the ligand with the aid of a proton attached to the ligand, producing O_2 and leaving the catalyst in the most stable $[Zn(Hqp1)]^+$ form. The second path occurs via an electron transfer to the opposite direction to create the *para*-quinone species $[Zn(qp1)]^{2+}$, with the addition of two protons converting O_2^{2-} into H_2O_2. The first path is exergonic by 6.4 kcal/mol [−9.5−(−3.1); Table 1], and the second path is endergonic by 2.7 kcal/mol [102.0−99.3; Table 1]. $[Zn(qp1)]^{2+}$ can also form from the disproportionation of $[Zn(qp1)]^{\bullet+}$; two of these ions can

https://doi.org/10.1021/acs.jpca.3c07403
J. Phys. Chem. A 2024, 128, 1491−1500

react to form [Zn(qp1)] and $[Zn(qp1)]^{2+}$. The disproportionation is unfavorable as well with ΔG = 21.3 kcal/mol.

Consequently, we believe that the H_2O_2 and O_2 production rely predominantly on the $qp1^{\bullet-}$/Hqp1$^-$ redox couple and that the doubly oxidized qp1 form of the ligand is rarely accessed. Nonetheless, the energies of the intermediates corresponding to the qp1/$qp1^{\bullet-}$ redox couple are not entirely prohibitive, accounting for the $[Zn(qp1)]^{2+}$ species that have been experimentally observed during and after catalysis.[37]

Preparation and Analysis of a Phenolic Version of $[Zn(H_2qp1)]^{2+}$: $[Zn(Hpp1)]^{2+}$. Even though the quinolic portion of the ligand does not need to donate two electrons for catalysis to proceed, the ability of the distal, noncoordinating hydroxyl group to deprotonate, yielding a dianionic ligand, is essential to the superoxide dismutation. To experimentally confirm this, we prepared a Zn(II) complex with Hpp1, $[Zn(Hpp1)](OTf)_2$ (**3**); the ligand is identical to H_2qp1 except for the lack of the second hydroxyl group (Scheme 2).[40] The phenol from Hpp1 should be able to coordinate to Zn(II) analogously to quinol from H_2qp1. The synthesis proceeds smoothly, and the identity and purity of the complex were confirmed by mass spectrometry and elemental analysis. Attempts to crystallize and structurally characterize **3** have thus far been unsuccessful. The NMR spectra are inconsistent with the existence of a single conformer in solution. This was anticipated since similarly complicated solution-state behavior was observed for the Zn(II)−H_2qp1 complex.[37]

Phenol and quinol have nearly identical pK_a values in water (9.9), but the second hydroxyl group does render quinol more susceptible to oxidation, as indicated by its lower O−H bond dissociation energy: 81.5 vs 89.9 kcal mol^{-1}, as assessed by measurements in DMSO.[59] Deprotonating the second hydroxyl group further weakens the remaining O−H bond to 73.0 kcal mol^{-1}. The phenol-for-quinol substitution would therefore be anticipated to hinder step B in our proposed mechanism (Figure 1, Table 1).

We analyzed the ability of **3** to serve as a SOD mimic using stopped-flow kinetics measurements on the direct reactions between **3** and $O_2^{\bullet-}$ in 60 mM MOPS buffered to pH 7.4 (Figure 3). This medium was found to support SOD mimicry for both **1** and **2**.[37,38] Unlike **1** and **2**, **3** does not accelerate the decomposition of $O_2^{\bullet-}$ in a buffered aqueous solution, even at a relatively high concentration of 4.5 μM. The removal of the second hydroxyl group completely eliminates catalysis by precluding the Hpp1 species from accessing the lower-energy intermediates available to H_2qp1.

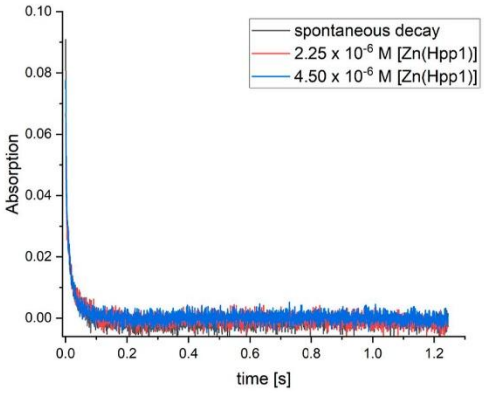

Figure 3. Kinetic traces of superoxide decomposition at 250 nm by **3** in 60 mM MOPS buffer, pH 7.4, and ionic strength of 150 mM. Either 0 (black), 2.25 (red), or 4.45 μM (blue) of **3** is present. The Zn(II) has no noticeable impact on the degradation of superoxide.

■ CONCLUSIONS

Our calculations support the previously proposed inner-sphere dismutation of superoxide by Zn(II) complexes with quinol-containing ligands. The activity relies upon superoxide being able to bind *cis* to the quinol-derived portion of the ligand. Keeping the quinol-derived portion of the ligand *mer* with the two amines appears to lower the free energies of the intermediates in the catalytic cycle. A constraining ligand that enforces such a conformation may further reduce the barrier for zinc-catalyzed superoxide dismutation.

The ability to deprotonate the nonmetal-bound OH group in the quinol-derived portion of the ligand lowers the energies of key intermediates. Specifically, the deprotonation of the OH group in $[O_2Zn(Hqp1)]^{\bullet}$ enables the transfer of one electron from the quinol-derived unit to the coordinated superoxide, which transiently becomes O_2^{2-} before it abstracts a proton from the solution. Substituting a phenol for the quinol removes the second hydroxyl group and is predicted to disrupt the catalysis of superoxide dismutation; we confirmed this experimentally. The second proton transfer to HOO^- is generally easier and can be improved if proper ligand design can place it across from the Zn−O bond of the quinol-derived portion of the ligand. The reduction of the semiquinone anion is facilitated by its initial protonation. Finally, Zn(II) benefits the reactivity by stabilizing $qp1^{2-}$. The inability of this metal to access the +3 oxidation state discourages phosphate coordination, thereby preventing this competing anion from inhibiting the reactivity.

■ ASSOCIATED CONTENT

Supporting Information

The Supporting Information is available free of charge at https://pubs.acs.org/doi/10.1021/acs.jpca.3c07403.

Reaction steps and orbital contours for intermediates of superoxide dismutation catalyzed by [Zn(qp1)] (**fac**/**cis** and **fac**/**trans**) and $[Zn(qp1)]^{\bullet+}$ (**mer**) and MN15/6-31g(d,p) Cartesian coordinates and energies for all discussed intermediates (PDF)

■ AUTHOR INFORMATION

Corresponding Authors

Evangelos Miliordos − *Department of Chemistry and Biochemistry, Auburn University, Auburn, Alabama 36849, United States*; orcid.org/0000-0003-3471-7133; Email: emiliord@auburn.edu

Christian R. Goldsmith − *Department of Chemistry and Biochemistry, Auburn University, Auburn, Alabama 36849, United States*; orcid.org/0000-0001-7293-1267; Email: crgoldsmith@auburn.edu

Authors

Jamonica L. Moore − *Department of Chemistry and Biochemistry, Auburn University, Auburn, Alabama 36849, United States*

https://doi.org/10.1021/acs.jpca.3c07403
J. Phys. Chem. A 2024, 128, 1491−1500

Segun V. Obisesan − *Department of Chemistry and Biochemistry, Auburn University, Auburn, Alabama 36849, United States*
Julian Oppelt − *Department of Chemistry, Ludwig-Maximilians-Universität München, 81377 München, Germany*
Ivana Ivanović-Burmazović − *Department of Chemistry, Ludwig-Maximilians-Universität München, 81377 München, Germany*

Complete contact information is available at: https://pubs.acs.org/10.1021/acs.jpca.3c07403

Notes

The authors declare no competing financial interest.

■ ACKNOWLEDGMENTS

We thank Auburn University (AU) and the National Science Foundation (NSF-CHE-1662875 and NSF-CHE-1954336) for financial support. E.M. is grateful for the financial support from the James E. Land endowment (AU). We also thank Dr. Ralph Puchta for early advice on functional and basis set optimizations.

■ REFERENCES

(1) Abreu, I. A.; Cabelli, D. E. Superoxide Dismutases- A Review of the Metal-Associated Mechanistic Variations. *Biochim. Biophys. Acta* **2010**, *1804*, 263−274.
(2) Sheng, Y.; Abreu, I. A.; Cabelli, D. E.; Maroney, M. J.; Miller, A.-F.; Teixeira, M.; Valentine, J. S. Superoxide Dismutases and Superoxide Reductases. *Chem. Rev.* **2014**, *114* (7), 3854−3918.
(3) Mosley, R. L.; Benner, E. J.; Kadiu, I.; Thomas, M.; Boska, M. D.; Hasan, K.; Laurie, C.; Gendelman, H. E. Neuroinflammation, Oxidative Stress, and the Pathogenesis of Parkinson's Disease. *Clin. Neurosci. Res.* **2006**, *6* (5), 261−281.
(4) Fearon, I. M.; Faux, S. P. Oxidative Stress and Cardiovascular Disease: Novel Tools Give (Free) Radical Insight. *J. Mol. Cell. Cardiol.* **2009**, *47* (3), 372−381.
(5) Roberts, C. K.; Sindhu, K. K. Oxidative Stress and Metabolic Syndrome. *Life Sci.* **2009**, *84* (21−22), 705−712.
(6) Eskici, G.; Axelsen, P. H. Copper and Oxidative Stress in the Pathogenesis of Alzheimer's Disease. *Biochemistry* **2012**, *51* (32), 6289−6311.
(7) AbdulSalam, S. F.; Thowfeik, F. S.; Merino, E. J. Excessive Reactive Oxygen Species and Exotic DNA Lesions as an Exploitable Liability. *Biochemistry* **2016**, *55* (38), 5341−5352.
(8) Ahmed, M. I.; Gladden, J. D.; Litovsky, S. H.; Lloyd, S. G.; Gupta, H.; Inusah, S.; Denney, T., Jr.; Powell, P.; McGiffin, D. C.; Dell'Italia, L. J. Increased Oxidative Stress and Cardiomyocyte Myofibrillar Degeneration in Patients with Chronic Isolated Mitral Regurgitation and Ejection Fraction > 60%. *J. Am. Coll. Cardiol.* **2010**, *55* (7), 671−679.
(9) Kinnula, V. L. Production and Degradation of Oxygen Metabolites During Inflammatory States in the Human Lung. *Curr. Drug Targets: Inflammation Allergy* **2005**, *4* (4), 465−470.
(10) Abouhashem, A. S.; Singh, K.; Azzazy, H. M. E.; Sen, C. K. Is Low Alveolar Type II Cell SOD3 in the Lungs of Elderly Linked to the Observed Severity of COVID-19? *Antioxid. Redox Signaling* **2020**, *33* (2), 59−65.
(11) Laforge, M.; Elbim, C.; Frère, C.; Hémadi, M.; Massaad, C.; Nuss, P.; Benoliel, J.-J.; Becker, C. Tissue Damage from Neutrophil-Induced Oxidative Stress in COVID-19. *Nat. Rev. Immunol.* **2020**, *20* (9), 515−516.
(12) Riley, D. P.; Weiss, R. H. Manganese Macrocyclic Ligand Complexes as Mimics of Superoxide Dismutase. *J. Am. Chem. Soc.* **1994**, *116* (1), 387−388.
(13) Riley, D. P.; Schall, O. F. Structure-Activity Studies and the Design of Synthetic Superoxide Dismutase (SOD) Mimetics as Therapeutics. *Adv. Inorg. Chem.* **2006**, *59*, 233−263.
(14) Riley, D. P.; Lennon, P. J.; Neumann, W. L.; Weiss, R. H. Toward the Rational Design of Superoxide Dismutase Mimics: Mechanistic Studies for the Elucidation of Substituent Effects on the Catalytic Activity of Macrocyclic Manganese(II) Complexes. *J. Am. Chem. Soc.* **1997**, *119* (28), 6522−6528.
(15) Riley, D. P. Functional Mimics of Superoxide Dismutase Enzymes as Therapeutic Agents. *Chem. Rev.* **1999**, *99* (9), 2573−2588.
(16) Senft, L.; Moore, J. L.; Franke, A.; Fisher, K. R.; Scheitler, A.; Zahl, A.; Puchta, R.; Fehn, D.; Ison, S.; Sader, S.; Ivanović-Burmazović, I.; Goldsmith, C. R. Quinol-Containing Ligands Enable High Superoxide Dismutase Activity by Modulating Coordination Number, Charge, Oxidation States and Stability of Manganese Complexes throughout Redox Cycling. *Chem. Sci.* **2021**, *12* (31), 10483−10500.
(17) Kenkel, I.; Franke, A.; Dürr, M.; Zahl, A.; Dücker-Benfer, C.; Langer, J.; Filipović, M. R.; Yu, M.; Puchta, R.; Fiedler, S. R.; Shores, M. P.; Goldsmith, C. R.; Ivanović-Burmazović, I. Switching between Inner- and Outer-Sphere PCET Mechanisms of Small-Molecule Activation: Superoxide Dismutation and Oxygen/Superoxide Reduction Reactivity Deriving from the Same Manganese Complex. *J. Am. Chem. Soc.* **2017**, *139* (4), 1472−1484.
(18) Ching, H. Y. V.; Kenkel, I.; Delsuc, N.; Mathieu, E.; Ivanović-Burmazović, I.; Policar, C. Bioinspired Superoxide-Dismutase Mimics: The Effects of Functionalization with Cationic Polyarginine Peptides. *J. Inorg. Biochem.* **2016**, *160*, 172−179.
(19) Mathieu, E.; Bernard, A.-S.; Delsuc, N.; Quévrain, E.; Gazzah, G.; Lai, B.; Chain, F.; Langella, P.; Bachelet, M.; Masliah, J.; Seksik, P.; Policar, C. A Cell-Penetrant Manganese Superoxide Dismutase (MnSOD) Mimic Is Able To Complement MnSOD and Exerts an Antiinflammatory Effect on Cellular and Animal Models of Inflammatory Bowel Diseases. *Inorg. Chem.* **2017**, *56* (5), 2545−2555.
(20) Vincent, A.; Thauvin, M.; Quévrain, E.; Mathieu, E.; Layani, S.; Seksik, P.; Batinic-Haberle, I.; Vriz, S.; Policar, C.; Delsuc, N. Evaluation of the Compounds Commonly Known as Superoxide Dismutase and Catalase Mimics in Cellular Models. *J. Inorg. Biochem.* **2021**, *219*, 111431.
(21) Mathieu, E.; Bernard, A.-S.; Quévrain, E.; Zoumpoulaki, M.; Iriart, S.; Lung-Soong, C.; Lai, B.; Medjoubi, K.; Henry, L.; Nagarajan, S.; Poyer, F.; Scheitler, A.; Ivanović-Burmazović, I.; Marco, S.; Somogyi, A.; Seksik, P.; Delsuc, N.; Policar, C. Intracellular Location Matters: Rationalization of the Anti-Inflammatory Activity of a Manganese(II) Superoxide Dismutase Mimic Complex. *Chem. Commun.* **2020**, *56* (57), 7885−7888.
(22) Policar, C. Mimicking SOD, Why and How: Bio-Inspired Manganese Complexes as SOD Mimic. In *Redox-Active Therapeutics. Oxidative Stress in Applied Basic Research and Clinical Practice.*; Batinić-Haberle, I., Rebouças, J., Spasojević, I., Eds.; Springer: Cham, 2016.
(23) Batinić-Haberle, I.; Rebouças, J. S.; Spasojević, I. Superoxide Dismutase Mimics: Chemistry, Pharmacology, and Therapeutic Potential. *Antioxid. Redox Signaling* **2010**, *13* (6), 877−918.
(24) Tovmasyan, A.; Carballal, S.; Ghazaryan, R.; Melikyan, L.; Weitner, T.; Maia, C. G. C.; Reboucas, J. S.; Radi, R.; Spasojevic, I.; Benov, L.; Batinic-Haberle, I. Rational Design of Superoxide Dismutase (SOD) Mimics: The Evaluation of the Therapeutic Potential of New Cationic Mn Porphyrins with Linear and Cyclic Substituents. *Inorg. Chem.* **2014**, *53* (21), 11467−11483.
(25) Salvemini, D.; Wang, Z.-Q.; Zweier, J. L.; Samouilov, A.; Macarthur, H.; Misko, T. P.; Currie, M. G.; Cuzzocrea, S.; Sikorski, J. A.; Riley, D. P. A Nonpeptidyl Mimic of Superoxide Dismutase with Therapeutic Activity in Rats. *Science* **1999**, *286* (5438), 304−306.
(26) Aston, K.; Rath, N.; Naik, A.; Slomczynska, U.; Schall, O. F.; Riley, D. P. Computer-Aided Design (CAD) of Mn(II) Complexes: Superoxide Dismutase Mimetics with Catalytic Activity Exceeding the Native Enzyme. *Inorg. Chem.* **2001**, *40* (8), 1779−1789.

(27) Bonetta, R. Potential Therapeutic Applications of MnSODs and SOD-Mimetics. *Chem. - Eur. J.* **2018**, *24* (20), 5032−5041.
(28) Anderson, C. M.; Allen, B. G.; Sun, W.; Lee, C. M.; Agarwala, S.; Venigalla, M.; Greenberg, L.; Adkins, D.; Chen, Y.; Zhen, W.; Mould, D.; Holmlund, J.; Brill, J.; Sonis, S.; Buatti, J. Phase 1b/2a Trial of Superoxide (SO) Dismutase (SOD) Mimetic GC4419 to Reduce Chemoradiation Therapy-Induced Oral Mucositis (OM) in Patients With Oral Cavity or Oropharyngeal Carcinoma (OCC). *Int. J. Radiat. Oncol., Biol., Phys.* **2016**, *94* (4), 869−870.
(29) Batinic-Haberle, I.; Spasojevic, I. 25 Years of Development of Mn Porphyrins — from Mimics of Superoxide Dismutase Enzymes to Thiol Signaling to Clinical Trials: The Story of Our Life in the USA. *J. Porphyrins Phthalocyanines* **2019**, *23* (11n12), 1326−1335.
(30) Batinic-Haberle, I.; Rajic, Z.; Tovmasyan, A.; Reboucas, J. S.; Ye, X.; Leong, K. W.; Dewhirst, M. W.; Vujaskovic, Z.; Benov, L.; Spasojevic, I. Diverse Functions of Cationic Mn(III) N-substituted Pyridylporphyrins, Recognized as SOD Mimics. *Free Radical Biol. Med.* **2011**, *51*, 1035−1053.
(31) Batinić-Haberle, I.; Liochev, S. I.; Spasojević, I.; Fridovich, I. A Potent Superoxide Dismutase Mimic: Manganese *β*-Octabromo-meso-tetrakis-(N-methylpyridinium-4-yl) Porphyrin. *Arch. Biochem. Biophys.* **1997**, *343* (2), 225−233.
(32) DeFreitas-Silva, G.; Rebouças, J. S.; Spasojević, I.; Benov, L.; Idemori, Y. M.; Batinić-Haberle, I. SOD-Like Activity of Mn(II) *β*-Octabromo-meso-tetrakis(N-methylpyridinium-3-yl)porphyrin Equals That of the Enzyme Itself. *Arch. Biochem. Biophys.* **2008**, *477* (1), 105−112.
(33) Zhang, D.; Busch, D. H.; Lennon, P. L.; Weiss, R. H.; Neumann, W. L.; Riley, D. P. Iron(III) Complexes as Superoxide Dismutase Mimics: Synthesis, Characterization, Crystal Structure, and Superoxide Dismutase (SOD) Activity of Iron(III) Complexes Containing Pentaaza Macrocyclic Ligands. *Inorg. Chem.* **1998**, *37* (5), 956−963.
(34) Riley, D. P.; Henke, S. L.; Lennon, P. J.; Weiss, R. H.; Neumann, W. L.; Rivers, W. J., Jr; Aston, K. W.; Sample, K. R.; Rahman, H.; Ling, C.-S.; Shieh, J.-J.; Busch, D. H.; et al. Synthesis, Characterization, and Stability of Manganese(II) C-Substituted 1,4,7,10,13-Pentaazacyclopentadecane Complexes Exhibiting Superoxide Dismutase Activity. *Inorg. Chem.* **1996**, *35* (18), 5213−5231.
(35) Goldstein, S.; Samuni, A.; Hideg, K.; Merenyi, G. Structure-Activity Relationship of Cyclic Nitroxides as SOD Mimics and Scavengers of Nitrogen Dioxide and Carbonate Radicals. *J. Phys. Chem. A* **2006**, *110* (10), 3679−3685.
(36) Ali, S. S.; Hardt, J. I.; Quick, K. L.; Sook Kim-Han, J.; Erlanger, B. F.; Huang, T.-T.; Epstein, C. J.; Dugan, L. L. A Biologically Effective Fullerene (C_{60}) Derivative with Superoxide Dismutase Mimetic Properties. *Free Radical Biol. Med.* **2004**, *37* (8), 1191−1202.
(37) Ward, M. B.; Scheitler, A.; Yu, M.; Senft, L.; Zillmann, A. S.; Gorden, J. D.; Schwartz, D. D.; Ivanović-Burmazović, I.; Goldsmith, C. R. Superoxide Dismutase Activity Enabled by a Redox-Active Ligand rather than Metal. *Nat. Chem.* **2018**, *10* (12), 1207−1212.
(38) Moore, J. L.; Oppelt, J.; Senft, L.; Franke, A.; Scheitler, A.; Dukes, M. W.; Alix, H. B.; Saunders, A. C.; Karbalaei, S.; Schwartz, D. D.; Ivanović-Burmazović, I.; Goldsmith, C. R. Diquinol Functionality Boosts the Superoxide Dismutase Mimicry of a Zn(II) Complex with a Redox-Active Ligand while Maintaining Catalyst Stability and Enhanced Activity in Phosphate Solution. *Inorg. Chem.* **2022**, *61* (49), 19983−19997.
(39) Yu, M.; Ambrose, S. L.; Whaley, Z. L.; Fan, S.; Gorden, J. D.; Beyers, R. J.; Schwartz, D. D.; Goldsmith, C. R. A Mononuclear Manganese(II) Complex Demonstrates a Strategy to Simultaneously Image and Treat Oxidative Stress. *J. Am. Chem. Soc.* **2014**, *136* (37), 12836−12839.
(40) Obisesan, S. V.; Rose, C.; Farnum, B. H.; Goldsmith, C. R. Co(II) Complex with a Covalently Attached Pendent Quinol Selectively Reduces O_2 to H_2O. *J. Am. Chem. Soc.* **2022**, *144* (50), 22826−22830.
(41) Friedel, F. C.; Lieb, D.; Ivanović-Burmazović, I. Comparative Studies on Manganese-Based SOD Mimetics, Including the Phosphate Effect, by Using Global Spectral Analysis. *J. Inorg. Biochem.* **2012**, *109*, 26−32.
(42) Bielski, B. H. J.; Cabelli, D. E.; Arudi, R. L.; Ross, A. B. Reactivity of HO_2/O_2^- Radicals in Aqueous Solution. *J. Phys. Chem. Ref. Data* **1985**, *14* (4), 1041−1100.
(43) Yu, H. S.; He, X.; Li, S. L.; Truhlar, D. G. MN15: A Kohn-Sham Global-Hybrid Exchange-Correlation Density Functional with Broad Accuracy for Multi-Reference and Single-Reference Systems and Noncovalent Interactions. *Chem. Sci.* **2016**, *7* (8), 5032−5051.
(44) Clark, T.; Chandrasekhar, J.; Spitznagel, G. W.; Schleyer, P. V. R. Efficient Diffuse Function-Augmented Basis Sets for Anion Calculations. III. The 3-21+G Basis Set for First-Row Elements, Li-F. *J. Comput. Chem.* **1983**, *4* (3), 294−301.
(45) Ditchfield, R.; Hehre, W. J.; Pople, J. A. Self-Consistent Molecular-Orbital Methods. IX. An Extended Gaussian-Type Basis for Molecular-Orbital Studies of Organic Molecules. *J. Chem. Phys.* **1971**, *54* (2), 724−728.
(46) Hariharan, P. C.; Pople, J. A. The Influence of Polarization Functions on Molecular Orbital Hydrogenation Energies. *Theor. Chim. Acta* **1973**, *28* (3), 213−222.
(47) Hehre, W. J.; Ditchfield, R.; Pople, J. A. Self—Consistent Molecular Orbital Methods. XII. Further Extensions of Gaussian—Type Basis Sets for Use in Molecular Orbital Studies of Organic Molecules. *J. Chem. Phys.* **1972**, *56* (5), 2257−2261.
(48) Rassolov, V. A.; Pople, J. A.; Ratner, M. A.; Windus, T. L. 6-31G* Basis Set for Atoms K Through Zn. *J. Chem. Phys.* **1998**, *109* (4), 1223−1229.
(49) Ervin, K. M.; Anusiewicz, I.; Skurski, P.; Simons, J.; Lineberger, W. C. The Only Stable State of O_2^- Is the $X^2\Pi_g$ Ground State and It (Still!) Has an Adiabatic Electron Detachment Energy of 0.45 eV. *J. Phys. Chem. A* **2003**, *107* (41), 8521−8529.
(50) Khan, S. N.; Miliordos, E. Methane to Methanol Conversion Facilitated by Transition-Metal Methyl and Methoxy Units: The Cases of $FeCH_3^+$ and $FeOCH_3^+$. *J. Phys. Chem. A* **2019**, *123* (26), 5590−5599.
(51) Claveau, E. E.; Heller, E. R.; Richardson, J. O.; Miliordos, E. Methane against Methanol: The Tortoise and the Hare of the Oxidation Race. *J. Phys. Chem. Lett.* **2023**, *14* (39), 8749−8754.
(52) Marenich, A. V.; Cramer, C. J.; Truhlar, D. G. Universal Solvation Model Based on Solute Electron Density and on a Continuum Model of the Solvent Defined by the Bulk Dielectric Constant and Atomic Surface Tensions. *J. Phys. Chem. B* **2009**, *113* (18), 6378−6396.
(53) Frisch, M. J.; T, G. W.; Schlegel, H. B.; Scuseria, G. E.; Robb, M. A.; Cheeseman, J. R.; Scalmani, G.; Barone, V.; Petersson, G. A.; Nakatsuji, H.; et al. *Gaussian 16*; Gaussian, Inc.: Wallingford CT, 2016.
(54) Suresh, S.; Chandra Srivastava, V.; Mani Mishra, I. Adsorption of Hydroquinone in Aqueous Solution by Granulated Activated Carbon. *J. Environ. Eng.* **2011**, *137* (12), 1145−1157.
(55) Lieb, D.; Friedel, F. C.; Yawer, M.; Zahl, A.; Khusniyarov, M. M.; Heinemann, F. W.; Ivanović-Burmazović, I. Dinuclear Seven-Coordinate Mn(II) Complexes: Effect of Manganese(II)-Hydroxo Species on Water Exchange and Superoxide Dismutase Activity. *Inorg. Chem.* **2013**, *52* (1), 222−236.
(56) Ivanović-Burmazović, I. Catalytic Dismutation vs. Reversible Binding of Superoxide. *Adv. Inorg. Chem.* **2008**, *60*, 59−100.
(57) Weekley, C. M.; Kenkel, I.; Lippert, R.; Wei, S.; Lieb, D.; Cranwell, T.; Wedding, J. L.; Zillmann, A. S.; Rohr, R.; Filipovic, M. R.; Ivanović-Burmazović, I.; Harris, H. H. Cellular Fates of Manganese(II) Pentaazamacrocyclic Superoxide Dismutase (SOD) Mimetics: Fluorescently Labeled MnSOD Mimetics, X-ray Absorption Spectroscopy, and X-ray Fluorescence Microscopy Studies. *Inorg. Chem.* **2017**, *56* (11), 6076−6093.
(58) Batinic-Haberle, I.; Tovmasyan, A.; Spasojevic, I. Mn Porphyrin-Based Redox-Active Drugs: Differential Effects as Cancer Therapeutics and Protectors of Normal Tissue Against Oxidative Injury. *Antioxid. Redox Signaling* **2018**, *29* (16), 1691−1724.

https://doi.org/10.1021/acs.jpca.3c07403
J. Phys. Chem. A 2024, 128, 1491−1500

(59) Bordwell, F. G.; Cheng, J. Substituent Effects on the Stabilities of Phenoxyl Radicals and the Acidities of Phenoxyl Radical Cations. *J. Am. Chem. Soc.* **1991**, *113* (5), 1736−1743.

https://doi.org/10.1021/acs.jpca.3c07403
J. Phys. Chem. A 2024, 128, 1491−1500

Computational Analysis of the Superoxide Dismutase Mimicry Exhibited by a Zinc(II) Complex with a Redox-Active Organic Ligand

Prof. Evangelos Miliordos,[a]* Jamonica L. Moore,[a] Segun Obisesan,[a] Julian Oppelt,[b] Prof. Ivana Ivanović-Burmazović,[b] and Prof. Christian R. Goldsmith[a]*

[a]Department of Chemistry and Biochemistry, Auburn University, Auburn, AL 36849, USA

[b]Department of Chemistry, Ludwig-Maximilians-Universität München, 81377 München, Germany

*Corresponding authors: emiliord@auburn.edu, crgoldsmith@auburn.edu

The chemical equations for the degradation of superoxide to hydrogen peroxide (Eq. 1 of the manuscript) facilitated by [Zn(qp1)] considered in this study are:

$$[Zn(qp1)] + O_2^{\bullet -} \rightarrow [O_2Zn(qp1)]^{\bullet -}$$
$$[O_2Zn(qp1)]^{\bullet -} + H_2PO_4^- \rightarrow [HOOZn(qp1)]^{\bullet} + HPO_4^{2-}$$
$$[HOOZn(qp1)]^{\bullet} + H_2PO_4^- \rightarrow [H_2O_2Zn(qp1)]^{\bullet +} + HPO_4^{2-}$$
$$[H_2O_2Zn(qp1)]^{\bullet +} \rightarrow [Zn(qp1)]^{\bullet +} + H_2O_2$$
$$[Zn(qp1)]^{\bullet +} + O_2^{\bullet -} \rightarrow [O_2Zn(qp1)]^{2\bullet}$$
$$[O_2Zn(qp1)]^{2\bullet} \rightarrow [Zn(qp1)] + O_2^{2\bullet}$$

The chemical equations for the degradation of superoxide to hydrogen peroxide (Eq. 1 of the manuscript) facilitated by $[Zn(qp1)]^{\bullet +}$ considered in this study are:

$$[Zn(qp1)]^{\bullet +} + O_2^{\bullet -} \rightarrow [O_2Zn(qp1)]^{2\bullet}$$
$$[O_2Zn(qp1)]^{2\bullet} + H_2PO_4^- \rightarrow [HOOZn(qp1)]^{+} + HPO_4^{2-}$$
$$[HOOZn(qp1)]^{+} + H_2PO_4^- \rightarrow [H_2O_2Zn(qp1)]^{2+} + HPO_4^{2-}$$
$$[H_2O_2Zn(qp1)]^{2+} \rightarrow [Zn(qp1)]^{2+} + H_2O_2$$
$$[Zn(qp1)]^{2+} + O_2^{\bullet -} \rightarrow [O_2Zn(qp1)]^{\bullet +}$$
$$[O_2Zn(qp1)]^{\bullet +} \rightarrow [Zn(qp1)]^{\bullet +} + O_2^{2\bullet}$$

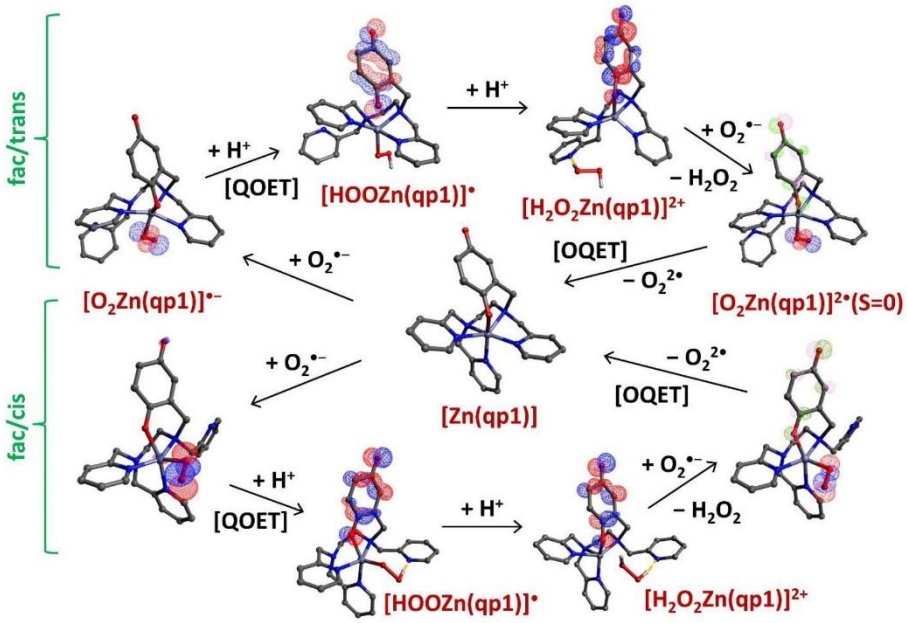

Figure S1. Molecular orbitals hosting the unpaired electrons of all species pertaining to the [Zn(qp1)] (**cis**) syn and anti cycles. The $[O_2Zn(qp1)]^{2\bullet}$ intermediate bears two unpaired electrons (open-shell singlet) and the related orbitals are depicted with different colors (blue/red vs. green/purple). QOET signifies electron transfer from the quinone ring to molecular oxygen and OQET is the electron transfer to the reverse direction.

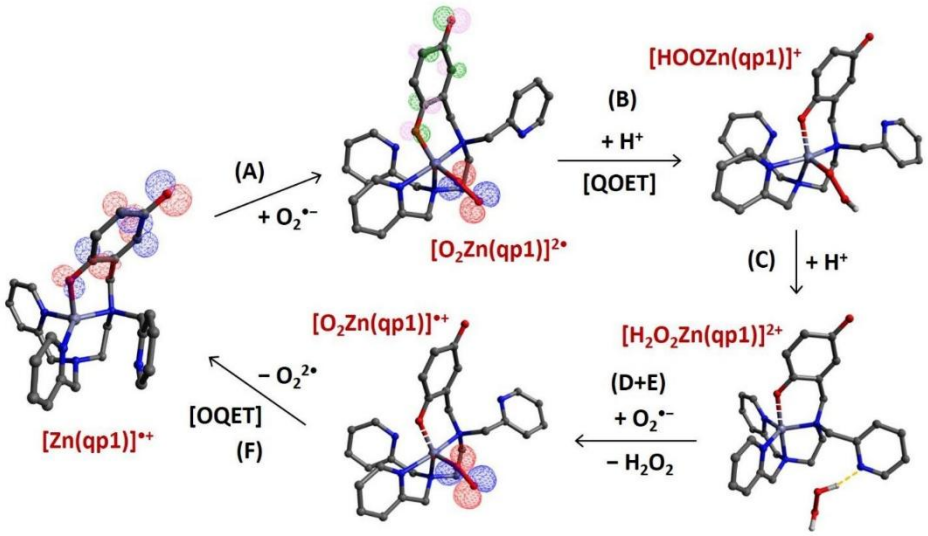

Figure S2. Molecular orbitals hosting the unpaired electrons of all species pertaining to the $[Zn(qp1)]^{\bullet+}$ (**mer**). The $[O_2Zn(qp1)]^{2\bullet}$ intermediate bears two unpaired electrons (open-shell singlet) and the related orbitals are depicted with different colors (blue/red vs. green/purple). QOET signifies electron transfer from the quinone ring to molecular oxygen and OQET is the electron transfer to the reverse direction.

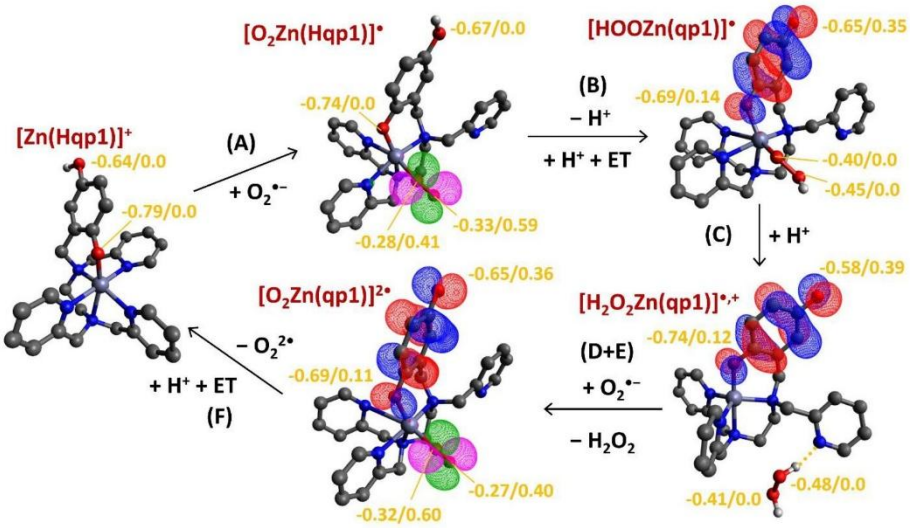

Figure S3. Modified version of Figure 2 of the manuscript to include Mulliken charges and spin densities on every oxygen atom.

Table S1. Cartesian coordinates (in Å) for all IS-E species for cycles facilitated by [Zn(qp1)] (**mer**)/(**fac/cis**)/(**fac/trans**).

	[Zn(qp1)] (**mer**)				[Zn(qp1)] (**fac/cis**)				[Zn(qp1)] (**fac/trans**)			
IS	C	-1.710471	-2.850485	-1.378070	C	1.013453	2.089130	2.293685	C	-1.012433	2.089307	-2.293585
	N	-1.999556	-1.717893	-0.714021	N	0.856912	1.714754	1.013571	N	-0.856229	1.714922	-1.013428
	C	-2.593615	-3.921238	-1.438453	C	2.100380	2.838039	2.727427	C	-2.099025	2.838593	-2.727506
	N	-2.242177	0.368398	1.093683	N	0.153348	1.267105	-1.495768	N	-0.152998	1.267331	1.496015
	C	-3.814878	-3.813779	-0.772390	C	3.069056	3.205498	1.788946	C	-3.067705	3.206420	-1.789169
	N	-0.950432	1.699026	-0.921937	N	-2.172583	1.408817	-0.035917	N	2.172979	1.408299	0.036206
	C	-4.112770	-2.641639	-0.080600	C	2.913736	2.811979	0.463761	C	-2.912706	2.812919	-0.463940
	N	0.649040	2.244722	1.906709	N	-1.950254	-1.464676	0.801405	N	1.950423	-1.465186	-0.801001
	C	-3.178909	-1.608858	-0.079847	C	1.791705	2.056726	0.116646	C	-1.790976	2.057299	-0.116626
	N	0.312055	-0.974065	1.452707	N	-0.189889	-1.535031	-1.299543	N	0.189464	-1.534922	1.299744
	C	-3.453656	-0.276659	0.567556	C	1.579313	1.538791	-1.287806	C	-1.578882	1.539369	1.287878
	C	-2.392392	1.829077	1.049940	C	-0.604648	2.522521	-1.521481	C	0.605300	2.522542	1.521749
	C	-1.835570	2.427828	-0.223531	C	-2.001315	2.342264	-0.988494	C	2.001806	2.342187	0.988347
	C	-2.159936	3.730724	-0.603413	C	-3.045011	3.154354	-1.432166	C	3.045473	3.154755	1.431257
	C	-1.528675	4.288147	-1.710878	C	-4.303245	3.014213	-0.855975	C	4.303545	3.014599	0.854726
	C	-0.592032	3.530921	-2.418725	C	-4.480510	2.059354	0.145108	C	4.480716	2.059213	-0.145884
	C	-0.334289	2.236534	-1.991185	C	-3.394088	1.276518	0.513682	C	3.394352	1.275935	-0.513679
	C	0.785693	3.429374	1.291756	C	-2.433299	-1.677857	2.035447	C	2.433177	-1.678832	-2.035069
	C	1.751639	3.682690	0.320615	C	-3.190778	-2.798419	2.358120	C	3.189413	-2.800223	-2.357828
	C	2.642075	2.658435	-0.005038	C	-3.444865	-3.737082	1.357219	C	3.442512	-3.739207	-1.356984
	C	2.513164	1.424966	0.630128	C	-2.922086	-3.529297	0.082817	C	2.920052	-3.530899	-0.082528
	C	1.480368	1.249714	1.559707	C	-2.175898	-2.376258	-0.156900	C	2.175153	-2.377050	0.157267
	C	1.240551	-0.087188	2.222280	C	-1.544596	-2.073866	-1.492427	C	1.544131	-2.073931	1.492743
	C	-0.866396	-1.344159	2.268104	C	0.320563	-0.954709	-2.552462	C	-0.320884	-0.954470	2.552649
	C	-1.821330	-0.160618	2.408950	C	-0.135170	0.486262	-2.707396	C	0.135172	0.486399	2.707650
	C	1.028819	-2.196457	0.983908	C	0.727613	-2.597470	-0.811756	C	-0.728219	-2.597309	0.812187
	C	2.201546	-1.856082	0.101767	C	2.006741	-2.002089	-0.294562	C	-2.007150	-2.001715	0.294705
	C	3.505659	-2.125358	0.537394	C	3.217386	-2.165540	-0.976697	C	-3.217965	-2.164748	0.976613
	C	4.656509	-1.789336	-0.214589	C	4.423655	-1.559719	-0.548883	C	-4.423999	-1.558740	0.548397
	C	4.405068	-1.142630	-1.450293	C	4.325524	-0.771445	0.624200	C	-4.325430	-0.770788	-0.624876
	C	3.110826	-0.867529	-1.891139	C	3.122684	-0.611017	1.314780	C	-3.122420	-0.610766	-1.315215
	C	1.978791	-1.204026	-1.130511	C	1.930124	-1.209937	0.873771	C	-1.930092	-1.209803	-0.873767
	Zn	-0.588350	-0.218975	-0.298108	Zn	-0.458422	0.037667	0.264676	Zn	0.458396	0.037451	-0.264460
	H	-5.049245	-2.519253	0.454652	H	3.642775	3.074783	-0.297049	H	-3.641742	3.076030	0.296767
	H	-4.221080	-0.379062	1.347331	H	2.150617	0.605453	-1.393902	H	-2.150468	0.606190	1.393936
	H	-3.865680	0.377960	-0.212149	H	1.969690	2.254314	-2.027028	H	-1.969152	2.255040	2.027001
	H	-1.825962	2.269166	1.876786	H	-0.634637	2.945074	-2.535699	H	0.635673	2.944896	2.536042
	H	-3.439076	2.134973	1.177157	H	-0.096345	3.259607	-0.888415	H	0.096968	3.259903	0.889016
	H	-2.888325	4.290686	-0.024347	H	-2.858042	3.879543	-2.218437	H	2.858606	3.880317	2.217210
	H	2.192860	-0.612543	2.354043	H	-1.527152	-2.977037	-2.120846	H	1.526563	-2.976748	2.121660
	H	0.817515	0.089237	3.216343	H	-2.148372	-1.317136	-2.011801	H	2.148082	-1.316998	2.011612
	H	-0.553407	-1.681257	3.266409	H	-0.005399	-1.546315	-3.420432	H	0.004914	-1.546161	3.420624
	H	-1.363751	-2.190402	1.780824	H	1.413523	-1.003250	-2.524360	H	-1.413858	-1.002741	2.524501
	H	-2.691317	-0.459746	3.009037	H	0.335553	0.940355	-3.592147	H	-0.335611	0.940534	3.592352
	H	-1.306898	0.644700	2.942594	H	-1.222012	0.526554	-2.857828	H	1.221991	0.526479	2.858276
	H	0.292826	-2.806391	0.442586	H	0.918492	-3.315669	-1.624968	H	-0.919321	-3.315227	1.625588
	H	1.367647	-2.773314	1.857480	H	0.202923	-3.129078	-0.007146	H	-0.203597	-3.129268	0.007768
	H	3.203537	0.610314	0.426839	H	-3.073232	-4.247519	-0.717281	H	3.070487	-4.249314	0.717529
	H	3.643439	-2.618448	1.501568	H	3.235165	-2.779700	-1.879222	H	-3.236118	-2.778745	1.879245
	O	0.735778	-0.902557	-1.567524	O	0.747536	-1.036646	1.508364	O	-0.747233	-1.036936	-1.508063
	H	2.954574	-0.358077	-2.842146	H	3.086291	0.017497	2.205916	H	-3.085702	0.017479	-2.206526

	H	5.258497	-0.860424	-2.066564	H	5.227471	-0.280604	0.990287	H	-5.227216	-0.279872	-0.991270
	H	-2.322795	-4.817537	-1.985515	H	2.182869	3.127279	3.769649	H	-2.181273	3.127832	-3.769748
	H	-0.738051	-2.880050	-1.861894	H	0.236810	1.770563	2.985530	H	-0.235788	1.770429	-2.985287
	H	-0.075279	3.931468	-3.283812	H	-5.440817	1.911411	0.627009	H	5.440913	1.911210	-0.627987
	H	0.379998	1.595311	-2.502348	H	-3.501650	0.513996	1.277796	H	3.501850	0.512956	-1.277347
	H	-1.762737	5.302456	-2.020394	H	-5.132138	3.634110	-1.184685	H	5.132396	3.634884	1.182809
	H	1.809468	4.657877	-0.152654	H	-3.564783	-2.930316	3.367604	H	3.563255	-2.932485	-3.367325
	H	0.091381	4.212716	1.592533	H	-2.199825	-0.921269	2.782181	H	2.200521	-0.921951	-2.781764
	H	3.429546	2.818331	-0.736586	H	-4.028816	-4.627276	1.571761	H	4.025481	-4.630031	-1.571592
	H	-4.524293	-4.635990	-0.787021	H	3.931606	3.793426	2.089008	H	-3.930009	3.794629	-2.089389
	O	5.891707	-2.063564	0.209001	O	5.573815	-1.717260	-1.208820	O	-5.574352	-1.715845	1.208095
A	C	2.559536	2.213499	1.993166	C	-3.750362	-1.709800	0.931281	C	1.474973	-0.334214	-2.301857
	N	2.034362	0.982548	2.055362	N	-2.760575	-1.258536	0.145416	N	1.149648	-0.099406	-1.022762
	C	3.928288	2.458185	1.891289	C	-5.023072	-1.981455	0.440501	C	2.672694	0.102469	-2.856266
	N	1.651363	-1.764061	0.618635	N	-0.565043	-0.987783	-1.407110	N	0.800415	-0.413047	1.644901
	C	4.794995	1.365904	1.866846	C	-5.270018	-1.778151	-0.917172	C	3.548233	0.831177	-2.046461
	N	2.691808	0.126955	-1.025935	N	0.303174	-3.372762	0.368855	N	4.074401	-1.065994	1.704303
	C	4.256217	0.081448	1.924729	C	-4.241666	-1.311358	-1.733794	C	3.210138	1.069509	-0.716948
	N	-3.845028	-1.882419	1.051732	N	3.955689	1.438107	0.974909	N	-2.766279	-1.349406	-0.577029
	C	2.868953	-0.066408	1.987719	C	-2.998658	-1.054572	-1.161674	C	1.999473	0.570472	-0.233370
	N	-1.099248	-0.983643	0.446529	N	0.879099	0.808966	0.243424	N	-1.964061	0.466556	1.282880
	C	2.219008	-1.428507	1.947068	C	-1.841539	-0.492949	-1.954200	C	1.536190	0.772036	1.191535
	C	2.706796	-2.180477	-0.319285	C	-0.429802	-2.431941	-1.735334	C	1.715829	-1.508968	2.060777
	C	3.437597	-0.979099	-0.876085	C	0.638074	-3.092928	-0.901619	C	2.971252	-1.676833	1.235305
	C	4.787530	-1.009100	-1.217649	C	1.915671	-3.343237	-1.409368	C	2.979204	-2.441089	0.063494
	C	5.380921	0.158625	-1.693377	C	2.897119	-3.842219	-0.552092	C	4.154447	-2.532339	-0.677518
	C	4.613239	1.318496	-1.807528	C	2.564921	-4.082210	0.779559	C	5.291878	-1.870907	-0.213473
	C	3.265658	1.256210	-1.465174	C	1.252775	-3.841466	1.187718	C	5.200133	-1.162429	0.982415
	C	-5.127457	-1.842176	1.448483	C	5.174367	1.866821	0.619734	C	-3.195001	-1.951338	-1.695102
	C	-6.159755	-1.322617	0.672922	C	5.902653	1.334245	-0.442538	C	-4.509092	-2.379753	-1.848169
	C	-5.846971	-0.824192	-0.593366	C	5.333478	0.295566	-1.175321	C	-5.401976	-2.166946	-0.795935
	C	-4.519516	-0.845444	-1.007773	C	4.063649	-0.155601	-0.819359	C	-4.954554	-1.536712	0.363183
	C	-3.544183	-1.369883	-0.150484	C	3.399276	0.445980	0.254703	C	-3.618240	-1.145364	0.435352
	C	-2.093136	-1.351057	-0.586274	C	2.025645	-0.031844	0.674543	C	-3.013167	-0.500596	1.655680
	C	-0.691897	-2.135477	1.283541	C	0.838239	1.051231	-1.206612	C	-1.190785	0.833223	2.485632
	C	0.582352	-2.773351	0.744199	C	0.577795	-0.238874	-1.969949	C	-0.081677	-0.156252	2.789744
	C	-1.499654	0.176968	1.293292	C	0.810714	2.069123	1.031379	C	-2.598845	1.693155	0.715418
	C	-2.056896	1.317530	0.486630	C	-0.319173	2.965684	0.602492	C	-1.571596	2.574313	0.064410
	C	-3.393310	1.693162	0.657714	C	-0.042770	4.248196	0.114461	C	-1.158508	3.776554	0.650121
	C	-4.013552	2.712109	-0.098505	C	-1.047786	5.138257	-0.329609	C	-0.123824	4.573434	0.105386
	C	-3.177226	3.362389	-1.036467	C	-2.370149	4.638924	-0.266143	C	0.474057	4.068333	-1.076199
	C	-1.839180	3.001416	-1.210597	C	-2.655287	3.357892	0.208482	C	0.058400	2.876647	-1.673518
	C	-1.244439	1.969527	-0.465981	C	-1.646720	2.488585	0.659032	C	-0.974484	2.095963	-1.123837
	H	4.890092	-0.800986	1.890616	Zn	-0.889043	-0.354066	0.682954	Zn	-0.804433	-0.502650	-0.281677
	H	1.403351	-1.431557	2.674979	H	-4.389633	-1.145276	-2.796524	H	3.873883	1.611747	-0.049742
	H	2.939224	-2.208058	2.235879	H	-1.854148	0.603794	-1.865498	H	0.861913	1.640502	1.187373
	H	2.229064	-2.710710	-1.153703	H	-1.945104	-0.745347	-3.019426	H	2.388947	1.014353	1.843319
	H	3.419632	-2.871931	0.152488	H	-0.211878	-2.537599	-2.808423	H	1.136813	-2.439071	2.060807
	H	5.357296	-1.923994	-1.085029	H	-1.388914	-2.918287	-1.531879	H	2.049993	-1.311907	3.091546
	H	-1.803433	-2.339318	-0.966488	H	2.133219	-3.127822	-2.452477	H	2.062304	-2.923500	-0.262270
	H	-2.000035	-0.656028	-1.429898	H	1.870077	-1.050749	0.297756	H	-3.789985	-0.012243	2.262407
	H	-1.487846	-2.884424	1.325064	H	1.985567	-0.077492	1.768042	H	-2.555323	-1.286354	2.271482
	H	-0.543265	-1.777117	2.307874	H	1.769602	1.511046	-1.571052	H	-1.860162	0.904650	3.355954
	H	0.892791	-3.611624	1.384671	H	0.030014	1.765148	-1.394142	H	-0.778876	1.833599	2.326684
	H	0.383716	-3.168472	-0.259962	H	0.405673	-0.016372	-3.032648	H	0.489455	0.213806	3.658394
	H	-0.591904	0.477856	1.834598	H	1.456688	-0.886689	-1.920113	H	-0.507440	-1.126959	3.078297

	H	-2.243824	-0.145690	2.032456	H	1.758771	2.615117	0.946156	H	-3.130680	2.220200	1.522795
	H	-4.223342	-0.434969	-1.969797	H	0.696201	1.760255	2.081550	H	-3.340289	1.358052	-0.021104
	H	-4.003729	1.140294	1.376443	H	3.592988	-0.977565	-1.353365	H	-5.620168	-1.346275	1.199602
	O	0.056597	1.630877	-0.651135	H	0.996634	4.578237	0.069862	H	-1.643835	4.109100	1.569930
	H	-1.227951	3.522209	-1.947455	O	-1.946122	1.256853	1.130607	O	-1.379726	0.922895	-1.660584
	H	-3.603701	4.160125	-1.644512	H	-3.686896	3.007281	0.241441	H	0.556996	2.516112	-2.574754
	H	4.298534	3.477035	1.840945	H	-3.181755	5.282421	-0.605678	H	1.283933	4.642710	-1.526198
	H	1.855980	3.042895	2.038266	H	-5.795680	-2.346610	1.108312	H	2.907761	-0.115787	-3.892396
	H	5.043849	2.251623	-2.154259	H	-3.508245	-1.851992	1.980980	H	0.742101	-0.882772	-2.891243
	H	2.618271	2.126613	-1.544951	H	3.295992	-4.458899	1.487484	H	6.231180	-1.908002	-0.756130
	H	6.434437	0.168876	-1.957222	H	0.951263	-4.040964	2.214439	H	6.075168	-0.653026	1.381752
	H	-7.177153	-1.315659	1.050516	H	3.902573	-4.031691	-0.916974	H	4.182634	-3.108729	-1.598133
	H	-5.339731	-2.251403	2.434501	H	6.889592	1.720487	-0.676221	H	-4.822485	-2.862649	-2.767434
	H	-6.620620	-0.414735	-1.237099	H	5.596935	2.670371	1.219828	H	-2.456181	-2.086879	-2.482857
	H	5.869586	1.510893	1.799241	H	5.868085	-0.159820	-2.004069	H	-6.437473	-2.483270	-0.881253
	O	-5.306514	3.018058	0.053857	H	-6.250223	-1.985433	-1.336321	H	4.489159	1.198646	-2.445955
	O	0.535140	-0.997238	-2.523575	O	-0.766473	6.363528	-0.787226	O	0.269067	5.718586	0.670591
	O	0.194928	-2.248489	-2.772412	O	-0.224048	-0.992217	2.503732	O	-0.225963	-2.543882	-0.414628
	Zn	0.606441	-0.241971	-0.597354	O	-1.006704	-1.878277	3.093803	O	-0.749146	-3.253694	0.570194
B	C	2.273087	2.097725	2.124588	C	-1.597791	-0.951904	2.306632	C	-1.136661	-0.044718	2.288893
	N	1.899504	0.812095	2.086300	N	-1.188620	-1.072785	1.030280	N	-0.937100	0.019343	0.962371
	C	3.604626	2.508969	2.083011	C	-2.700854	-1.632169	2.804303	C	-2.310782	0.404931	2.880142
	N	1.686413	-1.826191	0.533109	N	0.046463	-1.605349	-1.320388	N	-0.771547	-0.632039	-1.670642
	C	4.594838	1.529906	2.008141	C	-3.413220	-2.467934	1.941107	C	-3.300700	0.950656	2.059361
	N	2.709074	0.138086	-1.005858	N	2.466467	-1.025699	-0.354922	N	-3.979185	-1.495828	-1.437831
	C	4.212920	0.190155	1.951503	C	-2.987598	-2.597760	0.623444	C	-3.092662	1.011538	0.683370
	N	-3.802341	-1.839699	1.195129	N	1.530149	1.780022	0.618258	N	2.712928	-0.983144	0.632320
	C	2.852324	-0.124120	1.963308	C	-1.863650	-1.882416	0.203287	C	-1.894293	0.523858	0.163391
	N	-1.068068	-0.973642	0.445956	N	0.076780	1.206773	-1.589629	N	1.857636	0.512889	-1.428282
	C	2.365149	-1.547814	1.824375	C	-1.366651	-1.976740	-1.218658	C	-1.582912	0.541534	-1.316052
	C	2.670040	-2.213436	-0.491479	C	0.908842	-2.751567	-1.028541	C	-1.629090	-1.824842	-1.927474
	C	3.444123	-0.985607	-0.920410	C	2.324253	-2.295440	-0.765289	C	-2.804534	-1.971991	-0.986414
	C	4.807606	-0.994644	-1.194581	C	3.412644	-3.159420	-0.890049	C	-2.669679	-2.561003	0.275726
	C	5.426083	0.207657	-1.539854	C	4.681488	-2.686322	-0.570006	C	-3.778109	-2.614538	1.117700
	C	4.667948	1.376665	-1.592132	C	4.828141	-1.364566	-0.142241	C	-4.990143	-2.092757	0.666128
	C	3.304073	1.295593	-1.319325	C	3.692731	-0.570078	-0.048075	C	-5.038403	-1.555145	-0.618266
	C	-5.071016	-1.776703	1.629814	C	1.915550	2.255914	1.815064	C	3.106338	-1.406776	1.842975
	C	-6.126578	-1.291070	0.862624	C	2.670385	3.415611	1.947500	C	4.444436	-1.631223	2.145202
	C	-5.853205	-0.853796	-0.434281	C	3.036208	4.108653	0.792704	C	5.396608	-1.405623	1.148908
	C	-4.539132	-0.899136	-0.889477	C	2.620148	3.627423	-0.445807	C	4.983633	-0.964611	-0.106810
	C	-3.538978	-1.386513	-0.039662	C	1.864124	2.457192	-0.490705	C	3.622280	-0.767051	-0.328074
	C	-2.103479	-1.398115	-0.525601	C	1.379327	1.856542	-1.783215	C	3.046262	-0.330029	-1.651257
	C	-0.618990	-2.090494	1.312621	C	-0.228860	0.367059	-2.760392	C	1.098625	0.666590	-2.685282
	C	0.589352	-2.795173	0.705676	C	0.376028	-1.020977	-2.629459	C	0.072219	-0.439350	-2.865554
	C	-1.463035	0.203005	1.264710	C	-0.970310	2.252771	-1.421538	C	2.309800	1.846351	-0.927458
	C	-2.020470	1.326309	0.435318	C	-2.253298	1.728955	-0.827300	C	1.207835	2.641723	-0.280492
	C	-3.326519	1.720511	0.571867	C	-3.264296	1.241747	-1.623133	C	0.470024	3.559715	-0.990499
	C	-3.898748	2.781698	-0.219298	C	-4.475371	0.668301	-1.094592	C	-0.644389	4.273253	-0.420323
	C	-3.015932	3.457435	-1.141101	C	-4.628600	0.687196	0.338462	C	-0.941334	4.012884	0.967004
	C	-1.707535	3.080470	-1.272297	C	-3.664600	1.226939	1.141746	C	-0.178002	3.151779	1.703936
	C	-1.162872	1.994524	-0.510656	C	-2.432015	1.765656	0.615184	C	0.938122	2.434984	1.132687
	Zn	0.632226	-0.310676	-0.690346	Zn	0.588718	-0.138042	0.300806	Zn	0.695800	-0.751534	-0.004116
	H	4.948955	-0.605028	1.869647	H	-3.499273	-3.249338	-0.078861	H	-3.847758	1.406608	0.010233
	H	1.654206	-1.739519	2.633001	H	-1.966173	-1.290662	-1.828010	H	-1.011659	1.454030	-1.518064
	H	3.202774	-2.248947	1.947911	H	-1.546050	-2.986902	-1.614054	H	-2.509206	0.594226	-1.903185
	H	2.123658	-2.610237	-1.358045	H	0.890433	-3.491589	-1.843004	H	-0.982811	-2.708149	-1.883491

	H	3.355660	-2.993399	-0.132433	H	0.525652	-3.247536	-0.125022	H	-2.042150	-1.739444	-2.942827
	H	5.368666	-1.920802	-1.114850	H	3.253709	-4.178823	-1.228680	H	-1.700614	-2.945189	0.583265
	H	-1.835366	-2.411266	-0.851007	H	1.329021	2.629104	-2.566176	H	3.801041	0.202075	-2.248043
	H	-2.039169	-0.754744	-1.412950	H	2.100542	1.097295	-2.116400	H	2.738744	-1.222023	-2.214583
	H	-1.432040	-2.803853	1.474522	H	0.128406	0.844860	-3.684992	H	1.780877	0.677551	-3.546880
	H	-0.359112	-1.671053	2.291187	H	-1.313084	0.289309	-2.852637	H	0.605684	1.641226	-2.671375
	H	0.891750	-3.644870	1.333719	H	0.019304	-1.663612	-3.448102	H	-0.543844	-0.218794	-3.750540
	H	0.325086	-3.184204	-0.285894	H	1.467159	-0.969371	-2.708862	H	0.574987	-1.399319	-3.045116
	H	-0.554933	0.532388	1.785211	H	-1.166627	2.715535	-2.401707	H	2.746030	2.403571	-1.769648
	H	-2.206451	-0.092194	2.014639	H	-0.561071	3.026620	-0.763640	H	3.101569	1.666236	-0.192582
	H	-4.273915	-0.540104	-1.880583	H	2.863451	4.144664	-1.369004	H	5.694326	-0.771913	-0.904461
	H	-3.983689	1.205914	1.273777	H	-3.170677	1.270477	-2.708294	H	0.705445	3.762407	-2.035165
	O	0.075685	1.634169	-0.666154	O	-1.547703	2.253135	1.402805	O	1.656243	1.656207	1.849251
	H	-1.043008	3.583538	-1.970731	H	-3.786626	1.256717	2.222487	H	-0.391188	2.969647	2.755517
	H	-3.430854	4.269233	-1.733511	H	-5.541835	0.268123	0.755832	H	-1.784351	4.539215	1.409635
	H	3.852043	3.565032	2.116681	H	-2.993682	-1.505216	3.840931	H	-2.442965	0.328279	3.953708
	H	1.472361	2.831271	2.206080	H	-1.009093	-0.289525	2.934653	H	-0.327657	-0.472228	2.877512
	H	5.117389	2.332979	-1.836989	H	5.800180	-0.956640	0.112648	H	-5.881195	-2.107872	1.285654
	H	2.665028	2.175153	-1.352228	H	3.755185	0.460845	0.295055	H	-5.973460	-1.158012	-1.008507
	H	6.491263	0.233814	-1.750222	H	5.546548	-3.337415	-0.654459	H	-3.697342	-3.056705	2.106830
	H	-7.131538	-1.263311	1.271173	H	2.958483	3.764614	2.933135	H	4.730344	-1.970086	3.134920
	H	-5.252465	-2.137620	2.640375	H	1.607533	1.679042	2.681967	H	2.319508	-1.567930	2.577343
	H	-6.646233	-0.474022	-1.072453	H	3.625973	5.018227	0.858058	H	6.451324	-1.566790	1.351330
	H	5.645852	1.804094	1.985432	H	-4.281540	-3.016455	2.294213	H	-4.230782	1.312625	2.487575
	O	-5.135075	3.094371	-0.114447	O	-5.374556	0.170324	-1.866165	O	-1.340029	5.099059	-1.116906
	O	0.391506	-0.831330	-2.580556	O	1.411788	-0.532543	2.189475	O	0.510429	-2.722114	0.320723
	O	0.027224	-2.222040	-2.779925	O	1.424359	-1.980085	2.350945	O	1.488898	-3.359840	-0.549957
	H	-0.933579	-2.177872	-2.919275	H	2.296305	-2.224439	1.994490	H	2.312714	-3.303123	-0.034828
C	C	-3.636117	2.202842	-0.251952	C	3.564748	0.298619	1.159170	C	-0.514978	-1.321072	-2.755734
	N	-2.987721	1.090759	-0.645813	N	2.709139	0.543789	0.150038	N	-0.438990	-1.174012	-1.422067
	C	-4.902366	2.523855	-0.718980	C	4.941036	0.327576	0.984049	C	-1.237576	-2.353410	-3.340515
	N	-1.781336	-1.333460	-0.948696	N	0.909281	1.556834	-1.597421	N	-0.732771	-0.365254	1.151496
	C	-5.518698	1.652158	-1.618902	C	5.442860	0.626645	-0.283909	C	-1.909181	-3.249480	-2.506375
	N	-1.169141	-0.985357	1.690120	N	-0.063599	2.478415	0.794755	C	-3.437815	-0.373663	2.851226
	C	-4.847726	0.501151	-2.022335	C	4.556233	0.885905	-1.325871	C	-1.842478	-3.081527	-1.124196
	N	2.980510	-2.249748	-0.755536	N	-4.045720	-1.129490	0.431337	N	0.218775	2.327700	-0.747315
	C	-3.572819	0.252343	-1.518864	C	3.187399	0.829528	-1.073854	C	-1.088208	-2.026937	-0.615024
	N	0.662488	0.210100	-0.792258	N	-0.967791	-0.373825	-0.640087	N	1.655861	1.081936	1.225575
	C	-2.760096	-0.939736	-1.967617	C	2.159955	1.039092	-2.161272	C	-0.882846	-1.796394	0.860451
	C	-2.367360	-2.267546	0.021343	C	1.000869	2.996434	-1.321971	C	-1.971023	0.408723	0.914710
	C	-1.645985	-2.195034	1.345014	C	0.087857	3.388661	-0.185898	C	-3.240589	-0.187920	1.480398
	C	-1.509532	-3.297462	2.184743	C	-0.529009	4.634736	-0.119137	N	-4.178216	-0.532849	0.579405
	C	-0.851141	-3.136825	3.402464	C	-1.309127	4.941547	0.993883	C	-5.334557	-1.062513	1.009909
	C	-0.340913	-1.883373	3.745934	C	-1.458813	3.995240	2.008630	C	-5.606568	-1.283373	2.355124
	C	-0.520034	-0.830920	2.858009	C	-0.822925	2.769708	1.866743	C	-4.634610	-0.932767	3.292445
	C	4.035752	-2.770504	-1.400129	C	-5.213937	-1.732071	0.167111	C	-0.312127	2.879683	-1.855436
	C	5.070561	-1.991190	-1.908345	C	-5.898018	-1.564508	-1.034348	C	-0.485017	4.249955	-1.982507
	C	5.016914	-0.612748	-1.710845	C	-5.347246	-0.724206	-1.999837	C	-0.080214	5.071343	-0.927168
	C	3.927783	-0.068104	-1.032566	C	-4.134971	-0.091021	-1.729369	C	0.475531	4.498017	0.212296
	C	2.913783	-0.914994	-0.580661	C	-3.503608	-0.327540	-0.506642	C	0.603760	3.111428	0.274584
	C	1.676424	-0.392430	0.114022	C	-2.189631	0.324960	-0.149741	C	1.112943	2.418863	1.517169
	C	0.340637	-0.648686	-1.951802	C	-0.724062	-0.207162	-2.088196	C	1.398993	0.103536	2.299446
	C	-0.518447	-1.829147	-1.526139	C	-0.269553	1.208374	-2.411825	C	-0.099637	-0.138572	2.467201
	C	1.023801	1.567870	-1.274455	C	-1.037022	-1.819777	-0.305310	C	3.098790	1.214325	0.915553
	C	1.395098	2.543648	-0.186309	C	0.302839	-2.449139	-0.052109	C	3.762666	-0.068728	0.495184
	C	2.534219	3.300643	-0.311643	C	0.782174	-3.494500	-0.797046	C	4.810618	-0.585717	1.213551

	C	2.922151	4.300513	0.653670	C	2.006002	-4.178686	-0.443892	C	5.522607	-1.770132	0.796112
	C	2.051046	4.480005	1.790012	C	2.690474	-3.734493	0.750033	C	5.090669	-2.393782	-0.432855
	C	0.911653	3.738397	1.921823	C	2.218451	-2.684553	1.491241	C	4.044251	-1.886803	-1.151579
	C	0.527112	2.757886	0.947837	C	1.033217	-1.990173	1.102595	C	3.330329	-0.723746	-0.714311
	H	-5.295810	-0.203774	-2.715809	Zn	0.645273	0.599317	0.363534	Zn	0.638706	0.346687	-0.494692
	H	-2.224887	-0.657460	-2.882246	H	4.907596	1.128991	-2.323794	H	-2.358045	-3.751596	-0.443120
	H	-3.422910	-1.773406	-2.233928	H	1.954440	0.068849	-2.630774	H	0.050285	-2.294381	1.157919
	H	-2.367529	-3.298796	-0.358521	H	2.558808	1.700485	-2.942426	H	-1.698059	-2.254507	1.437791
	H	-3.413646	-1.975079	0.183461	H	0.786062	3.596527	-2.216010	H	-2.110187	0.513912	-0.167088
	H	-1.903686	-4.260186	1.873842	H	2.032744	3.220050	-1.019014	H	-1.806604	1.416075	1.316404
	H	1.211981	-1.226295	0.649270	H	-0.395623	5.342351	-0.931273	H	1.861422	3.046845	2.018648
	H	1.942270	0.365443	0.859728	H	-2.171149	1.354891	-0.520320	H	0.268511	2.330780	2.209039
	H	1.250061	-0.990781	-2.462147	H	-2.115687	0.361754	0.943384	H	1.838508	0.429996	3.253079
	H	-0.213551	-0.027903	-2.666495	H	-1.615504	-0.469589	-2.673480	H	1.889313	-0.831958	2.003719
	H	-0.705086	-2.497743	-2.377221	H	0.062663	-0.923797	-2.357725	H	-0.255474	-0.992283	3.138248
	H	-0.001657	-2.413627	-0.756788	H	-0.050979	1.299942	-3.484050	H	-0.578281	0.721079	2.944254
	H	0.142407	1.944181	-1.812464	H	-1.062901	1.929558	-2.182545	H	3.622930	1.623065	1.791740
	H	1.845719	1.510692	-2.003054	H	-1.575624	-2.362038	-1.094279	H	3.178244	1.950353	0.102867
	H	3.867003	0.997717	-0.835631	H	-1.622092	-1.913164	0.614183	H	0.807096	5.103965	1.049857
	H	3.186404	3.164620	-1.173333	H	-3.683066	0.592352	-2.443541	H	5.142262	-0.096381	2.127756
	O	-0.589346	2.115303	1.109137	H	0.232792	-3.852948	-1.665637	O	2.324930	-0.275510	-1.404934
	H	0.247395	3.871816	2.772312	O	0.618194	-0.927009	1.749876	H	3.712069	-2.357387	-2.073887
	H	2.331601	5.222681	2.532555	H	2.737806	-2.341097	2.382505	H	5.623210	-3.282802	-0.761530
	H	-5.394526	3.427420	-0.376876	H	3.599022	-4.260934	1.030956	H	-1.275781	-2.447062	-4.420154
	H	-3.114121	2.834853	0.461116	H	5.599271	0.127241	1.822023	H	0.025596	-0.591847	-3.354369
	H	0.188487	-1.722759	4.678499	H	3.116874	0.079757	2.124923	H	-0.915686	4.662006	-2.888128
	H	-0.137117	0.165162	3.067558	H	-2.061656	4.195247	2.887313	H	-0.587181	2.191689	-2.650840
	H	-0.727326	-3.982626	4.072199	H	-0.915834	1.988553	2.617406	H	-0.191702	6.149255	-0.996503
	H	5.899372	-2.458322	-2.429420	H	-1.801248	5.906766	1.065864	H	-2.485722	-4.066502	-2.929869
	H	4.048517	-3.852440	-1.507073	H	-6.841464	-2.074351	-1.198382	O	6.492266	-2.241734	1.482455
	H	5.814408	0.029985	-2.071929	H	-5.616894	-2.368571	0.951092	O	-3.747298	-0.376349	-2.120804
	H	-6.514540	1.864818	-1.996140	H	-5.856650	-0.556172	-2.944140	O	-3.097167	0.879638	-2.320253
	O	3.989745	4.987082	0.506299	H	6.514262	0.663994	-0.456706	H	-3.822706	1.459865	-2.611867
	O	1.505186	-3.925058	0.828036	O	2.453861	-5.143316	-1.147452	H	-3.898190	-0.402758	-1.121981
	O	0.669437	-4.690606	-0.041913	O	-1.795974	-0.739626	3.122773	H	-2.668494	-0.075530	3.557069
	Zn	-1.211869	0.450608	0.212281	O	-2.645588	-1.834470	2.773995	H	-4.809572	-1.086340	4.353258
	H	1.149518	-5.534057	-0.118924	H	-3.155329	-1.504124	1.976169	H	-6.554414	-1.716661	2.656055
	H	1.999365	-3.317866	0.191882	H	-0.969062	-0.899909	2.598992	H	-6.061397	-1.318511	0.243052
D	C	-1.355039	-2.599164	-1.618125	C	-0.942808	-1.076371	2.561648	C	-0.942632	-1.077466	2.561869
	N	-1.733084	-1.674900	-0.716797	N	-0.728462	-1.178103	1.237099	N	-0.728574	-1.178664	1.237235
	C	-2.081758	-3.760644	-1.847922	C	-1.961562	-1.771488	3.198106	C	-1.961340	-1.772783	3.198185
	N	-2.118706	-0.030532	1.472231	N	0.134021	-1.629670	-1.270043	N	0.133610	-1.629076	-1.270148
	C	-3.242300	-3.976201	-1.103934	C	-2.783967	-2.598837	2.429379	C	-2.783922	-2.599755	2.429236
	N	-1.874714	1.606030	-0.647372	N	2.468213	-1.183355	0.058527	N	2.468260	-1.183084	0.057954
	C	-3.634156	-3.022929	-0.168009	C	-2.560416	-2.702477	1.059290	C	-2.560592	-2.702882	1.059073
	N	0.928003	1.527348	0.518000	N	1.561043	1.693307	0.647898	N	1.560845	1.692810	0.648695
	C	-2.855898	-1.877918	-0.007078	C	-1.524228	-1.964464	0.489609	C	-1.524453	-1.964674	0.489551
	N	0.554320	-1.051455	1.403046	N	0.054304	1.196456	-1.544611	N	0.054197	1.197043	-1.544092
	C	-3.267225	-0.772563	0.932549	C	-1.269999	-1.959605	-1.001766	C	-1.270379	-1.959186	-1.001848
	C	-2.467513	1.379180	1.688605	C	0.998080	-2.787739	-1.014276	C	0.997711	-2.787216	-1.014627
	C	-2.628863	2.079101	0.358485	C	2.378635	-2.364140	-0.578546	C	2.378442	-2.363718	-0.579381
	C	-3.481224	3.166864	0.181415	C	3.488826	-3.183264	-0.770001	C	3.488561	-3.182773	-0.771532
	C	-3.535595	3.781182	-1.067847	C	4.721707	-2.770543	-0.272705	C	4.721674	-2.770062	-0.274803
	C	-2.747106	3.288334	-2.108805	C	4.813080	-1.545216	0.389136	C	4.813324	-1.544822	0.387159
	C	-1.930476	2.193533	-1.855045	C	3.663223	-0.779367	0.526178	C	3.663483	-0.779070	0.524992
	C	1.235164	2.594530	-0.240620	C	1.935857	2.096716	1.873056	C	1.935862	2.095815	1.873929

	C	2.475180	3.218317	-0.188573	C	2.595766	3.301831	2.078670	C	2.596557	3.300449	2.079764
	C	3.440658	2.706851	0.682134	C	2.867746	4.108159	0.971909	C	2.869187	4.106756	0.973139
	C	3.128300	1.599649	1.464818	C	2.463064	3.692699	-0.295245	C	2.464312	3.691740	-0.294090
	C	1.856654	1.035445	1.353327	C	1.808478	2.470338	-0.419900	C	1.808898	2.469831	-0.418971
	C	1.428902	-0.152622	2.177413	C	1.330443	1.914067	-1.739580	C	1.330625	1.914133	-1.738842
	C	-0.460848	-1.687720	2.264440	C	-0.239397	0.340636	-2.715750	C	-0.239864	0.341537	-2.715386
	C	-1.536059	-0.680382	2.660051	C	0.400261	-1.037371	-2.590968	C	0.399628	-1.036605	-2.591032
	C	1.364040	-2.083098	0.709053	C	-1.031834	2.198219	-1.342345	C	-1.031579	2.199097	-1.341528
	C	2.444730	-1.459313	-0.133340	C	-2.270604	1.599610	-0.737059	C	-2.270491	1.600399	-0.736672
	C	3.769054	-1.627903	0.181519	C	-3.319775	1.184642	-1.522100	C	-3.319873	1.186538	-1.522006
	C	4.824201	-0.980983	-0.560535	C	-4.490336	0.542502	-0.980282	C	-4.490578	0.544193	-0.980722
	C	4.427238	-0.141600	-1.667460	C	-4.532412	0.375879	0.451900	C	-4.532398	0.375867	0.451279
	C	3.110036	0.018745	-1.996744	C	-3.521165	0.832395	1.250240	C	-3.520881	0.831186	1.249944
	C	2.068326	-0.624405	-1.250521	C	-2.348775	1.478021	0.709197	C	-2.348429	1.477229	0.709452
	Zn	-0.552902	0.030777	-0.119519	Zn	0.637069	-0.089715	0.137151	Zn	0.636599	-0.089935	0.137349
	H	-4.526622	-3.153393	0.436364	H	-3.176640	-3.335259	0.428042	H	-3.176918	-3.335426	0.427687
	H	-3.894559	-1.173364	1.740255	H	-1.916852	-1.191961	-1.443594	H	-1.917327	-1.191392	-1.443279
	H	-3.893643	-0.074760	0.361098	H	-1.556813	-2.922748	-1.444564	H	-1.557181	-2.922191	-1.444971
	H	-1.642153	1.853748	2.235047	H	1.054953	-3.446626	-1.891149	H	1.054172	-3.446130	-1.891508
	H	-3.378790	1.499102	2.290902	H	0.553240	-3.374412	-0.199344	H	0.553078	-3.373804	-0.199526
	H	-4.087295	3.515456	1.011963	H	3.374103	-4.125611	-1.296712	H	3.373608	-4.125029	-1.298356
	H	2.306970	-0.691735	2.559490	H	1.227881	2.715608	-2.484138	H	1.228459	2.715957	-2.483155
	H	0.876863	0.221366	3.046595	H	2.074299	1.197343	-2.115190	H	2.074188	1.197206	-2.114648
	H	0.002747	-2.112044	3.166456	H	0.102334	0.824764	-3.640616	H	0.101782	0.825825	-3.640197
	H	-0.901864	-2.518433	1.702180	H	-1.323976	0.238817	-2.796078	H	-1.324486	0.239877	-2.795473
	H	-2.309909	-1.183720	3.254139	H	0.041444	-1.687519	-3.400898	H	0.040434	-1.686522	-3.400979
	H	-1.104447	0.099849	3.294697	H	1.491383	-0.961466	-2.685829	H	1.490731	-0.960894	-2.686160
	H	0.680306	-2.674725	0.087390	H	-1.259753	2.664621	-2.311970	H	-1.259218	2.666004	-2.310971
	H	1.821989	-2.753353	1.451384	H	-0.638241	2.974543	-0.677166	H	-0.637783	2.974989	-0.675936
	H	3.853925	1.156162	2.140792	H	2.641761	4.299454	-1.177353	H	2.643496	4.298458	-1.176126
	H	4.055885	-2.246809	1.030365	H	-3.283908	1.325643	-2.602250	H	-3.284028	1.328619	-2.602014
	O	0.823741	-0.437875	-1.562798	O	-1.430019	1.932308	1.475515	O	-1.429559	1.930580	1.476157
	H	2.807126	0.653762	-2.826221	H	-3.567444	0.724196	2.332045	H	-3.566970	0.721765	2.331637
	H	5.214601	0.358100	-2.226426	H	-5.408076	-0.110940	0.875946	H	-5.408134	-0.111169	0.874931
	H	-1.737808	-4.478429	-2.584462	H	-2.104687	-1.665760	4.267762	H	-2.104360	-1.667465	4.267897
	H	-0.435489	-2.388316	-2.157075	H	-0.272670	-0.417399	3.107483	H	-0.272291	-0.418834	3.107851
	H	-2.765974	3.736026	-3.096293	H	5.754607	-1.184392	0.787915	H	5.755061	-1.183958	0.785406
	H	-1.296512	1.765535	-2.628510	H	3.687411	0.183382	1.028851	H	3.687875	0.183587	1.027833
	H	-4.191491	4.631203	-1.230586	H	5.601481	-3.393442	-0.403674	H	5.601421	-3.392880	-0.406342
	H	2.680397	4.074664	-0.821659	H	2.885138	3.598673	3.080624	H	2.886055	3.596945	3.081786
	H	0.459149	2.948822	-0.915353	H	1.696103	1.429529	2.697593	H	1.695657	1.428653	2.698355
	H	4.426122	3.159480	0.740761	H	3.380858	5.056891	1.097326	H	3.382971	5.055099	1.098747
	H	-3.830363	-4.877862	-1.247393	H	-3.589383	-3.158439	2.895489	H	-3.589251	-3.159551	2.895263
	O	6.053337	-1.135976	-0.245901	O	-5.446454	0.139507	-1.737008	O	-5.447000	0.142492	-1.737722
E	C	2.364081	2.186669	2.027026	C	-4.038110	0.248743	0.876656	C	-1.179935	0.026125	2.293958
	N	1.924547	0.921718	2.058580	N	-2.992325	0.150057	0.040258	N	-0.959066	0.040771	0.968800
	C	3.714270	2.525772	1.951372	C	-5.275743	0.733017	0.468362	C	-2.367594	0.487978	2.846593
	N	1.670660	-1.806356	0.597011	N	-1.032005	-0.636138	-1.601695	N	-0.720074	-0.681840	-1.650680
	C	4.652885	1.494882	1.917677	C	-5.428472	1.127152	-0.861095	C	-3.348328	0.991495	1.988796
	N	2.682291	0.104391	-1.032155	N	-1.034111	-2.397644	0.502940	N	-3.916898	-1.607910	-1.403691
	C	4.202436	0.175504	1.938767	C	-4.344552	1.023110	-1.730109	C	-3.117580	1.001364	0.615138
	N	-3.825313	-1.871415	1.090316	N	4.236426	-0.877827	1.004454	N	2.672194	-0.973350	0.697220
	C	2.827957	-0.067726	1.979515	C	-3.135303	0.535697	-1.239349	C	-1.906303	0.506232	0.134992
	N	-1.082345	-0.994538	0.442070	N	1.183332	0.070264	0.056753	N	1.881305	0.514601	-1.389489
	C	2.270530	-1.470838	1.913005	C	-1.899863	0.432444	-2.103982	C	-1.562271	0.485779	-1.336600
	C	2.708894	-2.213350	-0.365637	C	-1.647009	-1.954804	-1.796475	C	-1.564587	-1.883041	-1.916912

	C	3.441723	-0.994560	-0.882067	C	-1.178720	-2.913246	-0.732043	C	-2.724921	-2.048437	-0.962979
	C	4.801275	-0.993759	-1.179715	C	-0.924435	-4.254545	-1.010289	C	-2.554721	-2.609916	0.306804
	C	5.388961	0.194959	-1.610752	C	-0.515956	-5.091984	0.025662	C	-3.645377	-2.666603	1.171516
	C	4.605841	1.343872	-1.724761	C	-0.369498	-4.560194	1.306055	C	-4.876147	-2.180363	0.730611
	C	3.248935	1.252882	-1.427390	C	-0.632633	-3.208309	1.497290	C	-4.960303	-1.674272	-0.564709
	C	-5.104033	-1.822354	1.496682	C	5.543419	-0.912853	0.708124	C	3.028124	-1.417461	1.912623
	C	-6.142355	-1.317933	0.718348	C	6.045173	-1.309245	-0.529930	C	4.348376	-1.708221	2.231751
	C	-5.839758	-0.844721	-0.559436	C	5.140170	-1.698990	-1.514976	C	5.323495	-1.529416	1.247879
	C	-4.515640	-0.876773	-0.985450	C	3.779043	-1.669071	-1.219196	C	4.949274	-1.063738	-0.010394
	C	-3.535066	-1.386550	-0.126016	C	3.363658	-1.240620	0.046576	C	3.602244	-0.797305	-0.250245
	C	-2.088449	-1.380121	-0.575850	C	1.890328	-1.197250	0.390621	C	3.075494	-0.327342	-1.583101
	C	-0.664860	-2.134716	1.295191	C	1.197745	0.386026	-1.383396	C	1.139272	0.644960	-2.658754
	C	0.589297	-2.799969	0.739459	C	0.329269	-0.589956	-2.163732	C	0.131850	-0.479523	-2.841687
	C	-1.484466	0.169418	1.276874	C	1.749706	1.167483	0.884366	C	2.322174	1.853464	-0.896603
	C	-2.044251	1.303711	0.463579	C	1.271949	2.548730	0.524356	C	1.204907	2.655299	-0.287152
	C	-3.348281	1.697797	0.620284	C	2.175262	3.546287	0.258628	C	0.481276	3.560166	-1.027475
	C	-3.929218	2.769181	-0.150564	C	1.773247	4.900759	-0.031895	C	-0.645199	4.281465	-0.491616
	C	-3.056755	3.455623	-1.074399	C	0.356120	5.172318	-0.041131	C	-0.971168	4.039827	0.892978
	C	-1.752310	3.074774	-1.229713	C	-0.552562	4.183757	0.214002	C	-0.223213	3.190730	1.658918
	C	-1.201603	1.975835	-0.492047	C	-0.140910	2.838916	0.505932	C	0.905337	2.466653	1.122150
	H	4.895673	-0.660335	1.895412	Zn	-0.932447	-0.201918	0.575681	Zn	0.692809	-0.697716	0.030623
	H	1.491251	-1.558393	2.674684	H	-4.424143	1.310544	-2.774135	H	-3.863067	1.365521	-0.085416
	H	3.054436	-2.205364	2.146455	H	-1.351029	1.382909	-2.050453	H	-1.004738	1.404363	-1.550678
	H	2.213727	-2.708840	-1.211295	H	-2.182621	0.271183	-3.154407	H	-2.475056	0.503241	-1.946138
	H	3.419033	-2.926071	0.075795	H	-1.433939	-2.353443	-2.797429	H	-0.909110	-2.758727	-1.892005
	H	5.382748	-1.901219	-1.047912	H	-2.736044	-1.851904	-1.715664	H	-1.987920	-1.786158	-2.926760
	H	-1.803314	-2.374635	-0.941797	H	-1.040398	-4.621712	-2.025463	H	-1.575039	-2.972445	0.605765
	H	-2.000315	-0.700808	-1.433322	H	1.388552	-2.021478	-0.124666	H	3.853268	0.216944	-2.137733
	H	-1.470771	-2.869334	1.374779	H	1.766345	-1.353736	1.469653	H	2.791278	-1.204322	-2.179276
	H	-0.482669	-1.751586	2.305040	H	2.218431	0.398614	-1.790973	H	1.833215	0.654379	-3.510866
	H	0.891254	-3.639262	1.381586	H	0.794980	1.397523	-1.504605	H	0.633255	1.612873	-2.662956
	H	0.371843	-3.197611	-0.260116	H	0.307230	-0.304885	-3.224724	H	-0.485204	-0.269158	-3.728086
	H	-0.580226	0.492793	1.808823	H	0.743047	-1.604056	-2.112505	H	0.648666	-1.431966	-3.016918
	H	-2.230961	-0.140736	2.017428	H	2.844476	1.164048	0.812030	H	2.779245	2.398511	-1.735725
	H	-4.227762	-0.490634	-1.959897	H	1.487986	0.938984	1.927386	H	3.095857	1.680591	-0.140816
	H	-3.998340	1.173539	1.321659	H	3.038194	-1.980607	-1.951797	H	5.679116	-0.903703	-0.797918
	O	0.030608	1.606804	-0.684704	H	3.243097	3.333162	0.265772	H	0.739988	3.747773	-2.069435
	H	-1.096406	3.582830	-1.932600	O	-1.020759	1.924186	0.739242	O	1.608337	1.696865	1.862980
	H	-3.476834	4.276752	-1.649966	H	-1.621731	4.383173	0.204655	H	-0.458080	3.025021	2.708585
	H	4.015414	3.568040	1.928053	H	0.038128	6.188399	-0.262291	H	-1.822985	4.572625	1.310316
	H	1.604024	2.964463	2.078665	H	-6.095534	0.793803	1.175876	H	-2.517005	0.453477	3.920012
	H	5.031524	2.291607	-2.036035	H	-3.866404	-0.070234	1.901466	H	-0.377272	-0.368134	2.912523
	H	2.590293	2.114557	-1.507542	H	-0.046090	-5.171863	2.141274	H	-5.754780	-2.198768	1.367519
	H	6.450223	0.228970	-1.838992	H	-0.508222	-2.748883	2.472926	H	-5.910929	-1.306742	-0.946168
	H	-7.156662	-1.302860	1.103746	H	-0.305758	-6.140104	-0.165835	H	-3.537593	-3.084246	2.168584
	H	-5.308264	-2.210513	2.492682	H	7.115672	-1.317276	-0.708153	H	4.603742	-2.062869	3.224274
	H	-6.618413	-0.448311	-1.205141	H	6.225880	-0.614369	1.501331	H	2.226105	-1.539690	2.637531
	H	5.716057	1.713337	1.870406	H	5.485999	-2.026220	-2.491330	H	6.365960	-1.744887	1.462665
	O	-5.163528	3.080854	-0.026751	H	-6.381914	1.505161	-1.218010	H	-4.288216	1.362189	2.386958
	O	0.514676	-0.987670	-2.552817	O	2.635822	5.816657	-0.273526	O	-1.325149	5.097770	-1.213440
	O	0.175112	-2.240759	-2.792000	O	-0.680239	-0.289010	2.626022	O	0.688575	-2.819190	0.132218
	Zn	0.620645	-0.312528	-0.627169	O	-1.740817	-0.758134	3.260322	O	1.408953	-3.264885	-0.883076

Table S2. Cartesian coordinates (in Å) for all IS-E species for cycles facilitated by $[Zn(Hqp1)]^{+}$ (**mer**) and $[Zn(qp1)]^{\bullet+}$ (**mer**).

	$[Zn(Hqp1)]^{+}$ (**mer**)			$[Zn(qp1)]^{\bullet+}$ (**mer**)		
IS	C	-1.517991	-2.614943	-1.601717	C	-1.355259	-2.599421	-1.618184
	N	-1.846217	-1.659609	-0.714503	N	-1.733198	-1.674835	-0.717151
	C	-2.294322	-3.750138	-1.801273	C	-2.081920	-3.761073	-1.847386
	N	-2.119741	0.003579	1.469583	N	-2.118351	-0.030395	1.472057
	C	-3.453807	-3.903571	-1.040768	C	-3.242280	-3.976459	-1.103068
	N	-1.853170	1.607382	-0.666279	N	-1.874527	1.606255	-0.647394
	C	-3.795269	-2.916833	-0.119326	C	-3.634046	-3.022851	-0.167425
	N	0.890236	1.519051	0.552020	N	0.927772	1.527221	0.518000
	C	-2.968019	-1.802933	0.011502	C	-2.855878	-1.877697	-0.007105
	N	0.513444	-1.093457	1.364579	N	0.554344	-1.051746	1.402668
	C	-3.314053	-0.664657	0.938489	C	-3.267078	-0.772006	0.932182
	C	-2.370422	1.430045	1.695854	C	-2.466722	1.379396	1.688700
	C	-2.507520	2.150343	0.373280	C	-2.628382	2.079430	0.358655
	C	-3.243330	3.326230	0.238584	C	-3.480724	3.167227	0.181750
	C	-3.285122	3.953805	-1.004159	C	-3.535403	3.781456	-1.067560
	C	-2.602924	3.385868	-2.081721	C	-2.747233	3.288494	-2.108713
	C	-1.898745	2.207551	-1.867997	C	-1.930577	2.193661	-1.855095
	C	1.198999	2.604544	-0.178566	C	1.234808	2.594575	-0.240452
	C	2.451319	3.205259	-0.140528	C	2.474724	3.218577	-0.188227
	C	3.428937	2.652710	0.691090	C	3.440243	2.707131	0.682452
	C	3.116220	1.527124	1.446182	C	3.128040	1.599722	1.464925
	C	1.834000	0.983633	1.342788	C	1.856491	1.035324	1.353267
	C	1.406731	-0.219431	2.143847	C	1.428866	-0.152924	2.177150
	C	-0.508196	-1.719640	2.221516	C	-0.460838	-1.688034	2.264065
	C	-1.558518	-0.693276	2.640006	C	-1.536072	-0.680737	2.659797
	C	1.304657	-2.121258	0.641088	C	1.364127	-2.083431	0.708809
	C	2.382856	-1.485333	-0.195143	C	2.444802	-1.459510	-0.133541
	C	3.727861	-1.667019	0.142719	C	3.769103	-1.627894	0.181414
	C	4.733699	-1.014691	-0.565309	C	4.824313	-0.980725	-0.560413
	C	4.397051	-0.167070	-1.621299	C	4.427214	-0.141275	-1.667304
	C	3.059765	0.013883	-1.965473	C	3.110051	0.018881	-1.996701
	C	2.019981	-0.636237	-1.270931	C	2.068353	-0.624558	-1.250682
	Zn	-0.568324	-0.005783	-0.169623	Zn	-0.553066	0.030620	-0.119724
	H	-4.685157	-2.998934	0.497378	H	-4.526368	-3.153184	0.437192
	H	-3.965941	-1.018666	1.748995	H	-3.894836	-1.172367	1.739773
	H	-3.894448	0.066033	0.359961	H	-3.893019	-0.074053	0.360389
	H	-1.506055	1.845036	2.230326	H	-1.641003	1.853661	2.234873
	H	-3.261866	1.610320	2.313455	H	-3.377741	1.499480	2.291349
	H	-3.770201	3.731336	1.097168	H	-4.086534	3.515928	1.012445
	H	2.285461	-0.774711	2.501202	H	2.306976	-0.691998	2.559183
	H	0.871577	0.139774	3.029970	H	0.876793	0.220928	3.046368
	H	-0.050534	-2.168678	3.115165	H	0.002766	-2.112427	3.166051
	H	-0.971822	-2.531374	1.649733	H	-0.901866	-2.518722	1.701775
	H	-2.347862	-1.191378	3.218262	H	-2.310137	-1.184308	3.253405
	H	-1.109160	0.056518	3.298553	H	-1.104674	0.099201	3.294947
	H	0.601958	-2.689418	0.017622	H	0.680439	-2.675099	0.087104
	H	1.755014	-2.814725	1.367801	H	1.822078	-2.753629	1.451181
	H	3.849260	1.052178	2.092176	H	3.853696	1.156268	2.140896
	O	0.741341	-0.448487	-1.611279	H	4.055908	-2.246805	1.030291
	H	2.791984	0.679660	-2.783651	O	0.823755	-0.438438	-1.563146

	H	5.185908	0.345825	-2.166251	H	2.807173	0.653977	-2.826134
	H	-1.989041	-4.495533	-2.527388	H	5.214544	0.358660	-2.226139
	H	-0.597961	-2.450771	-2.155881	H	-1.738047	-4.479106	-2.583721
	H	-2.617073	3.841262	-3.065798	H	-0.435855	-2.388721	-2.157445
	H	-1.346778	1.721804	-2.669684	H	-2.766367	3.736113	-3.096231
	H	-3.849611	4.872408	-1.134001	H	-1.296811	1.765582	-2.628685
	H	2.654888	4.078381	-0.751060	H	-4.191303	4.631499	-1.230177
	H	0.412810	2.998235	-0.819619	H	2.679842	4.075068	-0.821152
	H	4.422387	3.088973	0.740693	H	0.458801	2.948843	-0.915201
	H	-4.080144	-4.782777	-1.159718	H	4.425623	3.159931	0.741217
	O	6.077277	-1.172804	-0.252923	H	-3.830272	-4.878249	-1.246034
	H	6.170063	-1.775628	0.501746	O	6.053443	-1.135591	-0.245718
	H	3.988227	-2.313743	0.980968				
A	C	2.513012	2.216452	2.001543	C	2.361858	2.188341	2.025115
	N	2.019751	0.972110	2.057125	N	1.923043	0.923179	2.058212
	C	3.875160	2.496700	1.902900	C	3.711822	2.528122	1.948516
	N	1.690019	-1.773075	0.613491	N	1.671118	-1.806130	0.598647
	C	4.769432	1.426956	1.873757	C	4.651004	1.497726	1.915589
	N	2.706578	0.132535	-1.025511	N	2.682503	0.103990	-1.031487
	C	4.263670	0.128751	1.923498	C	4.201308	0.178114	1.938320
	N	-3.804791	-1.906952	1.070600	N	-3.824778	-1.870639	1.090349
	C	2.880629	-0.055038	1.984320	C	2.826982	-0.065846	1.979854
	N	-1.068013	-1.012201	0.444328	N	-1.081898	-0.994625	0.441968
	C	2.265089	-1.433356	1.938186	C	2.270302	-1.469307	1.914592
	C	2.742747	-2.178090	-0.332945	C	2.709795	-2.213305	-0.363382
	C	3.464426	-0.966280	-0.878999	C	3.442294	-0.994560	-0.880408
	C	4.816271	-0.978025	-1.212847	C	4.801940	-0.993411	-1.177603
	C	5.398351	0.199972	-1.677680	C	5.389266	0.195236	-1.609353
	C	4.617789	1.351381	-1.788683	C	4.605715	1.343739	-1.724475
	C	3.269133	1.271443	-1.454004	C	3.248761	1.252423	-1.427395
	C	-5.086964	-1.873166	1.467637	C	-5.103447	-1.821330	1.496850
	C	-6.126246	-1.384898	0.680504	C	-6.141797	-1.316990	0.718502
	C	-5.820253	-0.912288	-0.596916	C	-5.839296	-0.844085	-0.559416
	C	-4.492711	-0.927079	-1.012519	C	-4.515221	-0.876335	-0.985551
	C	-3.511144	-1.420433	-0.144427	C	-3.534622	-1.386064	-0.126118
	C	-2.061353	-1.396528	-0.583416	C	-2.088041	-1.379875	-0.576020
	C	-0.647110	-2.155326	1.287963	C	-0.664862	-2.134666	1.295527
	C	0.627715	-2.788633	0.744673	C	0.589856	-2.799851	0.741006
	C	-1.478640	0.146261	1.287036	C	-1.483688	0.169599	1.276640
	C	-2.045919	1.279544	0.478465	C	-2.043842	1.303694	0.463318
	C	-3.381956	1.648807	0.650638	C	-3.347749	1.697912	0.620702
	C	-3.942411	2.674160	-0.104389	C	-3.929334	2.768507	-0.150745
	C	-3.157359	3.352123	-1.036214	C	-3.057684	3.453987	-1.076095
	C	-1.821634	2.990000	-1.211412	C	-1.753381	3.073004	-1.232098
	C	-1.235134	1.946073	-0.471512	C	-1.201930	1.975037	-0.493513
	H	4.920113	-0.736763	1.885281	H	4.894989	-0.657385	1.895555
	H	1.458982	-1.464194	2.676052	H	1.490815	-1.556579	2.676088
	H	3.008311	-2.196329	2.212059	H	3.054510	-2.203228	2.148956
	H	2.262901	-2.701680	-1.170388	H	2.215124	-2.709620	-1.208861
	H	3.460466	-2.870655	0.129210	H	3.420172	-2.925374	0.078738
	H	5.396081	-1.886938	-1.082937	H	5.383756	-1.900525	-1.044937
	H	-1.765474	-2.386279	-0.954550	H	-1.803054	-2.374392	-0.942157
	H	-1.974205	-0.710296	-1.434928	H	-1.999711	-0.700528	-1.433438
	H	-1.438674	-2.908117	1.340881	H	-1.470739	-2.869370	1.374612
	H	-0.492900	-1.787215	2.307967	H	-0.483533	-1.751356	2.305458
	H	0.944423	-3.623452	1.386257	H	0.891507	-3.638759	1.383782

	H	0.427516	-3.187395	-0.257778	H	0.373159	-3.198079	-0.258506
	H	-0.573956	0.463674	1.823352	H	-0.579279	0.492972	1.808269
	H	-2.218610	-0.178254	2.028747	H	-2.230007	-0.140405	2.017444
	H	-4.202610	-0.539032	-1.985560	H	-4.227398	-0.490427	-1.960107
	H	-4.005009	1.103362	1.360360	H	-3.997299	1.174198	1.322951
	O	0.050667	1.610540	-0.656226	O	0.029967	1.605685	-0.687035
	H	-1.207807	3.515232	-1.940110	H	-1.098157	3.580174	-1.936255
	H	-3.593808	4.155381	-1.626966	H	-3.478321	4.274395	-1.652278
	H	4.219389	3.524895	1.858607	H	4.012355	3.570536	1.923865
	H	1.788253	3.027237	2.050298	H	1.601383	2.965767	2.076181
	H	5.039403	2.291718	-2.126846	H	5.031083	2.291407	-2.036378
	H	2.612251	2.134896	-1.531245	H	2.589793	2.113782	-1.508303
	H	6.453158	0.224453	-1.935322	H	6.450580	0.229497	-1.837313
	H	-7.143540	-1.382331	1.058365	H	-7.156067	-1.301748	1.103992
	H	-5.293427	-2.261314	2.463281	H	-5.307616	-2.209245	2.492956
	H	-6.599604	-0.529049	-1.249824	H	-6.617988	-0.447766	-1.205131
	H	5.840062	1.599695	1.808628	H	5.714033	1.716727	1.867615
	O	-5.286039	2.967758	0.094551	O	-5.163555	3.080190	-0.026343
	O	0.543902	-0.987332	-2.529221	O	0.517610	-0.991548	-2.551819
	O	0.232111	-2.246379	-2.776128	O	0.173903	-2.243538	-2.791362
	Zn	0.631437	-0.265454	-0.601833	Zn	0.621218	-0.313677	-0.627277
	H	-5.562275	3.671855	-0.512874				
B	C	2.072473	1.994521	2.139807	C	-1.815399	-1.542398	2.712868
	N	1.683674	0.714302	2.081499	N	-1.957724	-0.572841	1.787627
	C	3.410322	2.386017	2.175094	C	-2.327588	-1.436320	4.000247
	N	1.435969	-1.884996	0.541353	N	-1.645002	1.675403	0.170320
	C	4.388354	1.391883	2.160786	C	-3.008405	-0.274300	4.356830
	N	2.720609	-0.084278	-0.973846	N	-2.600634	-0.202275	-1.464004
	C	3.991527	0.057685	2.079476	C	-3.157536	0.732440	3.406960
	N	-4.445233	-0.602834	0.211404	N	3.666711	1.729357	0.431656
	C	2.627952	-0.235513	2.011013	C	-2.625479	0.547552	2.133922
	N	-1.193220	-0.682511	0.367229	N	0.872344	0.463982	0.651948
	C	2.127829	-1.650767	1.836792	C	-2.813473	1.581253	1.057842
	C	2.388295	-2.405432	-0.452382	C	-2.064361	2.142582	-1.156311
	C	3.326506	-1.277744	-0.824592	C	-2.836250	1.054271	-1.869137
	C	4.700022	-1.427773	-0.974375	C	-3.713068	1.335778	-2.916345
	C	5.465402	-0.297653	-1.268425	C	-4.343305	0.277202	-3.564236
	C	4.837732	0.940565	-1.394851	C	-4.088115	-1.030929	-3.145725
	C	3.454207	1.002877	-1.241622	C	-3.208656	-1.225142	-2.088702
	C	-5.632356	-0.999720	0.690155	C	4.611903	2.665243	0.594717
	C	-5.982155	-2.336015	0.877238	C	4.574816	3.915977	-0.019669
	C	-5.047171	-3.315641	0.549959	C	3.492444	4.213571	-0.844136
	C	-3.807859	-2.914720	0.054779	C	2.496942	3.252788	-1.011909
	C	-3.540516	-1.549443	-0.094549	C	2.618157	2.022303	-0.359146
	C	-2.206064	-1.096012	-0.642905	C	1.564663	0.956893	-0.567375
	C	-0.867103	-1.785213	1.300625	C	0.429322	1.575164	1.514952
	C	0.212808	-2.688518	0.716111	C	-0.557609	2.471686	0.772828
	C	-1.595447	0.520814	1.130539	C	1.672609	-0.491668	1.460222
	C	-1.885591	1.734239	0.288246	C	2.208693	-1.640210	0.647538
	C	-3.074411	2.406894	0.418866	C	3.491438	-1.694930	0.244483
	C	-3.309319	3.614010	-0.283126	C	4.007049	-2.807637	-0.578939
	C	-2.321804	4.172566	-1.132832	C	3.069726	-3.866539	-1.002537
	C	-1.127896	3.522901	-1.274872	C	1.792776	-3.837582	-0.595147
	C	-0.862062	2.284307	-0.584443	C	1.304444	-2.780915	0.320402
	Zn	0.615933	-0.303389	-0.756550	Zn	-0.967949	-0.422496	-0.068156
	H	4.719566	-0.747879	2.037400	H	-3.673776	1.659318	3.637078

	H	1.425856	-1.869041	2.647146	H	-3.048358	2.556713	1.503897
	H	2.962837	-2.358359	1.930598	H	-3.682754	1.283231	0.457820
	H	1.825704	-2.717791	-1.342378	H	-1.167497	2.377080	-1.744318
	H	2.952602	-3.269975	-0.077792	H	-2.670580	3.057902	-1.100155
	H	5.154497	-2.404940	-0.842706	H	-3.887797	2.366607	-3.209363
	H	-1.766761	-1.914945	-1.220593	H	0.804423	1.346419	-1.253622
	H	-2.355452	-0.252375	-1.326605	H	2.006785	0.092615	-1.071053
	H	-1.760727	-2.364777	1.560760	H	1.284939	2.176378	1.854203
	H	-0.498892	-1.332822	2.227780	H	-0.032784	1.138579	2.407888
	H	0.381775	-3.555308	1.369172	H	-0.960235	3.221549	1.465209
	H	-0.094591	-3.061150	-0.269966	H	-0.042823	3.017354	-0.023717
	H	-0.748662	0.756929	1.788099	H	1.007669	-0.878910	2.243412
	H	-2.471588	0.304173	1.755651	H	2.510906	0.026829	1.938224
	H	-3.046859	-3.641248	-0.220594	H	1.632825	3.442399	-1.644407
	H	-3.858172	2.021664	1.064283	H	4.191845	-0.898113	0.483626
	O	0.269556	1.712484	-0.742161	O	0.207715	-2.898689	0.872981
	H	-0.342121	3.911972	-1.915496	H	1.070632	-4.602730	-0.866885
	H	-2.533384	5.101599	-1.655523	H	3.467876	-4.649864	-1.641082
	H	3.671471	3.438257	2.221245	H	-2.182589	-2.249039	4.703369
	H	1.277493	2.738979	2.172028	H	-1.271470	-2.425768	2.403750
	H	5.401772	1.842773	-1.605227	H	-4.562492	-1.881260	-3.623177
	H	2.914381	1.942520	-1.332854	H	-2.970204	-2.221656	-1.723905
	H	6.542064	-0.382052	-1.383066	H	-5.029108	0.468163	-4.384281
	H	-6.962891	-2.594335	1.263546	H	5.375360	4.629478	0.146507
	H	-6.344122	-0.211847	0.929434	H	5.445174	2.401996	1.243338
	H	-5.278437	-4.369816	0.672924	H	3.421590	5.174521	-1.345549
	H	5.442787	1.650704	2.199864	H	-3.410582	-0.151018	5.357921
	O	-4.503074	4.197515	-0.105194	O	5.195607	-2.837228	-0.920878
	O	0.233121	-0.678994	-2.653413	O	-0.020074	-1.555335	-1.416593
	O	0.061278	-2.098606	-2.909548	O	0.007204	-0.824311	-2.668558
	H	-0.862938	-2.151761	-3.205421	H	-0.716399	-1.231596	-3.175457
	H	-4.586873	5.020858	-0.619257				
C	C	-3.545682	2.343710	-0.257294	C	-3.628086	2.164972	-0.275377
	N	-2.952609	1.194956	-0.634503	N	-2.974654	1.048773	-0.651754
	C	-4.783576	2.731421	-0.748178	C	-4.884711	2.484700	-0.766876
	N	-1.848894	-1.276132	-0.929783	N	-1.746695	-1.368291	-0.937672
	C	-5.431332	1.890308	-1.655326	C	-5.486125	1.608738	-1.672851
	N	-1.202275	-0.940883	1.704059	N	-1.140672	-0.993773	1.695188
	C	-4.818141	0.701998	-2.041496	C	-4.810272	0.454500	-2.057759
	N	2.828832	-2.416623	-0.771203	N	2.955871	-2.267904	-0.743046
	C	-3.567801	0.385758	-1.514390	C	-3.544891	0.205673	-1.530879
	N	0.667064	0.173134	-0.784920	N	0.683438	0.226243	-0.762772
	C	-2.815333	-0.850607	-1.948431	C	-2.727639	-0.990026	-1.962399
	C	-2.466369	-2.182372	0.048438	C	-2.321527	-2.308971	0.034409
	C	-1.742126	-2.128202	1.372160	C	-1.620073	-2.207900	1.367187
	C	-1.665063	-3.224308	2.227458	C	-1.504659	-3.291380	2.234161
	C	-1.000310	-3.082057	3.443711	C	-0.863409	-3.108143	3.457246
	C	-0.424018	-1.853102	3.771870	C	-0.348660	-1.850940	3.781388
	C	-0.546233	-0.804286	2.870877	C	-0.507723	-0.816617	2.869914
	C	3.844310	-3.006710	-1.419289	C	3.988177	-2.817588	-1.399676
	C	4.932515	-2.299576	-1.922175	C	5.037191	-2.066733	-1.922418
	C	4.977012	-0.922530	-1.715305	C	5.023793	-0.687756	-1.725164
	C	3.928324	-0.306195	-1.034161	C	3.957789	-0.113065	-1.034222
	C	2.856265	-1.081367	-0.588437	C	2.926258	-0.931379	-0.570854
	C	1.659430	-0.479701	0.114352	C	1.709019	-0.378715	0.137051
	C	0.294194	-0.673453	-1.941796	C	0.362850	-0.635772	-1.927994

	C	-0.605197	-1.819825	-1.507482	C	-0.468499	-1.836569	-1.507689
	C	1.104117	1.499348	-1.287464	C	1.068071	1.564358	-1.275060
	C	1.511092	2.474371	-0.214714	C	1.435288	2.572521	-0.219100
	C	2.703910	3.150571	-0.301245	C	2.558749	3.308697	-0.302391
	C	3.061878	4.118684	0.670492	C	2.877060	4.376900	0.672930
	C	2.199478	4.423262	1.754291	C	1.916294	4.649108	1.764084
	C	1.002381	3.774836	1.851092	C	0.784460	3.937721	1.851829
	C	0.604474	2.789003	0.876395	C	0.476887	2.879330	0.873698
	H	-5.291918	0.019965	-2.740690	H	-5.247142	-0.252993	-2.755629
	H	-2.274289	-0.608865	-2.871151	H	-2.193949	-0.718422	-2.880971
	H	-3.517943	-1.656384	-2.196875	H	-3.386947	-1.829506	-2.216735
	H	-2.504068	-3.215162	-0.324721	H	-2.291097	-3.342510	-0.336665
	H	-3.501096	-1.851206	0.209686	H	-3.376503	-2.041088	0.180512
	H	-2.109283	-4.169017	1.929177	H	-1.900731	-4.258017	1.938456
	H	1.154000	-1.280371	0.662403	H	1.239959	-1.197576	0.690423
	H	1.978076	0.265519	0.852108	H	1.999013	0.382634	0.870041
	H	1.183547	-1.049499	-2.462924	H	1.275815	-0.951710	-2.447508
	H	-0.243991	-0.029580	-2.648061	H	-0.211231	-0.020507	-2.631434
	H	-0.817631	-2.484434	-2.355290	H	-0.635217	-2.504790	-2.362546
	H	-0.108489	-2.419068	-0.736610	H	0.056466	-2.412354	-0.737933
	H	0.251745	1.919967	-1.838171	H	0.202495	1.952570	-1.828267
	H	1.930510	1.387295	-2.003608	H	1.901136	1.482771	-1.987175
	H	3.945324	0.759653	-0.830908	H	3.931569	0.954019	-0.838884
	H	3.391594	2.958070	-1.123045	H	3.282250	3.159267	-1.100955
	O	-0.542458	2.237725	0.983751	O	-0.600550	2.271436	0.975213
	H	0.307959	3.978712	2.660460	H	0.045190	4.094530	2.631576
	H	-5.230466	3.662882	-0.419102	H	2.177032	5.433930	2.467638
	H	-3.002526	2.950527	0.461597	H	-5.381217	3.390968	-0.438611
	H	0.112131	-1.708994	4.703189	H	-3.119538	2.801188	0.443279
	H	-0.111653	0.173047	3.067432	H	0.168418	-1.674263	4.717868
	H	-0.922657	-3.924227	4.124843	H	-0.122415	0.181420	3.063816
	H	5.726741	-2.820913	-2.445664	H	-0.755860	-3.939864	4.147054
	H	3.780331	-4.086179	-1.532764	H	5.846238	-2.556465	-2.453635
	H	5.818843	-0.335886	-2.071067	H	3.970752	-3.899663	-1.504423
	H	-6.406494	2.156229	-2.052202	H	5.833937	-0.066958	-2.096109
	O	4.222063	4.781494	0.611879	H	-6.474453	1.821185	-2.069331
	O	1.282582	-4.005987	0.843066	O	3.922554	5.020510	0.572091
	O	0.395596	-4.728398	-0.012676	O	1.489655	-3.918787	0.884062
	Zn	-1.212174	0.463883	0.221380	O	0.641238	-4.686715	0.028677
	H	0.835296	-5.592307	-0.103670	Zn	-1.214355	0.395457	0.203696
	H	1.798221	-3.428445	0.198226	H	1.118850	-5.531319	-0.051780
	H	4.763454	4.512093	-0.151731	H	1.979945	-3.321054	0.237959
	H	2.513649	5.166365	2.480299				
D	C	0.338717	3.073937	0.819265	C	1.126296	2.504687	-1.763672
	N	-0.497113	2.242061	0.168621	N	1.589372	1.681892	-0.801705
	C	0.285870	4.452277	0.668752	C	1.706504	3.735629	-2.038368
	N	-1.870814	0.412797	-1.409352	N	2.164603	0.216191	1.504884
	C	-0.665203	4.988887	-0.201780	C	2.803731	4.141471	-1.279584
	N	-2.272279	-0.202524	1.173862	N	2.175351	-1.558795	-0.524227
	C	-1.524969	4.130932	-0.879657	C	3.283727	3.296317	-0.283537
	N	-0.254862	-1.996834	-0.126187	N	-0.867068	-1.440831	0.069398
	C	-1.416367	2.756907	-0.662694	C	2.658698	2.068378	-0.077643
	N	1.005753	0.072449	-1.491565	N	-0.599184	0.955534	1.337613
	C	-2.377177	1.792924	-1.316841	C	3.204734	1.083126	0.924569
	C	-2.948080	-0.545535	-1.137162	C	2.707289	-1.118327	1.799355
	C	-3.268508	-0.556019	0.341606	C	2.981699	-1.857241	0.511169

	C	-4.512956	-0.958507	0.821394	C	3.991978	-2.809406	0.405796
	C	-4.716166	-1.014005	2.197985	C	4.161859	-3.476308	-0.805190
	C	-3.677576	-0.653440	3.058410	C	3.328920	-3.161988	-1.879463
	C	-2.470332	-0.249061	2.503044	C	2.351144	-2.192185	-1.697567
	C	-1.010051	-2.931888	0.486512	C	-1.136492	-2.427368	-0.806739
	C	-1.118720	-4.233467	0.021056	C	-2.264134	-3.228650	-0.695994
	C	-0.427819	-4.583545	-1.141463	C	-3.146781	-2.994695	0.361763
	C	0.359003	-3.626845	-1.771218	C	-2.869473	-1.973383	1.264881
	C	0.432185	-2.343200	-1.226320	C	-1.711806	-1.215872	1.089995
	C	1.354359	-1.315887	-1.835595	C	-1.320158	-0.113654	2.046107
	C	0.255359	0.713546	-2.592955	C	0.318360	1.695523	2.230879
	C	-1.156955	0.154745	-2.671874	C	1.498775	0.837188	2.666759
	C	2.213196	0.874006	-1.200099	C	-1.544195	1.943440	0.748548
	C	3.063040	0.323903	-0.085491	C	-2.714528	1.316223	0.040270
	C	4.413541	0.153536	-0.271865	C	-3.949709	1.313119	0.573194
	C	5.241836	-0.299576	0.783536	C	-5.078074	0.617181	-0.083107
	C	4.701667	-0.599885	2.059769	C	-4.838794	-0.063169	-1.374235
	C	3.360886	-0.444396	2.265762	C	-3.623176	-0.032792	-1.938173
	C	2.488206	0.021426	1.214561	C	-2.500210	0.679149	-1.290628
	Zn	-0.417866	0.122823	0.219329	Zn	0.721544	-0.080921	-0.073824
	H	-2.273282	4.506407	-1.571029	H	4.133273	3.571318	0.333703
	H	-2.665198	2.168984	-2.307739	H	3.759883	1.610702	1.710675
	H	-3.290117	1.784969	-0.707087	H	3.925859	0.446982	0.394594
	H	-2.607121	-1.547353	-1.431319	H	1.950004	-1.672132	2.368454
	H	-3.855376	-0.326869	-1.716541	H	3.618320	-1.068793	2.410402
	H	-5.298149	-1.223801	0.120076	H	4.628478	-3.011965	1.261575
	H	2.363653	-1.532445	-1.463136	H	-2.203303	0.272256	2.574238
	H	1.392139	-1.454042	-2.924879	H	-0.656988	-0.549061	2.801853
	H	0.775624	0.562095	-3.549434	H	-0.219249	2.061541	3.117298
	H	0.226742	1.793027	-2.404466	H	0.669811	2.573434	1.675538
	H	-1.688204	0.594745	-3.526453	H	2.203518	1.455521	3.236742
	H	-1.120228	-0.929420	-2.831796	H	1.165305	0.037708	3.334351
	H	1.878749	1.884218	-0.931525	H	-0.977477	2.576604	0.055200
	H	2.836008	0.964095	-2.102229	H	-1.941559	2.576125	1.555170
	H	0.916628	-3.854993	-2.674687	H	-3.537053	-1.745265	2.090880
	H	4.867909	0.371822	-1.236479	H	-4.161132	1.780305	1.532708
	O	1.244085	0.166877	1.455281	O	-1.398581	0.734118	-1.839623
	H	2.903239	-0.665499	3.225428	H	-3.400281	-0.516066	-2.885508
	H	0.978122	5.084909	1.213229	H	-5.684920	-0.575933	-1.822372
	H	1.071499	2.604687	1.470280	H	1.296872	4.359328	-2.825145
	H	-3.799239	-0.680527	4.135562	H	0.262834	2.157875	-2.318990
	H	-1.628585	0.043576	3.125769	H	3.436937	-3.649351	-2.842025
	H	-5.675690	-1.329923	2.596336	H	1.689166	-1.901221	-2.508946
	H	-1.737778	-4.948850	0.551051	H	4.942101	-4.223812	-0.913204
	H	-1.543940	-2.617483	1.379695	H	-2.447668	-4.009663	-1.425340
	H	-0.503019	-5.587624	-1.548140	H	-0.425824	-2.563745	-1.617020
	H	-0.730178	6.062168	-0.353882	H	-4.044107	-3.595793	0.473768
	O	6.561210	-0.467602	0.623676	H	3.275805	5.102829	-1.458705
	H	6.854664	-0.241982	-0.277445	O	-6.189362	0.584832	0.452969
	H	5.368028	-0.950052	2.841832				
E	C	-2.154010	0.172294	3.066821	C	2.379387	-0.346723	-2.933042
	N	-2.377926	0.317146	1.751020	N	2.471620	0.017347	-1.643801
	C	-2.866272	0.890391	4.020865	C	3.191043	0.208853	-3.915410
	N	-2.218557	1.179258	-0.878250	N	2.040984	1.293583	0.763138
	C	-3.833886	1.795391	3.585835	C	4.117531	1.181521	-3.541085
	N	-1.849135	-1.486569	-1.337396	N	1.560283	-1.263528	1.659717

	C	-4.058611	1.951710	2.218293	C	4.205030	1.564978	-2.202779
	N	1.788942	3.073872	-1.801419	N	-3.204765	2.332638	-0.097144
	C	-3.310221	1.190452	1.326831	C	3.364032	0.956484	-1.277707
	N	0.379450	1.016286	0.227427	N	-0.478288	0.898347	-0.476038
	C	-3.502772	1.253416	-0.167040	C	3.399076	1.267215	0.197294
	C	-2.420353	0.706421	-2.251086	C	2.078595	1.065203	2.213395
	C	-2.443587	-0.804985	-2.330232	C	2.067220	-0.408758	2.564411
	C	-3.003749	-1.461607	-3.425740	C	2.508679	-0.856160	3.809204
	C	-2.920576	-2.848387	-3.495888	C	2.396380	-2.208137	4.118450
	C	-2.288256	-3.550031	-2.466072	C	1.854317	-3.086602	3.176618
	C	-1.769313	-2.829940	-1.400519	C	1.452859	-2.573577	1.952451
	C	2.720211	4.006460	-2.041918	C	-3.997720	3.411447	-0.051882
	C	4.083699	3.808814	-1.828200	C	-3.853312	4.437004	0.881533
	C	4.503668	2.572140	-1.344514	C	-2.828676	4.336496	1.819148
	C	3.543458	1.595093	-1.084801	C	-1.990512	3.223205	1.776351
	C	2.196052	1.886943	-1.313629	C	-2.205833	2.246211	0.800640
	C	1.128816	0.850899	-1.043055	C	-1.325763	1.017343	0.738491
	C	-0.349711	2.296572	0.331033	C	0.265380	2.139146	-0.777604
	C	-1.417284	2.416849	-0.757108	C	1.259236	2.477564	0.337648
	C	1.224687	0.815824	1.430885	C	-1.216467	0.423112	-1.674416
	C	1.918176	-0.523701	1.497786	C	-1.862574	-0.924901	-1.472843
	C	3.306660	-0.566597	1.665233	C	-3.222246	-1.078099	-1.492351
	C	3.977302	-1.776859	1.829327	C	-3.856774	-2.380544	-1.413950
	C	3.255637	-2.970254	1.831800	C	-2.985845	-3.534355	-1.324208
	C	1.873069	-2.937675	1.663488	C	-1.629540	-3.389542	-1.283628
	C	1.170803	-1.729419	1.485937	C	-1.016445	-2.090592	-1.314035
	H	-4.795350	2.653149	1.839584	H	4.905711	2.325756	-1.873859
	H	-4.063161	2.156428	-0.445508	H	3.928649	2.211339	0.381581
	H	-4.103881	0.383477	-0.466243	H	3.956048	0.465925	0.702627
	H	-1.589290	1.056133	-2.874672	H	1.189163	1.519740	2.666776
	H	-3.339535	1.112739	-2.695250	H	2.948957	1.546370	2.679178
	H	-3.488269	-0.882316	-4.205821	H	2.927233	-0.145432	4.515247
	H	0.406583	0.854233	-1.867177	H	-0.673087	0.992465	1.619383
	H	1.581481	-0.143327	-1.008831	H	-1.956676	0.125464	0.777053
	H	0.335424	3.150714	0.262964	H	-0.420214	2.985926	-0.920188
	H	-0.806268	2.324206	1.327130	H	0.788870	1.982748	-1.727398
	H	-2.063002	3.275080	-0.531010	H	1.927756	3.272707	-0.014497
	H	-0.930407	2.621304	-1.714906	H	0.723260	2.872834	1.205236
	H	0.546921	0.922031	2.291158	H	-0.471494	0.342520	-2.479425
	H	1.971184	1.621490	1.500398	H	-1.971781	1.156103	-1.977200
	H	3.824197	0.611518	-0.717588	H	-1.181615	3.100104	2.492447
	H	3.873981	0.362531	1.687734	H	-3.871782	-0.210972	-1.594907
	O	-0.158916	-1.745044	1.345817	O	0.269229	-1.973616	-1.238987
	H	1.301663	-3.863774	1.663474	H	-0.966580	-4.247748	-1.202076
	H	3.775704	-3.916276	1.970373	H	-3.453805	-4.514809	-1.285904
	H	-2.657705	0.746409	5.075197	H	3.088409	-0.109538	-4.946845
	H	-1.380266	-0.538025	3.346296	H	1.631851	-1.099642	-3.167208
	H	-2.205698	-4.631056	-2.483390	H	1.754112	-4.146573	3.381542
	H	-1.276291	-3.320065	-0.564929	H	1.037155	-3.207335	1.172597
	H	-3.346675	-3.379336	-4.341888	H	2.732137	-2.576852	5.083025
	H	4.790300	4.603219	-2.045835	H	-4.532242	5.283560	0.871113
	H	2.362642	4.957039	-2.432853	H	-4.794560	3.457020	-0.791652
	H	5.557353	2.368635	-1.176363	H	-2.683336	5.107845	2.569984
	H	-4.402370	2.379734	4.303204	H	4.760064	1.643562	-4.284633
	O	5.353753	-1.743718	2.007296	O	-5.122968	-2.501773	-1.455902
	O	1.619021	-2.699901	-1.576062	O	-1.725682	-2.247873	1.447123

	O 2.770216 -2.362190 -1.458046 Zn -1.122804 -0.413144 0.262412 H 5.690994 -2.645997 2.124690	O -2.938960 -2.232384 1.454043 Zn 1.093788 -0.463446 -0.173583

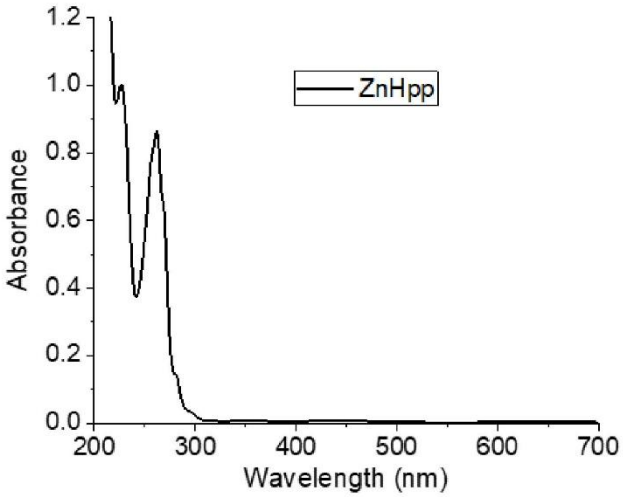

Figure S4. UV/vis spectrum for $[Zn(Hpp1)](OTf)_2$. The data were taken for a 1.0 mM sample of the complex in MeOH at 293 K with a 1.0 cm pathlength.

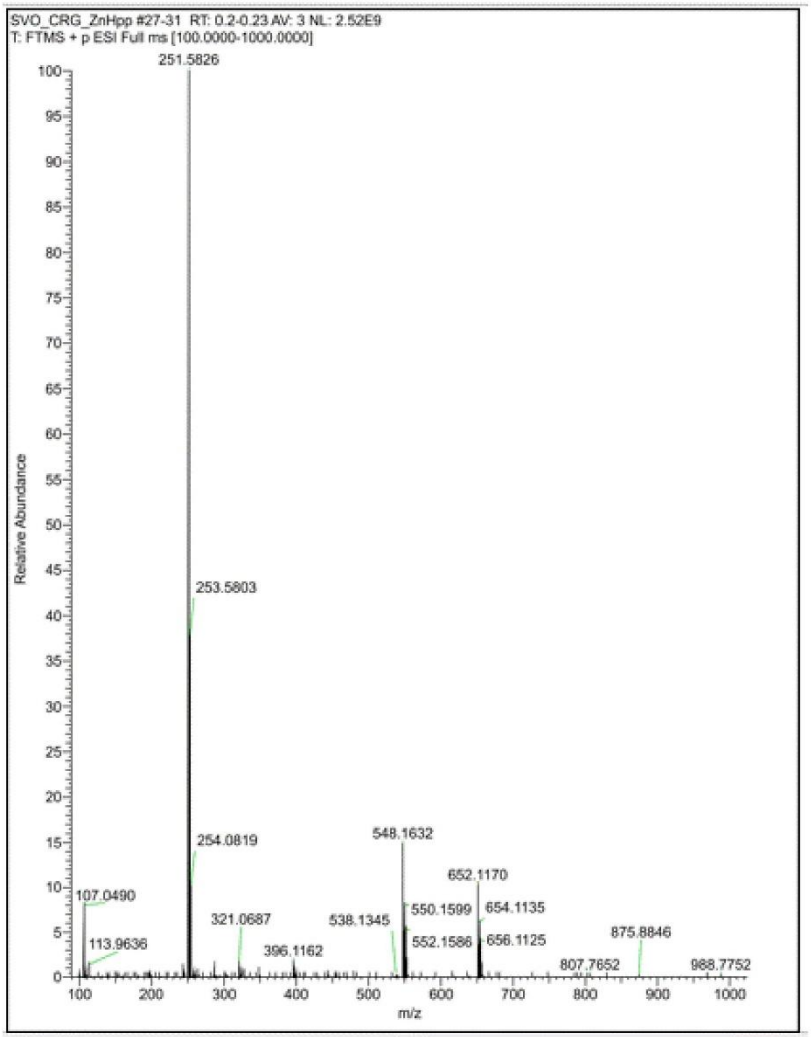

Figure S5. ESI-MS data (positive mode) for $[Zn(Hpp1)](OTf)_2$. The m/z peak at 251.5826 is assigned to $[Zn^{II}(Hpp1)]^{2+}$ (theoretical m/z = 251.5832). The m/z feature at 548.1642 is assigned to $[Zn^{II}(Hpp1)(HCO_2)]^{+}$ (theoretical m/z = 548.1612). The m/z feature at 652.1170 is assigned to $[Zn^{II}(Hpp1)(OTf)]^{+}$ (theoretical m/z = 652.1124).

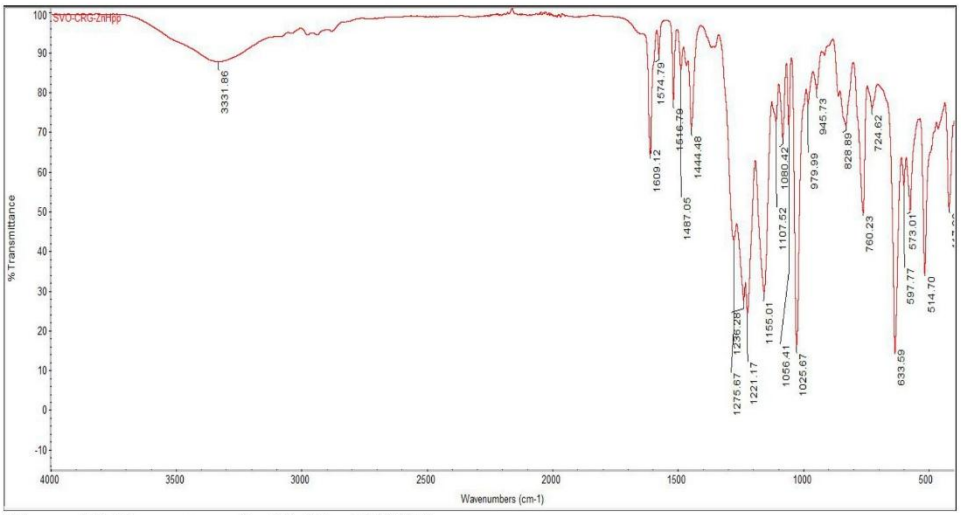

Figure S6. IR spectrum for $[Zn(Hpp1)](OTf)_2$.

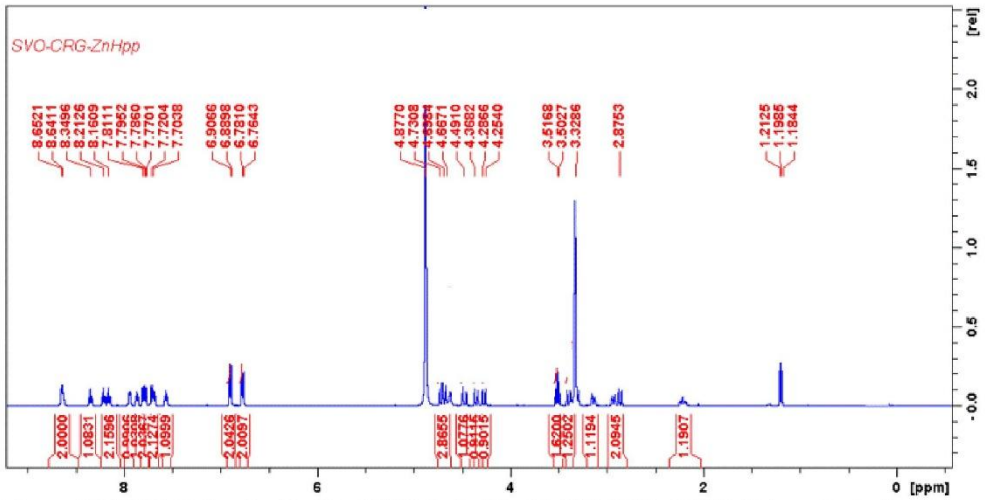

Figure S7. ^1H NMR data for $[Zn(Hpp1)](OTf)_2$ in CD_3OD (500 MHz, 293K). Solvent Peaks from water (4.87), methanol (3.35), and diethyl ether (1.18) are present.

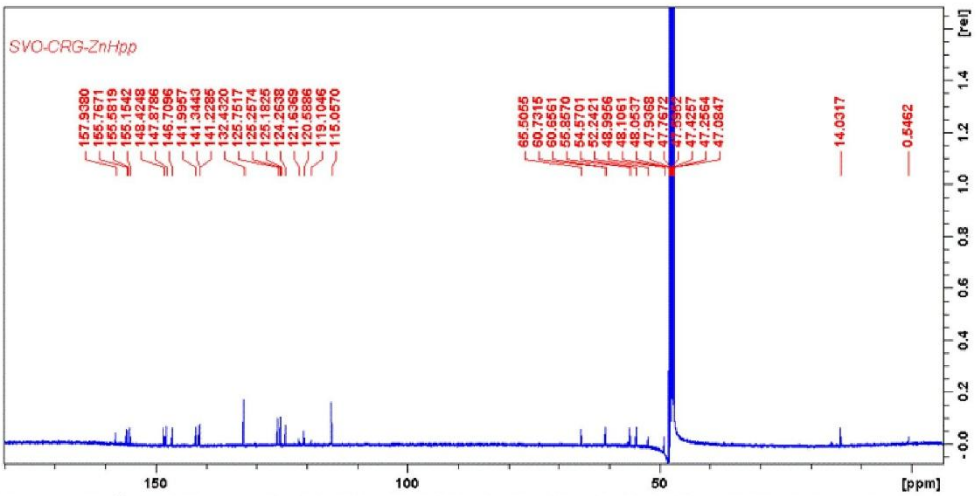

Figure S8. ^{13}C NMR data for $[Zn(Hpp1)](OTf)_2$ in CD_3OD (125 MHz, 293K). Solvent Peaks formethanol (49.36) and diethyl ether (15.14 and 66.82) are present.

Publication 3: Nickel(II) Complexes with Covalently Attached Quinols Rely on Ligand-Derived Redox Couples to Catalyze Superoxide Dismutation

R. Boothe, J. Oppelt, A. Franke, J. L. Moore, A. Squarcina, A. Zahl, L. Senft, I. Kellner, A. L. Awalah, A. Bradford, S. V. Obisesan, D. D. Schwartz, I. Ivanović-Burmazović, and C. R. Goldsmith

Dalton Trans., **2025**, Advance Article.

Summary: The field of nickel containing superoxide dismutase mimetics is relatively new and consists mainly of peptide-based molecules. Based on the ligand design that considers redox active organic functionalities, two Ni(II)complexes, Ni(H_4qp2) and Ni(H_2qp1) were synthesized by Robert Boothe in the group of Goldsmith. Both complexes are potent SOD mimetics, with Ni(H_4qp2) exhibiting exceptional performance in the degradation of the superoxide anion radical, achieving a k_{cat} value of 1.28×10^8 M^{-1} s^{-1} in MOPS buffered solutions at pH 7.4. Data from cryo-spray mass spectrometry suggest that Ni(H_4qp2) demonstrates remarkable stability against oxidative modification and decomposition, which may explain its superior SOD activity compared to analogues containing other metal centers.

Contribution: JO played a key role in identifying the antioxidative properties of both nickel complexes using the stopped-flow technique at physiological pH. JO demonstrated a seven-fold higher SOD activity for the H_4qp2 complex compared to its H_2qp1 analogue at pH 7.4. JO also conducted low-temperature UV/Vis experiments to determine intermediates during the reaction with superoxide and provided critical interpretation of the data acquired from cryo-spray MS for the same purpose. Additionally, JO contributed significantly to testing and documenting the operando stability of Ni(H_4qp2) and its Zn analogue using time-resolved UV/Vis, revealing greater resistance to oxidative degradation for the nickel complex. These were unique measurements on any Ni based SODm, being key to advancing our understanding of nickel SOD mimetics. JO shares first authorship with Robert Boothe on this publication, with JO's contributions being central to the experimental design, data analysis, and mechanistic insights presented.

Dalton Transactions

ROYAL SOCIETY OF CHEMISTRY

PAPER

View Article Online
View Journal

Cite this: DOI: 10.1039/d4dt03331k

Nickel(II) complexes with covalently attached quinols rely on ligand-derived redox couples to catalyze superoxide dismutation†

Robert Boothe,‡[a] Julian Oppelt,‡[b,c] Alicja Franke,[b,c] Jamonica L. Moore,[a] Andrea Squarcina,[b] Achim Zahl,[c] Laura Senft,[b] Ina Kellner,[b] Akudo L. Awalah,[a] Alisabeth Bradford,[a] Segun V. Obisesan,[a] Dean D. Schwartz,[d] Ivana Ivanović-Burmazović*[b] and Christian R. Goldsmith*[a]

Received 28th November 2024,
Accepted 7th January 2025

DOI: 10.1039/d4dt03331k

rsc.li/dalton

Although nickel is found in the active sites of a class of superoxide dismutase (SOD), nickel complexes with non-peptidic ligands normally do not catalyze superoxide degradation, and none has displayed activity comparable to those of the best manganese-containing SOD mimics. Here, we find that nickel complexes with polydentate quinol-containing ligands can exhibit catalytic activity comparable to those of the most efficient manganese-containing SOD mimics. The nickel complexes retain a significant portion of their activity in phosphate buffer and under operando conditions and rely on ligand-centered redox processes for catalysis. Although nickel SODs are known to cycle through Ni(II) and Ni(III) species during catalysis, cryo-mass spectrometry studies indicate that the nickel atoms in our catalysts remain in the +2 oxidation state throughout SOD mimicry.

Introduction

The over-production of reactive oxygen species (ROS) has been linked to a wide array of cardiovascular,[1,2] neurological,[3] and inflammatory disorders[4] as well as tumorigenesis.[5] Understanding when and where ROS concentrations spike during the progression of these pathologies could lead to improved ways to diagnose and treat these conditions. These potential benefits have motivated efforts by ourselves and others to develop redox-responsive probes capable of investigating the involvement of ROS in normal and aberrant physiology in conjunction with non-invasive magnetic resonance imaging (MRI) instrumentation.[6–14] The links between oxidative stress and the aforementioned health conditions have also motivated efforts to develop small molecule antioxidants that could potentially slow or even reverse disease progression. Many of these antioxidants are functional mimics of superoxide dismutases (SODs), which are enzymes that catalyze the degradation of $O_2^{\bullet -}$ to O_2 and H_2O_2 (eqn (1)).[15–21]

$$2\ O_2^{\bullet -} + 2\ H^+ \rightarrow O_2 + H_2O_2 \quad (1)$$

Our laboratories have developed and studied a series of Mn(II)-containing contrast agents for magnetic resonance imaging (MRI) that display changes to their T_1-weighted relaxivity (r_1) upon reaction with H_2O_2.[22–25] The more recent of these contrast agents feature ligands that contain quinol groups (Scheme 1).[23–25] Upon oxidation by H_2O_2, the quinols convert to *para*-quinones (Scheme 2). The manganese complexes with both H_2qp1 and H_4qp2 were also found to be cata-

[a]Department of Chemistry and Biochemistry, Auburn University, Auburn, AL 36849, USA. E-mail: Ivana.Ivanovic-Burmazovic@cup.uni-muenchen.de, crgoldsmith@auburn.edu
[b]Department of Chemistry, Ludwig-Maximilians-Universität München, 81377 München, Germany
[c]Department of Chemistry and Pharmacy, Friedrich-Alexander-Universität Erlangen-Nürnberg, Egerlandster. 1, 91508 Erlangen, Germany
[d]Department of Anatomy, Physiology, and Pharmacology, College of Veterinary Medicine, Auburn University, Auburn, AL 36849, USA

†Electronic supplementary information (ESI) available. CCDC 2390972 and 2390973. For ESI and crystallographic data in CIF or other electronic format see DOI: https://doi.org/10.1039/d4dt03331k

‡These authors contributed equally to the manuscript.

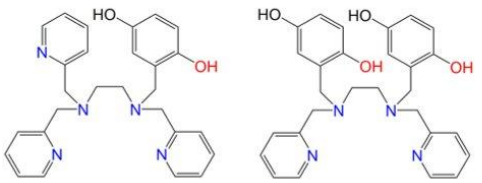

H_2qp1 H_4qp2

Scheme 1

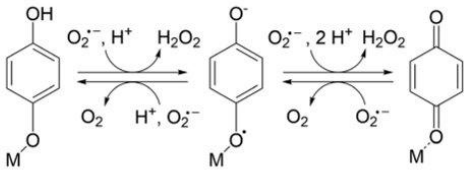

Scheme 2 Redox reactions involving quinols. This graphic was modified from one that appeared in reference.[28]

lysts for $O_2^{\bullet-}$ decomposition, as assessed by the commonly used hypoxanthine/xanthine oxidase/lucigenin assay[26,27] and subsequent stopped-flow kinetics analysis of the direct reactions between the compounds and superoxide.[24,25,28] Zn(II) complexes with H_2qp1 and H_4qp2 can also catalyze $O_2^{\bullet-}$ degradation, indicating that the redox activity of the ligand can allow even a redox-inactive metal ion to catalyze SOD-like reactivity.[29,30] The quinolic ligands are inactive as catalysts in the absence of a bound metal ion.

The manganese and zinc SOD mimics prepared with quinolic ligands have provided two different sets of benefits. The Mn(II) complex with H_2qp1 is highly active in 4-(2-hydroxyethyl)-1-piperazineethanesulfonic acid (HEPES) buffer and appears to rely mostly on metal-centered redox processes for its SOD mimicry. Unfortunately, the catalyst loses over 90% of its activity in phosphate buffer. The Zn(II) complexes with H_2qp1 and H_4qp2, conversely, are more stable than their Mn(II) analogs but are less effective as SOD mimics in aqueous solutions with sulfonate-containing buffers.[29,30] In phosphate solution, however, the Zn(II) complexes gain activity to the extent that they overtake their manganese analogs as catalysts. That these Zn(II)-containing catalysts are not inhibited by phosphate is noteworthy since some non-porphyrin-based manganese-based SOD mimics exhibit somewhat lower activity in phosphate buffer.[31–33] Given the high levels of phosphate in mammalian cells,[34,35] this represents a substantial advantage for the Zn(II) complexes.

The use of Mn(II) poses a problem for both MRI and SOD mimicry in that this metal ion tends to bind to ligands more weakly than most other transition metal ions.[36,37] The affinity of this metal ion for water is great enough to destabilize Mn(II) complexes with acyclic tetradentate linear ligands in aqueous solutions. When we partially oxidized the Mn(II)–H_4qp2 complex with H_2O_2, we measured a high aquation number that was difficult to rationalize unless at least some of the metal ion were released and complexed as $[Mn(H_2O)_6]^{2+}$.[25] Although "free" Mn(II) is not as toxic as unchelated iron or copper, it is nonetheless still harmful and has been documented to disrupt neurological function.[38] Most reported manganese-containing MRI contrast agents and SOD mimics have ligands that use macrocycles and/or a large number of anionic coordinating groups to stabilize the complex in water, but even these measures are not always sufficient to ensure suitably long-term stability.[20,21,39,40] Such measures also pose severe constraints on the design and synthesis of manganese-containing MRI contrast agents and antioxidants.

The use of another transition metal ion could potentially relax these requirements due to the intrinsically greater complex stability.[37] The Zn(II) complexes demonstrate this as they are indeed more thermodynamically stable than their Mn(II) analogs.[28–30] The lack of redox activity for the metal, however, may limit the peak catalysis; without phosphate inhibition, the manganese compounds are more active. Ni(II) compounds generally have aqueous (thermodynamic) stabilities similar to Zn(II) complexes while displaying more extensive metal-centered redox activity and higher kinetic stability.[36] We initially decided to investigate Ni(II) complexes with H_2qp1 and H_4qp2 as redox-responsive MRI contrast agents that would operate through a chemical exchange saturation transfer (CEST) pathway involving bulk water exchanging ^{1}H nuclei with the quinolic OH groups.[41,42] Although these complexes did not give rise to a practical and readily replicable CEST response to H_2O_2, we find both that the Ni(II)-for-Mn(II) substitution does indeed stabilize the complexes in water and that the Ni(II) compounds are potent antioxidants.

The use of nickel can heighten both the stability and activity of the SOD mimic. Unlike the zinc complexes, the activity is diminished by phosphate, but not to anywhere near the same extent as the Mn–H_2qp1 complex. The nickel complex with H_4qp2 is the more active of the two catalysts, and even with the inhibitory effect, it is a highly functioning SOD mimic in phosphate solution. Mechanistically, the H_4qp2 complex with Ni(II) behaves like its Zn(II) analog in that it relies on ligand-centered redox for catalysis but appears to better resist decomposition.

Experimental section

Materials

Most of the chemical precursors and solvents were bought from Sigma-Aldrich and used as received. 2,2-Diphenyl-1-picryl-hydrazyl hydrate (DPPH) was bought from EMD Millipore. All deuterated solvents were purchased from Cambridge Isotopes. Fisher supplied the diethyl ether (ether) and methanol (MeOH). Methylene chloride (CH_2Cl_2) was acquired from Mallinckrodt Baker. The ligands *N*-(2,5-dihydroxybenzyl)-*N*,*N*′,*N*′-tris(2-pyridinylmethyl)-1,2-ethanediamine (H_2qp1) and *N*,*N*′-bis(2,5-dihydroxybenzyl)-*N*,*N*′-bis(2-pyridinylmethyl)-1,2-ethanediamine (H_4qp2) were prepared as previously described.[24,25]

Instrumentation

All ^{1}H, ^{13}C, and ^{17}O NMR spectra were recorded on a 400 MHz AV Bruker NMR spectrometer. The ^{17}O NMR data were specifically collected on a Bruker AVANCE DRX 400WB spectrometer with a superconducting wide-bore magnet operating at a 54.24 MHz resonance frequency and a 9.4 T magnetic induction. All reported NMR resonance peak frequencies were referenced to internal standards. Water exchange experiments

involving **1** and **2** were performed in 60 mM MOPS, pH = 7.4 (+20% v/v MeCN) as well as in pure distilled water (+20% v/v MeCN). Neither **1** nor **2** exhibited significant broadening of the ^{17}O signal in either buffered or unbuffered water in comparison to the reference samples without the compounds. Optical data were collected on a Varian Cary 50 spectrophotometer and analyzed using software from the WinUV Analysis Suite. Electron paramagnetic resonance (EPR) spectra were collected using a Bruker EMX-6/1 X-band EPR spectrometer operated in perpendicular mode and analyzed with the program EasySpin. Each EPR sample was run as a frozen solution in a quartz tube. High-resolution mass spectrometry (HR-MS) data were obtained at the Mass Spectrometer Center at Auburn University on a Bruker microflex LT MALDI-TOF mass spectrometer *via* direct probe analysis operated in the positive ion mode. Infrared spectroscopy (IR) data were obtained with a Shimadzu IR Prestige-21 FT-IR spectrophotometer. A Johnson Matthey magnetic susceptibility balance (model MK I#7967) was used to measure the magnetic properties of the Ni(II) complexes; the reported μ_{eff} values are the average of two independent measurements, each of which corresponded to a unique solid sample. Atlantic Microlabs (Norcross, GA) performed the elemental analyses (C, H, N). All samples submitted for elemental analysis were dried under vacuum prior to their shipment.

Cyclic voltammetry (CV) in aqueous solutions was performed using a Pine WaveDriver bipotentiostat using a 3 mm glassy carbon working electrode that was polished between each experiment, a Pt wire counter electrode, and a non-aqueous Ag^+/Ag pseudoreference electrode. Samples were analyzed in a 20 mL electrochemical glass cell with a Teflon cell top purchased from BASi Inc. Cyclic voltammetry measurements in MeCN were performed using an Autolab instrument with a PGSTAT 101 potentiostat. A three-electrode arrangement was employed consisting of a glassy carbon disk working electrode (A = 0.07 cm^2) (Metrohm), a platinum counter electrode (Metrohm), and a silver wire (Metrohm) as reference electrode. Potentials were referenced to the redox couple of the internal standard $Fc^{+/0}$. Prior to each experiment, the electrode was polished with 1 μm alumina, rinsed with deionized water, and wiped with a paper tissue. All CV experiments were conducted at a scan rate of 100 mV s^{-1} at 293 K unless otherwise stated.

X-ray crystallography

Crystals were mounted in paratone oil on a glass fiber and aligned on a Bruker SMART APEX CCD X-ray diffractometer. Intensity measurements were performed using graphite monochromated Mo Kα radiation (λ = 0.71073 Å) from a sealed tube and monocapillary collimator. SMART (v 5.624) was used to determine the preliminary cell constants and regulate data acquisition. The intensities of reflections of a sphere were collected through the compilation of three sets of exposures (frames). Each set had a different ϕ angle for the crystal, with each exposure spanning a range of 0.3° in ω. A total of 1800 frames were collected with exposure times of 40 s per frame. The data were corrected for Lorentz and polarization effects. Structures were solved using direct methods and expanded using Fourier techniques. All non-hydrogen atoms were refined anisotropically. Hydrogen atoms were included at idealized positions 0.95 Å from their parent atoms prior to the final refinement. Further details regarding the data acquisition and analysis are included in Tables 1 and 2.

Potentiometric titrations

The speciation chemistry of the Ni(II) complexes in water was probed using a METROHM 765 Dosimat with a jacketed, air-tight glass titration vessel. A Fisher Scientific Accumet Research AR15 pH meter was used to determine the pH of the sample solutions during the titrations. The electrode was calibrated before each titration using commercially available standard solutions buffered to pH 4.0, 7.0, and 10.0. All samples were purged with argon prior to analysis and subsequently analyzed under an argon atmosphere at 25 °C. All solution samples were prepared in solutions of 100 mM KCl in deionized Millipore water. The titrations investigating metal–ligand speciation were run with solutions that contained a 1 : 1 molar mixture of the ligand and $Ni(OTf)_2$. Carbonate-free solutions of 0.10 M KOH and 0.10 M HCl were prepared using argon-saturated deionized Millipore water. We attempted to analyze and fit the data to speciation models using the Hyperquad2006 software.[43]

Analysis of the antioxidant properties of the coordination complexes

We initially assessed the antioxidant activities of the Ni(II) complexes through the DPPH assay (DPPH = 2,2-diphenyl-1-picrylhydrazyl radical hydrate).[44–46] In this assay, potential antioxidants are tested for their abilities to donate hydrogen atoms to the radical to generate the corresponding hydrazine. Aqueous solutions of either **1**, **2**, or ascorbic acid were added

Table 1 Selected crystallographic data for **1** and **2**

Parameter	[Ni(H$_2$qp1)(MeCN)](OTf)$_2$ (**1**)	[Ni(H$_4$qp2)(MeCN)$_2$](OTf)$_2$ (**2**)
Formula	$C_{31}H_{34}F_6N_6NiO_9S_2$	$C_{38}H_{42}F_6N_8NiO_{10}S_2$
MW	871.47	1007.62
Crystal system	Orthorhombic	Orthorhombic
Space group	$Pca2_1$	$P2_12_12_1$
a (Å)	16.662(2)	12.8113(6)
b (Å)	12.3619(16)	17.4024(9)
c (Å)	17.649(2)	20.1442(10)
α (°)	90	90
β (°)	90	90
γ (°)	90	90
V (Å^3)	3635.2(8)	4491(4)
Z	4	4
Crystal color	Clear light purple	Clear violet
T (K)	180	180
Reflns collected	29 809	105 753
Unique reflns	3992	9748
R_1 (F, $I > 2\sigma(I)$)	0.0620	0.0730
wR_2 (F^2, all data)	0.1175	0.1496

$R_1 = \sum||F_o| - |F_c||/\sum|F_o|$; $wR_2 = [\sum w(F_o^2 - F_c^2)^2/\sum w(F_o^2)^2]^{1/2}$.

Table 2 Selected bond lengths (Å) for complexes **1** and **2**

Complex	1	2
Ni–N(1)	2.150(7)	2.079(3)
Ni–N(2)	2.140(8)	2.125(3)
Ni–N(3)	2.101(7)	2.137(4)
Ni–N(4)	2.077(8)	2.078(3)
Ni–N(5)	2.100(8)	2.110(4)
Ni–N(6)	2.062(8)	2.067(4)
C–O(1)	1.369(11)	1.369(6)
C–O(2)	1.381(12)	1.370(6)
C–O(3)		1.375(6)
C–O(4)		1.372(7)

N(1) and N(4) correspond to pyridine nitrogens; N(2) and N(3) correspond to amine nitrogens; N(6) corresponds to a MeCN nitrogen. N(5) corresponds to a pyridine nitrogen for **1** and a MeCN nitrogen in **2**. The atoms in **1** and **2** have been relabeled to facilitate comparisons between the structures.

to a solution of 0.10 mM DPPH in MeOH, such that the final reaction volume was 0.2 mL. Samples were incubated in the dark for 30 min at room temperature (RT) before being spectrophotometrically analyzed on a Molecular Devices Spectramax Plus spectrophotometer. The absorbance at 517 nm, the λ_{max} of the hydrazine product, was recorded. Experiments were performed in triplicate.

Determination of *in vitro* SOD activity *via* stopped-flow techniques

The ability of **1** and **2** to catalytically degrade superoxide was assessed by a direct method using stopped-flow techniques that has been more fully described in prior work from one of our laboratories.[31] Stopped-flow measurements were performed on a Biologic SFM-400 four syringe stopped-flow system using only the first three syringes and a Berger Ball mixer to minimize mixing effects between aqueous buffered solutions and DMSO solutions of KO_2. A J&M TIDAS S MMS UV/VIS diode array detector (integration time 0.5 ms, 180 nm–720 nm wavelength) and an Energetiq LDLS ENQ EQ-99-FC laser driven light source were used.

Superoxide solutions were prepared by suspending 220–240 mg KO_2 in 20 mL dry DMSO. The suspension was stirred for at least 30 min under an inert atmosphere before the suspension was filtered through a PTFE syringe filter ($Ø$ = 0.45 μm) to give a saturated KO_2 solution, which was transferred to the stopped-flow setup. The potential SOD mimics (SODm) were dissolved in aqueous solutions buffered to either pH 7.4 or 7.8. The buffers were prepared from Millipore water and either 4-morpholinepropanesulfonic acid (MOPS) or sodium dihydrogen phosphate. The concentration of the buffer was 60 mM, and the ionic strength was adjusted to 150 mM for each solution through the addition of NaCl. Prior to use, all buffered solutions were treated with Chelex 100 sodium exchange resin for at least 24 h to remove adventitious metal ions. Stock solutions containing 0.10 mM of each tested SODm were prepared in each buffer; if necessary, the stock solution contained 10% DMSO to ensure that the complexes dissolved fully. The stock solutions were diluted in buffer to give a series of SODm concentrations suitable for the stopped-flow experiments.

Kinetic measurements were performed adding a large excess of superoxide to the putative SOD mimetic: $[O_2^{\bullet-}]$ = 100–200 μM, [SODm] = 0.045–4.5 μM. The aqueous solution containing the studied Ni(II) complex was mixed in a 9 : 1 ratio with the superoxide solution in DMSO using a high-density mixer. In each experiment, the concentration of superoxide exceeded that of the nickel-containing catalyst by at least ten-fold to ensure catalytic conditions. All kinetic data were fit with the program Biokine 32 V4.80. Each presented k_{obs} value represents an average of at least ten measurements. Each k_{cat} was determined from the slope of k_{obs} *vs.* [SODm]. All measurements were performed at 21 °C.

Cryospray-ionization mass spectrometry

Cryospray-ionization mass spectrometry (CSI-MS) measurements were performed on a UHR-TOF Bruker Daltonik maXis Plus, an ESI-quadrupole time-of-flight (qToF) mass spectrometer capable of a resolution of at least 60.000 (FWHM), which was coupled to a Bruker Daltonik Cryospray unit. The detector was run in positive ion mode with a source voltage of 3.5 kV and a flow rate of 240 μL h^{-1}. The temperatures of the N_2 spray gas and the dry gas used for solvent removal were −40 °C. The mass spectrometer was calibrated prior to each experiment *via* direct infusion of an Agilent ESI-TOF low concentration tuning mixture, which provided a *m*/*z* range of singly charged peaks up to 2700 Da in both ion modes. For the reactions with $O_2^{\bullet-}$, 1×10^{-5} M solutions of each compound in MeCN were cooled to −40 °C and mixed with excess solid KO_2. Aliquots from the resultant mixtures were then injected into the mass spectrometer. To ensure the survival of metastable reaction species generated at low temperatures, the injection syringe and the tubing of the mass spectrometer were pre-cooled with −40 °C solvent. After tempering, the reaction solutions were injected as quickly as possible, with the recording of mass spectrometry data commencing immediately afterwards. Multiple samples were collected and analyzed over time to determine whether the product distribution was changing during the reaction. Aliquots were also analyzed after the reactions warmed to RT. The solvents were not rigorously dried to ensure a source of protons. The measured data were processed and analyzed with Bruker Data Analysis 5.2.

Syntheses

Acetonitrilo(*N*-(2,5-dihydroxybenzyl)-*N*,*N*′,*N*′-tris(2-pyridinylmethyl)-1,2-ethanediamine) nickel(II) triflate ([Ni(H_2qp1)(MeCN)](OTf)$_2$, 1). The H_2qp1 ligand (105 mg, 0.230 mmol) and nickel(II) triflate (Ni(OTf)$_2$, 83 mg, 0.23 mmol) were dissolved in 3 mL of acetonitrile (MeCN) under air. The solution was stirred for 30 min at RT. The solvent was removed to yield an oily reddish solid. The crude was recrystallized from a mixture of MeCN and ether to yield the product as dark red crystals that were suitable for single crystal X-ray diffraction (179 mg, 89%). ^{1}H NMR (500 MHz, CD_3CN, 294 K): 51.9, 45.9,

15.2, 14.4, 8.8, 6.7 (quinol O–H), 4.9, 3.3. Optical spectroscopy (MeOH): 255 nm (6800 M^{-1} cm^{-1}), 299 nm (3430 M^{-1} cm^{-1}), 444 nm (285 M^{-1} cm^{-1}), 504 nm (195 M^{-1} cm^{-1}), 674 (150 M^{-1} cm^{-1}). Solid-state magnetic susceptibility (294 K): μ_{eff} = 3.4μ_B. IR (KBr, cm^{-1}): 3529 (s), 3289 (s), 2286 (m), 1608 (s), 1574 (m), 1463 (s), 1364 (m), 1278 (s), 1256 (s), 1226 (s), 1158 (s), 1073 (w), 1056 (w), 1029 (s), 949 (w), 824 (m), 766 (s), 730 (w), 639 (s), 573 (w), 517 (m), 429 (w). CV (100 mM phosphate buffer, pH 7.2, 100 mV s^{-1}): E_{pa} = 60 mV *vs.* Ag/AgCl, E_{pc} = 0 mV *vs.* Ag/AgCl. Elemental analysis (crystals): Calcd for $C_{31}H_{32}N_6F_6O_8S_2Ni{\cdot}2H_2O$: C, 41.86%; H, 4.08%; N, 9.45%; Found: C, 41.76%; H, 3.91%; N, 9.38%.

***cis*-Diacetonitrilo(*N*,*N*′-bis(2,5-dihydroxybenzyl)-*N*,*N*′-bis(2-pyridinylmethyl)-1,2-ethanediamine)nickel(II) triflate ([Ni(H_4qp2)($MeCN)_2$]($OTf)_2$, 2).** The H_4qp2 ligand (152 mg, 0.312 mmol) and $Ni(OTf)_2$ (114 mg, 0.319 mmol) were dissolved in 3 mL of MeCN under N_2. The solution was stirred for 30 min at RT. Ether was gradually added to the reaction mixture to yield large, purple crystals of the product that were suitable for single crystal X-ray diffraction (95 mg, 42%). ^{1}H NMR (400 MHz, CD_3CN, 294 K): 54.9, 41.2, 16.7, 9.7, 6.7 (quinol O–H), 4.9, 3.3. Optical spectroscopy (MeCN): 298 nm (7550 M^{-1} cm^{-1}), 438 nm (610 M^{-1} cm^{-1}), 493 nm (380 M^{-1} cm^{-1}), 668 (130 M^{-1} cm^{-1}). Solid-state magnetic susceptibility (294 K): μ_{eff} = 3.4μ_B. IR (KBr, cm^{-1}): 3371 (s), 1610 (s), 1574 (m), 1509 (s), 1454 (s), 1252 (s), 1201 (s), 1173 (s), 1107 (w), 1029 (s), 948 (w), 879 (w), 818 (m), 761 (s), 729 (w), 639 (s), 578 (w), 519 (m), 422 (m). CV (100 mM phosphate buffer, pH 7.2, 100 mV s^{-1}): E_{pa} = 170 *vs.* Ag/AgCl, E_{pc} = −140 mV *vs.* Ag/AgCl, −670 mV *vs.* Ag/AgCl. Elemental analysis: Calcd for $C_{34}H_{36}N_6F_6O_{10}S_2Ni{\cdot}2.0H_2O$ C, 42.47%; H, 4.19%; N, 8.74%; Found: C, 42.13%; H, 3.98%; N, 8.32%.

Results

Synthesis and characterization

The syntheses of the Ni(II) complexes are facile, and both complexes form upon simply mixing the ligand and $Ni^{II}(OTf)_2$ in MeCN under N_2. Pure $[Ni^{II}(H_2qp1)(MeCN)](OTf)_2$ (**1**) and $[Ni^{II}(H_4qp2)(MeCN)_2](OTf)_2$ (**2**) can be crystallized in approximately 90% and 40% yields, respectively. The yield of **2** is substantially lower than the 75% value typically found for $[Mn^{II}(H_4qp2)Br_2]$.[25] We speculate that the greater solubility of **2** in MeCN reduces the amount of material that we can cleanly precipitate and crystallize from this solvent. Elemental analysis indicates that both **1** and **2** are hygroscopic, which was also observed for the Mn(II) complex with H_2qp1 and the Zn(II) complex with H_4qp2.[24,30]

The nickel remains in the +2 oxidation state upon complexation by either quinol-containing ligand. For both **1** and **2**, the solid-state magnetic susceptibility measurements are consistent with μ_{eff} values of 3.4μ_B; these are in the middle of the 2.8–4.0μ_B range reported for previously characterized Ni(II) complexes.[47] The complexes are both EPR-silent but display paramagnetic ^{1}H NMR spectra (Fig. S1 and S2†); these spectroscopic characteristics are likewise consistent with the assignment of S = 1 metal centers. Upon adding D_2O to the NMR samples, the peaks at 6.7 ppm decrease in intensity for both **1** and **2**, leading us to assign these to quinolic O–H resonances. The complexes were also characterized by IR and UV/vis (Fig. S3–S5†). In MeCN, both Ni(II) complexes display bands around 300 nm; we have observed similar features for other metal complexes with polydentate quinol-containing ligands.[23–25,29,30,48–50]

Complexes **1** and **2** are readily crystallized from mixtures of MeCN and ether (Table 1). The crystal structures show that the H_2qp1 and H_4qp2 ligands are bound to the metal center in pentadentate and tetradentate fashions, respectively, through their amine and pyridine groups (Fig. 1). None of the quinols are bound to the Ni(II) in either structure. Each Ni(II) center is coordinated by a distorted octahedral array of donor atoms consisting of the N-donors from the polydentate ligands and either one (**1**) or two (**2**) MeCN molecules occupying the remaining coordination sites. The metal–ligand bond distances corroborate the assignment of +2 oxidation states for the nickel ions (Table 2).[51] The C–O bond distances average 1.37 Å, demonstrating that the quinols remain both protonated and in their reduced states.[24,52]

Characterization of the aqueous chemistry of the Ni(II) complexes

Potentiometric pH titration data suggest that the quinols readily deprotonate and bind to the Ni(II) centers in anaerobic aqueous solutions, contrary to what is observed in the crystal structures (Fig. S6†). The H_2qp1 ligand by itself was previously found to undergo two ionization events with pK_a values of 4.72 and 7.24;[29] these are consistent with the protonation of a pyridine ring and the tertiary amines, respectively.[36] Due to the previously observed precipitation of the ligands under basic and metal-free conditions, we were unable to measure the pK_a values of the O–H protons; these are estimated to be about 10, the pK_a value for free 1,4-hydroquinone.[53] Intramolecular hydrogen bonding was observed in the crystal structure of the ligand, which we believe renders it unavailable for further protonation.[29]

Our best fits of the data collected for **1** suggest that free ligand is not present to an appreciable degree between pH 2.5 and 9.0. Since we do not observe dissociation of the ligand, we cannot calculate formation constants for either $[Ni(Hqp1)]^+$ or $[Ni(H_2qp1)]^{2+}$, where $Hqp1^-$ is the singly deprotonated form of the ligand. We observe an ionization event consistent with a pK_a value of 6.33 (±0.05), which is assigned to the deprotonation of a Ni(II)-bound quinol as the pH is increased.[9,54,55] The ionization event is replicated upon reacidification of the basic end-solution (Fig. S6†). Consequently, we believe that the predominant species between pH 7.0 and 7.4 is $[Ni(Hqp1)]^+$.

The Ni(II) complex with H_4qp2 also appears to be stable in water, and the lack of free ligand under even the most acidic of the tested conditions again precluded us from calculating accurate stability constants. The H_4qp2 ligand was previously observed to display two ionization events upon either basifica-

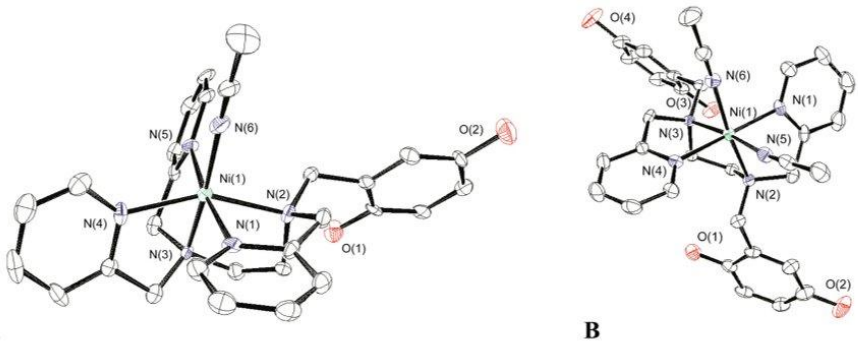

Fig. 1 ORTEP representations of (A) $[Ni(H_2qp1)(MeCN)]^{2+}$ (**1**) and (B) $[Ni(H_4qp2)(MeCN)_2]^{2+}$ (**2**). All hydrogen atoms, triflate counteranions, and solvent molecules have been removed for clarity. All ellipsoids are at 50% probability. Full crystallographic data are provided in the ESI and in the Cambridge Structural Database (numbers 2390972 and 2390973).†

tion of an acidic solution or acidification of a basic solution. The corresponding pK_a values of 4.47 and 7.18 were assigned to the (de)protonation events involving a pyridine and tertiary amine, respectively.[25] When **2** is subjected to the same conditions, we observe two clear ionization events between pH 3 and 10. The corresponding pK_a values of 5.99 (±0.05) and 8.24 (±0.05) are assigned to the sequential deprotonation of metal-bound quinols as pH is increased. Consequently, we believe that the complex is predominantly $[Ni(H_3qp2)]^+$ between pH 7.0 and 7.4, with H_3qp2^- being the singly deprotonated form of the ligand. As was found in MeCN solution, the ^{1}H NMR spectra of the Ni(II) complexes in 20% MeCN/80% water are consistent with paramagnetic metal centers (Fig. S1 and S2†). Overall, the data indicate that the ligands fully coordinate the metal centers of both **1** and **2** in water.

The species assignments are supported by spectrophotometric pH titrations in aqueous solutions (Fig. S7†). The UV/vis spectra of both **1** and **2** at pH 7.0 feature bands at 313 nm, consistent with metal-bound quinolate ligands.[25] Upon acidification, these bands disappear and new peaks appear at 294 and 293 nm for **1** and **2**, respectively. Similar changes were observed for the protonation of $[Mn(H_3qp2)]^+$ and $[Zn(Hqp1)]^+$ in water.[25,29] Given the noted tendency of Ni(II) to avoid hepta-coordination, even transiently as an intermediate in ligand exchange,[56,57] it is unlikely that water molecules are directly coordinated to the metal center in **1** when it is dissolved in water. Since the quinols are relatively poor ligands for metal ions, a water molecule could conceivably enter the coordination sphere in **2**, yielding $[Ni(H_3qp2)(H_2O)]^+$.

^{17}O NMR measurements of the complexes in the presence of ^{17}O-labeled water, however, indicate that rapid water molecule exchange does not occur on the metal centers of either **1** or **2**. Water exchange kinetics were probed in 60 mM MOPS buffered to pH 7.4 and buffer-free distilled water, with 20% v/v MeCN added to solubilize the coordination complexes in both types of aqueous solutions. Samples containing **1** or **2** do not display broadened ^{17}O NMR signals relative to the nickel-free standards. Since the complexes remain paramagnetic in water (Fig. S1 and S2†), the data are consistent with negligible water molecule exchange between the Ni(II) centers and the bulk solvent.

Electrochemical behavior

Both **1** and **2** were analyzed by cyclic voltammetry (CV) in 100 mM phosphate solution buffered to pH 7.2 (Fig. 2 and Table 3). Each nickel complex displays a redox feature with an $E_{1/2}$ between 15 and 30 mV *vs.* Ag/AgCl. Redox events with similar $E_{1/2}$ values were observed for Mn(II) and Zn(II) com-

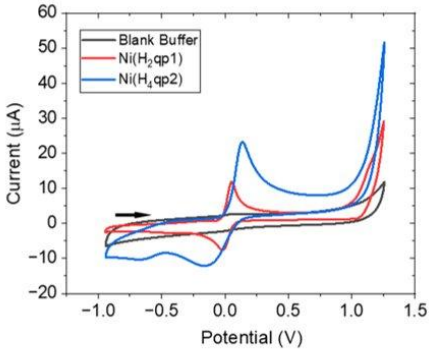

Fig. 2 Cyclic voltammetry of 1.0 mM solutions of **1** (red) and **2** (blue) in water containing 100 mM phosphate buffered to pH 7.2. Data for nickel-free phosphate buffer (black) are provided for comparative purposes. The reference electrode was Ag/AgCl. The scan rate for all three sets of data was 100 mV s^{-1}. The arrow indicates the starting potential and initial scan direction. Complex **1** has $E_{1/2}$ = 29 mV *vs.* Ag/AgCl (ΔE = 59 mV). Complex **2** has $E_{1/2}$ = 15 mV *vs.* Ag/AgCl (ΔE = 310 mV).

Table 3 Summary of electrochemical data for ligand-associated redox processes of H_2qp1 and H_4qp2 complexes

Complex	$E_{1/2}$ (mV)	ΔE (mV)	Ref.
Ni-H_2qp1 (**1**)	29	59	This work
Mn-H_2qp1	115	135	24
Zn-H_2qp1	110	95	29
Ni-H_4qp2 (**2**)	15	310	This work
Mn-H_4qp2	57	232	25
Zn-H_4qp2	195	208	30

All CV was done in 100 mM phosphate solution buffered to pH 7.2 with a 100 mV s^{-1} scan rate.

plexes with H_2qp1 and H_4qp2 (Table 3), leading us to assign these features to the oxidation and reduction of the quinolic portions of the organic ligands.[24,25,29,30] The currents for **2** are approximately double those for **1**. This further supports their assignment to ligand-derived redox processes since **2** has two quinols *versus* the single quinol for **1**. As assessed by the ΔE values measured with a 100 mV s^{-1} scan rate, the ligand oxidation for **1** is reversible, whereas that for **2** is irreversible. The ΔE for manganese and zinc complexes with H_4qp2 were likewise much greater than their H_2qp1 analogs.[24,25,29,30] Notably, no higher potential oxidations are observed for **1** and **2**. With the manganese analogs, conversely, we detected peaks consistent with the oxidation of Mn(II) to Mn(III).[24,25] For complex **2**, we observe an additional reduction with $E_{pc} = -670$ *vs.* Ag/AgCl.

Analysis of the nickel complexes in MeCN likewise fail to detect oxidation of the metal to Ni(III) (Fig. S8–S11†). The data differ from those collected in buffered water in that the redox processes associated with the oxidation of the quinol to the semiquinone are highly irreversible, likely due to subsequent deprotonation of the oxidized form of the ligand. Upon adding triethylamine, these features shift to lower potentials and become much more reversible, supporting our hypothesis that the irreversibility results from acid/base reactions that occur after redox. For both **1** and **2**, we observe currents corresponding to the oxidation of the quinol to semiquinone and its subsequent reduction. For **1**, we also detect quasi-reversible features consistent with the oxidation of the semiquinone to the *para*-quinone and its subsequent reduction. As with the aqueous data, the magnitude of the currents for **2** are approximately twice those for **1**, supporting the assignment of the redox events to ligand- rather than metal-derived processes.

Antioxidant activity

We attempted to screen **1** and **2** for antioxidant activity using two common assays. The xanthine oxidase/hypoxathine/lucigenin assay is frequently used to probe the ability of an antioxidant to decompose superoxide.[24–27] Unfortunately, we were unable to obtain reliable data from this method. We believe that the photophysical properties of the Ni(II) complexes obfuscate the analysis. Lucigenin needs to absorb light at 460 nm to produce a chemiluminescent signal, but both **1** and **2** absorb strongly in this region as well.

The DPPH assay tests the ability of antioxidants to donate hydrogen atoms to 2,2-diphenyl-1-picrylhydrazyl radical hydrate (DPPH).[44–46,58] Hydrogen atom transfer to DPPH yields a distinctly colored hydrazine product which can be identified and quantified by UV/vis. Both **1** and **2** are strong antioxidants by this measure, with 12.5 μM (**1**) and 6.3 μM (**2**) being sufficient to convert half the radical to the hydrazine (Fig. S12†). 21.9 μM of ascorbic acid was needed to elicit a similar response. Other divalent metal complexes with the H_2qp1 and H_4qp2 ligands likewise outperformed ascorbic acid in these measurements by approximately the same extent.[24,25,29] The high sensitivity of the DPPH assay precludes us from drawing more quantitative conclusions regarding the relative reactivities of the H_2qp1 and H_4qp2 complexes.

The aforementioned assays are imperfect measures of the actual reactivity with $O_2^{\bullet-}$ due to the possibility of competing side-reactions between the various components in the reaction mixtures.[19,31,59–62] We more thoroughly and accurately gauged the antioxidant activity by following the direct reactions between the Ni(II) compounds and KO_2 with stopped-flow kinetics methods. These studies confirm that both **1** and **2** are highly capable SOD mimics (Fig. 3, Table 4 and Fig. S13–S16†). $O_2^{\bullet-}$ spontaneously dismutates without a catalyst; the rate law for this background reactivity is second-order in $[O_2^{\bullet-}]$. The metal-free H_2qp1 and H_4qp2 ligands were previously found to be incapable of catalyzing superoxide degradation.[28,29] With either **1** or **2**, however, the decay rate instead becomes first-order in $[O_2^{\bullet-}]$. Varying the amount of catalyst reveals that the rate also has a first-order dependence on the concentration of the nickel complex, consistent with the catalyst and $O_2^{\bullet-}$ reacting in the rate-determining step. The H_4qp2 complex is the more active of the two in all three studied aqueous media by approximately six- to eight-fold. The activity is highest in MOPS buffered to pH 7.4 and lowest in pH 7.4 phosphate solutions. Approximately half of the activity is lost going from MOPS to phosphate buffer.

Mass spectrometry analysis of intermediates and end-products

The activity between the Ni(II) complexes and excess KO_2 in MeCN was probed by CSI-MS at −40 °C (Fig. 4 and Fig. S17–S22†). Without any KO_2, the quinols and metal center of **2** remain in their reduced forms: $[Ni^{II}(H_4qp2)]^{2+}$ and its conjugate base $[Ni^{II}(H_3qp2)]^{+}$ (Fig. S17†). With **1**, conversely, we detect traces of $[Ni^{II}(qp1)]^{2+}$, where *qp1* is the *para*-quinone form of the ligand (Scheme 3), even in the absence of oxidant (Fig. S18†). Within 1 min after the addition of KO_2, we detect Ni(II) species with two-electron oxidized mono-*para*-quinone forms of the ligands (*qp1*, H_2qp2, and $Hqp2^-$) for both **1** and **2** (Fig. 4). We also find traces of oxygenated ligands. The data support the formation of Ni(II) complexes with semiquinone ligands. For **1**, a *m*/*z* peak at 511.1513 is consistent with $[Ni(qp1^{\bullet})]^{+}$, where the ligand is $qp1^{\bullet-}$. For **2**, *m*/*z* peaks at 271.5766 and 270.5687 can be assigned to $[Ni^{II}(H_3qp2^{\bullet})]^{2+}$ and $[Ni^{II}(Hqp2^{\bullet})]^{2+}$, which feature $H_3qp2^{\bullet}$ and the mono-*para*-quinone $Hqp2^{\bullet}$, respectively. We observe neither the di-*para*-quinone form of the ligand, *qp2* (Scheme 3), nor its Ni(II)

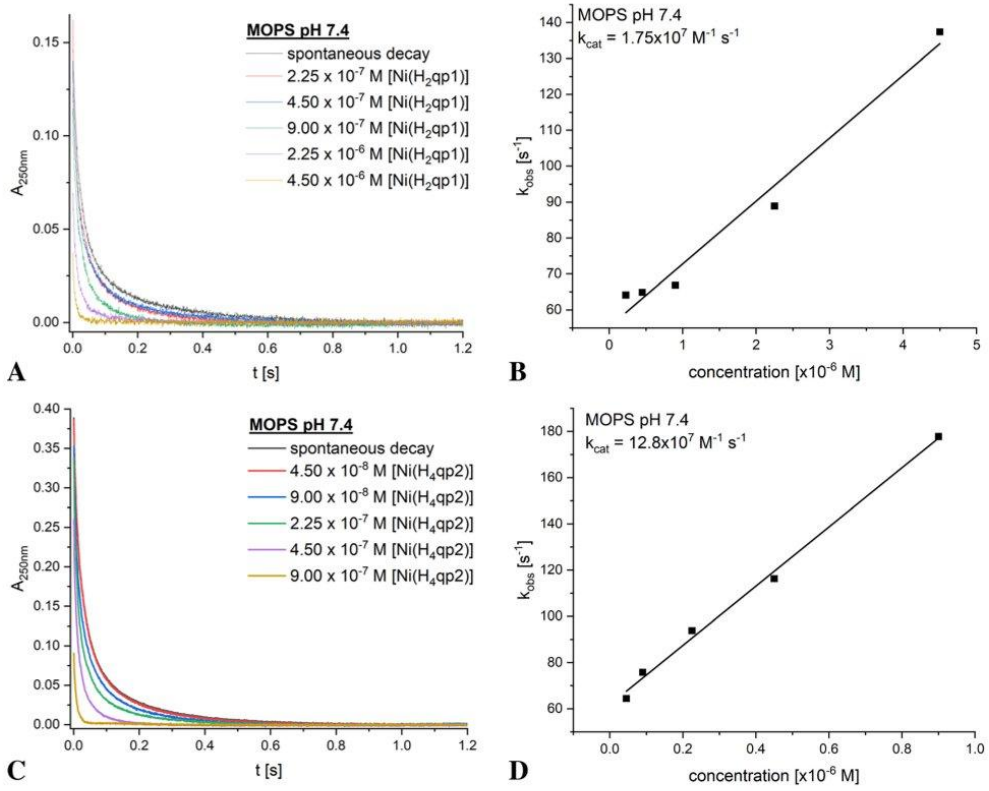

Fig. 3 Kinetic traces and k_{obs} *vs.* concentration plots for nickel-catalyzed superoxide decomposition. The data were taken in 60 mM MOPS buffered to pH 7.4. The absorbance at 250 nm was followed. Each trace is labelled with the concentration of added Ni(II) complex. (A) Kinetic traces for **1**. (B) Plot of k_{obs} *vs.* [**1**]. (C) Kinetic traces for **2**. (D) Plot of k_{obs} *vs.* [**2**].

Table 4 Catalytic rate constants, k_{cat} (M^{-1} s^{-1}), measured by stopped-flow kinetics for the direct reactions of **1** and **2** with superoxide

Buffer, pH	**1** (Ni-H_2qp1)	**2** (Ni-H_4qp2)	Mn-H_2qp1	Mn-H_4qp2	Zn-H_2qp1	Zn-H_4qp2
60 mM MOPS, 7.4	1.75×10^7	12.8×10^7	9.7×10^7 [a]	1.2×10^7 [a]	3.4×10^6 [b]	1.56×10^7 [c]
60 mM MOPS, 7.8	1.18×10^7	9.74×10^7				4.94×10^7 [c]
50 mM Phosphate, 7.4	1.08×10^7	6.21×10^7	8.0×10^6 [a]	1.0×10^7 [a]	1.9×10^7 [b]	2.54×10^7 [c]

[a] Data from ref. 28. 60 mM HEPES used instead of MOPS. [b] Data from ref. 29. 60 mM HEPES used instead of MOPS. [c] Data from ref. 30.

complex at 1 min. After 5 min, *m*/*z* peaks consistent with the loss of the quinol arm for **1** appear (Fig. S19†), but this sort of degradation is not observed for **2** (Fig. S20†), suggesting that this compound is more oxidatively robust.

The Ni(II) compounds and their Zn(II) analogs differ substantially when the reaction aliquots are warmed to RT before MS analysis. Compound **1** appears to completely degrade (Fig. S21†), but the *m*/*z* peaks observed for **2** are consistent with Ni(II) complexes with oxidized forms of the ligands (Fig. S22†). These initially include the mono-*para*-quinone *H_2qp2* itself and singly and doubly oxygenated forms of both *H_2qp2* and H_4qp2. That some of the dioxygenated ligands contain quinols may suggest that the *para*-quinones are still capable of cycling back to the quinol oxidation state even after other portions of the ligand have been oxidized. When we warmed solutions of $[Zn^{II}(H_4qp2)]^{2+}$ and KO_2 to RT before analysis, we instead observe metal-free oxidized ligands rather than Zn(II) complexes.[30]

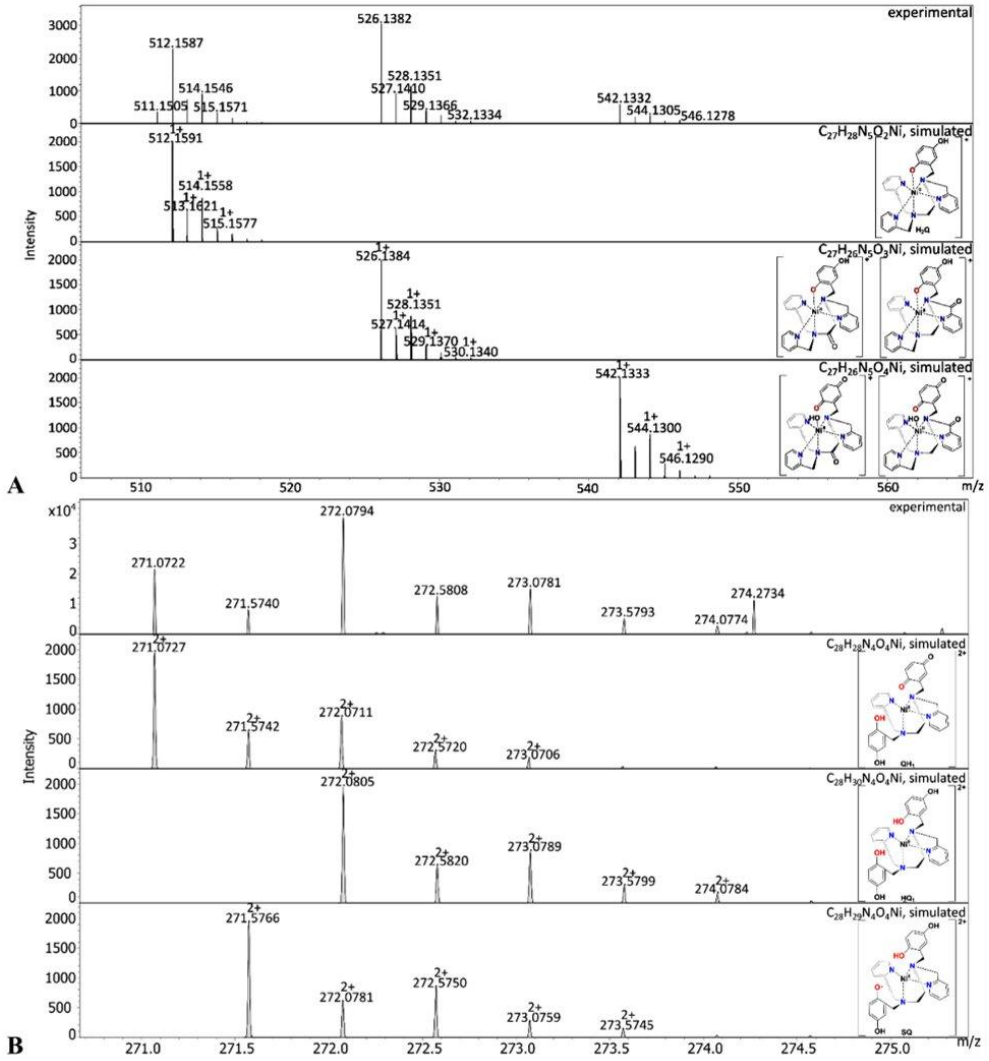

Fig. 4 CSI-MS spectrometry of (A) **1** and (B) **2** after a 1 min reaction with KO_2. The graphics depict possible structures; we cannot preclude other modes of ligand coordination or sites of ligand oxidation. Experimental conditions: 1 mM solutions of each Ni(II) complex in MeCN (1% DMF) were cooled to −40 °C and then mixed with an excess of solid KO_2. Subsequently, the mixture was diluted in a pre-cooled syringe with pre-cooled MeCN to approximately 1×10^{-5} M and quickly injected into the mass spectrometer 1 min after the start of the reaction.

Low-temperature UV/vis analysis

The proposed semiquinone intermediates are corroborated by UV/vis measurements taken at −40 °C (Fig. 5). The reaction between **1** and KO_2 results in the formation of bands at 430 and 454 nm. Much smaller bands at 430 and 448 nm develop during analogous reactions with **2**. The energies of these features are close to those of the 422 and 448 nm bands seen for manganese and zinc complexes with the semiquinone forms of these ligands[28,30] as well as those of semiquinone radical by itself.[63,64] The manganese and zinc complexes with H_4qp2 were previously found to give rise to features at 520 that are

Scheme 3 Oxidized versions of the H_2qp1 and H_4qp2 ligands. Oxidized forms of the ligand are denoted by italics throughout the manuscript.

consistent with quinhydrone species,[28,30] but we unable to unambiguously detect a similar feature for **2**.

Operando stability of the Ni(II)–H_4qp2 catalyst

The CSI-MS experiments failed to detect metal-free oxidized ligands in the reactions between **2** and KO_2, suggesting that **2** does not release its metal ion upon reaction with KO_2 and subsequent warming to RT. The Zn(II) analog of **2**, $[Zn^{II}(H_4qp2)]^{2+}$, does release the metal ion as the ligand is oxidized.[30] We took the resultant solutions for **2** and $[Zn^{II}(H_4qp2)]^{2+}$ and added fresh KO_2 from a 0.5–1.0 mM stock solution to determine whether the metal-containing products were still viable SOD mimetics. The activity of the nickel complex remains high, whereas that for the zinc is almost completely eliminated (Fig. 6). For **2**, a 0.9 μM solution that was treated with 9 μM KO_2 retains 89% of its initial activity. Even with a much larger 120 μM KO_2 pre-treatment, **2** is 43% as active as a fresh batch. With $[Zn^{II}(H_4qp2)]^{2+}$, on the other hand, a two-fold excess of KO_2 is sufficient to eliminate 39% of the activity.

EPR analysis of viable intermediates for SOD mimicry

We attempted to independently generate possible intermediates relevant to the SOD mimicry by reacting **1** and **2** with stoichiometric amounts of Ag(OTf) and Et_3N in MeCN (Fig. 7). We previously ran analogous studies with the Zn(II) complexes with H_2qp1 and H_4qp2 to demonstrate that Zn(II)-quinoxyl radical species were viable intermediates in the catalytic cycles for $O_2^{\bullet-}$ dismutation.[29,30]

EPR analysis of the reaction mixtures suggests that a small amount of the nickel has been oxidized to the +3 oxidation state for both **1** and **2**. For **1**, two small features appear with g = 2.22 and g = 2.00. The intensities of the features maximize by 45 min. The g = 2.00 feature resembles that found for the aforementioned Zn(II)–quinoxyl radical species and resembles features seen for previously reported Ni(II) complexes with organic radicals.[65,66] The g = 2.22 feature may be consistent with a Ni(III) species,[66] although we cannot completely preclude contamination from the silver. Complex **2** gives rise to a stronger feature at g = 2.22 upon reaction with the Ag(I) oxidant and base. No features that can be unambiguously distinguished from noise are seen around g = 2.00, suggesting that organic radicals are not present above the limit of detection. The approximately ten-fold greater intensity of the g = 2.22 feature may suggest that the additional quinolate in the H_4qp2 framework can stabilize Ni(III) to a greater extent than H_2qp1 since the dianionic H_2qp2^{2-} ligand would be anticipated to better neutralize a higher positive charge on the metal center. Nonetheless, the signal-to-noise for both **1** and **2** are poor, and the signal intensities are much weaker than those of the Zn(II)-quinoxyl radical species detected in our prior studies.[29,30] Reacting an equivalent amount of H_4qp2 with Ag(OTf) and Et_3N results in a much more intense EPR signal, further demonstrating that any Ni(III) produced by these non-catalytic conditions accumulates to near negligible concentrations.

Discussion

The *N*-(2,5-dihydroxybenzyl)-*N*,*N*′,*N*′-tris(2-pyridinylmethyl)-1,2-ethanediamine (H_2qp1) and *N*,*N*′-bis(2,5-dihydroxybenzyl)-*N*,

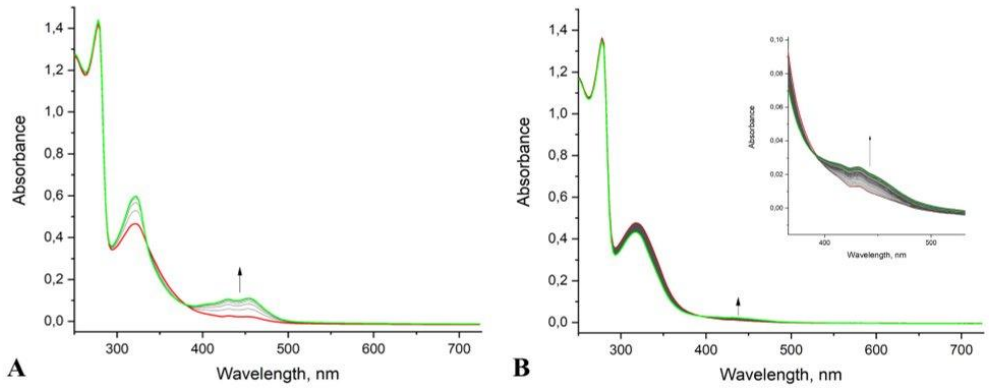

Fig. 5 UV/vis data for the −40 °C MeCN reactions between excess KO_2 and (A) 0.1 mM **1** and (B) 0.1 mM **2**. Data were acquired with a 1.0 cm pathlength.

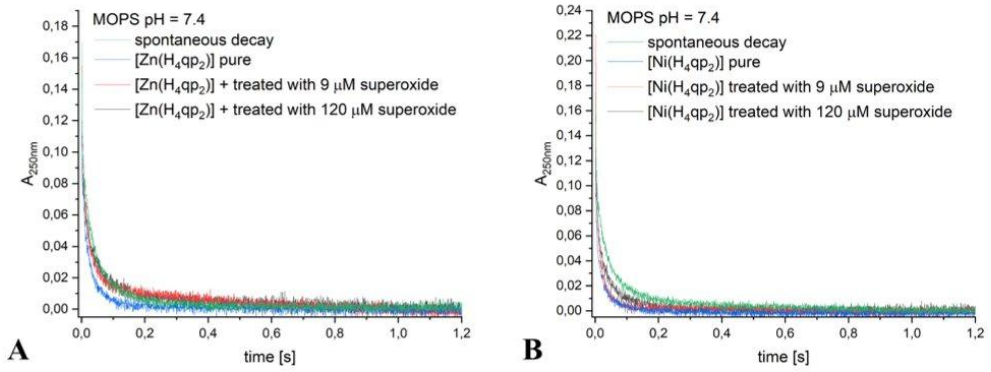

Fig. 6 Kinetic traces of superoxide decomposition at 250 nm in 60 mM MOPS buffer, pH 7.4 for H_4qp2 complexes after pre-treatment with either 9 or 120 μM KO_2. (A) Data for $[Zn^{II}(H_4qp2)](OTf)_2$. (B) Data for **2**.

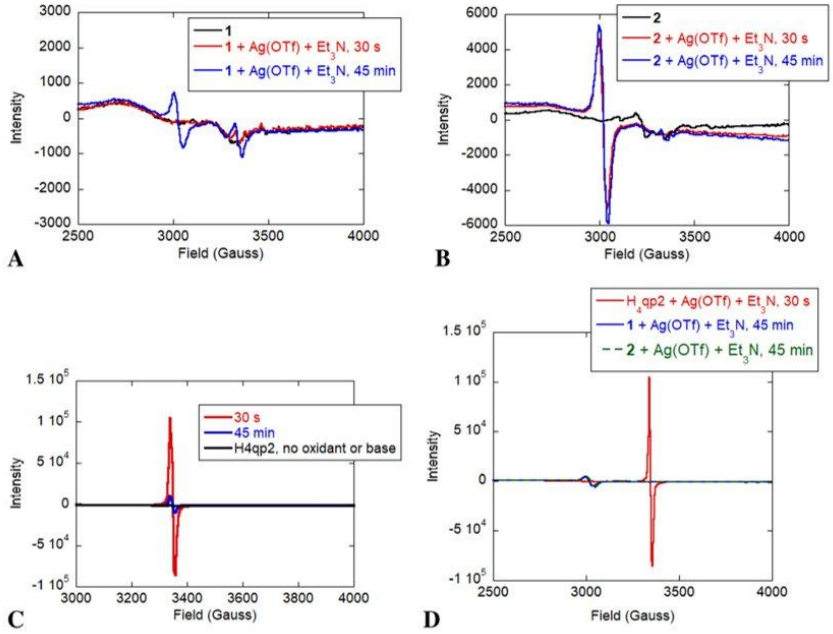

Fig. 7 X-band EPR data for the reactions between (A) 1.0 mM **1**, (B) 1.0 mM **2**, and (C) H_4qp2 with 1.0 mM Ag(OTf) and 1.0 mM Et_3N in MeCN. At the given time points, aliquots were rapidly filtered and frozen at 77 K. (D) Signal intensity comparison.

N′-bis(2-pyridinylmethyl)-1,2-ethanediamine (H_4qp2) ligands were previously used to prepare complexes with Mn(II) and Zn(II), and precipitation from organic solvents enabled us to obtain $[Mn^{II}(H_2qp1)(MeCN)](OTf)_2$, $[Mn^{II}(H_4qp2)Br_2]$, $[Zn^{II}(H_2qp1)(OTf)](OTf)$, $[Zn^{II}(H_2qp1)(MeCN)](OTf)_2$, and $[Zn^{II}(H_4qp2)](OTf)_2$ in moderately high yields ranging from 70% to 90%.[24,25,29,30] The syntheses of Ni(II) complexes with these ligands likewise proceed smoothly, and crystalline samples of both $[Ni^{II}(H_2qp)(MeCN)](OTf)_2$ (**1**) and $[Ni^{II}(H_4qp2)(MeCN)_2](OTf)_2$ (**2**) can be obtained in yields exceeding 40%.

In the crystal structures of $[Mn^{II}(H_4qp2)Br_2]$, $[Zn^{II}(H_2qp1)(OTf)](OTf)$, and $[Zn^{II}(H_2qp1)(MeCN)](OTf)_2$, which were all obtained from MeCN/ether solutions, the protonated quinols do not bind to the metal center.[25,29] In the structures of **1** and **2**, the quinolic portions of the ligands likewise do not coordinate to the Ni(II) (Fig. 1). Overall, the structural data for the Mn(II), Zn(II), and Ni(II) complexes suggest that the pyridines in the ligand are stronger ligands than the quinols. As with the aforementioned Mn(II) and Zn(II) complexes, however, the solid-state structures of **1** and **2** grown from MeCN solution do not appear to be maintained in water.[25,29] UV/vis measurements show that at pH 7.0, a single quinol from each complex has deprotonated to a quinolate, which would have a stronger affinity for cationic metal centers. The pK_a values obtained from potentiometric pH titrations range from 5.8–7.1; these are more consistent with M(II)-phenol complexes than free phenols.[9,23,25,28–30,54,55] The pH titration data for **1** and **2** likewise demonstrate that a quinol from each ligand has deprotonated at pH 7.0. Given that Ni(II) ions rarely have coordination numbers that exceed six,[56,57] the major aqueous cations at this pH are likely $[Ni^{II}(Hqp1)]^+$ and $[Ni^{II}(H_3qp2)]^+$. Although the second quinol in the H_3qp2^- complex interacts weakly with the metal center and could be displaced by water to yield $[Ni^{II}(H_3qp2)(H_2O)]^+$, our ^{17}O NMR data indicate that water molecules are not exchanging at the metal center, suggesting that water is not coordinating to the Ni(II). Although firm stability constants have not been measured for either **1** or **2** due to the lack of metal ion dissociation under acidic conditions, they are unambiguously more stable than their Mn(II) analogs, which release their metal ions under such conditions.[25,28]

Although there is a class of superoxide dismutases (SODs) that naturally contains nickel, neither **1** nor **2** resemble these either structurally or spectroscopically. Nickel-containing SODs cycle between five-coordinate Ni(III) and four-coordinate Ni(II) species.[67] Further, the coordination spheres of the enzymes include two cysteinates and two backbone amidates, with an imidazole ligand completing the coordination of the Ni(III) form. Instead of an S_2N_3 or S_2N_2 coordination sphere, **1** and **2** have N_5O and N_4O_2 sets of donor atoms in aqueous solution, respectively.

Despite their lack of resemblance to the active sites in nickel SODs, both **1** and **2** are nonetheless functional mimics of these enzymes. Stopped-flow kinetics analyses of the direct reactions between the Ni(II) complexes and KO_2 demonstrate that **1** and **2** are highly capable antioxidants (Fig. 3 and Table 4). The metal-free quinolic ligands do not display this behavior.[28,29] The SOD mimicry exhibited by **1** and **2** is noteworthy since nickel has rarely supported this sort of reactivity in small molecule complexes. Complexes with short peptide chains, or maquettes, have been able to reproduce many of the spectroscopic features of nickel-containing SODs and much of the reactivity.[68–75] Complexes with non-peptide-derived ligands, conversely, may react stoichiometrically with superoxide but usually do not act as catalysts.[76–78] Two studies reported catalysis by nickel complexes with azo-aldehyde and Schiff base ligands.[79,80] The reported k_{cat} values range from 1×10^6 M^{-1} s^{-1} to 8×10^6 M^{-1} s^{-1}, but it should be noted that these rate constants were determined through assays, rather than stopped-flow kinetics measurements. Duboc's group, conversely, reported a series of Ni(II) complexes with peptide-containing ligands that were demonstrated to be catalysts by stopped-flow kinetics.[75,81–83] The most active of these compounds catalytically degraded $O_2^{\bullet-}$ with a $k_{cat} = 8.6 \times 10^6$ M^{-1} s^{-1} in 60 mM HEPES solution buffered to pH 8.1.[75] Complexes **1** and **2** are approximately 1.4 and 11 times more active, respectively, under similar conditions (Table 4), with the caveats that we use MOPS instead of HEPES as the sulfonate-derived buffer and operate at pH 7.8 rather than 8.1.

The activities of the nickel complexes, particularly that of **2**, compare well to those of manganese-containing SOD mimics.[15,19,20,31,33,84–87] The k_{cat} measured for **2** in pH 7.4 MOPS buffer exceeds the 9.7×10^7 M^{-1} s^{-1} value measured for $[Mn^{II}(H_2qp1)(MeCN)]^{2+}$ in pH 7.4 HEPES.[28] Although it is not the most active of manganese-porphyrin SOD mimics, the well-characterized $MnBr_8TM\text{-}4\text{-}PyP^{4+}$ has a k_{cat} of 21.9×10^7 M^{-1} s^{-1}; this rate constant, however, may not be directly comparable to the other mentioned values since this k_{cat} was measured through an assay rather than stopped-flow kinetics.[88] The manganese-pentaazamacrocycle M40401 is unambiguously more active as an SOD mimic, with a $k_{cat} = 1.5 \times 10^9$ M^{-1} s^{-1} in pH 7.4 HMES buffer,[89,90] but this complex is much less water-stable than both $[Mn^{II}(H_2qp1)(MeCN)]^{2+}$ and **2**.[28]

Another notable feature about **1** and **2** is that they only lose about 50% of their catalytic activity upon switching from a sulfonic acid-based buffer to phosphate buffer (Table 4). Many manganese complexes that have been studied in phosphate buffer, conversely, lose much more of their activity upon such a switch,[28,31,91,92] and examples that retain most of their activity, such as $[Mn^{II}(H_4qp2)Br_2]$, often tend to be poorer catalysts under all studied conditions.[28,31] The Zn(II) complexes with H_2qp1 and H_4qp2, $[Zn^{II}(H_2qp1)(OTf)]^+$ and $[Zn^{II}(H_4qp4)]^{2+}$, conversely, display enhanced SOD mimicry in phosphate buffer to the extent where they outperform their manganese analogs in this medium (Table 4).[29,30]

That **2** is more catalytically active than **1** may be initially surprising since the Mn(II) complex with H_4qp2 is much less active than the one with H_2qp1 in HEPES solution (although the catalysts are approximately equivalent in phosphate buffer).[28] With Mn(II), the ligands fully deprotonate to $Hqp1^-$ and H_2qp2^{2-}, rendering their complexes monocationic and neutral, respectively. Higher positive charges on SOD mimics tend to lead to faster catalysis, explaining the higher k_{cat} for the H_2qp1 complex. With Ni(II), conversely, the H_4qp2 does not fully deprotonate under catalytic conditions; consequently, both **1** and **2** form predominantly monocationic species in water between pH 7 and 7.8.

Although the Ni(II) complex with H_2qp1 is approximately half as active as its Zn(II) analog in phosphate buffer based on their k_{cat} values, the Ni(II) complex with H_4qp2 is over twice as active as $[Zn^{II}(H_4qp2)]^{2+}$ under such conditions (Table 4). Complex **2** appears to be much more stable than both **1** (Fig. S19–S22†) and the Zn(II) complexes. The reaction between **2** and KO_2 does not promote metal ion dissociation from the

oxidized forms of H_4qp2 as it does with $[Zn^{II}(H_4qp2)]^{2+}$,[30] and samples of **2** that have previously reacted with $O_2^{\bullet-}$ can be used to catalyze subsequent superoxide degradation reactions (Fig. 6). The greater *operando* stability of **2** likely explains its higher activity.

Phosphate is generally believed to inhibit SOD mimetics by acting as a competitive inhibitor that blocks the coordination of $O_2^{\bullet-}$ to the metal center. A recent computational analysis from our groups suggests that phosphate binds to M(III) ions much more tightly than to M(II) ions.[93] Manganese can readily access the +3 oxidation state;[57] consequently, phosphate inhibition has been observed to be particularly severe for manganese-catalyzed superoxide dismutation.[28,31] Zinc, conversely, cannot access the +3 oxidation state, and phosphate actually enhances, rather than hampers, zinc-catalyzed $O_2^{\bullet-}$ dismutation due to its ability to more efficiently transfer protons to and from the positively charged species on the catalytic cycle.[29,30] The redox activity of nickel is intermediary to those of manganese and zinc. Although Ni(III) is relevant to the activities of nickel SODs, Ni(III) species are not observed during catalysis.[57] Even though we could use Ag(OTf) to oxidize trace portions of samples of **1** and **2** to what may be Ni(III) species (Fig. 7), we do not observe any Ni(III) complexes in samples of **1** and **2** oxidized by KO_2 in our cryo-MS experiments (Fig. 4), nor can we access Ni(III) by CV (Fig. 2). If the $O_2^{\bullet-}$ reactions oxidize the metal center to Ni(III) under catalytic conditions, such species would have to be extremely short-lived. Although it was initially tempting to attribute the partial phosphate inhibition of **1** and **2** to the anions' coordination to Ni(III) metal centers, our evidence suggests that these higher-valent metal centers are not abundant enough during catalysis to have an impact. Consequently, the rationale for why phosphate only partly inhibits nickel-driven SOD mimicry remains unclear.

Mechanistically, the SOD mimicry exhibited by **1** and **2** appears to more strongly resemble that of their Zn(II) analogs.[29,30] Even though a prior report found that Ni(III) complexes could directly oxidize quinols,[94] our CSI-MS and UV/vis results suggest that the SOD catalysis for **1** and **2** primarily involves changes to the oxidation states of the ligands rather than the metal center. This differs markedly from what was observed for $[Mn^{II}(H_2qp1)]^{2+}$ and $[Mn^{II}(H_4qp2)]^{2+}$, which proceed through M(III) and M(IV) species during catalysis.[28] The MS data show that the quinols within the ligands oxidize to *para*-quinones. Our MS results also suggest that the *para*-quinones can continue to reduce back to quinols even after other portions of the ligand begin to get oxidized. The oxidation state of the nickel in all species identified by either MS or CSI-MSI is +2. Although traces of Ni(III) may form with a different oxidant (Fig. 7), we do not observe any Ni(III) species in the $O_2^{\bullet-}$ reactions even with H_4qp2, which was found to support the +3 and even the +4 oxidation state for manganese under similar conditions.[28] The cryo-MS and UV/vis data are consistent with the formation of metal complexes with semiquinone radicals (Fig. 4 and 5); analogous intermediates were previously observed in the SOD mimicry with manganese and zinc complexes with these ligands.[28,30]

The lack of rapid water molecule exchange for **1** and **2** further differentiates these compounds from their manganese analogs.[25,28] That the Ni(II) centers are coordinatively saturated at the beginning of the catalysis may suggest that the initial reactions with superoxide are outer-sphere. With the more labile manganese H_2qp1 and H_4qp2 complexes, cryo-MS detected intermediates that are consistent with inner-sphere reactions with $O_2^{\bullet-}$.[28] $[Zn^{II}(H_2qp1)]^{2+}$ was also proposed to reduce and oxidize $O_2^{\bullet-}$ through inner-sphere pathways, albeit on the basis of calculations.[93] Although cryo-MS did not detect intermediates that could be assigned as nickel-superoxide adducts, further studies are needed to determine the relevance of inner- and outer-sphere pathways for $O_2^{\bullet-}$ reduction and oxidation and more fully elucidate the mechanism.

Conclusions

We find that polydentate ligands with redox-active quinols can enable nickel to catalytically degrade superoxide at rates that are highly competitive with those of the most active reported manganese-containing SOD mimics. Although phosphate inhibits catalysis, the diminishment in activity is not as severe as seen for other similarly high performing antioxidants. The ligand design has a noticeable impact on the reactivity in that the complex with the second quinol is much more active. The catalytic cycle remains under investigation but likely involves primarily ligand-centered redox cycles and possibly outer-sphere pathways for at least some of the individual reactions. Overall, the nickel-containing catalysts more strongly resemble their zinc-containing analogs than their manganese-containing counterparts but are more robust than either.

Data availability

Data supporting this article have been included as part of the ESI.† Crystallographic data for **1** and **2** have been deposited at the Cambridge Crystallographic Data Centre under 2390972 and 2390973.

Conflicts of interest

There are no conflicts to declare.

Acknowledgements

We thank Auburn University (AU) and the National Science Foundation (NSF-CHE-1662875, NSF-CHE-1954336) for funding. Additionally, A. F. and I. I.-B. thank the Deutsche Forschungsgemeinschaft (DFG) for their support through the IV 80/13-1 project. Lastly, J. O. and I. I.-B. acknowledge the DFG (Research Unit FOR 5215 "Bioinspired Oxidation Catalysis with Iron Complexes "BioOxCat") TP6 for financial support".

References

1 ,M. I. Ahmed, J. D. Gladden, S. H. Litovsky, S. G. Lloyd, H. Gupta, S. Inusah, T. Denney Jr., P. Powell, D. C. McGiffin and L. J. Dell'Italia, Increased Oxidative Stress and Cardiomyocyte Myofibrillar Degeneration in Patients with Chronic Isolated Mitral Regurgitation and Ejection Fraction >60%, *J. Am. Coll. Cardiol.*, 2010, **55**(7), 671–679.

2 I. M. Fearon and S. P. Faux, Oxidative Stress and Cardiovascular Disease: Novel Tools Give (Free) Radical Insight, *J. Mol. Cell. Cardiol.*, 2009, **47**(3), 372–381.

3 G. Eskici and P. H. Axelsen, Copper and Oxidative Stress in the Pathogenesis of Alzheimer's Disease, *Biochemistry*, 2012, **51**(32), 6289–6311.

4 V. L. Kinnula, Production and Degradation of Oxygen Metabolites During Inflammatory States in the Human Lung, *Curr. Drug Targets:Inflammation Allergy*, 2005, **4**(4), 465–470.

5 S. F. AbdulSalam, F. S. Thowfeik and E. J. Merino, Excessive Reactive Oxygen Species and Exotic DNA Lesions as an Exploitable Liability, *Biochemistry*, 2016, **55**(38), 5341–5352.

6 Q. N. Do, J. S. Ratnakar, Z. Kovács and A. D. Sherry, Redox- and Hypoxia-Responsive MRI Contrast Agents, *ChemMedChem*, 2014, **9**(6), 1116–1129.

7 Z. Lou, P. Li and K. Han, Redox-Responsive Fluorescent Probes with Different Design Strategies, *Acc. Chem. Res.*, 2015, **48**(5), 1358–1368.

8 G. S. Loving, S. Mukherjee and P. Caravan, Redox-Activated Manganese-Based MR Contrast Agent, *J. Am. Chem. Soc.*, 2013, **135**(12), 4620–4623.

9 E. M. Gale, S. Mukherjee, C. Liu, G. S. Loving and P. Caravan, Structure-Redox-Relaxivity Relationships for Redox Responsive Manganese-Based Magnetic Resonance Imaging Probes, *Inorg. Chem.*, 2014, **53**(19), 10748–10761.

10 E. M. Gale, C. M. Jones, I. Ramsay, C. T. Farrar and P. Caravan, A Janus Chelator Enables Biochemically Responsive MRI Contrast with Exceptional Dynamic Range, *J. Am. Chem. Soc.*, 2016, **138**(49), 15861–15864.

11 B. Song, Y. Wu, M. Yu, P. Zhao, C. Zhou, G. E. Kiefer and A. D. Sherry, A Europium(III)-Based PARACEST Agent for Sensing Singlet Oxygen by MRI, *Dalton Trans.*, 2013, **42**(22), 8066–8069.

12 S. J. Ratnakar, S. Viswanathan, Z. Kovacs, A. K. Jindal, K. N. Green and A. D. Sherry, Europium(III) DOTA-tetraamide Complexes as Redox-Active MRI Sensors, *J. Am. Chem. Soc.*, 2012, **134**(13), 5798–5800.

13 P. B. Tsitovich, J. A. Spernyak and J. R. Morrow, A Redox-Activated MRI Contrast Agent that Switches Between Paramagnetic and Diamagnetic States, *Angew. Chem., Int. Ed.*, 2013, **52**(52), 13997–14000.

14 P. B. Tsitovich, P. J. Burns, A. M. McKay and J. R. Morrow, Redox-Activated MRI Contrast Agents Based on Lanthanide and Transition Metal Ions, *J. Inorg. Biochem.*, 2014, **133**, 143–154.

15 D. P. Riley and R. H. Weiss, Manganese Macrocyclic Ligand Complexes as Mimics of Superoxide Dismutase, *J. Am. Chem. Soc.*, 1994, **116**(1), 387–388.

16 D. P. Riley, P. J. Lennon, W. L. Neumann and R. H. Weiss, Toward the Rational Design of Superoxide Dismutase Mimics: Mechanistic Studies for the Elucidation of Substituent Effects on the Catalytic Activity of Macrocyclic Manganese(II) Complexes, *J. Am. Chem. Soc.*, 1997, **119**(28), 6522–6528.

17 A. Tovmasyan, S. Carballal, R. Ghazaryan, L. Melikyan, T. Weitner, C. G. C. Maia, J. S. Reboucas, R. Radi, I. Spasojevic, L. Benov and I. Batinic-Haberle, Rational Design of Superoxide Dismutase (SOD) Mimics: The Evaluation of the Therapeutic Potential of New Cationic Mn Porphyrins with Linear and Cyclic Substituents, *Inorg. Chem.*, 2014, **53**(21), 11467–11483.

18 I. A. Abreu and D. E. Cabelli, Superoxide Dismutases- A Review of the Metal-Associated Mechanistic Variations, *Biochim. Biophys. Acta*, 2010, **1804**, 263–274.

19 D. P. Riley, Functional Mimics of Superoxide Dismutase Enzymes as Therapeutic Agents, *Chem. Rev.*, 1999, **99**(9), 2573–2588.

20 I. Batinic-Haberle, J. S. Reboucas and I. Spasojevic, Superoxide Dismutase Mimics: Chemistry, Pharmacology, and Therapeutic Potential, *Antioxid. Redox Signal.*, 2010, **13**, 877–918.

21 I. Batinic-Haberle, Z. Rajic, A. Tovmasyan, J. S. Reboucas, X. Ye, K. W. Leong, M. W. Dewhirst, Z. Vujaskovic, L. Benov and I. Spasojevic, Diverse Functions of Cationic Mn(III) N-substituted Pyridylporphyrins, Recognized as SOD Mimics, *Free Radicals Biol. Med.*, 2011, **51**, 1035–1053.

22 M. Yu, R. J. Beyers, J. D. Gorden, J. N. Cross and C. R. Goldsmith, A Magnetic Resonance Imaging Contrast Agent Capable of Detecting Hydrogen Peroxide, *Inorg. Chem.*, 2012, **51**, 9153–9155.

23 S. Karbalaei, E. Knecht, A. Franke, A. Zahl, A. C. Saunders, P. R. Pokkuluri, R. J. Beyers, I. Ivanović-Burmazović and C. R. Goldsmith, A Macrocyclic Ligand Framework That Improves Both the Stability and T_1-Weighted MRI Response of Quinol-Containing H_2O_2 Sensors, *Inorg. Chem.*, 2021, **60**(12), 8368–8379.

24 M. Yu, S. L. Ambrose, Z. L. Whaley, S. Fan, J. D. Gorden, R. J. Beyers, D. D. Schwartz and C. R. Goldsmith, A Mononuclear Manganese(II) Complex Demonstrates a Strategy to Simultaneously Image and Treat Oxidative Stress, *J. Am. Chem. Soc.*, 2014, **136**, 12836–12839.

25 M. Yu, M. B. Ward, A. Franke, S. L. Ambrose, Z. L. Whaley, T. M. Bradford, J. D. Gorden, R. J. Beyers, R. C. Cattley, I. Ivanović-Burmazović, D. D. Schwartz and C. R. Goldsmith, Adding a Second Quinol to a Redox-Responsive MRI Contrast Agent Improves Its Relaxivity Response to H_2O_2, *Inorg. Chem.*, 2017, **56**(5), 2812–2826.

26 O. Iranzo, Manganese Complexes Displaying Superoxide Dismutase Activity: A Balance between Different Factors, *Bioorg. Chem.*, 2011, **39**, 73–87.

27 J. M. McCord and I. Fridovich, Superoxide Dismutase: An Enzymic Function for Erythrocuprein (Hemocuprein), *J. Biol. Chem.*, 1969, **244**(22), 6049–6055.
28 L. Senft, J. L. Moore, A. Franke, K. R. Fisher, A. Scheitler, A. Zahl, R. Puchta, D. Fehn, S. Ison, S. Sader, I. Ivanović-Burmazović and C. R. Goldsmith, Quinol-Containing Ligands Enable High Superoxide Dismutase Activity by Modulating Coordination Number, Charge, Oxidation States and Stability of Manganese Complexes throughout Redox Cycling, *Chem. Sci.*, 2021, **12**(31), 10483–10500.
29 M. B. Ward, A. Scheitler, M. Yu, L. Senft, A. S. Zillmann, J. D. Gorden, D. D. Schwartz, I. Ivanović-Burmazović and C. R. Goldsmith, Superoxide Dismutase Activity Enabled by a Redox-Active Ligand rather than a Metal, *Nat. Chem.*, 2018, **10**(12), 1207–1212.
30 J. L. Moore, J. Oppelt, L. Senft, A. Franke, A. Scheitler, M. W. Dukes, H. B. Alix, A. C. Saunders, S. Karbalaei, D. D. Schwartz, I. Ivanović-Burmazović and C. R. Goldsmith, Diquinol Functionality Boosts the Superoxide Dismutase Mimicry of a Zn(II) Complex with a Redox-Active Ligand while Maintaining Catalyst Stability and Enhanced Activity in Phosphate Solution, *Inorg. Chem.*, 2022, **61**(49), 19983–19997.
31 F. C. Friedel, D. Lieb and I. Ivanović-Burmazović, Comparative Studies on Manganese-Based SOD Mimetics, Including the Phosphate Effect, by Using Global Spectral Analysis, *J. Inorg. Biochem.*, 2012, **109**, 26–32.
32 D. Lieb, F. C. Friedel, M. Yawer, A. Zahl, M. M. Khusniyarov, F. W. Heinemann and I. Ivanović-Burmazović, Dinuclear Seven-Coordinate Mn(II) Complexes: Effect of Manganese(II)-Hydroxo Species on Water Exchange and Superoxide Dismutase Activity, *Inorg. Chem.*, 2013, **52**(1), 222–236.
33 I. Kenkel, A. Franke, M. Dürr, A. Zahl, C. Dücker-Benfer, J. Langer, M. R. Filipović, M. Yu, R. Puchta, S. R. Fiedler, M. P. Shores, C. R. Goldsmith and I. Ivanović-Burmazović, Switching between Inner- and Outer-Sphere PCET Mechanisms of Small Molecule Activation: Superoxide Dismutation and Oxygen/Superoxide Reduction Reactivity Deriving from the Same Manganese Complex, *J. Am. Chem. Soc.*, 2017, **139**(4), 1472–1484.
34 C. Bergwitz and H. Jüppner, Phosphate Sensing, *Adv. Chronic Kidney Dis.*, 2011, **18**(2), 132–144.
35 A. Bevington, K. I. Mundy, A. J. Yates, J. A. Kanis, R. G. Russell, D. J. Taylor, B. Rajagopalan and G. K. Radda, A Study of Intracellular Orthophosphate Concentration in Human Muscle and Erythrocytes by ^{31}P Nuclear Magnetic Resonance Spectroscopy and Selective Chemical Assay, *Clin. Sci.*, 1986, **71**(6), 729–735.
36 A. E. Martell, *Critical Stability Constants*, Plenum Press, 1974.
37 H. Irving and R. J. P. Williams, The Stability of Transition-Metal Complexes, *J. Chem. Soc.*, 1953, 3192–3210.
38 P. Chen, S. Chakraborty, S. Mukhopadhyay, E. Lee, M. M. B. Paoliello, A. B. Bowman and M. Aschner, Manganese Homeostasis in the Nervous System, *J. Neurochem.*, 2015, **134**(4), 601–610.
39 B. Drahoš, I. Lukeš and É. Tóth, Manganese(II) Complexes as Potential Contrast Agents for MRI, *Eur. J. Inorg. Chem.*, 2012, **2012**(12), 1975–1986.
40 J. B. Aitken, E. L. Shearer, N. M. Giles, B. Lai, S. Vogt, J. S. Reboucas, I. Batinic-Haberle, P. A. Lay and G. I. Giles, Intracellular Targeting and Pharmacological Activity of the Superoxide Dismutase Mimics MnTE-2-PyP^{5+} and MnTnHex-2-PyP^{5+} Regulated by Their Porphyrin Ring Substituents, *Inorg. Chem.*, 2013, **52**, 4121–4123.
41 P. C. M. van Zijl and N. N. Yadav, Chemical Exchange Saturation Transter (CEST): What Is in a Name and What Isn't?, *Magn. Reson. Med.*, 2011, **65**, 927–948.
42 S. Zhang, M. Merritt, D. E. Woessner, D. E. Lenkinski and A. D. Sherry, PARACEST Agents: Modulating MRI Contrast via Water Proton Exchange, *Acc. Chem. Res.*, 2003, **36**(10), 783–790.
43 P. Gans, A. Sabatini and A. Vacca, *Talanta*, 1996, **43**, 1739–1753.
44 S. B. Kedare and R. P. Singh, Genesis and Development of DPPH Method of Antioxidant Assay, *J. Food Sci. Technol.*, 2011, **48**(4), 412–422.
45 M. S. Blois, Antioxidant Determinations by Use of a Stable Free Radical, *Nature*, 1958, **181**, 1199–1200.
46 E. R. Milaeva, D. B. Shpakovsky, Y. A. Gracheva, S. I. Orlova, V. V. Maduar, B. N. Tarasevich, N. N. Meleshonkova, L. G. Dubova and E. F. Shevtsova, Metal Complexes with Functionalised 2,2′-Dipicolylamine Ligand Containing an Antioxidant 2,6-Di-*tert*-butylphenol Moiety: Synthesis and Biological Studies, *Dalton Trans.*, 2013, **42**(19), 6817–6828.
47 R. S. Drago, *Physical Methods for Chemists*, Surfside Scientific Publishers, 1992.
48 S. V. Obisesan, C. Rose, B. H. Farnum and C. R. Goldsmith, Co(II) Complex with a Covalently Attached Pendent Quinol Selectively Reduces O_2 to H_2O, *J. Am. Chem. Soc.*, 2022, **144**(50), 22826–22830.
49 S. Karbalaei, A. Franke, A. Jordan, C. Rose, P. R. Pokkuluri, R. J. Beyers, A. Zahl, I. Ivanović-Burmazović and C. R. Goldsmith, A Highly Water- and Air-Stable Iron-Containing MRI Contrast Agent Sensor for H_2O_2, *Chem. – Eur. J.*, 2022, **28**, e202201179.
50 S. Karbalaei, A. Franke, J. Oppelt, T. Aziz, A. Jordan, P. R. Pokkuluri, D. D. Schwartz, I. Ivanović-Burmazović and C. R. Goldsmith, A Macrocyclic Quinol-Containing Ligand Enables High Catalase Activity even with a Redox-Inactive Metal at the Expense of the Ability to Mimic Superoxide Dismutase, *Chem. Sci.*, 2023, **14**, 9910–9922.
51 R. D. Shannon, Revised Effective Ionic Radii and Systematic Studies of Interatomic Distances in Halides and Chalcogenides, *Acta Crystallogr., Sect. A*, 1976, **32**, 751–767.
52 T.-L. Chan and T. C. W. Mak, X-Ray Crystallographic Study of Guest-Molecule Orientations in the β-Hydroquinone Clathrates of Acetonitrile and Methyl Isocyanide, *J. Chem. Soc., Perkin Trans. 2*, 1983, (6), 777–781.
53 M. Quan, D. Sanchez, M. F. Wasylkiw and D. K. Smith, Voltammetry of Quinones in Unbuffered Aqueous Solution: Reassessing the Roles of Proton Transfer and Hydrogen

Bonding in the Aqueous Electrochemistry of Quinones, *J. Am. Chem. Soc.*, 2007, **129**(42), 12847–12856.
54 S. C. Sahoo, M. Dubey, M. A. Alam and M. Ray, Effect of Metal Coordination and Intra-Molecular H-Bond on the Acidity of Phenolic Proton in a Set of Structurally Characterized Octahedral Ni(II) Complexes of l-Histidine Derivative, *Inorg. Chim. Acta*, 2010, **363**(12), 3055–3060.
55 Y. Iitaka, T. Koike and E. Kimura, Molecular Structure of a Nickel(II) Complex with Phenolate Appended Cyclam, *Inorg. Chem.*, 1986, **25**(4), 402–404.
56 D. Casanova, P. Alemany, J. M. Bofill and S. Alvarez, Shape and Symmetry of Heptacoordinate Transition-Metal Complexes: Structural Trends, *Chem. – Eur. J.*, 2003, **9**(6), 1281–1295.
57 F. A. Cotton and G. Wilkinson, *Advanced Inorganic Chemistry*, John Wiley & Sons, 1988.
58 J. Ancerewicz, E. Migliavacca, P.-A. Carrupt, B. Testa, F. Brée, R. Zini, J.-P. Tillement, S. Labidalle, D. Guyot, A.-M. Chauvet-Monges, A. Crevat and A. Le Ridant, Structure-Property Relationships of Trimetazidine Derivatives and Model Compounds as Potential Antioxidants, *Free Radicals Biol. Med.*, 1998, **25**(1), 113–120.
59 I. Fridovich, Superoxide Anion Radical (O_2^-), Superoxide Dismutases, and Related Matters, *J. Biol. Chem.*, 1997, **272**(30), 18515–18517.
60 S. I. Liochev, Superoxide Dismutase Mimics, Other Mimics, Antioxidants, Prooxidants, and Related Matters, *Chem. Res. Toxicol.*, 2013, **26**, 1312–1319.
61 D. P. Riley, W. J. Rivers and R. H. Weiss, Stopped-Flow Kinetic Analysis for Monitoring Superoxide Decay in Aqueous Systems, *Anal. Biochem.*, 1991, **196**, 344–349.
62 S. I. Liochev and I. Fridovich, Lucigenin (Bis-N-methylacridinium) as a Mediator of Superoxide Anion Production, *Arch. Biochem. Biophys.*, 1997, **337**, 115–120.
63 A. J. Swallow, in *Functions of Quinones in Energy Converting Systems*, ed. B. L. Trumpower, Elsevier, Inc., 1982, pp. 59–72.
64 X. Zhao, H. Imahori, C.-G. Zhan, Y. Sakata, S. Iwata and T. Kitagawa, Resonance Raman and FTIR Spectra of Isotope-Labeled Reduced 1,4-Benzoquinone and Its Protonated Forms in Solutions, *J. Phys. Chem. A*, 1997, **101**(4), 622–631.
65 T. D. Manuel and J.-U. Rohde, Reaction of a Redox-Active Ligand Complex of Nickel with Dioxygen Probes Ligand-Radical Character, *J. Am. Chem. Soc.*, 2009, **131**(43), 15582–15583.
66 R. Kunert, C. Philouze, O. Jarjayes and F. Thomas, Stable M(II)-Radicals and Nickel(III) Complexes of a Bis(phenol) N-Heterocyclic Carbene Chelated to Group 10 Metal Ions, *Inorg. Chem.*, 2019, **58**(12), 8030–8044.
67 D. P. Barondeau, C. J. Kassmann, C. K. Bruns, J. A. Tainer and E. D. Getzoff, Nickel Superoxide Dismutase Structure and Mechanism, *Biochemistry*, 2004, **43**(25), 8038–8047.
68 J. Shearer, Insight into the Structure and Mechanism of Nickel-Containing Superoxide Dismutase Derived from Peptide-Based Mimics, *Acc. Chem. Res.*, 2014, **47**(8), 2332–2341.
69 J. Shearer and L. M. Long, A Nickel Superoxide Dismutase Maquette That Reproduces the Spectroscopic and Functional Properties of the Metalloenzyme, *Inorg. Chem.*, 2006, **45**(6), 2358–2360.
70 M. Schmidt, S. Zahn, M. Carella, O. Ohlenschläger, M. Görlach, E. Kothe and J. Weston, Solution Structure of a Functional Biomimetic and Mechanistic Implications for Nickel Superoxide Dismutases, *ChemBioChem*, 2008, **9**(13), 2135–2146.
71 M. E. Krause, A. M. Glass, T. A. Jackson and J. S. Laurence, Novel Tripeptide Model of Nickel Superoxide Dismutase, *Inorg. Chem.*, 2010, **49**(2), 362–364.
72 M. E. Krause, A. M. Glass, T. A. Jackson and J. S. Laurence, Embedding the Ni-SOD Mimetic Ni-NCC within a Polypeptide Sequence Alters the Specificity of the Reaction Pathway, *Inorg. Chem.*, 2013, **52**(1), 77–83.
73 J. Shearer, Use of a Metallopeptide-Based Mimic Provides Evidence for a Proton-Coupled Electron-Transfer Mechanism for Superoxide Reduction by Nickel-Containing Superoxide Dismutase, *Angew. Chem., Int. Ed.*, 2013, **52**(9), 2569–2572.
74 J. Shearer, K. P. Neupane and P. E. Callan, Metallopeptide Based Mimics with Substituted Histidines Approximate a Key Hydrogen Bonding Network in the Metalloenzyme Nickel Superoxide Dismutase, *Inorg. Chem.*, 2009, **48**(22), 10560–10571.
75 P. Guinard, S. Hostachy, L. Diebold, J. Pécaut, A. Le Goff, C. Duboc and P. Delangle, Outstanding Superoxide Dismutase Catalytic Activity Of Simple Peptide-Based Nickel(II) Complexes, *Angew. Chem., Int. Ed.*, 2024, **63**(41), e202409343.
76 S. K. Chatterjee, R. C. Maji, S. K. Barman, M. M. Olmstead and A. K. Patra, Hexacoordinate Nickel(II)/(III) Complexes that Mimic the Catalytic Cycle of Nickel Superoxide Dismutase, *Angew. Chem., Int. Ed.*, 2014, **53**(38), 10184–10189.
77 D. Nakane, Y. Wasada-Tsutsui, Y. Funahashi, T. Hatanaka, T. Ozawa and H. Masuda, A Novel Square-Planar Ni(II) Complex with an Amino—Carboxamido—Dithiolato-Type Ligand as an Active-Site Model of NiSOD, *Inorg. Chem.*, 2014, **53**(13), 6512–6523.
78 V. G. Snider, E. R. Farquhar, M. Allen, A. Abu-Spetani and A. Mukherjee, Design and Reactivity of Ni-Complexes Using Pentadentate Neutral-Polypyridyl Ligands: Possible Mimics of NiSOD, *J. Inorg. Biochem.*, 2017, **175**, 110–117.
79 R. Kose, S. A. Gungor, S. E. Kariper, M. Kose and M. Kurtoglu, The New O,O and N,O Type Ligands and their Cu(II) and Ni(II) Complexes: Crystal Structure, Absorption-Emission Properties and Superoxide Dismutase Mimetic Studies, *Inorg. Chim. Acta*, 2017, **462**, 130–141.
80 H.-D. Bian, J. Wang, Y. Wei, J. Tang, F.-P. Huang, D. Yao, Q. Yu and H. Liang, Superoxide Dismutase Activity Studies of Mn(III)/Cu(II)/Ni(II) Complexes with Schiff Base Ligands, *Polyhedron*, 2015, **90**, 147–153.
81 J. Domergue, P. Guinard, M. Douillard, J. Pécaut, S. Hostachy, O. Proux, C. Lebrun, A. Le Goff, P. Maldivi,

C. Duboc and P. Delangle, A Series of Ni Complexes Based on a Versatile ATCUN-Like Tripeptide Scaffold to Decipher Key Parameters for Superoxide Dismutase Activity, *Inorg. Chem.*, 2023, **62**(23), 8747–8760.

82 J. Domergue, P. Guinard, M. Douillard, J. Pécaut, O. Proux, C. Lebrun, A. Le Goff, P. Maldivi, P. Delangle and C. Duboc, A Bioinspired Ni^{II} Superoxide Dismutase Catalyst Designed on an ATCUN-like Binding Motif, *Inorg. Chem.*, 2021, **60**(17), 12772–12780.

83 J. Domergue, J. Pécaut, O. Proux, C. Lebrun, C. Gateau, A. Le Goff, P. Maldivi, C. Duboc and P. Delangle, Mononuclear Ni(II) Complexes with a S_3O Coordination Sphere Based on a Tripodal Cysteine-Rich Ligand: pH Tuning of the Superoxide Dismutase Activity, *Inorg. Chem.*, 2019, **58**(19), 12775–12785.

84 D. P. Riley, S. L. Henke, P. J. Lennon, R. H. Weiss, W. L. Neumann, W. J. Rivers, K. W. Aston, K. R. Sample, H. Rahman, C.-S. Ling, J.-J. Shieh and D. H. Busch, Synthesis, Characterization, and Stability of Manganese(II) C-Substituted 1,4,7,10,13-Pentaazacyclopentadecane Complexes Exhibiting Superoxide Dismutase Activity, *Inorg. Chem.*, 1996, **35**(18), 5213–5231.

85 G.-F. Liu, K. Dürr, R. Puchta, F. W. Heinemann, R. van Eldik and I. Ivanović-Burmazović, Chelate Electronic Properties Control the Redox Behaviour and Superoxide Reactivity of Seven-Coordinate Manganese(II) Complexes, *Dalton Trans.*, 2009, 6292–6295.

86 I. Batinic-Haberle and I. Spasojevic, 25 Years of Development of Mn Porphyrins—from Mimics of Superoxide Dismutase Enzymes to Thiol Signaling to Clinical Trials: The Story of Our Life in the USA, *J. Porphyrins Phthalocyanines*, 2019, **23**(11–12), 1326–1335.

87 C. Policar, Mimicking SOD, Why and How: Bio-Inspired Manganese Complexes as SOD Mimic, in *Redox-Active Therapeutics. Oxidative Stress in Applied Basic Research and Clinical Practice*, ed. I. Batinić-Haberle, J. Rebouças and I. Spasojević, Springer, Cham, 2016.

88 I. Batinić-Haberle, S. I. Liochev, I. Spasojević and I. Fridovich, A Potent Superoxide Dismutase Mimic: Manganese β-Octabromo-meso-tetrakis-(N-methylpyridinium-4-yl) Porphyrin, *Arch. Biochem. Biophys.*, 1997, **343**(2), 225–233.

89 D. Salvemini, Z.-Q. Wang, J. L. Zweier, A. Samouilov, H. Macarthur, T. P. Misko, M. G. Currie, S. Cuzzocrea, J. A. Sikorski and D. P. Riley, A Nonpeptidyl Mimic of Superoxide Dismutase with Therapeutic Activity in Rats, *Science*, 1999, **286**(5438), 304–306.

90 K. Aston, N. Rath, A. Naik, U. Slomczynska, O. F. Schall and D. P. Riley, Computer-Aided Design (CAD) of Mn(II) Complexes: Superoxide Dismutase Mimetics with Catalytic Activity Exceeding the Native Enzyme, *Inorg. Chem.*, 2001, **40**(8), 1779–1789.

91 D. Lieb, *Mechanistic and Synthetic Approaches for Activation of Water-and Oxygen-Species by Biomimetic Systems (Containing Manganese and Cobalt)*, University of Erlangen-Nuremberg, 2013.

92 I. Kenkel, A. Franke, M. Dürr, A. Zahl, C. Dücker-Benfer, J. Langer, M. R. Filipović, M. Yu, R. Puchta, S. R. Fiedler, M. P. Shores, C. R. Goldsmith and I. Ivanović-Burmazović, Switching between Inner- and Outer-Sphere PCET Mechanisms of Small-Molecule Activation: Superoxide Dismutation and Oxygen/Superoxide Reduction Reactivity Deriving from the Same Manganese Complex, *J. Am. Chem. Soc.*, 2017, **139**(4), 1472–1484.

93 E. Miliordos, J. L. Moore, S. V. Obisesan, J. Oppelt, I. Ivanović-Burmazović and C. R. Goldsmith, Computational Analysis of the Superoxide Dismutase Mimicry Exhibited by a Zinc(II) Complex with a Redox-Active Organic Ligand, *J. Phys. Chem. A*, 2024, **128**(8), 1491–1500.

94 J. C. Brodovitch, A. McAuley and T. Oswald, Kinetics and Mechanism of the Oxidation of Hydroquinone and Catechol by $[Ni(III)cyclam]^{3+}$ in Aqueous Perchlorate Media, *Inorg. Chem.*, 1982, **21**(9), 3442–3447.

Supplementary Information (SI) for Dalton Transactions.

Supporting Information for

Nickel(II) Complexes with Covalently Attached Quinols Rely on Ligand-Derived Redox Couples to Catalyze Superoxide Dismutation

Robert Boothe,[†,a] Julian Oppelt,[‡,§,a] Alicja Franke,[‡,§] Jamonica L. Moore,[†] Andrea Squarcina,[‡] Achim Zahl,[§] Laura Senft,[‡] Ina Kellner,[‡] Akudo L. Awalah,[†] Alisabeth Bradford,[†] Segun V. Obisesan,[†] Dean D. Schwartz,[¥] Ivana Ivanović-Burmazović,[‡,*] and Christian R. Goldsmith[†,*]

[†]Department of Chemistry and Biochemistry, Auburn University, Auburn, AL 36849, USA
[‡]Department of Chemistry, Ludwig-Maximilians-Universität München, 81377 München, Germany
[§]Department of Chemistry and Pharmacy, Friedrich-Alexander-Universität Erlangen-Nürnberg, Egerlandster. 1, 91508 Erlangen, Germany
[¥]Department of Anatomy, Physiology, and Pharmacology, College of Veterinary Medicine, Auburn University, Auburn, AL 36849, USA

*Corresponding authors: Ivana.Ivanovic-Burmazovic@cup.uni-muenchen.de, crgoldsmith@auburn.edu

[a]These authors contributed equally to the manuscript.

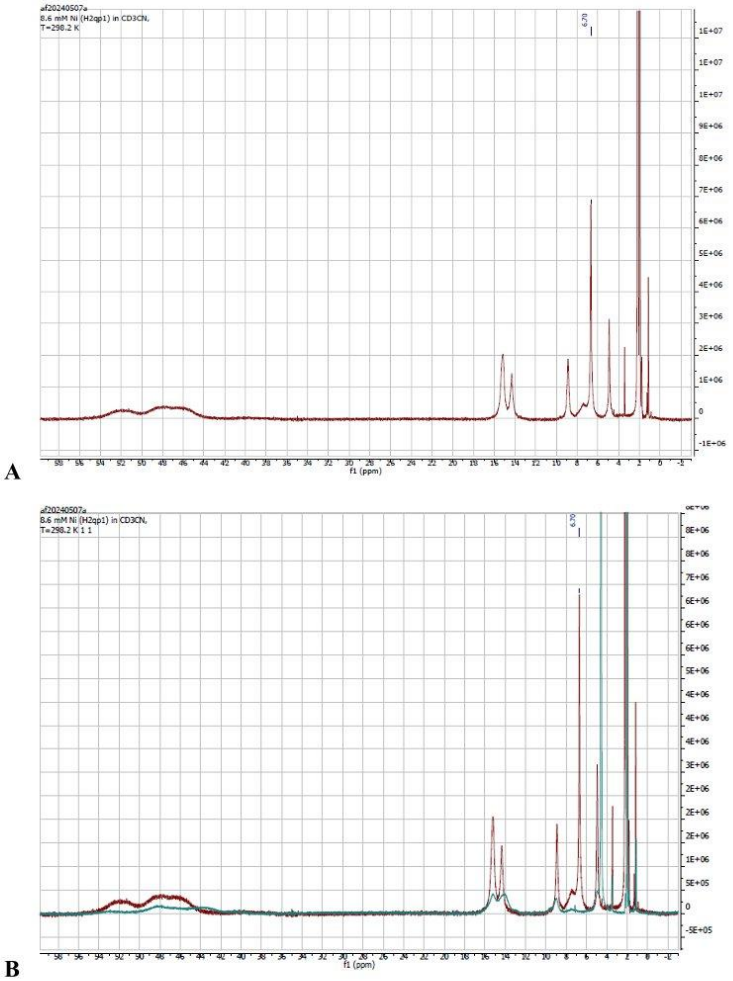

Figure S1. A) ^{1}H NMR data (400 mHz, 294 K) for a 6.8 mM sample of **1** in CD_3CN. B) Comparison of data from panel A (brown) to spectrum obtained for 6.8 mM sample of **1** in 20% CD_3CN/80% D_2O (blue). The presence of D_2O causes the feature at 6.7 ppm to vanish.

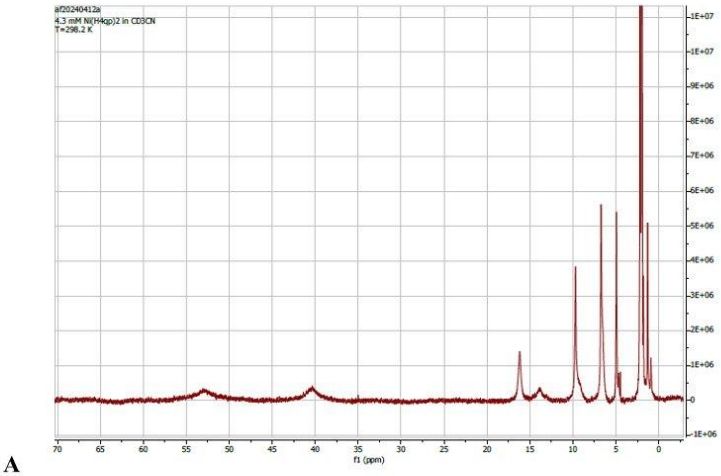

A

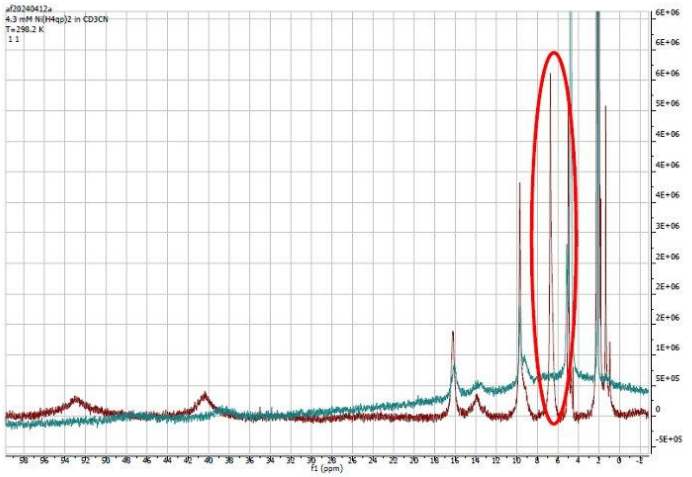

B

Figure S2. A) ^{1}H NMR data (400 mHz, 294 K) for a 4.3 mM sample of **2** in CD_3CN. B) Response of B) Comparison of data from panel A (brown) to spectrum obtained for 4.3 mM sample of **2** in 20% CD_3CN/80% D_2O (blue). The presence of D_2O causes the feature at 6.7 ppm to vanish.

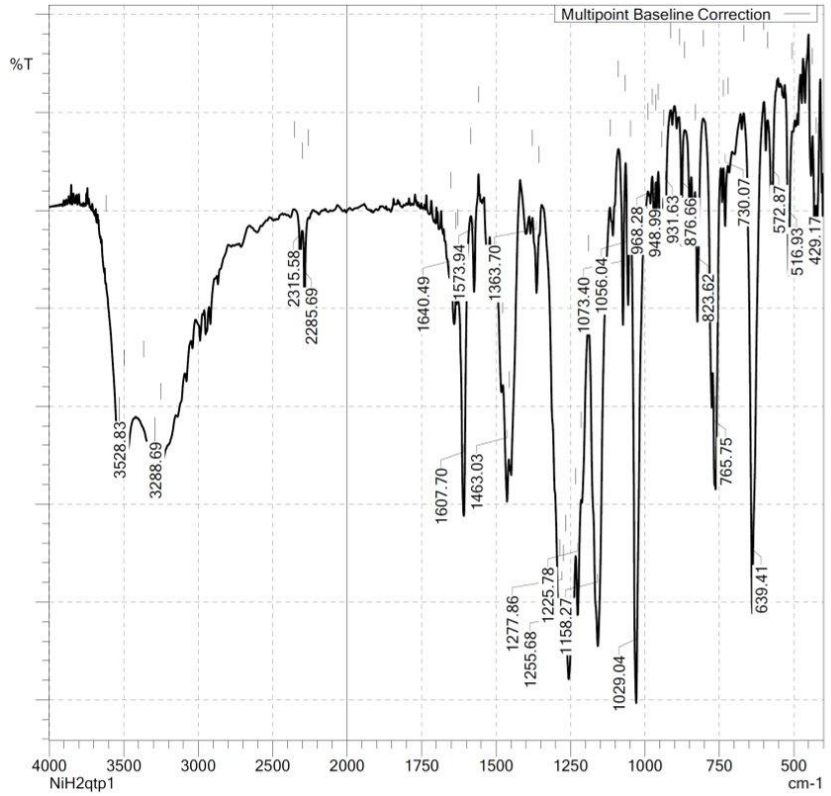

Figure S3. IR data (KBr) for [Ni(H_2qp1)(MeCN)](OTf)$_2$ (**1**).

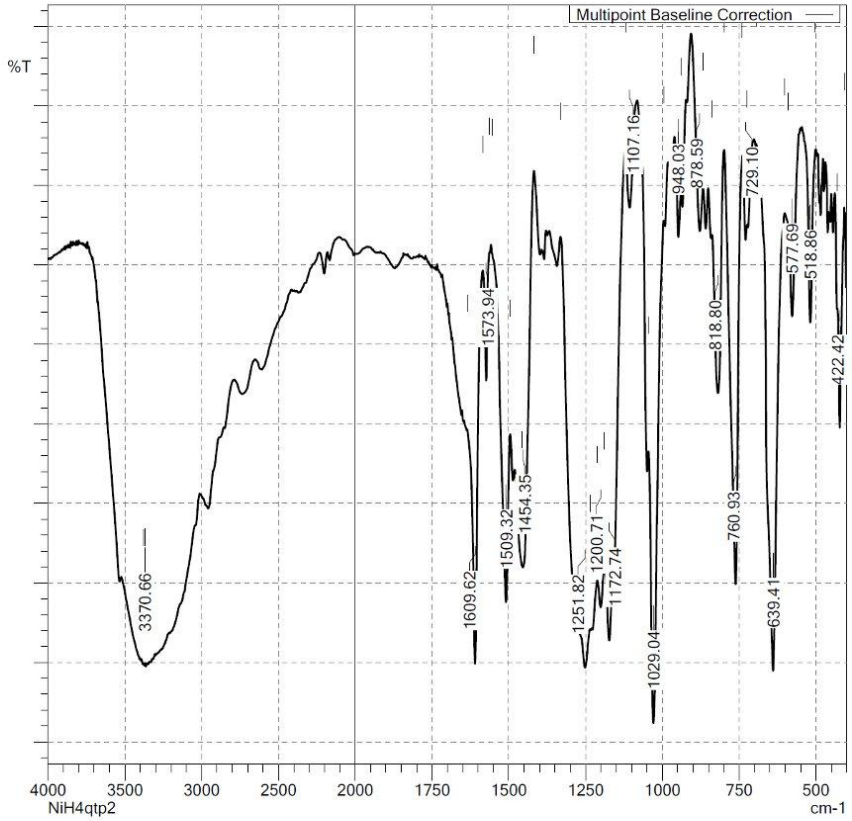

Figure S4. IR data (KBr) for $[Ni(H_4qp2)(MeCN)_2](OTf)_2$ (**2**).

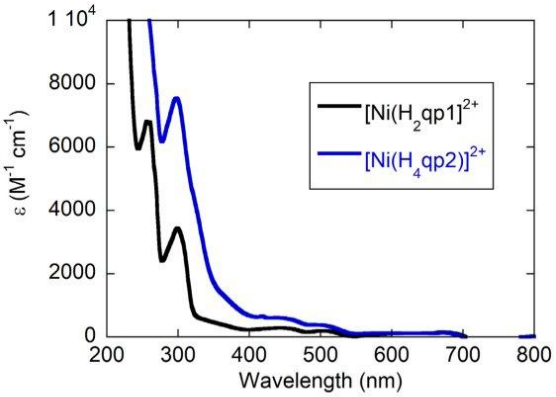

Figure S5. UV/vis data for **1** and **2**. The data for **1** were acquired for a 0.1 mM solution of the Ni(II) complex in MeOH whereas those for **2** were obtained using a 0.1 mM solution of the complex in MeCN. Both sets of data were obtained at 298 K using a 1.0 cm quartz cuvette. Observed peaks:

1 - 255 nm (6800 M^{-1} cm^{-1}), 299 nm (3430 M^{-1} cm^{-1}), 444 nm (285 M^{-1} cm^{-1}), 504 nm (195 M^{-1} cm^{-1}), 674 (150 M^{-1} cm^{-1})

2 - 298 nm (7550 M^{-1} cm^{-1}), 438 nm (610 M^{-1} cm^{-1}), 493 nm (380 M^{-1} cm^{-1}), and 668 (130 M^{-1} cm^{-1})

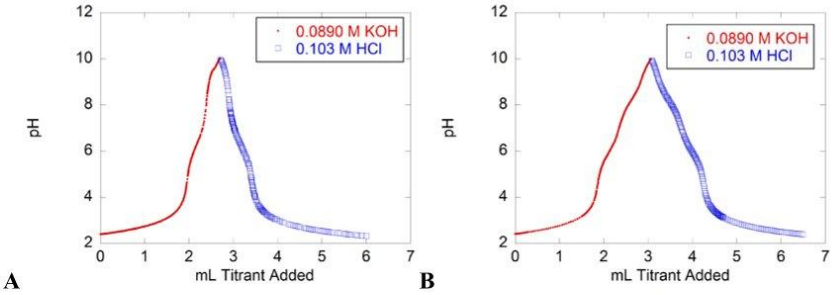

Figure S6. Potentiometric pH titration data for A) **1** and B) **2** in aqueous 100 mM KCl solutions. For the analysis of **1**, 0.10 mmol of H_2qtp1 and Ni(OTf)$_2$ were added to 48 mL of the KCl solution. 2.0 mL of 0.1018 M HCl was added to make the solution acidic, and the resultant mixture was subsequently titrated with 0.1008 M KOH (red data points). After 2.700 mL of KOH solution were added, the mixture was titrated with 0.1018 M HCl (blue data points). For the analysis of **2**, 0.10 mmol of H_4qtp2 and Ni(OTf)$_2$ were added to 50 mL of the KCl solution. 2.0 mL of 0.1018 M HCl was added to make the solution acidic, and the resultant mixture was subsequently titrated with 0.1008 M KOH (red data points). After 3.060 mL of KOH solution were added, the mixture was titrated with 0.1018 M HCl (blue data points). The data demonstrate that the titrations are reversible. Analyses of the data confirm a pK_a value of 6.33 (±0.05) for **1** and pK_a values of 5.99 (±0.05) and 8.24 (±0.05) for **2**.

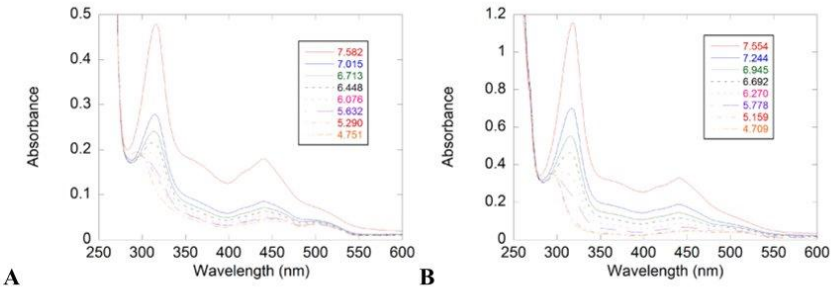

Figure S7. Spectrophotometric pH titration data for A) **1** and B) **2** in aqueous solutions. The data were acquired at 294 K with a 1.0 cm pathlength. The concentrations of Ni(II) and ligand in each sample were 0.10 mM. The pH was controlled through the addition of KOH and HCl. The peaks at 313 nm correspond to deprotonated quinols, whereas the peaks at 293-294 nm correspond to protonated quinols.

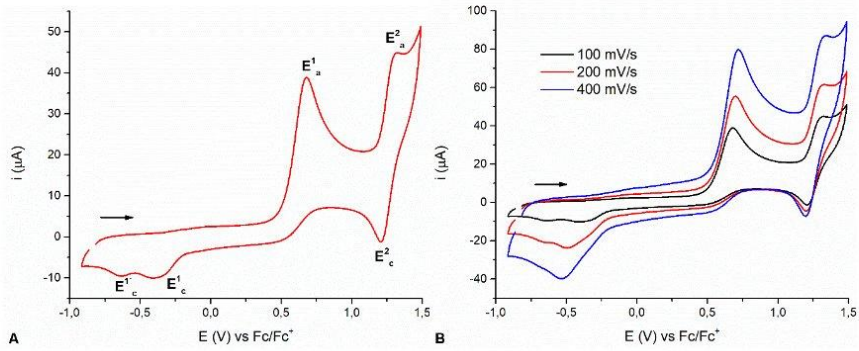

Figure S8. A) CV of 1.0 mM **1** in MeCN with 100 mM tetraethylammonium tetrafluoroborate ($TEABF_4$) at 100 mV/s. Features observed at E_a^1 = 680 mV, E_c^1 = -369 mV, and $E_c^{1'}$ = -629 mV correspond to the oxidation of the ligand to semiquinone. Features at E_a^2 = 1322 mV and E_c^2 = 1205 mV correspond to the oxidation to *para*-quinone. B) CV for the oxidation of 1.0 mM **1** to *para*-quinone in MeCN containing 100 mM $TEABF_4$ at different scan rates. The arrow shows the initial starting point and direction of the scans.

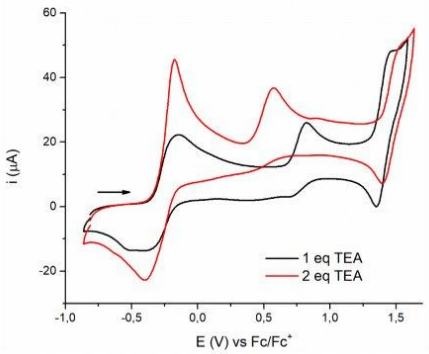

Figure S9. CV for 1.0 mM samples of **1** with 1.0 and 2.0 equiv. of triethylamine (TEA). Data were collected in MeCN containing 100 mM $TEABF_4$ with a 100 mV/s scan rate. The arrow shows the initial starting point and direction of the scans.

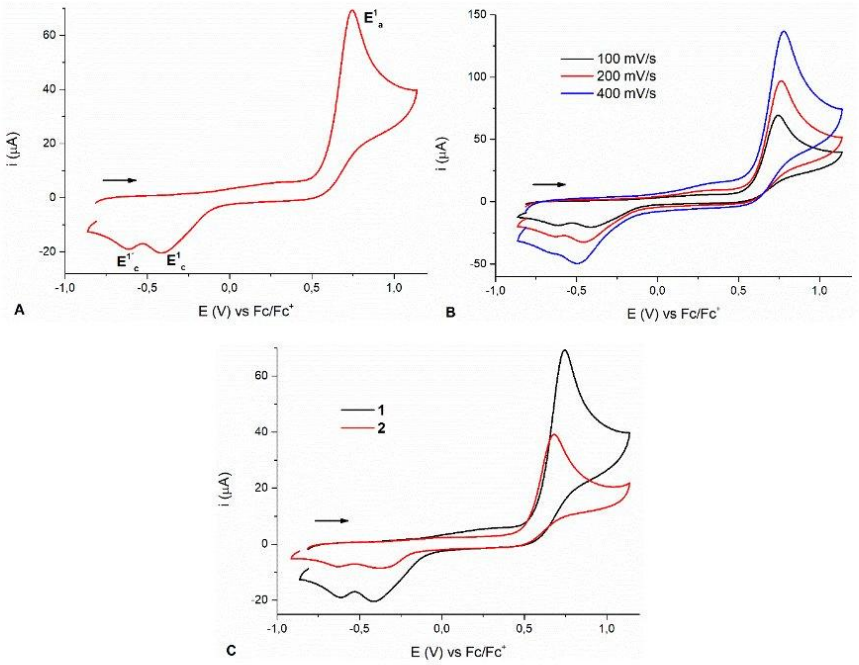

Figure S10. A) CV of 1.0 mM **2** in MeCN containing 100 mM $TEABF_4$ at 100 mV/s. The features at E_a^{1} = 745 mV, E_c^{1} = -411 mV, and $E_c^{1'}$ = -614 mV correspond to the oxidation of ligand oxidation to semiquinone and its subsequent reduction back to the quinol. B) CV for the oxidation of 1.0 mM **2** to semiquinone in MeCN containing 100 mM $TEABF_4$ at different scan rates. C) Comparison between the CVs of 1.0 mM **1** and 1.0 mM **2** in MeCN containing 100 mM $TEABF_4$ at 100 mV/s. . The arrows show the initial starting point and direction of the scans.

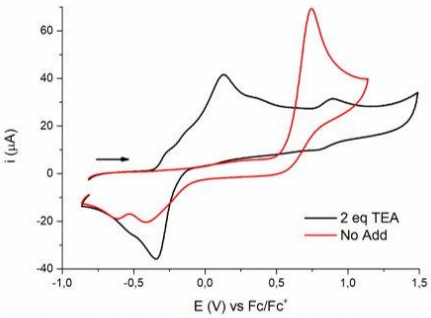

Figure S11. CV for 1.0 mM samples of **2** with 1.0 and 2.0 equiv. of TEA. Data were collected in MeCN containing 100 mM $TEABF_4$ with a 100 mV/s scan rate. The arrow shows the initial starting point and direction of the scans.

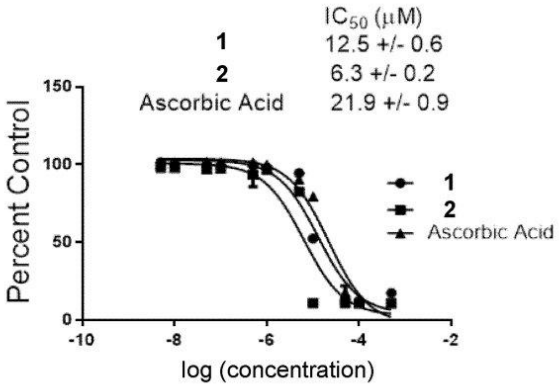

Figure S12. DPPH free radical scavenging assay of **1**, **2**, and ascorbic acid. The antioxidants were added to DPPH and incubated in the dark for 30 min at 298 K. Spectroscopic measurements were performed at 517 nm. The data were normalized to the absorbance in the presence of vehicle. All experiments were performed in triplicate and repeated twice.

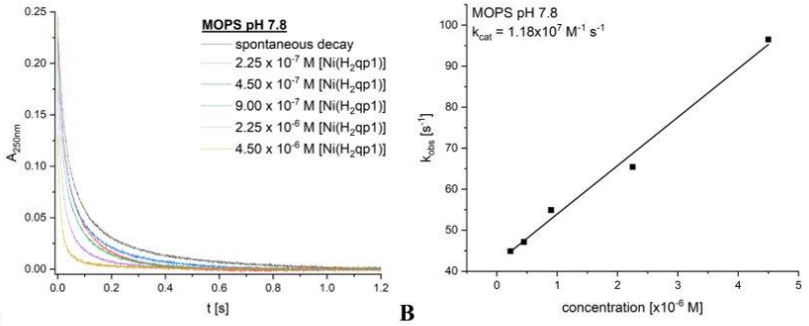

A B

Figure S13. A) Kinetic traces of superoxide decomposition at 250 nm (60 mM MOPS buffer, pH 7.8, ionic strength of 150 mM) by **1.** B) Plot of k_{obs} vs. [**1**].

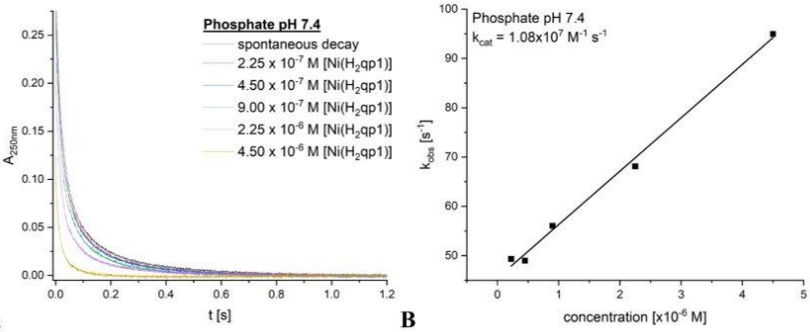

A B

Figure S14. A) Kinetic traces of superoxide decomposition at 250 nm (50 mM phosphate buffer, pH 7.4, ionic strength of 150 mM) by **1.** B) Plot of k_{obs} vs. [**1**].

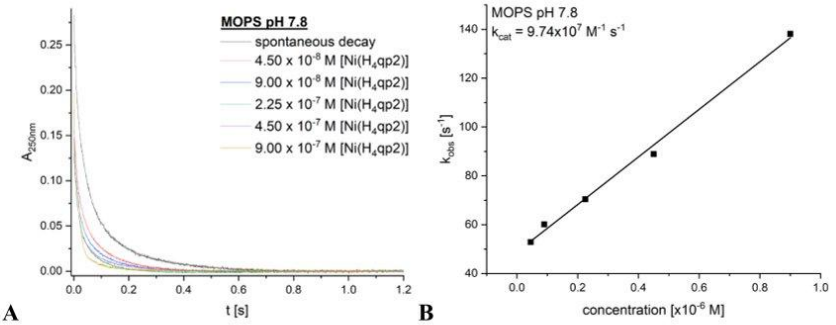

Figure S15. A) Kinetic traces of superoxide decomposition at 250 nm (60 mM MOPS buffer, pH 7.8 ionic strength of 150 mM) by **2.** B) Plot of k_{obs} vs. [**2**].

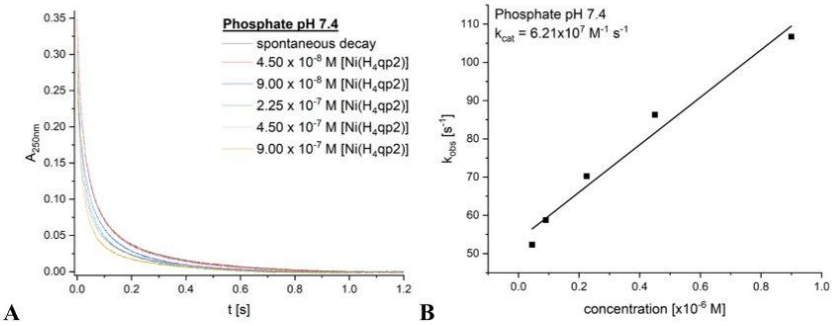

Figure S16. Kinetic traces of superoxide decomposition at 250 nm (50 mM phosphate buffer, pH 7.4, ionic strength of 150 mM) by **2.**

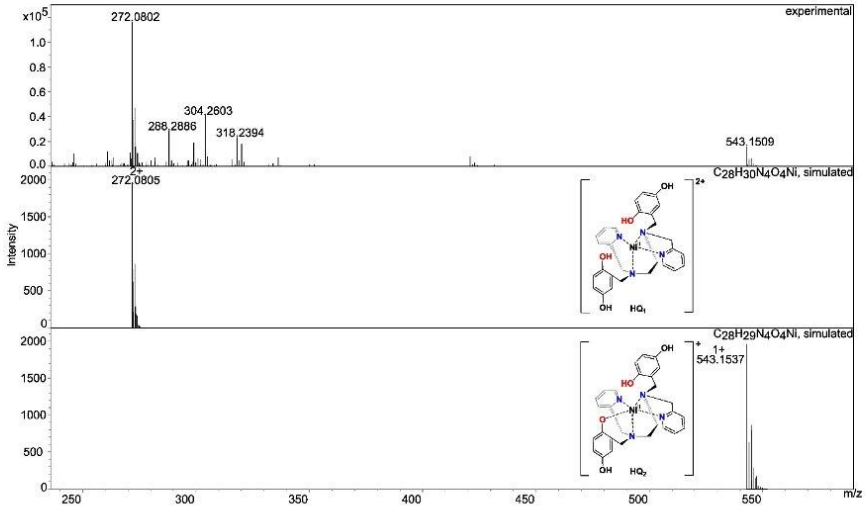

Figure S17. CSI-MS spectrometry of **2** prior to its reaction with KO_2. The graphics depict possible structures; we cannot preclude other modes of ligand coordination. Experimental conditions: a 1 mM solution of **2** in MeCN (1% DMF) was cooled to -40 °C, diluted in a pre-cooled syringe with pre-cooled MeCN to approximately 1×10^{-5} M, and quickly injected into the mass spectrometer. The predominant species are $[Ni^{II}(H_4qp2)]^{2+}$ (m/z = 272.0802) with a smaller amount of $[Ni^{II}(H_3qp2)]^{+}$ (m/z = 543.1537), where H_3qp2^- is the singly deprotonated form of the ligand.

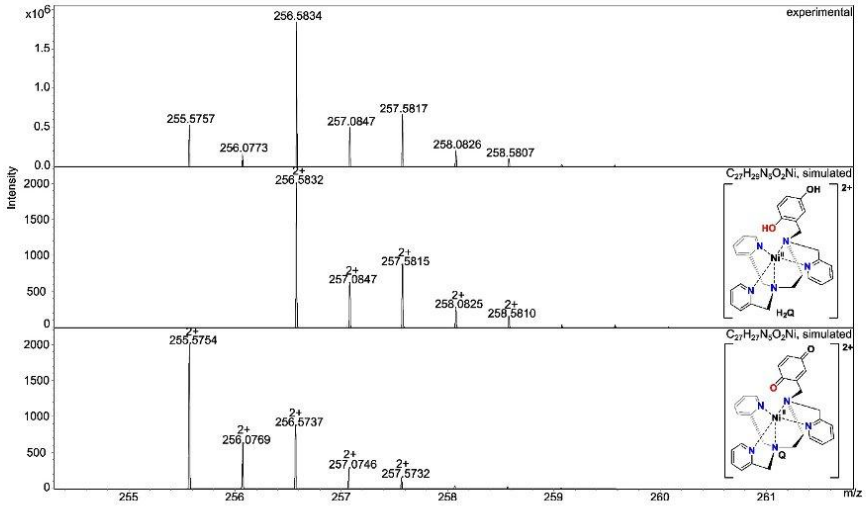

Figure S18. CSI-MS spectrometry of **1** prior to its reaction with KO_2. The graphics depict possible structures; we cannot preclude other modes of ligand coordination. Experimental conditions: a 1 mM solution of **1** in MeCN (1% DMF) was cooled to -40 °C, diluted in a pre-cooled syringe with pre-cooled MeCN to approximately 1×10^{-5} M, and quickly injected into the mass spectrometer. The predominant species are $[Ni^{II}(H_2qp1)]^{2+}$ (m/z = 256.5834) with a trace amount of $[Ni^{II}(qp1)]^{2+}$ (m/z = 255.5757), where *qp1* is the *para*-quinone form of the ligand.

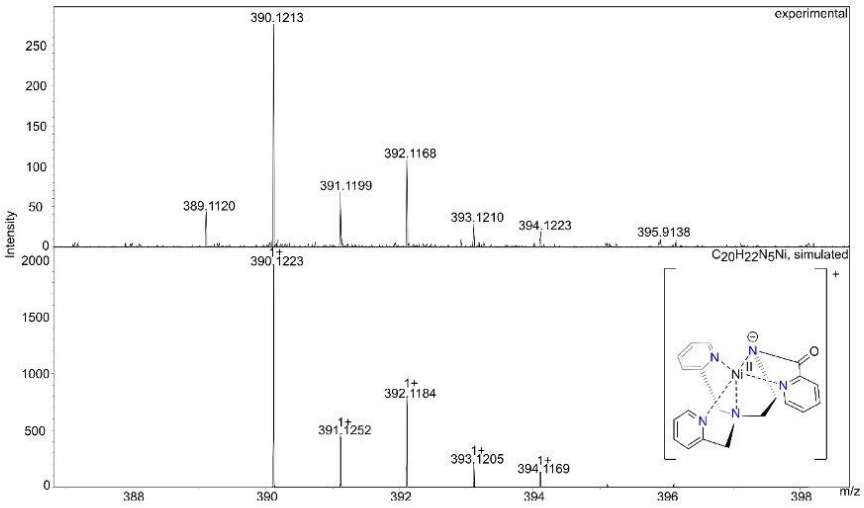

Figure S19. CSI-MS spectrometry of **1** after a 5 min reaction with KO_2. The graphics depict possible structures; we cannot preclude other modes of ligand coordination or sites of ligand oxidation. Experimental conditions: a 1 mM solution of **1** in MeCN (1% DMF) was cooled to -40 °C and then mixed with an excess of solid KO_2. Subsequently, the mixture was diluted in a pre-cooled syringe with pre-cooled MeCN to approximately 1×10^{-5} M and quickly injected into the mass spectrometer 5 min after the start of the reaction. The 390.1223 m/z peak is consistent with the loss of the quinol group and oxidation at one of the picolylic positions.

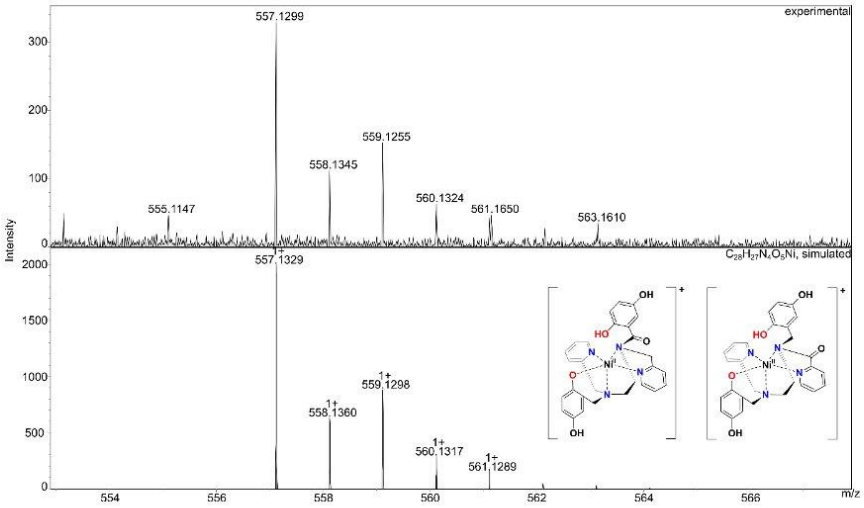

Figure S20. CSI-MS spectrometry of **2** after a 5 min reaction with KO_2. The graphics depict possible structures; we cannot preclude other modes of ligand coordination or sites of ligand oxidation. Experimental conditions: a 1 mM solution of **2** in MeCN (1% DMF) was cooled to -40 °C and then mixed with an excess of solid KO_2. Subsequently, the mixture was diluted in a pre-cooled syringe with pre-cooled MeCN to approximately 1×10^{-5} M and quickly injected into the mass spectrometer 5 min after the start of the reaction. The m/z peak at 557.1329 is consistent with oxidation at a benzylic or picoylic carbon.

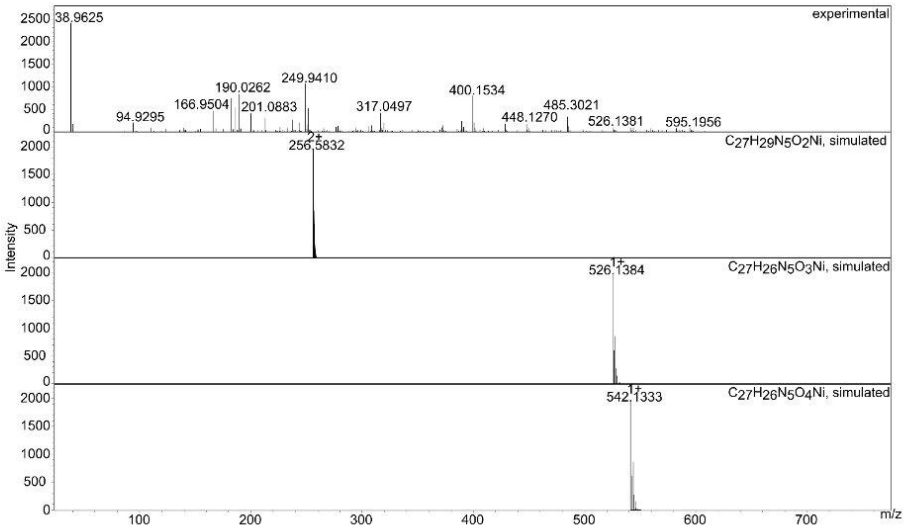

Figure S21. CSI-MS spectrometry of **1** after a sample from an extended reaction with KO_2 was warmed to room temperature (RT). Experimental conditions: a 1 mM solution of **1** in MeCN (1% DMF) was cooled to -40 °C and then mixed with an excess of solid KO_2. Subsequently, the mixture was diluted in a pre-cooled syringe with pre-cooled MeCN to approximately 1×10^{-5} M and allowed to warm to RT before injection into the mass spectrometer. The complex has undergone substantial degradation, and the products cannot be readily identified.

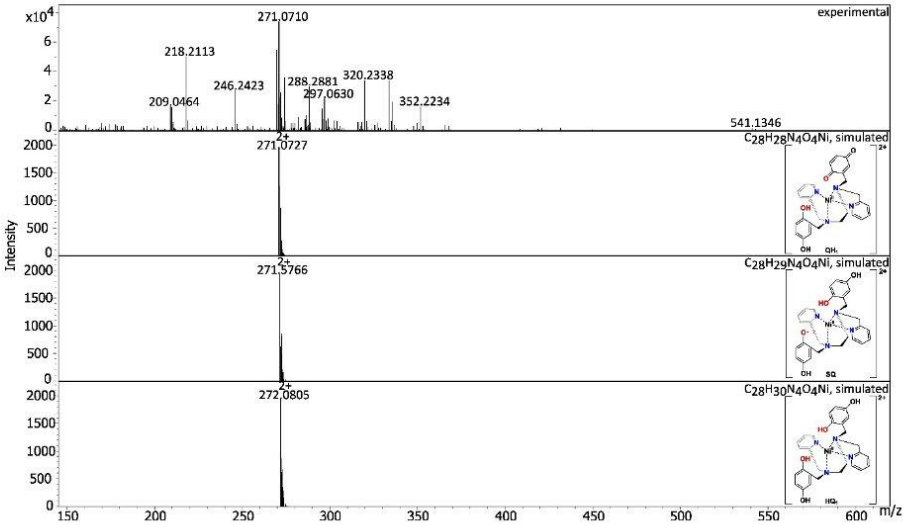

Figure S22. CSI-MS spectrometry of **2** after a sample from an extended reaction with KO_2 was warmed to RT. The graphics depict possible structures; we cannot preclude other modes of ligand coordination or sites of ligand oxidation.Experimental conditions: a 1 mM solution of **1** in MeCN (1% DMF) was cooled to -40 °C and then mixed with an excess of solid KO_2. Subsequently, the mixture was diluted in a pre-cooled syringe with pre-cooled MeCN to approximately 1×10^{-5} M and allowed to warm to RT before injection into the mass spectrometer.

Publication 4: A macrocyclic quinol-containing ligand enables high catalase activity even with a redox-inactive metal at the expense of the ability to mimic superoxide dismutase

S. Karbalaei, A. Franke, J. Oppelt, T. Aziz, A. Jordan, P. R. Pokkuluri, D. D. Schwartz, I. Ivanović-Burmazović and C. R. Goldsmith

Chemical Science, **2023**, *14*, 9910.

Summary: A series of transition metal complexes with the macrocyclic 1,8-Bis(2,5-dihydroxybenzyl)-1,4,8,11-tetraazacyclotetradecane (H_4qp4) ligand were synthesized by the Goldsmith group with manganese, iron and zinc as metal center, respectively. The macrocyclic [Fe(H_3qp4)]OTf, [Mn(H_3qp4)]OTf and [Zn(H_3qp4)]OTf complexes were investigated for their catalase mimicking characteristics, showing equal activity of all three complexes towards hydrogen peroxide. However, the redox-inactive Zn^{2+} seems to rely on a ligand-based mechanism, whereas Mn and Fe complexes operate through metal centered redox cycling involving high-valent metal species. Additionally, SOD activity was tested using indirect assays, as well as more reliable direct stopped-flow methods.

Contribution: JO performed stopped-flow experiments and determined the corresponding catalytic rate constants for every complex in phosphate (pH 7.4) and MOPS buffer (pH 7.4 and 7.8). Opposing to the results from the indirect hypoxanthine/xanthine oxidase/lucigenin assay, only the manganese complex showed catalytic activity towards superoxide. JO incorporated the k_{cat} values for the corresponding complex of 6.0 x 10^6 M^{-1} s^{-1} (MOPS, pH 7.4), 4.5 x 10^6 M^{-1} s^{-1} (MOPS pH 7.8) and 2.9 x 10^6 M^{-1} s^{-1} (Phosphate, pH 7.4) into the overall mechanism.

Chemical Science

ROYAL SOCIETY OF CHEMISTRY

EDGE ARTICLE

View Article Online
View Journal | View Issue

Cite this: *Chem. Sci.*, 2023, **14**, 9910

All publication charges for this article have been paid for by the Royal Society of Chemistry

A macrocyclic quinol-containing ligand enables high catalase activity even with a redox-inactive metal at the expense of the ability to mimic superoxide dismutase†

Sana Karbalaei,[a] Alicja Franke,[b] Julian Oppelt,[b] Tarfi Aziz,[a] Aubree Jordan,[a] P. Raj Pokkuluri,[a] Dean D. Schwartz,[c] Ivana Ivanović-Burmazović *[b] and Christian R. Goldsmith *[a]

Previously, we found that linear quinol-containing ligands could allow manganese complexes to act as functional mimics of superoxide dismutase (SOD). The redox activity of the quinol enables even Zn(II) complexes with these ligands to catalyze superoxide degradation. As we were investigating the abilities of manganese and iron complexes with 1,8-bis(2,5-dihydroxybenzyl)-1,4,8,11-tetraazacyclotetradecane (H_4qp4) to act as redox-responsive contrast agents for magnetic resonance imaging (MRI), we found evidence that they could also catalyze the dismutation of H_2O_2. Here, we investigate the antioxidant behavior of Mn(II), Fe(II), and Zn(II) complexes with H_4qp4. Although the H_4qp4 complexes are relatively poor mimetics of SOD, with only the manganese complex displaying above-baseline catalysis, all three display extremely potent catalase activity. The ability of the Zn(II) complex to catalyze the degradation of H_2O_2 demonstrates that the use of a redox-active ligand can enable redox-inactive metals to catalyze the decomposition of reactive oxygen species (ROS) besides superoxide. The results also demonstrate that the ligand framework can tune antioxidant activity towards specific ROS.

Received 10th May 2023
Accepted 25th August 2023

DOI: 10.1039/d3sc02398b

rsc.li/chemical-science

Introduction

High concentrations of reactive oxygen species (ROS), such as hydrogen peroxide (H_2O_2) and superoxide ($O_2^{\bullet-}$) are capable of damaging biomolecules, and the accumulation of these species has been linked to a wide array of health conditions.[1–5] In response, the body produces a variety of antioxidants to manage ROS concentrations. These include superoxide dismutases (SODs), which catalyze the conversion of $O_2^{\bullet-}$ to O_2 and H_2O_2, and catalases, which promote the dismutation of H_2O_2 to O_2 and H_2O. The high activities of these enzymes have motivated us and other researchers to develop small molecules capable of replicating this catalysis. Such compounds could potentially be used to bolster the body's defenses against ROS and treat health conditions associated with oxidative stress.

In previous work from our laboratories, we found that linear polydentate ligands with 1,4-hydroquinone (quinol) groups could be used as the organic components in a variety of SOD mimics (Scheme 1).[6–10] A manganese complex with H_2qp1 displayed activity that was comparable to those of the most effective SOD mimetics reported to date: manganese complexes with pentaazamacrocycle and cationic porphyrin ligands.[11–14] The redox activity of the quinol group enables it to act as the redox partner for $O_2^{\bullet-}$ and can allow SOD mimicry even without a redox-active metal. Although the ligands by themselves are inactive, the Zn(II) complexes with H_2qp1 and H_4qp2 are functional SOD mimics, with the latter ligand resulting in higher activity.[9,10]

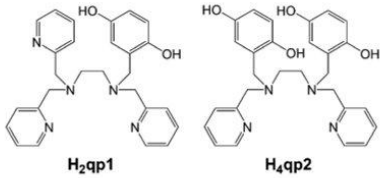

H_2qp1 H_4qp2

Scheme 1 Linear polydentate quinol-containing ligands from prior work.

[a]*Department of Chemistry and Biochemistry, Auburn University, Auburn, AL 36849, USA. E-mail: crgoldsmith@auburn.edu*

[b]*Department of Chemistry, Ludwig-Maximilians-Universität München, 81377 München, Germany. E-mail: ivana.ivanovic-burmazovic@cup.uni-muenchen.de*

[c]*Department of Anatomy, Physiology, and Pharmacology, College of Veterinary Medicine, Auburn University, Auburn, AL 36849, USA*

† Electronic supplementary information (ESI) available. CCDC 2173563. For ESI and crystallographic data in CIF or other electronic format see DOI: https://doi.org/10.1039/d3sc02398b

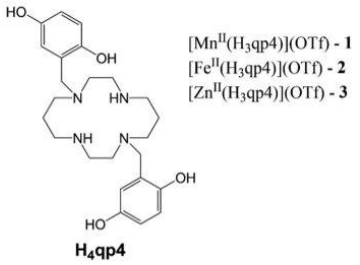

Scheme 2 Structure of H_4qp4 ligand and formulations of the discussed coordination complexes.

More recent work has focused on the macrocyclic ligand 1,8-bis(2,5-dihydroxybenzyl)-1,4,8,11-tetraazacyclotetradecane (H_4qp4, Scheme 2).[15,16] Our initial interest in this molecule was as a component in highly water-stable magnetic resonance imaging (MRI) contrast agent sensors for H_2O_2. When the quinols are oxidized to *para*-quinones, water molecules displace these groups, increasing the T_1-weighted relaxivity (r_1) of its Mn(II) complex, [Mn^{II}(H_3qp4)](OTf) (**1**).[15] Although quinol oxidation and an accompanying enhancement in r_1 also occur when the Fe(II) complex, [Fe^{II}(H_3qp4)](OTf) (**2**), reacts with H_2O_2, it is instead metal oxidation that is primarily responsible for the increase in relaxivity.[16] For both **1** and **2**, we found that the oxidation of the quinols and the accompanying activation of the sensor occur more slowly in higher concentrations of H_2O_2.[15,16] This led us to speculate that the initial reactions with H_2O_2 may be generating a higher-valent metal species that can either react intramolecularly to oxidize the ligand or intermolecularly with a second equiv. of H_2O_2 (Scheme 3).[15] The intermolecular activity depletes H_2O_2, thereby mimicking catalase. The intramolecular reaction was proposed to be inherently slower, only proceeding to a noticeable extent after the [H_2O_2] decreases enough to make the intermolecular reaction less competitive.

Replicating the activity of catalase enzymes has proven to be challenging, and the best small molecule mimics reported thus far have displayed modest reactivity with H_2O_2. Two metrics are commonly used to assess catalysis: the rate constant for the reaction between H_2O_2 and the antioxidant and the turnover number (TON).[17–27] Comparisons are often difficult to make since the reaction conditions and protocols can vary considerably. The highest rate constant for H_2O_2 degradation corresponded to a second-order reaction with an Fe(III) complex with a fluorinated corrole (k_2 = 4300 M^{-1} s^{-1} in 37 °C pH 7.4 phosphate buffer).[27] The highest TON corresponded to a manganese porphyrin complex (TON = 12.54 in 25 °C pH 7.8 Tris buffer).[22]

In the present manuscript, we thoroughly investigate the abilities of the Mn(II) and Fe(II) complexes with H_4qp4 to mimic both SOD and catalase. We also prepare and evaluate the antioxidant properties of a Zn(II) complex with H_4qp4: [Zn^{II}(H_3qp4)](OTf) (**3**). We find that although the SOD activities are severely attenuated relative to those of complexes with linear quinol-containing ligands, all three H_4qp4 complexes act as highly potent catalase mimics, with activities that greatly exceed those exhibited by most other reported small molecule mimics of these enzymes.[17–27] The Zn(II) complex is further notable in that it represents the first instance, to the best of our knowledge, where a coordination complex with a redox-inactive metal ion successfully catalyzed the degradation of H_2O_2.

Experimental section

Materials

All chemicals and solvents were purchased from Sigma-Aldrich and used without further purification unless otherwise noted. All deuterated solvents were bought from Cambridge Isotopes. Diethyl ether (ether) and methanol (MeOH) were bought from Fisher. Methylene chloride (CH_2Cl_2) was purchased from Mallinckrodt Baker. 1,8-Bis(2,5-dihydroxybenzyl)-1,4,8,11-tetraazacyclotetradecane (H_4qp4), [Mn^{II}(H_3qp4)](OTf), and [Fe^{II}(H_3qp4)](OTf) were synthesized and purified as previously described.[15,16]

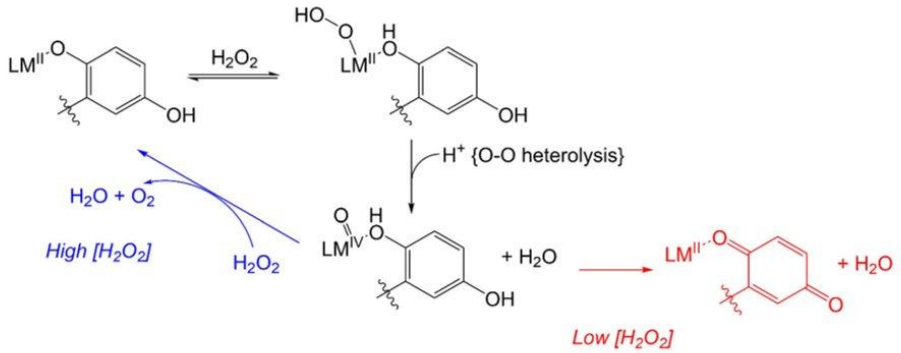

Scheme 3 Previously proposed mechanism for competing H_2O_2 degradation (blue) and quinol oxidation (red). The above graphic was slightly modified from one that originally appeared in ref. 15.

Instrumentation

All nuclear magnetic resonance (NMR) data were collected on a 500 mHz AV Bruker NMR spectrometer. All NMR resonance peak frequencies were referenced to internal standards. UV/vis were collected on a Varian Cary 50 spectrophotometer and analyzed using software from the WinUV Analysis Suite. Electron paramagnetic resonance (EPR) data were obtained on a Bruker EMX-6/1 X-band EPR spectrometer operated in the perpendicular mode. The EPR data were subsequently analyzed and processed with the program EasySpin. All EPR samples were run as frozen solutions in quartz tubes. High-resolution mass spectrometry (HR-MS) data were obtained at the Mass Spectrometer Center at Auburn University on a Bruker Microflex LT MALDI-TOF mass spectrometer *via* direct probe analysis operated in the positive ion mode. Infrared spectroscopy (IR) data were obtained with a Shimadzu IR Prestige-21 FT-IR spectrophotometer. Cyclic voltammetry (CV) was performed under N_2 at 294 K using an Epsilon electrochemistry workstation (Bioanalytical System, Inc.), a gold working electrode, a platinum wire auxiliary electrode, and a silver/silver(I) chloride reference electrode. All elemental analyses (C, H, N) were performed by Atlantic Microlabs (Norcross, GA); samples were dried under vacuum and placed under a N_2 atmosphere prior to shipment.

X-ray crystallography

Crystallographic data for $[Zn^{II}(H_3qp4)](OTf)$ (**3**) were collected using a Bruker D8 VENTURE κ-geometry diffractometer system equipped with a Incoatec IμS 3.0 microfocus sealed tube and a multilayer mirror monochromator (Mo Kα, $\lambda = 0.71073$ Å). Diffraction data were integrated with the Bruker SAINT software package using a narrow-frame algorithm. Data were corrected for absorption effects using the Multi-Scan method (SADABS). The structure was solved and refined using the Bruker SHELXTL Software Package. Selected crystallographic data are presented in the ESI and can be found in the Cambridge Structural Database (number 2173563†).

Antioxidant assays

The ability of coordination complexes to catalyze the degradation of $O_2^{\bullet-}$ was initially screened using the hypoxanthine/xanthine oxidase/lucigenin assay.[28,29] The reaction between hypoxanthine and xanthine oxidase generates $O_2^{\bullet-}$, which can then subsequently react either with lucigenin to provide a luminescent response or an antioxidant. The extent to which various concentrations of an antioxidant eliminate the lucigenin response provides a quantitative measure of its activity. These assays were performed with 1 mL of saline solutions buffered with 50 mM phosphate to pH 7.2. The solutions also contained 50 μM hypoxanthine, 0.005 U mL^{-1} xanthine oxidase (Calbiochem), 5 μM dark adapted lucigenin, and the tested antioxidant in concentrations ranging from 0.1 nM to 10 μM. Reactions were carried out at room temperature (RT) and were initiated by the addition of xanthine oxidase to the hypoxanthine-containing solution. The copper/zinc superoxide dismutase isolated from bovine erythrocytes (0.0001–10 U mL^{-1}, Calbiochem) was used as a positive control ($IC_{50} = 40$ nM).[30] Luminescence was measured using a TD-20/20 (Turner Designs) luminometer and expressed as relative light units (RLU). Luminescence was measured for four 10 s integrations after an initial delay of 3 s. The four RLU values were averaged, and each concentration was expressed as a percent of that produced in the presence of the vehicle. Each measurement within an individual run was performed in triplicate, and each assay was repeated three times.

Kinetic assessment of superoxide dismutase activity

The ability of the H_4qp4 complexes to catalytically degrade superoxide was tested by a direct method using stopped-flow techniques described in a previous publication from one of our laboratories.[31] Experiments were carried out using syringes 1, 2, and 3 on a Biologic SFM-400 instrument that was equipped with an Energetiq LDLS ENQ EQ-99-FC laser driven light source and a J&M TIDAS diode array detector (integration time = 0.5 ms, $\lambda = 180$–724 nm). The source of superoxide was commercially available KO_2 dissolved in dry and non-buffered DMSO ($[O_2^{\bullet-}] \approx 1$–2 mM). Complexes **1–3** were each tested at four different concentrations between 0.9 and 9 μM in aqueous solutions buffered with HEPES or sodium phosphate to either pH 7.4 or pH 8.1. The ionic strength of all solutions was 111 mM. The aqueous solution containing the studied coordination complex was mixed in a 9 : 1 ratio with the superoxide solution in DMSO using a high-density mixer. The initial concentration of the superoxide is determined from the intensity of the UV band at 250 nm as assessed immediately after stopped-flow mixing of the superoxide DMSO solution with the appropriate buffer. The 250 nm band is characteristic for superoxide and has well-known and -established molar extinction coefficients for each buffer and pH used.[32] In each experiment, the concentration of superoxide exceeded that of the metal-containing catalyst by at least ten-fold to ensure catalytic conditions. Millipore water was used for the preparation of the buffer solutions. All of the prepared buffers were treated with Chelex 100 sodium exchange resin for at least 12 h before use in order to remove adventitious metal ions. The data analysis was performed using the BioKine V4.66 software. Each reported k_{obs} value is the average of at least 10 measurements. The reported k_{cat} values were determined from the slope of the k_{obs} *vs.* [SODm] plot. The presence of H_2O_2 was qualitatively confirmed using Baker Testrips for Peroxides.

Kinetic assessment of catalase and peroxidase activity

The abilities of the antioxidants to catalyze H_2O_2 degradation were initially evaluated by monitoring the decrease in the absorbance of H_2O_2 at 240 nm ($\varepsilon_{240} = 39.4$ M^{-1} cm^{-1})[33] over time. These measurements were performed in 200 mM phosphate solutions buffered to pH 7.0 that contained 100 nM of the tested compound and 1–500 mM H_2O_2 at RT. The changes in the UV/vis data were followed using a Shimadzu UV-1601 spectrophotometer (Columbia, MD). Under the described conditions, we observed a single hyperbolic phase and could fit

the data to a standard Michaelis–Menten equation to obtain apparent k_{cat} and k_{on} values (Eq. (1)).

$$\frac{v_o}{[1]_T} = \frac{k_{cat}[H_2O_2]}{k_{cat}/k_{on} + [H_2O_2]} = \frac{k_{cat}[H_2O_2]}{K_M + [H_2O_2]} \quad (1)$$

The catalase activity was more stringently quantitated by polarographically following O_2 production using a Clark-type O_2 sensitive electrode (Hansatech Pentney, Norfolk, England). We first calibrated the system using a N_2 saturated solution to establish a zero O_2 level within the reaction chamber prior to experimental measurements. The initial series of reactions contained 1 nM of the tested antioxidant and were carried out at RT in solutions containing 50 mM tris(hydroxymethyl)aminomethane (Tris) buffered to pH 7.2. The buffer and solution containing the coordination complex were initially mixed in the reaction chamber for 20 s to establish a baseline, after which H_2O_2 was injected to initiate the evolution of O_2.[34] Subsequently, we measured the initial rates of reactions between 10 mM H_2O_2 and 1.0–100 nM of the catalysts to calculate k_2 rate constants. The data were corrected to account for uncatalyzed H_2O_2 decomposition.

Peroxidase activity can also contribute to the degradation of H_2O_2, representing a means to consume H_2O_2 without generating O_2. This potential reactivity was evaluated by monitoring the abilities of the antioxidants to promote the reaction between H_2O_2 and 2,2′-azinobis(3-ethylbenzothiazoline-6-sulfonate) (ABTS); this reaction generates the radical cation $ABTS^{\cdot+}$ (ε_{417} = 34.7 mM^{-1} cm^{-1}).[35] One series of reactions were run in RT 50 mM acetate solution buffered to pH 5.0, with reaction concentrations of 10 mM ABTS, 0.1 mM coordination complex, and 1–500 mM H_2O_2. Another series of reactions were run in RT 50 mM acetate solution buffered to pH 5.0, with reaction concentrations of 10 mM H_2O_2, 0.1 mM coordination complex, and 1–500 mM ABTS. The conversion of ABTS to its radical cation was followed using a Shimadzu UV-1601 spectrophotometer (Columbia, MD). The following equation is used to convert the absorbance data into initial rates ($v_o/[M]_T$):

$$\frac{v_o}{[M]_T} = \frac{\Delta Abs \text{ (at 417 nm for 60 s)}}{60 \text{ s} \times 100 \ \mu M \times 0.0347 \ \mu M^{-1} \text{ cm}^{-1} \times 1 \text{ cm}}$$

where 100 μM is concentration of the catalyst and 0.0347 μM^{-1} cm^{-1} is the molar absorptivity of $ABTS^{\cdot+}$ at 417 nm.

Syntheses

(1-(2,5-Dihydroxybenzyl)-8-(2,5-dihydroxybenzylalkoxide)-1,4,8,11-tetraazacyclotetradecane)zinc(II) triflate ([Zn^{II}(H_3qp4)](OTf), 3). H_4qp4 (500 mg, 1.12 mmol) and $Zn^{II}(OTf)_2$ (415 mg, 1.12 mmol) were dissolved in 5 mL of dry MeCN and then stirred at 60 °C for 24 h. The slow addition of ether to the MeCN solution deposited the product as a colorless powder that could be isolated by filtration (703 mg, 88% yield). Crystals suitable for single crystal X-ray diffraction were grown by layer diffusion of ether to a saturated solution of the crude product in MeOH. Optical spectroscopy (H_2O, 294 K): 299 nm (ε = 7000 M^{-1} cm^{-1}). IR (cm^{-1}): 3403 (s), 3260 (s), 3055 (s), 2988 (w), 2887 (w), 2724 (m), 1607 (w), 1508 (s), 1432 (w), 1375 (m), 1300 (m), 1247 (w), 1217 (w), 1196 (w), 1147 (w), 1115 (w), 1101 (m), 1077 (m), 1061 (s), 1021 (s), 1004 (w), 961 (m), 939 (w), 914 (m), 894 (m), 869 (w), 830 (m), 781 (m), 759 (m), 630 (s), 567 (w). ^{1}H NMR (500 MHz, CD_3OD, 298 K): δ 6.64–6.75 (m, 6H), 4.57 (s, 3H), 2.68 (d, J = 25 Hz, 6), 2.28 (s, 2H), 2.03 (s, 2H), 1.34–1.35 (m, 4H). ^{13}C NMR (125 MHz, CD_3OD, 298 K): δ 151.83, 149.78, 149.00, 122.99, 120.48, 119.96, 119.84, 119.45, 117.92, 117.69, 117.56, 117.16, 116.99, 58.54, 54.84, 54.54, 53.80, 53.67, 53.05, 51.91, 51.79, 50.99, 25.82, 25.78, 24.23. MS (ESI): calcd for $[Zn(H_3qp4)]^+$, m/z 507.1944; found, m/z 507.1941. Elemental analysis (powder) calcd for $C_{25}H_{35}N_4O_7F_3S_1Zn \cdot 0.5(C_2H_5)_2O \cdot 0.5$ MeCN (powder): C, 46.99%; H, 5.84%; N, 8.81%. Found: C, 46.52%; H, 5.99%; N, 8.81%.

Results

Synthesis and structural characterization of [Zn^{II}(H_3qp4)](OTf)

Mn(II) and Fe(II) complexes with H_4qp4 were previously reported.[15,16] The isolated compounds, [Mn^{II}(H_3qp4)](OTf) (**1**) and [Fe^{II}(H_3qp4)](OTf) (**2**), feature the singly deprotonated ligand H_3qp4^-; we believe that the residual non-complexed ligand deprotonates the metal-bound H_4qp4. The complexation of Zn(II) to H_4qp4 similarly yields a H_3qp4^- complex: [Zn^{II}(H_3qp4)](OTf) (**3**). As with **1** and **2**, the synthesis of **3** required us to heat the mixture of ligand and metal salt for a prolonged period of time (24 h) to maximize complexation of the metal ion. Complex **3** was characterized by NMR, IR, MS, and UV/vis (Fig. S1–S5†).

The redox capabilities of **3** were initially assessed using cyclic voltammetry (CV, Fig. S6†). In phosphate solution buffered to pH 7.2, we observe one irreversible redox event with an E_{pa} = 225 mV and an E_{pc} = −11 mV (*vs.* Ag/AgCl). This resembles irreversible CV features seen for both **1** and **2**. The redox event for the Mn(II) complex has an E_{pa} = 240 mV and an E_{pc} = −20 mV;[15] whereas, that for the Fe(II) compound has an E_{pa} = 240 mV and an E_{pc} = −60 mV. A smaller feature is observed with E_{pc} = 5 mV; this may be attributable to acid/base behavior for either the quinol or the semiquinone. A similar feature was observed for **2**.[16]

We crystallized **3** from MeOH/ether and structurally characterized the complex through single crystal X-ray diffraction (Fig. 1 and Table S1†). The H_3qp3^- ligand coordinates to the Zn(II) through five out of its six possible donor atoms, with the neutral quinol not directly binding to the metal center. The coordination geometry of the N_4O donors around the Zn(II) is best described as a distorted trigonal bipyramidal, with a τ_5 value of 0.70.[36] The pendent quinol may hydrogen bond to the outer-sphere triflate; the distance between O(3) and O(6) is 2.72 Å.

Aqueous solution characterization of [Zn^{II}(H_3qp4)](OTf)

We investigated the stability and speciation of **3** in water using potentiometric pH titrations (Fig. S7†). As the pH of a 1 : 1 mixture of $Zn^{II}(OTf)_2$ and H_4qp4 was increased from 2.5 to 10, we observe two ionization events consistent with pK_a values of 6.16 and 9.71 (Table S2†). We assign these to the deprotonation

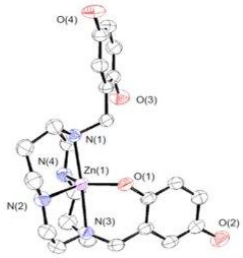

Fig. 1 ORTEP representation of the structure of $[Zn^{II}(H_3qp4)]^+$. The triflate counteranion and all H atoms are omitted for clarity. All ellipsoids are drawn at 50% probability. Full crystallographic data are provided in the ESI and in the Cambridge Structural Database (number 2173563†).

of the quinols. Although the first value is consistent with other M(II)-quinol pK_a values that we have measured,[6,8,9,15] the second value is much higher and more consistent with a metal-free quinol or phenol. The solid-state structure featuring a pentacoordinate metal center (Fig. 1) may therefore be retained in water. Despite the one fewer chelating group, the Zn(II)–H_3qp4 complex appears to be extremely stable against metal ion dissociation, with a log $K_{ML} = 41.1$; this value is higher than the analogous values for **1** and **2**.[15,16]

Superoxide dismutase mimicry

Compounds **1**, **2**, and **3** were initially screened using the hypoxanthine/xanthine oxidase/lucigenin assay (Fig. 2).[28,29] By this measure, both **1** and **2** initially appeared to be capable of catalyzing superoxide dismutation. The Mn(II) complex **1** is most active, with an IC_{50} value of 15 nM. The Fe(II) complex **2** also has above-baseline activity, with an IC_{50} value of 21 nM. These IC_{50} values are similar to those measured for $[Mn^{II}(H_2qp1)(MeCN)]^{2+}$ (**4**) and $[Mn^{II}(H_4qp2)Br_2]$ (**5**, Scheme 1),[6] which were subsequently confirmed to be functional SOD mimics *via* analysis of the direct reactions between the manganese compounds and KO_2.[8] Surprisingly, the assay data suggest that **1** and **2** could outperform the copper/zinc superoxide dismutase that served as the positive control ($IC_{50} = 40$ nM).[30] Compound **3** is essentially inactive, with an IC_{50} of 515 nM.

The aforementioned assay is somewhat notorious for providing misleading results due to possible side reactions between its components.[31,37–43] In the case of **4** and **5**, the assay predicted similar activities, but later stopped-flow kinetics analysis of the direct reactions between the Mn(II) compounds and KO_2 indicated that the H_2qp1 complex was much more active than the H_4qp2 complex in HEPES solutions.[8] Further, both compounds had k_{cat} values that were much lower than those predicted by the assay. Complexes **1**, **2**, and **3** were studied in 60 mM MOPS buffered to either pH 7.4 or pH 7.8 and 50 mM phosphate buffered to pH 7.4 (Table 1). The stopped-flow kinetics data indicate that **1** is significantly less active than either **4** or **5** in either a sulfonate-containing buffer or phosphate (Fig. S8†). As with **4** and many other manganese-containing SOD mimics studied by ourselves,[8,31,44] complex **1** is less catalytically active in phosphate buffer. The iron and zinc complexes, **2** and **3**, have no noticeable impact on the rate of decomposition of $O_2^{\bullet-}$ when analyzed by stopped-flow kinetics. The free H_4qp4 ligand is likewise inactive as a catalyst.

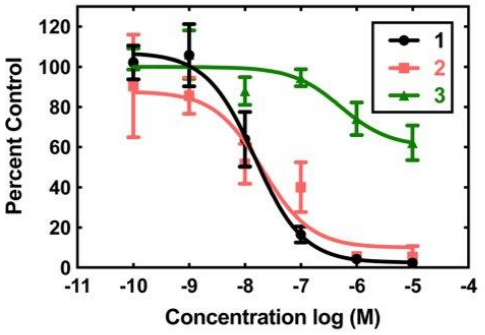

Fig. 2 Superoxide scavenging effects of **1** (black), **2** (pink), and **3** (green). $O_2^{\bullet-}$ was generated from the reaction between hypoxanthine and xanthine oxidase reaction and detected using the chemiluminescent probe lucigenin. All reactions were carried out in pH 7.2 phosphate buffered saline (PBS) (50 mM phosphate). Data for the various concentrations of the three coordination complexes are expressed as percentages of luminescence in the presence of vehicle.

Table 1 Catalytic rate constants, k_{cat} (M^{-1} s^{-1}), measured by stopped-flow kinetics for the direct reactions of **1**, **2**, and **3** with superoxide

Buffer, pH	1	2	3	4[a]	5[a]
60 mM MOPS/HEPES, 7.4	6.0×10^6	N.A.	N.A.	9.7×10^7	1.2×10^7
60 mM MOPS, 7.8	4.5×10^6	N.A.	N.A.	N.D.	N.D.
50 mM phosphate, 7.4	2.9×10^6	N.A.	N.A.	8.0×10^6	1.0×10^7

[a] Data from ref. 8; the first-row data for **4** and **5** were collected in HEPES, rather than MOPS.

The obtained results further demonstrate that indirect assays often cannot even qualitatively distinguish between SOD active and inactive compounds. Instead of being more active than the SOD used as the positive control, **2** does not display any catalytic SOD activity at all and that for **1** is rather low (Table 1).

Although **3** is not an effective SOD mimic, it does react with KO_2, as assessed by EPR, UV/vis, and MS analysis (Fig. S9–S11†). The EPR data show a weak signal at $g = 2$ at 30 s that completely disappears within 15 min. We do not believe that the EPR feature corresponds to residual $O_2^{\bullet-}$ since the oxidant should be consumed to levels below the limit of EPR detection within 1 s, even in the absence of a catalyst.[9] The g value of the signal and its short lifetime are consistent with organic radicals similar to what we observed for previous Zn(II)-quinoxyl radical species.[9,10] A Zn(II)-semiquinone species observed with the H_4qp2 ligand, for instance, persists to detectable levels for over 45 min.[10] The UV/vis data indicate that the complex is initially deprotonated by KO_2, which is a base as well as an oxidant, and

then slowly oxidized to Zn(II)-*para*-quinone species over 90 s. The MS data indicate that the reaction with $O_2^{\bullet-}$ degrades the complex (Fig. S11†). Although **3** does react with $O_2^{\bullet-}$, this activity is not enough to noticeably accelerate superoxide degradation beyond the rate observed for the uncatalyzed reaction.

Catalase activity

Previously, **1** and **2** had been found to react with excess H_2O_2 in a manner consistent with catalase activity.[15,16] We further investigated this potential catalysis by monitoring the reactions of these two compounds, **3**, and metal-free H_4qp4 with H_2O_2 using oxygraphy and UV/vis.

The metal-free H_4qp4 ligand was unable to catalyze the degradation of H_2O_2. Each coordination complex, conversely, catalyzes the decomposition of H_2O_2. In all three cases, the reactivity is consistent with Michaelis–Menten kinetics with clear saturation behavior observed at high concentrations of H_2O_2 (Fig. 3). Oxygraphic measurements confirm that O_2 is being evolved; these data were fitted to the re-arranged Michaelis–Menten equation, which has parameters k_{cat} and k_{cat}/K_M (Tables 2 and S3†). The iron complex **2** appears to be slightly more active than the other two, but the individual rate constants do not vary much within this series.

Full details regarding the models used to fit the data for the three compounds are provided in Table S3 in the ESI.† The listed errors represent one standard deviation.

Second-order rate constants (k_2) were calculated by measuring the initial rates of O_2 production *via* oxygraphy with catalyst concentrations ranging from 1.0 to 100 nM (Fig. 4). The k_2 values are much lower than the k_{cat}/K_M values obtained from the Michaelis–Menten models but more accurately represent the activities of the catalysts.[22] We also measured turnover numbers (TON) by quantifying the total O_2 made over time (Fig. S12†). This parameter depends on both the robustness and activity of the catalyst and is arguably the most accurate measure of the practicality of a catalase mimic. Due to the high activity of the three complexes, we needed to perform these measurements with lower concentrations of the coordination complexes; otherwise, the O_2 evolution is too fast to monitor *via* oxygraphy. Mahammed and Gross encountered similar issues in their studies of the Fe(III) complex with the fluorinated corrole.[27] Although the conversions of H_2O_2 to O_2 are relatively low for these measurements, the amount of generated O_2 (A) still greatly exceeds that of the uncatalyzed reaction and (B) is highly replicable between experiments. We obtained similar TON and 10-fold greater conversions when the initial concentration of H_2O_2 was 1.0 mM rather than 10 mM (Fig. S12†). As assessed by both the initial rates analysis and the overall O_2 production, **2** clearly outperforms its manganese and zinc analogs.

The activity was qualitatively confirmed with parallel experiments that monitored the disappearance of H_2O_2 (Fig. S13 and Table S4†). The rate constants from these experiments are much less reliable than those calculated from O_2 production since all three complexes absorb strongly at the monitored 240 nm wavelength, and this technique generally tends to overestimate the activities of catalase mimics.[22] Nonetheless, the activities of the complexes follow the same general order, with **2** and **3** being the most and least effective catalase mimics, respectively.

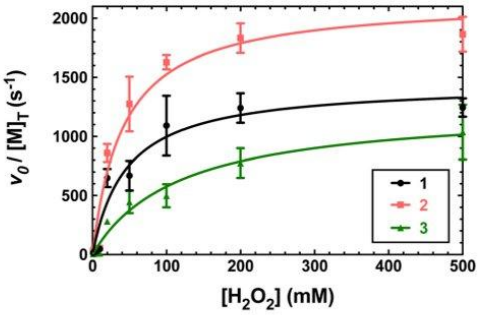

Fig. 3 Plots of v_o/[M] *vs.* the concentration of H_2O_2, where [M] is the concentration of the tested H_4qp4 complex: **1** (black), **2** (pink), **3** (green). The v_o corresponds to the formation of O_2, which was measured through oxygraphy. All reactions were performed in 25 °C 50 mM Tris buffered to pH 7.2. 1 nM of each coordination complex was present as a catalyst. Each shown data point is the average of at least five independent runs. Further details regarding the models used to fit the data can be found in Table S3.†

Peroxidase activity

The three H_4qp4 complexes were also assessed as peroxidase mimics using an established protocol that assesses the ability of a compound to catalyze the reaction between H_2O_2 and 2,2′-azinobis(3-ethylbenzothiazoline-6-sulfonate) (ABTS).[35] Both **1** and **2** appear to catalyze the reaction, as evidenced by the formation of $ABTS^+$. Complex **3**, conversely, shows no activity. Above 20 mM H_2O_2, the reactivity seen for **1** and **2** displays no dependence on the concentration of H_2O_2, suggesting that the activation of the bound H_2O_2, rather than H_2O_2 binding itself, has become rate-determining (Fig. S14†). The initial rates scale with $[ABTS]_o$. Using these data, we calculated third-order rate constants of 0.41 ± 0.02 M^{-2} s^{-1} and 33.8 ± 1.2 M^{-2} s^{-1} for **1** and **2**, respectively. At 10 mM H_2O_2 and 10 mM ABTS, the peroxidase activity (k_{obs} = 4.1 × 10^{-5} s^{-1} for **1**, 3.4 × 10^{-3} for **2**) is negligible compared to the catalase activity (k_{obs} = 13 s^{-1} for **1**, 17 s^{-1} for **2**).

Mechanistic studies

Previous UV/vis and EPR analyses of the reactions between **1** and **2** and excess H_2O_2 indicated that the quinol portions of the ligands oxidize to *para*-quinones after a variable induction period and that the Fe(II) in **2** eventually oxidizes to Fe(III).[15,16] Magnetic susceptibility measurements suggest that **2** is mostly oxidized to high-spin Fe(III) species at RT, but EPR measurements taken at 77 K show a small amount of a low-spin signal (g = 2.55, 2.27, 1.99), possibly indicating that some of the Fe(III) undergoes a spin-crossover upon cooling.[16]

We further analyzed the reactions between H_2O_2 and the three H_4qp4 complexes by EPR, with an emphasis on collecting

Table 2 Michaelis–Menten rate constants, k_2 rate constants, and turnover numbers (TON) calculated from oxygraphic data

Complex	k_{cat} (s^{-1})	k_{cat}/K_M (M^{-1} s^{-1})	K_M (M)	k_2 (M^{-1} s^{-1})	TON
1 (Mn)	1.4×10^3	3.2×10^4	4.6×10^{-2}	$1.5\ (\pm 0.1) \times 10^3$	80 ($\pm$3)
2 (Fe)	2.2×10^3	5.2×10^4	4.2×10^{-2}	$2.2\ (\pm 0.1) \times 10^3$	130 ($\pm$1)
3 (Zn)	1.3×10^3	1.1×10^4	1.2×10^{-1}	$1.2\ (\pm 0.1) \times 10^3$	51 ($\pm$1)

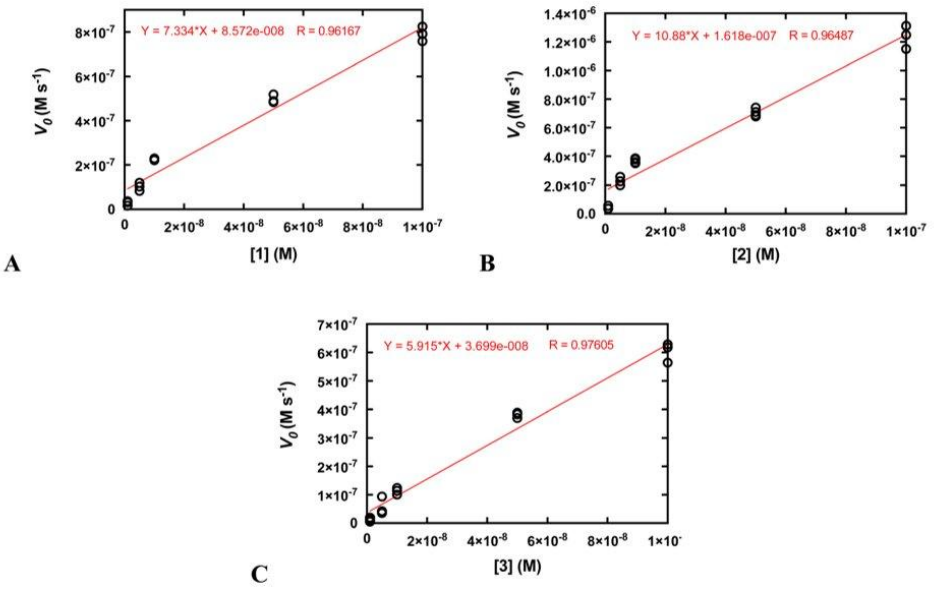

Fig. 4 Determination of k_2 from plots of the initial rates (v_o) *vs.* concentration of catalyst. All reactions were run at 25 °C in 50 mM Tris buffered to pH 7.2. The initial concentration of H_2O_2 was 10.0 mM for all reactions. The reaction was run at least three times at each catalyst concentration. The k_2 values on Table 2 were calculated by dividing the slopes of the shown linear fits by the concentration of H_2O_2 (0.010 M) and multiplying by two to account for the reaction stoichiometry (2 equiv. of H_2O_2 are consumed per equiv. of O_2 produced). (A) Data for **1**. (B) Data for **2**. (C) Data for **3**.

data at an earlier time point that would coincide with higher catalase activity. EPR analysis suggests that some of the Mn(II) and Fe(II) in **1** and **2** has been oxidized 30 s after the reactions begin (Fig. S15†). With **1**, the signal intensity for the Mn(II) decreases by approximately 10%. When **2** is oxidized by H_2O_2, a weak signal develops with $g = 2.04, 1.99$. Relative to the intensity of the Fe(III) end-products,[16] approximately 25% of the iron has been oxidized to Fe(III) by 30 s. The Fe(III) feature is distinct from the high-spin Fe(III) product that was previously observed as the major end-product of the reaction[16] and is instead consistent with a low-spin Fe(III) species. With **3**, we observe a weak signal with $g = 2$. The intensity of the signal is barely above the noise level, however, and it is ambiguous whether this can be attributed to a species on the main catalytic cycle.

UV/vis analysis suggests that the quinols are oxidized during the reaction between **3** and H_2O_2 (Fig. 5). With an initial concentration of 0.6 mM H_2O_2, the 299 nm band attributable to the quinols almost completely vanishes by 15 min. The rate of quinol oxidation is approximately as fast as that observed for **1**, which likewise lacks obfuscating charge transfer bands, under the same conditions.[15] When the initial concentration of H_2O_2 is 10 mM, the rate of quinol oxidation slows relative to that seen at 0.6 mM H_2O_2, as was previously seen with **1** and **2**.[15,16] Such behavior is in agreement with the catalase activity of these complexes. An initially generated catalytically active species can either oxidize H_2O_2 or undergo self-oxidation (*e.g.* oxidation of the quinols, which is monitored in Fig. 5). Therefore, the more H_2O_2 that is initially present in the solution, the longer catalytic H_2O_2 decomposition proceeds and the longer the quinol groups of the ligand remain in their original reduced states. This explains why the quinols are oxidized more slowly with 10 mM H_2O_2. When there is a lower concentration of H_2O_2, the initially generated active species does not have enough substrate (H_2O_2) with which to react and more readily attacks the quinol moieties

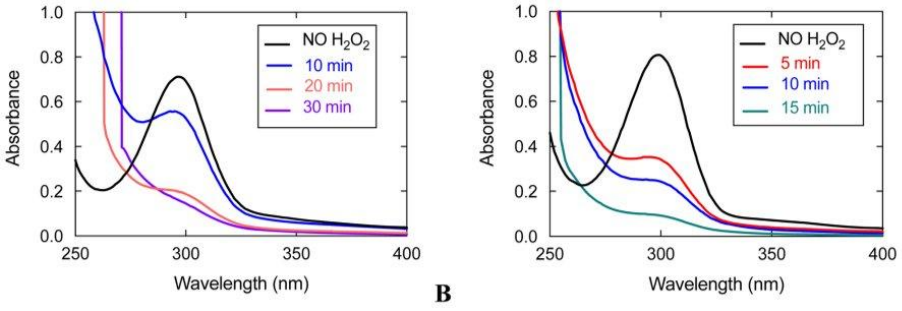

Fig. 5 UV/vis spectra of reactions between **3** and H_2O_2. (A) Data for the reaction between 0.1 mM **3** and 10 mM H_2O_2. (B) Data for the reaction between 0.1 mM **3** and 0.60 mM H_2O_2. All data were taken in 50 mM HEPES buffered to pH 7.00 at 298 K with a 1.0 cm cuvette.

of the ligand, thereby resulting in faster ligand oxidation shown in Fig. 5.

With an initial concentration of 10 mM H_2O_2, however, the quinols in **3** oxidize much more quickly than those in **1** under the same conditions. The quinols in **3** appear to be almost entirely consumed by 30 min; whereas, ligand oxidation does not occur to a noticeable extent for **1** by 30 min. The results suggest that the redox-active ligand is more heavily involved in H_2O_2 degradation for **3** than it is for **1**. Since **3** has lower catalase activity than **1**, it is more susceptible to degradation than the more active **1** in the presence of the same concentration of H_2O_2.

We reacted each H_4qp4 complex with equimolar amounts of H_2O_2 in attempts to identify intermediates that might precede quinol oxidation by UV/vis (*e.g.* M–OOH species). In each case, however, the quinol oxidation occurs immediately, and no new features were observed (Fig. S16†). The final spectra for **1** and **2** resemble those observed for the end-products of previous reactions with large excesses of the terminal oxidant.[15,16]

MS studies of reactions between 10 mM H_2O_2 and the H_4qp4 complexes in MeCN further suggest that ligand-derived redox is more prevalent for **3** than it is for the two H_4qp4 complexes with redox-active metals. The data for **1** and **2** at 30 s look identical to those in solutions that lack H_2O_2;[15,16] the major *m*/*z* peaks are consistent with $[Mn^{III}(H_2qp4)]^+$ and $[Fe^{III}(H_2qp4)]^+$, respectively (Fig. S17 and S18†). Without H_2O_2, the Mn(II) and Fe(II) appear to oxidize spontaneously under MS ionizing conditions. The data are inconsistent with M(II) or M(III) complexes with oxidized forms of the ligand, leading us to conclude that the ligand exists as the doubly deprotonated H_2qp4^{2-} rather than the monoquinol/mono-*para*-quinone H_2qp4. When we react **3** and 10 mM H_2O_2, however, we observe a much different set of *m*/*z* peaks that are consistent with ligand oxidation (Fig. S19 and S20†). Specifically, we detect a *m*/*z* peak at 505.1790 at 30 s that is consistent with a Zn(II) complex with the monoquinolate/mono-*para*-quinone form of the ligand (calculated *m*/*z* = 505.1794). Further, we observe peaks that are consistent with the addition of one oxygen atom to the mono-*para*-quinone complex ($[Zn(Hqp4 + O)]^+$) with *m*/*z* = 521.1736 (calculated *m*/*z* = 521.1743) and with the addition of two oxygen atoms to the diquinol complex ($[Zn(H_3qp4 + 2O)]^+$) with *m*/*z* = 539.1395 (calculated *m*/*z* = 539.1848). After 60 s, oxygenated products appear to become more prominent (Fig. S21†). We analyzed longer-term reactions between **1** and **2** with larger excess of H_2O_2 and likewise found evidence of ligand oxidation beyond the quinol-to-*para*-quinone conversion. With **1**, we detect *m*/*z* peaks consistent with the loss of quinol groups (Fig. S22†). With **2**, new *m*/*z* peaks are observed, but these are more difficult to assign to specific oxidation products (Fig. S23†).

Discussion

The manganese and iron complexes with 1,8-bis(2,5-dihydroxybenzyl)-1,4,8,11-tetraazacyclotetradecane (H_4qp4) were previously found to act as T_1-weighted MRI contrast agent sensors for H_2O_2.[15,16] The responses, which rely either wholly or partly on the oxidation of the quinolic portions of the ligand, were found to both display an induction period and be noticeably slower with larger excesses of H_2O_2. This initially counter-intuitive observation led us to speculate that both $[Mn^{II}(H_3qp4)](OTf)$ (**1**) and $[Fe^{II}(H_3qp4)](OTf)$ (**2**) were proceeding through higher-valent metal species that could either self-oxidize to the activated sensor or catalyze the decomposition of the excess H_2O_2 (Scheme 3).

Given that other quinol-containing ligands had been found to allow the redox-inactive metal ion Zn(II) to catalyze the dismutation of superoxide,[9,10] we also prepared and tested the reactivity of a Zn(II) complex with H_4qp4, $[Zn^{II}(H_3qp4)](OTf)$ (**3**). The synthesis of the Zn(II) complex was identical in most aspects to those used to prepare both **1** and **2**, and as with these syntheses, a complex with singly deprotonated ligand (H_3qp4^-) was the isolated product.[15,16] Unlike the manganese and iron systems, we were able to obtain a crystal structure for the divalent metal. The H_3qp4^- ligand does not fully coordinate to the metal center (Fig. 1), which may suggest that the Zn(II) is too small to be fully accommodated by the ligand pocket. Only one of the quinols is coordinated in the crystal structure, and it appears that it remains unassociated with the metal center in aqueous solution since the second measured pK_a of 9.71 is only slightly lower than the value of ~10 expected for a non-

coordinated quinol. Nonetheless, the Zn(II) complex with the H_3qp4^- form of the ligand is highly stable in water like **1** and **2**; the analogous log K_{ML} values for Mn(II) and Fe(II) are 18.22 and 27.16, respectively.[15,16]

Given that manganese and zinc complexes with other quinol-containing ligands were found to act as functional mimics of superoxide dismutase (SOD),[8–10] we initially assessed the abilities of the three complexes to catalyze the degradation of $O_2^{\bullet-}$. We screened **1**, **2**, and **3** using the xanthine oxidase/hypoxanthine/lucigenin assay (Fig. 2).[28,29] Although the assay suggests that **1** and **2** are potent antioxidants, subsequent stopped-flow analysis of the direct reactions between KO_2 and the complexes found that only the manganese complex **1** had a noticeable effect on $O_2^{\bullet-}$ decomposition. The activity of **1** was generally inferior to those displayed by two manganese complexes that were previously reported by our lab groups: $[Mn^{II}(H_2qp1)(MeCN)](OTf)_2$ (**4**) and $[Mn^{II}(H_4qp2)Br_2]$ (**5**, Scheme 1).[8] As with many other manganese-containing SOD mimics studied by our groups, **1** is most effective as a catalyst in pH 7.4 solutions with sulfonate-based buffers (HEPES/MOPS) and becomes less active as the solution becomes more basic or the buffer switches to phosphate.[31,45–51] In the presence of phosphate ions that can coordinate to the metal center, the reaction step involving $O_2^{\bullet-}$ binding will compete with the rate-determining step that would be observed without phosphate. Superoxide coordination becomes the rate-determining step once the phosphate concentration exceeds a specific concentration.[31]

We determined that **1**, **2**, and **3** are all highly active catalase mimics using a Clark-type O_2 sensitive electrode to follow O_2 production polarographically (Fig. 3). This technique provides a more reliable measure of catalase activity than spectrophotometrically following H_2O_2 depletion. We measured second-order rate constants by assessing the initial rates of O_2 production (Fig. 4) and determined overall turnover numbers (TON) by monitoring the reactions until completion. Of the three complexes, the iron-containing **2** is the most active, followed by **1**, then **3**. Given the magnitudes of these constants, care must be taken to ensure that these are calculated properly.[19,25] Inspection of the plots from Fig. 3 shows that the rates per M of catalyst do indeed plateau at the k_{cat} values. The k_2 values of the three H_4qp4 complexes might be exceeded only by an Fe(III) complex with a fluorinated corrole prepared by Mahammed and Gross.[27] The reactivity between this compound and H_2O_2 follows second-order kinetics with a $k_2 = 4300\ M^{-1}\ s^{-1}$ in 37 °C pH 7.4 phosphate buffer. The Fe(III)–corrole has a tendency to condense into a less active binuclear Fe(III) species; this process can be hindered by adding imidazole to the solution, increasing the k_2 to 6400 $M^{-1}\ s^{-1}$. Comparisons between Mahammed and Gross's results and ours, however, are obfuscated by the higher temperature at which they studied their catalase activity and by the fact that they had to follow the kinetics by UV/vis rather than oxygraphy. The TON of the H_4qp4 complexes range from 51 (**3**) to 130 (**2**). These compare extremely well to TON values reported for other catalase mimics. In a recent review of catalase mimics, the best listed TON was 12.54, and we were unable to locate a higher value.[22] Mahammed and Gross did not report a TON for their Fe(III)–corrole complex, but the overall O_2 production appears to be severely limited by the formation of the binuclear ferric side-product, even when imidazole is present to hinder that particular reaction.[27] Although the three reported metal complexes with H_4qp4 are active CAT mimics, the free ligand is not; the coordinated metal ion is essential to the reactivity.

The high stabilities of the H_4qp4 complexes in aqueous solutions contribute to their abilities to act as effective catalysts in water. In this, they resemble other CAT mimics with macrocyclic ligands, such as porphyrins and corroles.[22,27] The activities of non-porphyrinic manganese-containing catalase mimics, conversely, are instead determined in MeCN.[17–23]

The activity of the Zn(II) complex is particularly notable in that all previously characterized systems capable of such catalysis contain a redox-active metal ion. Catalases themselves use either dinuclear manganese or heme groups in their active sites to degrade H_2O_2, and most small molecule functional mimics of these enzymes likewise contain either manganese or iron.[17–23,26,27] Our results demonstrate that quinol complexes with redox-inactive metal ions can be used to catalyze the degradation of reactive oxygen species (ROS) other than $O_2^{\bullet-}$. The inability of **3** to act as an SOD mimic, however, shows that one cannot simply assume that SOD and catalase activities scale with each other for this class of antioxidants. In other words, one cannot expect that a strategy that leads to SOD mimicry will invariably also lead to catalase activity.

We also analyzed the capabilities of the complexes to act as peroxidase mimics using 2,2′-azinobis(3-ethylbenzothiazoline-6-sulfonate) (ABTS) as the substrate. We found that **1** and **2**, but not **3**, can catalyze the oxidation of ABTS to $ABTS^+$ by H_2O_2. Enzymes that can perform both catalase and peroxidase activity have been proposed to go through a common intermediate, and the same could conceivably hold for **1** and **2**. The reactivity of **3**, however, is less straightforward, but it appears that whatever intermediates are generated from the reaction between the Zn(II) complex and H_2O_2 cannot be directed towards other substrates. With **1** and **2**, the peroxidase activity is much slower than the catalase activity. This reaction selectivity is an attractive quality for a catalase mimic since competing *in vivo* peroxidase activity could potentially oxidize essential biomolecules as well as the catalysts themselves.

The relative lack of peroxidase activity should protect the three H_4qp4 complexes from oxidative ligand degradation and may also contribute to their high catalase activity. Iron porphyrin and corrole mimics of catalase, conversely, more readily commonly undergo oxidative degradation,[26] and the remarkable catalase activity exhibited by Mahammad and Gross's complex has been attributed to its ability to temporarily resist such decomposition.[27] As mentioned above, the three H_4qp4 complexes are also all highly water-stable, and metal ion dissociation from the ligand is negligible even under highly acidic conditions.[15,16] This represents a substantial advantage over most manganese-containing catalase mimics.[17–23] With these compounds, the aqueous stabilities have not been rigorously established, and the catalysis is studied in organic solvents instead of water.[21,23–25] The abilities of the H_4qp4

complexes to function in water would facilitate the application of either these complexes or more highly performing derivatives towards the clinical treatment of oxidative stress.

Despite the lesser peroxidase activities, complexes **1–3** do eventually degrade when exposed to exceedingly high concentrations of H_2O_2 (Fig. S21–S23†). This limits the TON, as evidenced by the low conversions (0.10–0.22%) observed in Fig. S12;† in these experiments, 0.1 μM of each complex reacts with 10 mM H_2O_2. In light of this result, we reviewed the conditions used to study the MRI properties of **1** and **2** and determined that the 0.1–1.0 mM concentrations for the MRI studies were sufficient to completely degrade the 10 mM of H_2O_2 used to activate the sensors.[15,16] We will also note that we did not observe any ligand oxidation beyond the quinol-to-*para*-quinone conversion in these prior studies.

That **1**, **2**, and **3** catalyze H_2O_2 dismutation at similar rates led us to initially hypothesize that the three catalysts mainly rely on a common mechanistic cycle that does not feature redox at the metal center. EPR analysis of the reactions between H_2O_2 and **1** and **2** at 30 s, however, reveals that the metals in these complexes do noticeably oxidize, with the Mn(II) signal diminishing and a novel low-spin Fe(III) signal appearing, respectively. The low-spin Fe(III) signal seen for **2** could potentially correspond to an Fe(III)–OOH species,[52] but other species could give rise to a similar signal. We attempted to determine whether any Fe(III)–OOH species were present using resonance Raman spectroscopy but were regrettably unable to locate any diagnostic O–O or Fe–O stretches. Our prior analysis of the reactions between H_2O_2 and **1** and **2** suggested that the quinols in the H_4qp4 ligand do not start to convert to *para*-quinones until most of the H_2O_2 has been depleted.[15,16] With a stoichiometric amount of H_2O_2, ligand oxidation occurs immediately for both **1** and **2** (Fig. S16†).

UV/vis and MS analysis of the reactions between **3** and H_2O_2, conversely, demonstrate that one of the quinols oxidizes to a *para*-quinone early in its reaction with a large excess of H_2O_2 (Fig. 5 and S19†). Additionally, we observe a *m*/*z* feature at 539.1396; the mass and charge are consistent with a Zn(II)–OOH complex with the mono-*para*-quinone form of the H_4qp4 ligand, H_2qp4. We caution that the data could also correspond to other species, such as a Zn(II)–OH complex with an oxygenated ligand and that we were likewise unsuccessful in our attempts to visualize a Zn(II)–OOH species with resonance Raman spectroscopy. The ambiguity in the MS data would not be resolvable by ^{18}O-labeling studies. We do not observe any MS data consistent with a diquinone (qp4) species. Based on these results, we tentatively propose that the H_2O_2 dismutation for **3** proceeds through the cycle shown in Scheme 4. H_2O_2 reacts with $[Zn(H_3qp4)]^+$ to yield a M(II)–OOH species (**B**), with subsequent intramolecular oxidation of one of the quinols to a *para*-quinone (**C**). The coordination of H_2O_2 to Zn(II) has been previously observed,[53] leading us to believe that Zn(II)–OOH species are indeed plausible intermediates. A second equiv. of H_2O_2 then coordinates the metal center as HOO^-, generating $[Zn(H_2qp4)(OOH)]^+$ (**D**), which we may be detecting by MS. The *para*-quinone can then oxidize this second equiv. of H_2O_2. Since **D** appears to accumulate, this may be the rate-limiting step in the catalase activity. A previous report found that acids could catalyze the reduction of *para*-quinone to quinol,[54] and the Zn(II) in **3** may

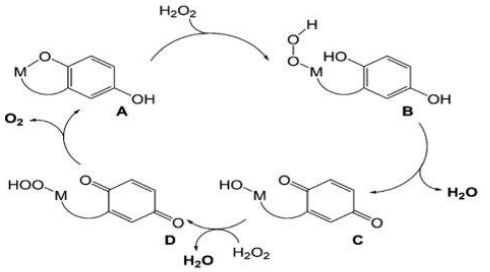

Scheme 4 Proposed mechanism for catalase activity that avoids metal-centered redox.

do likewise in its capacity as a Lewis acid. The Zn(II) could either coordinate water and facilitate the delivery of protons to the *para*-quinone, or it could promote the reduction portion of the PCET by coordinating the *para*-quinone.

Redox-inactive metal ions, such as Al(III) and Ga(III), are capable of activating H_2O_2; in this chemistry, hydroxyl and hydroperoxyl radicals are released upon the coordination of multiple equiv. of the oxidant to the metal center.[55–57] Given the observed Michaelis–Menten kinetics and lack of a second-order dependence of the rate on $[H_2O_2]$, we do not believe that the simultaneous coordination of two equiv. of H_2O_2 is required for catalase activity to proceed. Further, the inability of **3** to oxidize external substrates such as ABTS is inconsistent with the release of highly oxidizing hydroxyl and hydroperoxyl radicals.

Since extensive ligand oxidation is not observed in the early stages of catalase activity, we propose that **1** and **2** mostly catalyze H_2O_2 dismutation through a fundamentally different mechanism (Scheme 5). The initial step corresponding to the coordination of H_2O_2 to the divalent metal ion remains the same, but once **B** is generated, the O–O bond may break heterolytically to yield a M(IV) species (**C′**). Such a high-valent species would stabilized by two factors: the presence of the anionic quinolate and the ability of the quinolate to donate an electron to the metal center to yield an isoelectronic M(III)-ligand radical. Species **C′** can either react with a second equiv. of H_2O_2, removing two net hydrogen atoms to yield O_2 and a M(II)–OH_2 species (**D′**), or it can further oxidize the ligand to a *para*-quinone species (**E**). Although **E** is shown as a hydroxyl complex in Scheme 5, the OH group is basic enough to abstract a proton from the buffered medium, yielding the aquated species observed in our prior report on **1**.[15] The Fe(II) in **2** eventually is oxidized to Fe(III),[16] and this may occur through a side reaction between Fe(II) species and 0.5 equiv. H_2O_2.

That **1** and **2** have higher TON than **3** likely results from improvements to both the speed and durability of the catalyst. The k_2 rate constants for **1** and **2** are both higher than that of **3** (Table 2); this is consistent with the redox-active metals opening new pathways for H_2O_2 dismutation (Scheme 5). Catalysts **1** and **2** also appear to better resist over-oxidation. If external oxidants are initially channeled towards converting quinols to *para*-quinones, one would anticipate that catalysts that can avoid the

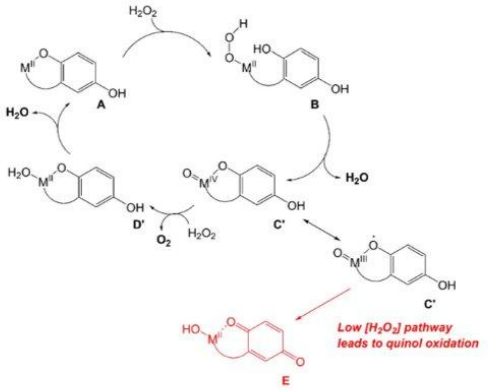

Scheme 5 Proposed mechanism for catalase activity with metal-centered redox.

full oxidation of the quinols (Scheme 5) would be less susceptible to alternative oxidation reactions, such as benzylic C–H activation, than catalysts that rely exclusively on the quinol/*para*-quinone redox couple (Scheme 4).

Conclusions

We find that quinol-containing ligands can substantially enhance the ability of metal ions to catalyze the dismutation of H_2O_2. The described complexes with the macrocyclic ligand H_4qp4 are arguably the most active small molecule catalase mimics reported to date and display negligible competing peroxidase activity. Notably, the redox-inactive Zn(II) activates the ligand for redox catalysis. Despite the similar rate constants for catalase activity, the Zn(II) complex appears to react with H_2O_2 through a fundamentally different mechanism than the complexes with manganese and iron; the complexes with the redox-active metals do not rely as heavily on ligand-centered redox processes. Although similar ligands have been used in highly efficient small molecule mimics of superoxide dismutases, the H_4qp4 ligand does not enable metals to rapidly dismutate superoxide. Only the manganese complex displays such activity, and even this compares poorly to those of manganese complexes with other polydentate quinol-containing ligands. As such, there appear to be subtle factors that direct antioxidant behavior towards specific reactive oxygen species. The exact factors that determine substrate selectivity and the mechanisms for how catalase mimicry is accomplished remain subjects of investigation.

Data availability

Most of the data that support the findings of this study are present in the article and its ESI.† The corresponding author will provide additional data not available in these documents upon request.

Author contributions

S. K., A. F., J. O., T. A., A. J., P. R. P., and D. D. S. conducted the experiments and collected and analyzed the data. S. K., A. F., J. O., P. R. P., and D. D. S. also wrote/edited portions of the manuscript. S. K., I. I.-B., and C. R. G. conceived the idea. I. I.-B. and C. R. G. also supervised the project, provided resources, and wrote/edited the manuscript.

Conflicts of interest

There are no conflicts to declare.

Acknowledgements

The authors thank Prof. Douglas C. Goodwin for his assistance with collecting and interpreting oxygraphy data. The research described here was financially supported by Auburn University and a grant from the National Science Foundation (NSF-CHE-1954336). A. F. and I. I.-B. thank the Deutsche Forschungsgemeinschaft (DFG) for their support through the IV 80/13-1 project. J. O. and I. I.-B. gratefully also acknowledges the DFG (Research Unit FOR 5215 "Bioinspired Oxidation Catalysis with Iron Complexes "BioOxCat") TP6 for financial support.

References

1 V. I. Lushchak, Free Radicals, Reactive Oxygen Species, Oxidative Stress and its Classification, *Chem. Biol. Interact.*, 2014, **224**, 164–175.
2 I. Batinic-Haberle and I. Spasojevic, 25 Years of Development of Mn Porphyrins — from Mimics of Superoxide Dismutase Enzymes to Thiol Signaling to Clinical Trials: The Story of Our Life in the USA, *J. Porphyr. Phthalocyanines*, 2019, **23**(11–12), 1326–1335.
3 R. L. Mosley, E. J. Benner, I. Kadiu, M. Thomas, M. D. Boska, K. Hasan, C. Laurie and H. E. Gendelman, Neuroinflammation, Oxidative Stress, and the Pathogenesis of Parkinson's Disease, *Clin. Neurosci. Res.*, 2006, **6**(5), 261–281.
4 I. M. Fearon and S. P. Faux, Oxidative Stress and Cardiovascular Disease: Novel Tools Give (Free) Radical Insight, *J. Mol. Cell. Cardiol.*, 2009, **47**(3), 372–381.
5 C. K. Roberts and K. K. Sindhu, Oxidative Stress and Metabolic Syndrome, *Life Sci.*, 2009, **84**(21–22), 705–712.
6 M. Yu, M. B. Ward, A. Franke, S. L. Ambrose, Z. L. Whaley, T. M. Bradford, J. D. Gorden, R. J. Beyers, R. C. Cattley, I. Ivanović-Burmazović, D. D. Schwartz and C. R. Goldsmith, Adding a Second Quinol to a Redox-Responsive MRI Contrast Agent Improves Its Relaxivity Response to H_2O_2, *Inorg. Chem.*, 2017, **56**(5), 2812–2826.
7 M. Yu, S. L. Ambrose, Z. L. Whaley, S. Fan, J. D. Gorden, R. J. Beyers, D. D. Schwartz and C. R. Goldsmith, A Mononuclear Manganese(II) Complex Demonstrates a Strategy to Simultaneously Image and Treat Oxidative Stress, *J. Am. Chem. Soc.*, 2014, **136**(37), 12836–12839.

8 L. Senft, J. L. Moore, A. Franke, K. R. Fisher, A. Scheitler, A. Zahl, R. Puchta, D. Fehn, S. Ison, S. Sader, I. Ivanović-Burmazović and C. R. Goldsmith, Quinol-Containing Ligands Enable High Superoxide Dismutase Activity by Modulating Coordination Number, Charge, Oxidation States and Stability of Manganese Complexes throughout Redox Cycling, *Chem. Sci.*, 2021, **12**(31), 10483–10500.

9 M. B. Ward, A. Scheitler, M. Yu, L. Senft, A. S. Zillmann, J. D. Gorden, D. D. Schwartz, I. Ivanović-Burmazović and C. R. Goldsmith, Superoxide Dismutase Activity Enabled by a Redox-Active Ligand rather than Metal, *Nat. Chem.*, 2018, **10**(12), 1207–1212.

10 J. L. Moore, J. Oppelt, L. Senft, A. Franke, A. Scheitler, M. W. Dukes, H. B. Alix, A. C. Saunders, S. Karbalaei, D. D. Schwartz, I. Ivanović-Burmazović and C. R. Goldsmith, Diquinol Functionality Boosts the Superoxide Dismutase Mimicry of a Zn(II) Complex with a Redox-Active Ligand while Maintaining Catalyst Stability and Enhanced Activity in Phosphate Solution, *Inorg. Chem.*, 2022, **61**(49), 19983–19997.

11 A. Tovmasyan, S. Carballal, R. Ghazaryan, L. Melikyan, T. Weitner, C. G. C. Maia, J. S. Reboucas, R. Radi, I. Spasojevic, L. Benov and I. Batinic-Haberle, Rational Design of Superoxide Dismutase (SOD) Mimics: The Evaluation of the Therapeutic Potential of New Cationic Mn Porphyrins with Linear and Cyclic Substituents, *Inorg. Chem.*, 2014, **53**(21), 11467–11483.

12 I. Batinić-Haberle, J. S. Rebouças and I. Spasojević, Superoxide Dismutase Mimics: Chemistry, Pharmacology, and Therapeutic Potential, *Antioxid. Redox Signaling*, 2010, **13**(6), 877–918.

13 K. Aston, N. Rath, A. Naik, U. Slomczynska, O. F. Schall and D. P. Riley, Computer-Aided Design (CAD) of Mn(II) Complexes: Superoxide Dismutase Mimetics with Catalytic Activity Exceeding the Native Enzyme, *Inorg. Chem.*, 2001, **40**(8), 1779–1789.

14 D. Salvemini, Z.-Q. Wang, J. L. Zweier, A. Samouilov, H. Macarthur, T. P. Misko, M. G. Currie, S. Cuzzocrea, J. A. Sikorski and D. P. Riley, A Nonpeptidyl Mimic of Superoxide Dismutase with Therapeutic Activity in Rats, *Science*, 1999, **286**(5438), 304–306.

15 S. Karbalaei, E. Knecht, A. Franke, A. Zahl, A. C. Saunders, P. R. Pokkuluri, R. J. Beyers, I. Ivanović-Burmazović and C. R. Goldsmith, A Macrocyclic Ligand Framework That Improves Both the Stability and T_1-Weighted MRI Response of Quinol-Containing H_2O_2 Sensors, *Inorg. Chem.*, 2021, **60**(12), 8368–8379.

16 S. Karbalaei, A. Franke, A. Jordan, C. Rose, P. R. Pokkuluri, R. J. Beyers, A. Zahl, I. Ivanović-Burmazović and C. R. Goldsmith, A Highly Water- and Air-Stable Iron-Containing MRI Contrast Agent Sensor for H_2O_2, *Chem.–Eur. J.*, 2022, **28**, e202201179.

17 A. Vincent, M. Thauvin, E. Quévrain, E. Mathieu, S. Layani, P. Seksik, I. Batinic-Haberle, S. Vriz, C. Policar and N. Delsuc, Evaluation of the Compounds Commonly Known as Superoxide Dismutase and Catalase Mimics in Cellular Models, *J. Inorg. Biochem.*, 2021, **219**, 111431.

18 G. N. Ledesma, H. Eury, E. Anxolabéhère-Mallart, C. Hureau and S. R. Signorella, A New Mononuclear Manganese(III) Complex of an Unsymmetrical Hexadentate N_3O_3 Ligand Exhibiting Superoxide Dismutase and Catalase-Like Activity: Synthesis, Characterization, Properties and Kinetics Studies, *J. Inorg. Biochem.*, 2015, **146**, 69–76.

19 S. Signorella, A. Rompel, K. Büldt-Karentzopoulos, B. Krebs, V. L. Pecoraro and J.-P. Tuchagues, Reevaluation of the Kinetics of Polynuclear Mimics for Manganese Catalases, *Inorg. Chem.*, 2007, **46**(25), 10864–10868.

20 M. Delroisse, A. Rabion, F. Chardac, D. Tétard, J.-B. Verlhac, L. Fraisse and J.-L. Séris, Synthesis of Di-μ-oxo Manganese(III/IV) Complexes as Functional Models of *L. Plantarum* Pseudo-catalase: Influence of Electronic and Steric Factors; Catalysis and Kinetics of Hydrogen Peroxide Disproportionation, *J. Chem. Soc., Chem. Commun.*, 1995, 949–950.

21 A. Gelasco, S. Bensiek and V. L. Pecoraro, The $[Mn_2(2\text{-}OHsalpn)_2]^{2-,1-,0}$ System: An Efficient Functional Model for the Reactivity and Inactivation of the Manganese Catalases, *Inorg. Chem.*, 1998, **37**(13), 3301–3309.

22 A. Tovmasyan, C. G. C. Maia, T. Weitner, S. Carballal, R. S. Sampaio, D. Lieb, R. Ghazaryan, I. Ivanovic-Burmazovic, G. Ferrer-Sueta, R. Radi, J. S. Reboucas, I. Spasojevic, L. Benov and I. Batinic-Haberle, A Comprehensive Evaluation of Catalase-Like Activity of Different Classes of Redox-Active Therapeutics, *Free Radic. Biol. Med.*, 2015, **86**, 308–321.

23 A. J. Wu, J. E. Penner-Hahn and V. L. Pecoraro, Structural, Spectroscopic, and Reactivity Models for the Manganese Catalases, *Chem. Rev.*, 2004, **104**(2), 903–938.

24 E. J. Larson and V. L. Pecoraro, The Peroxide-Dependent μ_2-O Bond Formation of $[Mn^{IV}SALPN(O)]_2$, *J. Am. Chem. Soc.*, 1991, **113**(10), 3810–3818.

25 M. U. Triller, W.-Y. Hsieh, V. L. Pecoraro, A. Rompel and B. Krebs, Preparation of Highly Efficient Manganese Catalase Mimics, *Inorg. Chem.*, 2002, **41**(21), 5544–5554.

26 A. Haber and Z. Gross, Catalytic Antioxidant Therapy by Metallodrugs: Lessons from Metallocorroles, *Chem. Commun.*, 2015, **51**(27), 5812–5827.

27 A. Mahammed and Z. Gross, Highly Efficient Catalase Activity of Metallocorroles, *Chem. Commun.*, 2010, **46**(37), 7040–7042.

28 J. M. McCord and I. Fridovich, Superoxide Dismutase: An Enzymic Function for Erythrocuprein (Hemocuprein), *J. Biol. Chem.*, 1969, **244**(22), 6049–6055.

29 O. Iranzo, Manganese Complexes Displaying Superoxide Dismutase Activity: A Balance between Different Factors, *Bioorg. Chem.*, 2011, **39**, 73–87.

30 U. Weser, L. M. Schubotz and E. Lengfelder, Imidazole-Bridged Copper Complexes as Cu_2Zn_2—Superoxide Dismutase Models, *J. Mol. Catal.*, 1981, **13**(2), 249–261.

31 F. C. Friedel, D. Lieb and I. Ivanović-Burmazović, Comparative Studies on Manganese-Based SOD Mimetics, Including the Phosphate Effect, by Using Global Spectral Analysis, *J. Inorg. Biochem.*, 2012, **109**, 26–32.

32 B. H. J. Bielski, D. E. Cabelli, R. L. Arudi and A. B. Ross, Reactivity of HO_2/O_2^- Radicals in Aqueous Solution, *J. Phys. Chem. Ref. Data*, 1985, **14**(4), 1041–1100.
33 D. P. Nelson and L. A. Kiesow, Enthalpy of Decomposition of Hydrogen Peroxide by Catalase at 25 °C (with Molar Extinction Coefficients of H_2O_2 Solutions in the UV), *Anal. Biochem.*, 1972, **49**(2), 474–478.
34 E. N. Ndontsa, R. L. Moore and D. C. Goodwin, Stimulation of KatG Catalase Activity by Peroxidatic Electron Donors, *Arch. Biochem. Biophys.*, 2012, **525**(2), 215–222.
35 S. L. Scott, W.-J. Chen, A. Bakac and J. H. Espenson, Spectroscopic Parameters, Electrode Potentials, Acid Ionization Constants, and Electron Exchange Rates of the 2,2'-Azinobis(3-ethylbenzothiazoline-6-sulfonate) Radicals and Ions, *J. Phys. Chem.*, 1993, **97**(25), 6710–6714.
36 A. W. Addison, T. N. Rao, J. Reedijk, J. van Rijn and G. C. Verschoor, Synthesis, Structure, and Spectroscopic Properties of Copper(II) Compounds Containing Nitrogen–Sulphur Donor Ligands; the Crystal and Molecular Structure of Aqua[1,7-bis(*N*-methylbenzimidazol-2′-yl)-2,6-dithiaheptane]copper(II) Perchlorate, *J. Chem. Soc., Dalton Trans.*, 1984, **7**, 1349–1356.
37 D. P. Riley, Functional Mimics of Superoxide Dismutase Enzymes as Therapeutic Agents, *Chem. Rev.*, 1999, **99**(9), 2573–2587.
38 I. Fridovich, Superoxide Anion Radical (O_2^-), Superoxide Dismutases, and Related Matters, *J. Biol. Chem.*, 1997, **272**(30), 18515–18517.
39 S. I. Liochev, Superoxide Dismutase Mimics, Other Mimics, Antioxidants, Prooxidants, and Related Matters, *Chem. Res. Toxicol.*, 2013, **26**(9), 1312–1319.
40 D. P. Riley, W. J. Rivers and R. H. Weiss, Stopped-Flow Kinetic Analysis for Monitoring Superoxide Decay in Aqueous Systems, *Anal. Biochem.*, 1991, **196**, 344–349.
41 S. I. Liochev and I. Fridovich, Lucigenin (Bis-N-methylacridinium) as a Mediator of Superoxide Anion Production, *Arch. Biochem. Biophys.*, 1997, **337**(1), 115–120.
42 S. I. Liochev and I. Fridovich, Lucigenin as Mediator of Superoxide Production: Revisited, *Free Radic. Biol. Med.*, 1998, **25**(8), 926–928.
43 I. B. Afanas'ev, E. A. Ostrakhovitch, E. V. Mikhal'chik and L. G. Korkina, Direct Enzymatic Reduction of Lucigenin Decreases Lucigenin-Amplified Chemiluminescence Produced by Superoxide Ion, *Luminescence*, 2001, **16**(5), 305–307.
44 I. Kenkel, A. Franke, M. Dürr, A. Zahl, C. Dücker-Benfer, J. Langer, M. R. Filipović, M. Yu, R. Puchta, S. R. Fiedler, M. P. Shores, C. R. Goldsmith and I. Ivanović-Burmazović, Switching between Inner- and Outer-Sphere PCET Mechanisms of Small-Molecule Activation: Superoxide Dismutation and Oxygen/Superoxide Reduction Reactivity Deriving from the Same Manganese Complex, *J. Am. Chem. Soc.*, 2017, **139**(4), 1472–1484.
45 D. Lieb, F. C. Friedel, M. Yawer, A. Zahl, M. M. Khusniyarov, F. W. Heinemann and I. Ivanović-Burmazović, Dinuclear Seven-Coordinate Mn(II) Complexes: Effect of Manganese(II)-Hydroxo Species on Water Exchange and Superoxide Dismutase Activity, *Inorg. Chem.*, 2013, **52**(1), 222–236.
46 I. Ivanović-Burmazović, Catalytic Dismutation vs. Reversible Binding of Superoxide, *Adv. Inorg. Chem.*, 2008, **60**, 59–100.
47 C. M. Weekley, I. Kenkel, R. Lippert, S. Wei, D. Lieb, T. Cranwell, J. L. Wedding, A. S. Zillmann, R. Rohr, M. R. Filipovic, I. Ivanović-Burmazović and H. H. Harris, Cellular Fates of Manganese(II) Pentaazamacrocyclic Superoxide Dismutase (SOD) Mimetics: Fluorescently Labeled MnSOD Mimetics, X-ray Absorption Spectroscopy, and X-ray Fluorescence Microscopy Studies, *Inorg. Chem.*, 2017, **56**(11), 6076–6093.
48 D. P. Riley and R. H. Weiss, Manganese Macrocyclic Ligand Complexes as Mimics of Superoxide Dismutase, *J. Am. Chem. Soc.*, 1994, **116**(1), 387–388.
49 D. P. Riley and O. F. Schall, Structure–Activity Studies and the Design of Synthetic Superoxide Dismutase (SOD) Mimetics as Therapeutics, *Adv. Inorg. Chem.*, 2006, **59**, 233–263.
50 D. P. Riley, S. L. Henke, P. J. Lennon, R. H. Weiss, W. L. Neumann, W. J. Rivers Jr, K. W. Aston, K. R. Sample, H. Rahman, C.-S. Ling, J.-J. Shieh and D. H. Busch, Synthesis, Characterization, and Stability of Manganese(II) C-Substituted 1,4,7,10,13-Pentaazacyclopentadecane Complexes Exhibiting Superoxide Dismutase Activity, *Inorg. Chem.*, 1996, **35**(18), 5213–5231.
51 D. P. Riley, P. J. Lennon, W. L. Neumann and R. H. Weiss, Toward the Rational Design of Superoxide Dismutase Mimics: Mechanistic Studies for the Elucidation of Substituent Effects on the Catalytic Activity of Macrocyclic Manganese(II) Complexes, *J. Am. Chem. Soc.*, 1997, **119**(28), 6522–6528.
52 Y. He and C. R. Goldsmith, Observation of a Ferric Hydroperoxide Complex during the Non-heme Iron Catalysed Oxidation of Alkenes and Alkanes by O_2, *Chem. Commun.*, 2012, **48**, 10532–10534.
53 C. M. Wallen, J. Bacsa and C. C. Scarborough, Hydrogen Peroxide Complex of Zinc, *J. Am. Chem. Soc.*, 2015, **137**(46), 14606–14609.
54 F. Minisci, A. Citterio, E. Vismara, F. Fontana, S. De Bernardinis and M. Correale, Facile and Convenient Syntheses of Quinones from Phenols, *J. Org. Chem.*, 1989, **54**(3), 728–731.
55 A. S. Novikov, M. L. Kuznetsov, A. J. L. Pombeiro, N. A. Bokach and G. B. Shul'pin, Generation of HO· Radical from Hydrogen Peroxide Catalyzed by Aqua Complexes of the Group III Metals $[M(H_2O)_n]^{3+}$ (M = Ga, In, Sc, Y, or La): A Theoretical Study, *ACS Catal.*, 2013, **3**(6), 1195–1208.
56 M. L. Kuznetsov, Y. N. Kozlov, D. Mandelli, A. J. L. Pombeiro and G. B. Shul'pin, Mechanism of Al^{3+}-Catalyzed Oxidations of Hydrocarbons: Dramatic Activation of H_2O_2 toward O-O Homolysis in Complex $[Al(H_2O)_4(OOH)(H_2O_2)]^{2+}$ Explains the Formation of HO˙ Radicals, *Inorg. Chem.*, 2011, **50**(9), 3996–4005.
57 A. S. Novikov, M. L. Kuznetsov, B. G. M. Rocha, A. J. L. Pombeiro and G. B. Shul'pin, Oxidation of Olefins with H_2O_2 Catalysed by Salts of Group III Metals (Ga, In, Sc, Y and La): Epoxidation versus Hydroperoxidation, *Catal. Sci. Technol.*, 2016, **6**(5), 1343–1356.

Electronic Supplementary Material (ESI) for Chemical Science.

Supporting Information for

A Macrocyclic Quinol-Containing Ligand Enables High Catalase Activity even with a Redox-Inactive Metal at the Expense of the Ability to Mimic Superoxide Dismutase

Sana Karbalaei,[†] Alicja Franke,[ǂ] Julian Oppelt,[ǂ] Tarfi Aziz,[†] Aubree Jordan,[†] P. Raj Pokkuluri,[†] Dean D. Schwartz,[¥] Ivana Ivanović-Burmazović,[ǂ] and Christian R. Goldsmith[†,*]

[†]Department of Chemistry and Biochemistry, Auburn University, Auburn, AL 36849, USA
[ǂ]Department of Chemistry, Ludwig-Maximilians-Universität München, 81377 München, Germany
[¥]Department of Anatomy, Physiology, and Pharmacology, College of Veterinary Medicine, Auburn University, Auburn, AL 36849, USA

*Corresponding author: crgoldsmith@auburn.edu

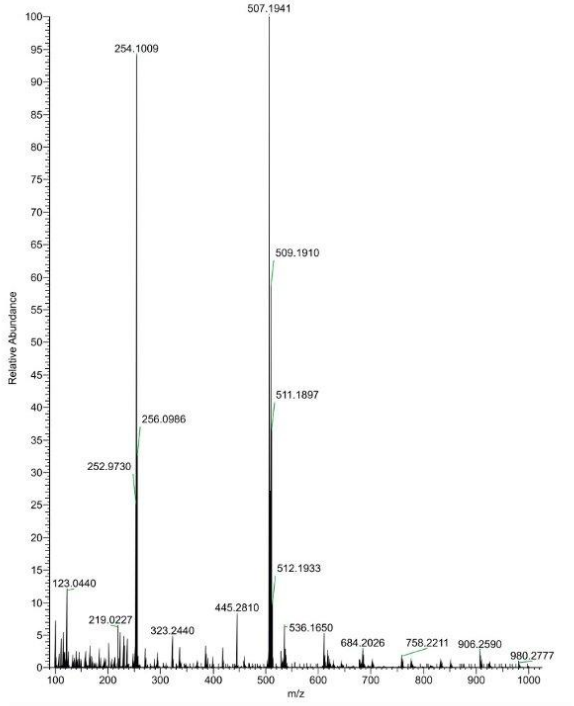

Figure S1. Mass spectrometry (ESI) of **3** in MeOH. The 507.1941 m/z feature is assigned to the Zn(II) complex with the singly deprotonated H_4qp4 ligand: $[Zn^{II}(H_3qp4)]^+$ (calculated m/z = 507.1944). The 254.1009 m/z feature is assigned to: $[Zn^{II}(H_4qp4)]^{2+}$ (calculated m/z = 254.1014).

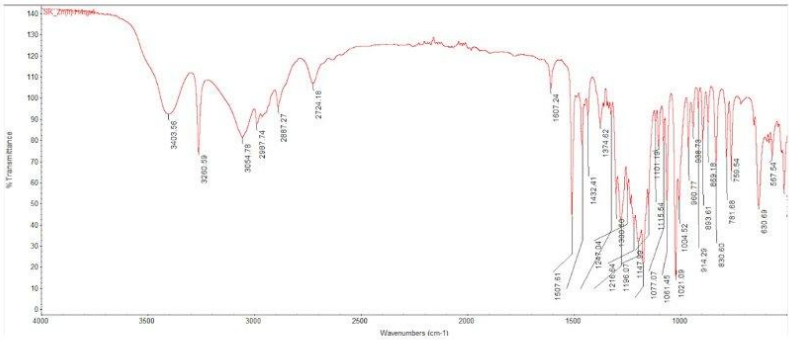

Figure S2. IR spectrum of **3.** The 3404 cm^{-1} feature is assigned to the O-H stretches associated with the quinol groups of the H_3qp4^- ligand.

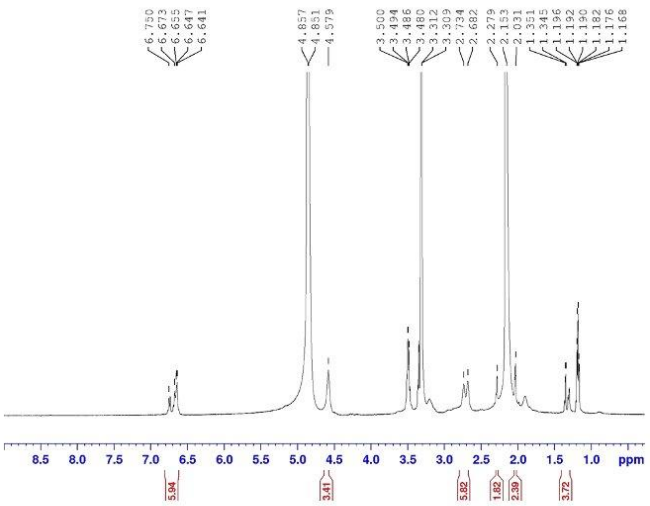

Figure S3. ^{1}H NMR spectrum of a crystalline sample of **3** dissolved in CD_3OD (500 MHz, 298 K). Solvent peaks from diethyl ether (1.16-1.19, 3.48-3.50), acetone (2.15), MeOH (3.31), and water (4.85) are present.

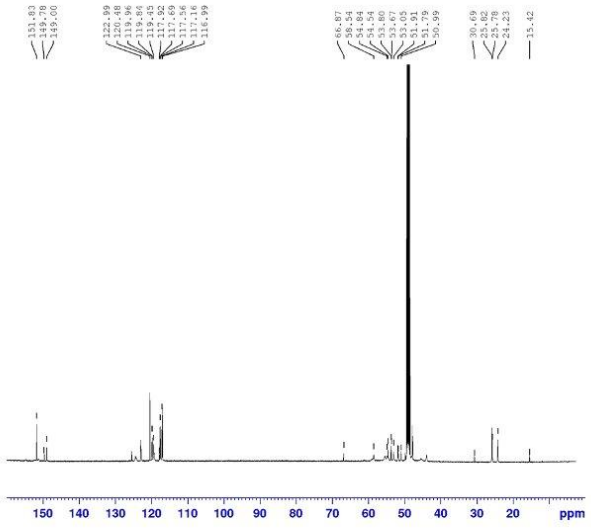

Figure S4. ^{13}C NMR spectrum of crystalline **3** in CD_3OD (125 MHz, 298 K). Solvent peaks from diethyl ether (15.42, 66.87 ppm), acetone (30.69) and MeOH (49.03) are present.

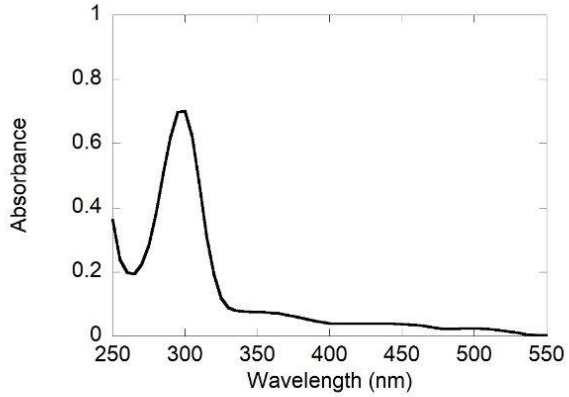

Figure S5. UV/vis data for a 0.10 mM solution of **3** in 294 K water. The major band at 299 nm (ε = 7000 M^{-1} cm^{-1}) is attributed to an intraligand transition associated with the quinol.

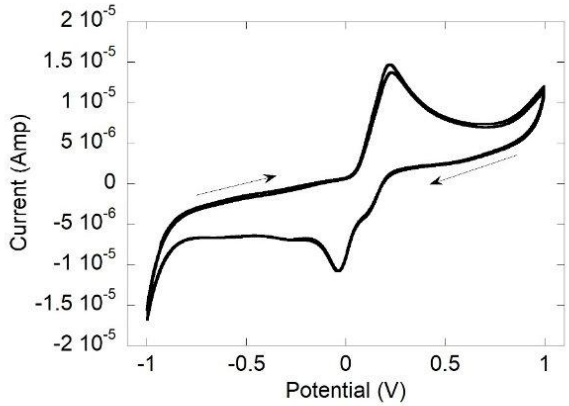

Figure S6. Cyclic voltammogram of 1.0 mM **3** in aqueous phosphate solution buffered to pH 7.2. An irreversible feature is observed with E_{pa} = 225 mV vs. Ag/AgCl and E_{pc} = -10 mV vs. Ag/AgCl. Another feature with E_{pc} = 5 mV vs. Ag/AgCl may be attributable to the acid/base behavior of either the quinol or the semiquinone oxidation product. The scan rate was 100 mV s^{-1}, and the scan commenced at -1.0 V.

Table S1. Selected crystallographic data for $[Zn^{II}(H_3qp4)](OTf)$ (**3**)

Parameter	$[Zn^{II}(H_3qp4)](OTf)$
Formula	$C_{25}H_{35}F_3N_4O_7SZn$
MW	658.00
Crystal system	Monoclinic
Space group	P 1 21/c 1
a (Å)	9.4279(5)
b (Å)	14.3589(7)
c (Å)	21.7932(9)
α (°)	90
β (°)	100.919(2)
γ (°)	90
V (Å^3)	2896.8(2)
Z	4
Crystal color	Colorless
T (K)	306(2)
Reflns collected	74846
Unique reflns	5940
R1 (F, I > 2σ(I))[a]	0.0318
wR2 (F^2, all data)[a]	0.0915

[a] $R1 = \Sigma \big| |F_o| - |F_c| \big| / \Sigma |F_o|$; $wR2 = [\Sigma w(F_o^2-F_c^2)^2/\Sigma w(F_o^2)^2]^{1/2}$.

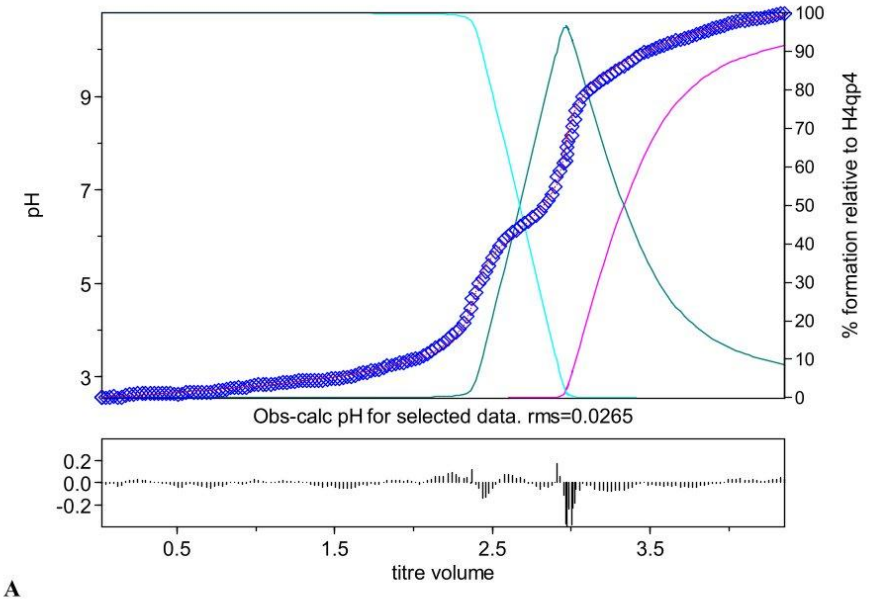

A

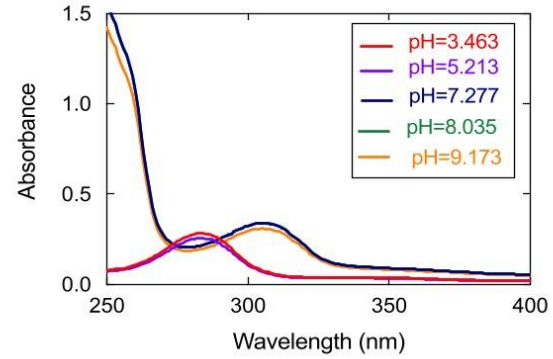

B

Figure S7. A) Hyperquad model (red line) overlaid on the experimental potentiometric pH titration data collected for **3** (blue). The curves represent the formation of various species including $[Zn^{II}(H_4qp4)]^{2+}$ (light blue), $[Zn^{II}(H_3qp4)]^{+}$ (green), and $[Zn^{II}(H_2qp4)]$ (pink). The deviations from the fit as a function of titre volume are provided below. B) Spectrophotometric pH titration of a 0.05 mM solution of **3** in water adjusted to various pH values between 3 and 10 through the addition of either KOH or HCl. All spectra were obtained at 298 K using a 1.0 cm pathlength cuvette. The data are consistent with a metal-bound quinol deprotonating to a quinolate between pH 5.2 and 7.3.

Table S2. Parameters for the Hyperquad model for the potentiometric pH titration data.

Species	Zn(II)	H_4qp4	H^+	log(β)	Derived Values
$[\mathbf{H_2}qp4]^{2-}$	0	1	-2	12.48[a]	
$[\mathbf{H_3}qp4]^{1-}$	0	1	-1	22.504[a]	pK_{L4} = 10.02 (±0.05)[a]
$\mathbf{H_4}qp4$	0	1	0	31.3[a]	pK_{L3} = 8.80 (±0.05)[a]
$[\mathbf{H_5}qp4]^{1+}$	0	1	1	39.005[a]	pK_{L2} = 7.70 (±0.05)[a]
$[\mathbf{H_6}qp4]^{2+}$	0	1	2	42.506[a]	pK_{L1} = 3.50 (±0.05)[a]
[Zn($\mathbf{H_2}$qp4)]	1	1	-2	53.891[b]	log K_{ML} (Zn(H_2qp4)) = 41.411[c]
[Zn($\mathbf{H_3}$qp4)]$^{1+}$	1	1	-1	63.601[b]	pK_a(Zn(H_3qp4)$^+$) = 9.71[b] log K_{ML} (Zn(H_3qp4))$^+$= 41.097[c]
[Zn($\mathbf{H_4}$qp4)]$^{2+}$	1	1	0	69.764[b]	pK_a(Zn(H_4qp4)$^{2+}$) = 6.163[b] log K_{ML} (Zn(H_4qp4))$^{2+}$= 38.464[c]
pZn (pH 7.4) = 37.01[d]					

[a]Ligand log(β) and derived pK_a values from reference 1:

$K_{L1} = [H_5qp4^+][H^+]/[H_6qp4^{2+}]$, $pK_{L1} = \log\beta_{012} - \log\beta_{011}$

$K_{L2} = [H_4qp4][H^+]/[H_5qp4^+]$, $pK_{L2} = \log\beta_{011} - \log\beta_{010}$

$K_{L3} = [H_3qp4^-][H^+]/[H_4qp4]$, $pK_{L3} = \log\beta_{010} - \log\beta_{01(-1)}$

$K_{L4} = [H_2qp4^{2-}][H^+]/[H_3qp4^-]$, $pK_{L4} = \log\beta_{01(-1)} - \log\beta_{01(-2)}$

[b]Metal complex pK_a values:

$K_a(Zn(H_4qp4)^{2+}) = [Zn(H_3qp4)^+][H^+]/[Zn(H_4qp4)^{2+}]$ ~ *deprotonation of first quinol*

$pK_a(Zn(H_4qp4)^{2+}) = \log\beta_{110} - \log\beta_{11(-1)}$

$K_a(Zn(H_3qp4)^+) = [Zn(H_2qp4)][H^+]/[Zn(H_3qp4)^+]$ ~ *deprotonation of second quinol*

$pK_a(Zn(H_3qp4)^+) = \log\beta_{11(-1)} - \log\beta_{11(-2)}$

[c]Metal complex K_{ML} values:

K_{ML} (Zn(H_2qp4)) = [Zn(H_2qp4)]/([Zn(II)][H_2qp4^{2-}])

log K_{ML} (Zn(H_2qp4)) = $\log\beta_{11(-2)} - \log\beta_{01(-2)}$

K_{ML} (Zn(H_3qp4))$^+$ = [Zn(H_3qp4)$^+$]/([Zn(II)][H_3qp4^-])

log K_{ML} (Zn(H_3qp4))$^+$ = $\log\beta_{11(-1)} - \log\beta_{01(-1)}$

K_{ML} (Zn(H_4qp4))$^{2+}$ = [Zn(H_4qp4)$^{2+}$]/([Zn(II)][H_4qp4])

log K_{ML} (Zn(H_4qp4))$^{2+}$ = $\log\beta_{110} - \log\beta_{010}$

[d]pZn(pH 7.4) = -log([free Zn(II)]) at pH 7.4 and 298 K with 1.00 mM Zn(II) and 1.00 mM H_4qp4

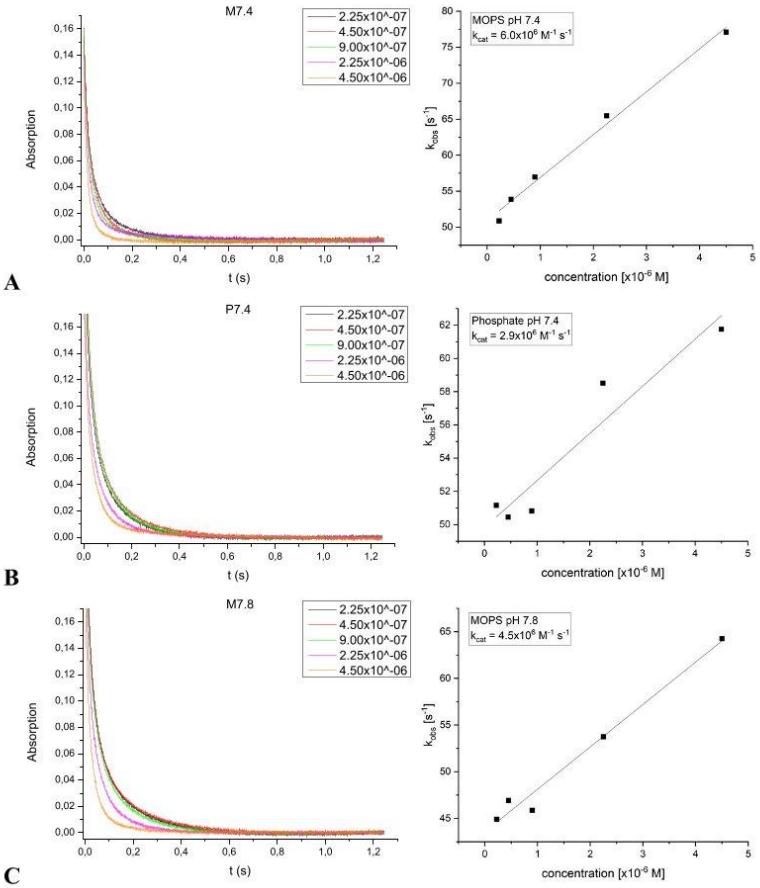

Figure S8. Kinetic traces and k_{obs} vs. catalyst concentration plots of superoxide decomposition at 250 nm by **1** in three different aqueous solutions. First-order decay is observed in all instances. The legends provide the k_{obs} measured for each trace. A) 60 mM MOPS buffer, pH 7.4, ionic strength of 111 mM. $k_{cat} = 5.96 \times 10^6$ M^{-1} s^{-1}. B) 50 mM phosphate buffer, pH 7.4, ionic strength of 111 mM. $k_{cat} = 2.94 \times 10^6$ M^{-1} s^{-1}. C) 60 mM MOPS buffer, pH 7.8, ionic strength of 111 mM. $k_{cat} = 4.54 \times 10^6$ M^{-1} s^{-1}.

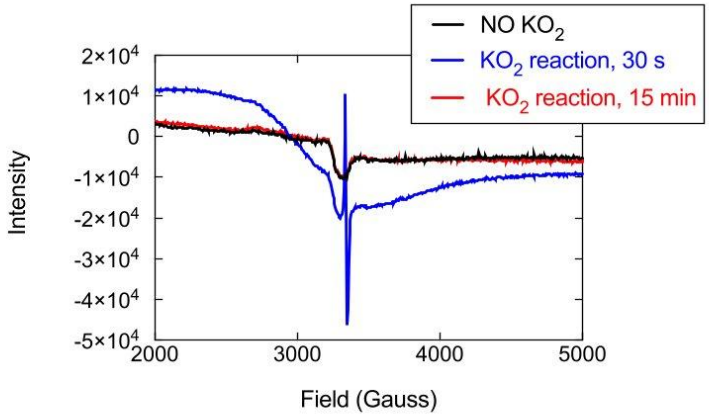

Figure S9. X-band EPR data for the reaction between 1.0 mM **3** and 20 equiv. KO_2 in 50 mM HEPES buffered to pH 7.0. The data were acquired at 77 K.

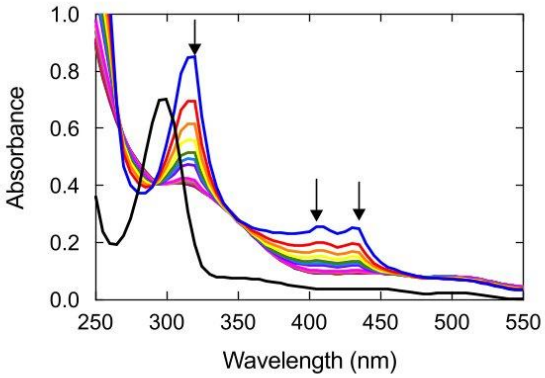

Figure S10. UV/vis data for the reaction between 0.10 mM **3** and 20 equiv. KO_2 in water. The black spectrum shows **3** prior to the addition of KO_2. The blue spectrum was obtained 20 s after KO_2 addition, with subsequent spectra taken every 15 s.

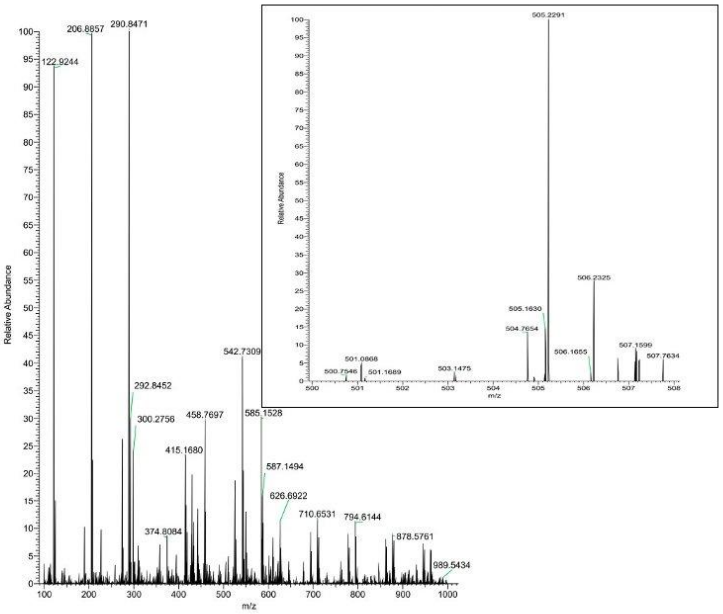

Figure S11. Mass spectrometry (ESI) of the reaction between 20 equiv. KO_2 and **3** in water at RT. The sample was analyzed 15 min after the beginning of the reaction. The 505.2291 m/z feature is assigned to the Zn(II) complex with the singly deprotonated form of the monoquinolate/mono*para*-quinone H_2qp4 ligand: $[Zn(Hqp4)]^+$ (calculated m/z = 505.1866). The appearance of many other peaks is consistent with the degradation of the complex.

Table S3. Parameters for the Michaelis-Menten models that were fitted to the oxygraphy data displayed in **Figure 3**.

Parameters	**1**	**2**	**3**
k_{cat}	1449 (±124)	2159 (±126)	1253 (±175)
k_{on}	31.59 (±7.13)	51.97 (±8.16)	10.67 (±2.63)
k_{cat} (95% Confidence Interval)	1199 – 1699	1905 – 2414	898.7 – 1607
k_{on} (95% Confidence Interval)	17.55 – 46.34	35.50 – 68.43	5.352 – 16.00
Goodness of Fit			
Degrees of Freedom	43	43	43
R^2	0.7990	0.8906	0.7426
Sum of Squares	2815011	3156069	1943522
Sy.x [a]	255.9	270.9	212.6

[a]Sy.x is defined as the standard deviation of the residuals associated with the model.

$$Sy.x = \sqrt{\frac{\Sigma(residual^2)}{n-K}}$$

In this equation, n – K = the Degrees of Freedom, and $\Sigma(residual^2)$ = Sum of Squares.

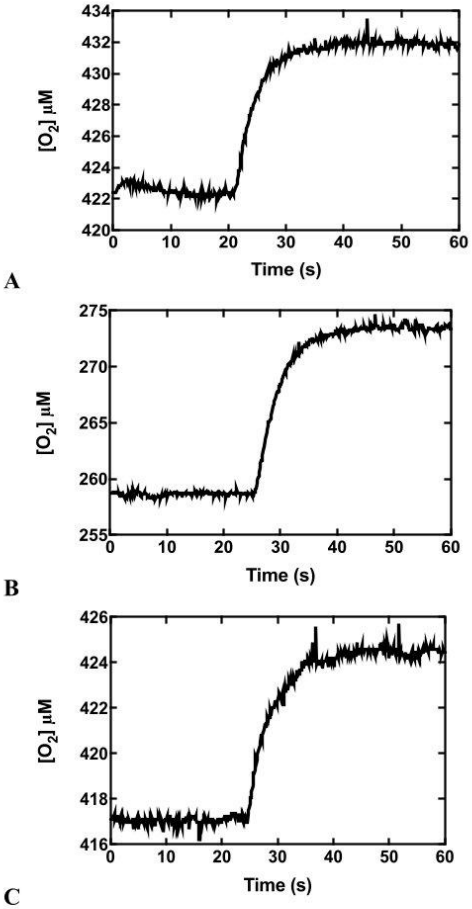

Figure S12. Kinetic traces of oxygen production upon reaction between 0.1 µM of each H_4qp4 catalyst and 10.0 mM H_2O_2 in 50 mM Tris buffered to pH 7.2 and 0.1 M EDTA to scavenge adventitious metal ions. A) Data for **1**. TON = 80 (0.16% conversion). B) Data for **2**. TON = 130 (0.22% conversion). C) Data for **3**. TON = 50 (0.1% conversion). The conversions correspond to the percentages of H_2O_2 that is either oxidized to O_2 or reduced to H_2O. In our control experiments, 2 µM of O_2 was produced from 10 mM H_2O_2 in the absence of a catalyst after 60 s. Data were also collected with 0.1 µM catalyst and 1.0 mM H_2O_2. The results for the lower concentration of H_2O_2 are as follows: **1** – conversion = 1.5%, TON =75; **2** – conversion = 2.4%, TON = 121; **3** – conversion = 1%, TON = 48.

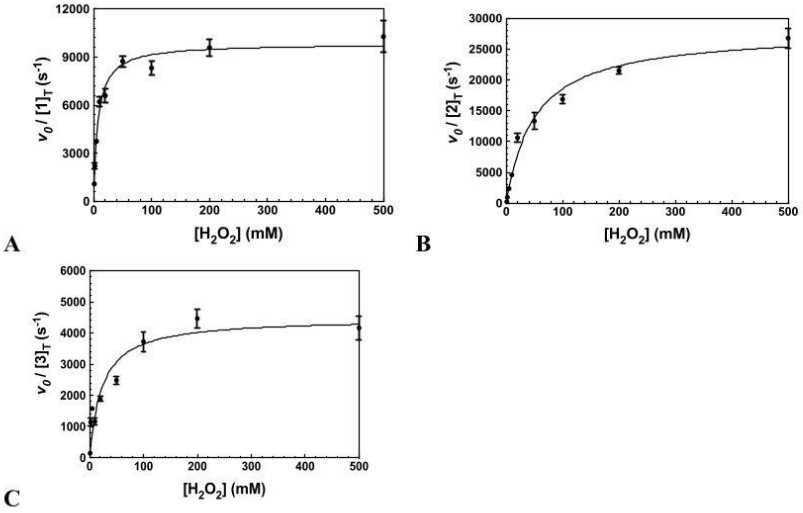

Figure S13. Plots of v_o/[**M**] vs. the concentration of H_2O_2, where [**M**] is the concentration of the tested H_4qp4 complex. The v_o corresponds to the decomposition of H_2O_2, which was measured through UV/vis. All reactions were performed in 25 °C 200 mM phosphate buffered to pH 7.0. 100 nM of each coordination complex was present as a catalyst. Five data points were taken for each shown data point. A) Data for **1**. $k_{cat} = 9.8 \times 10^3$ s^{-1}, $k_{on} = 1.3 \times 10^6$ M^{-1} s^{-1}. B) Data for **2**. $k_{cat} = 2.8 \times 10^4$ s^{-1}, $k_{on} = 5.5 \times 10^5$ M^{-1} s^{-1}. C) Data for **3**. $k_{cat} = 4.5 \times 10^3$ s^{-1}, $k_{on} = 2.0 \times 10^5$ M^{-1} s^{-1}.

Table S4. Parameters for the Michaelis-Menten models that were fitted to the UV/vis data displayed in **Figure S13**.

Parameters	**1**	**2**	**3**
k_{cat}	9838 (±285)	27909 (±1060)	4474 (±232)
k_{on}	1306 (±154)	553 (±53)	196 (±33)
k_{cat} (95% Confidence Interval)	9264 - 10412	25773 - 30044	4005 - 4943
k_{on} (95% Confidence Interval)	996 - 1615	447 – 660	130 - 262
Goodness of Fit			
Degrees of Freedom	43	43	43
R^2	0.9005	0.9508	0.8252
Sum of Squares	47117198	185718722	17267586
Sy.x [a]	1047	2078	634

[a]Sy.x is defined as the standard deviation of the residuals associated with the model.

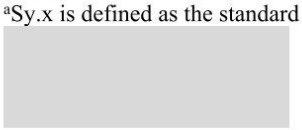

In this equation, n – K = the Degrees of Freedom, and Σ(residual^2) = Sum of Squares.

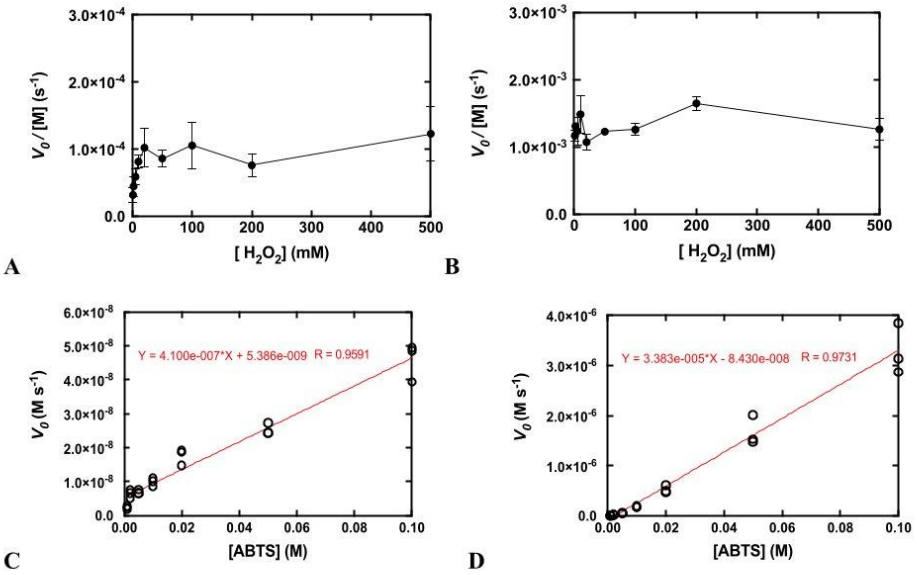

Figure S14. Peroxidase activity for complexes **1** and **2** as assessed by their ability to catalyze the reaction between H_2O_2 and 2,2'-azinobis(3-ethylbenzothiazoline-6-sulfonate) (ABTS). Each v_o corresponds to the initial rate of formation of $ABTS^{\cdot+}$, as measured through UV/vis. All reactions were run in RT 50 mM acetate solution buffered to pH 5.0 with 0.10 mM of the tested catalyst. All kinetic runs were performed in triplicate. A) Plot of v_o/[**M**] vs. the concentration of H_2O_2, where [**M**] is the concentration of **1**. 10 mM ABTS was initially present. B) Plot of v_o/[**M**] vs. the concentration of H_2O_2, where [**M**] is the concentration of **2**. 10 mM ABTS was initially present. C) Plot of v_o vs. the concentration of [ABTS] for **1**. 10 mM H_2O_2 was initially present. The k_3 rate constant was determined from the slope of the plot. D) Plot of v_o vs. the concentration of [ABTS] for **2**. 10 mM H_2O_2 was initially present. The k_3 rate constant was determined from the slope of the plot.

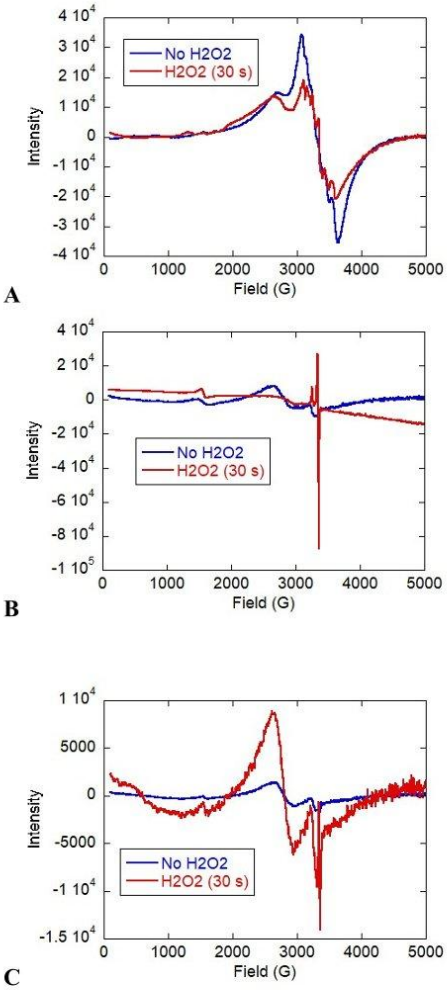

Figure S15. X-band EPR spectra of 1.0 mM solutions of **1**, **2**, and **3** in MeCN in the absence and presence of 10 mM H_2O_2. The reactions between each metal complex and H_2O_2 proceeded for 30 s before the samples were frozen and analyzed at 77 K. A) The intensity of the Mn(II) signal decreases by ~10% upon oxidation. B) A new signal with g = 2.04 and 1.99 appears upon oxidation. The new features are consistent with an axial low-spin Fe(III) species. The intensity of the Fe(III) signal is ~25% of the maximal oxidation observed under these conditions.[2]

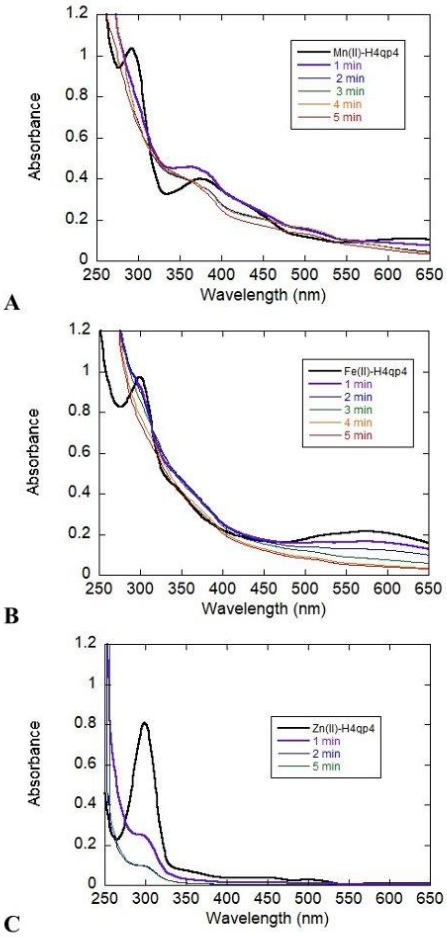

Figure S16. UV/vis data for the reactions between the H_4qp4 complexes and equimolar amounts of H_2O_2. All data were taken in aqueous solutions containing 50 mM HEPES buffered to pH 7.0 at 298 K with a 1.0 cm pathlength. A) 0.14 mM **1** reacting with 0.14 mM H_2O_2. B) 0.10 mM **2** reacting with 0.10 mM H_2O_2. C) 0.10 mM **3** reacting with 0.10 mM H_2O_2. In each case, the quinol band at ~300 nm decays quickly, without the noticeable induction period observed for the reactions between **1** and **2** with larger excess of terminal oxidant.

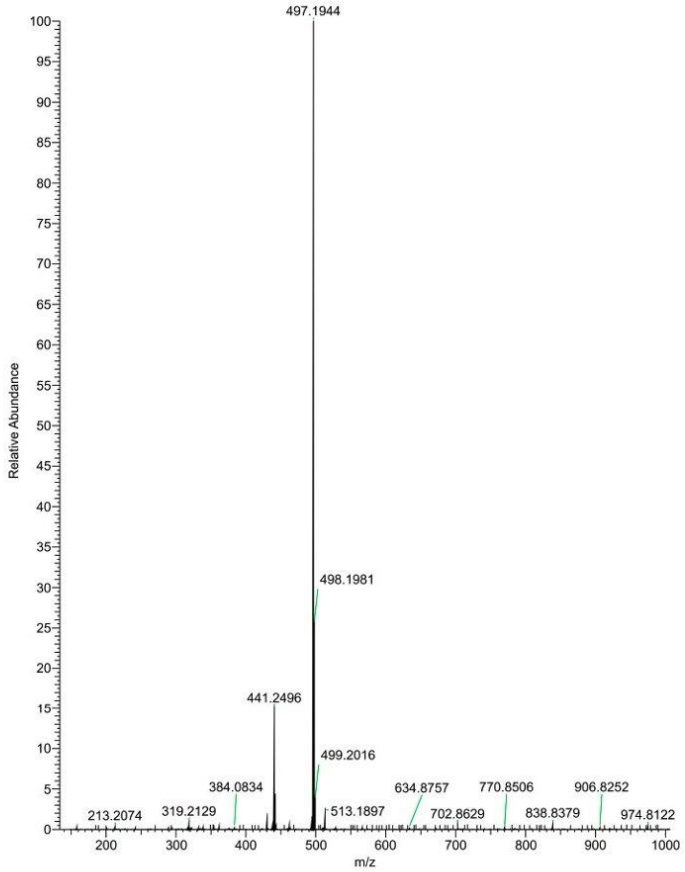

Figure S17. Mass spectrometry (ESI) of the reaction between 10 mM H_2O_2 and **1** in MeCN at RT. The sample was analyzed 30 s after the beginning of the reaction. The 497.1944 m/z feature is assigned to the Mn(III) complex with the doubly protonated H_4qp4 ligand, H_2qp4^{2-}: $[Mn^{III}(H_2qp4)]^+$ (calculated m/z = 497.1955).

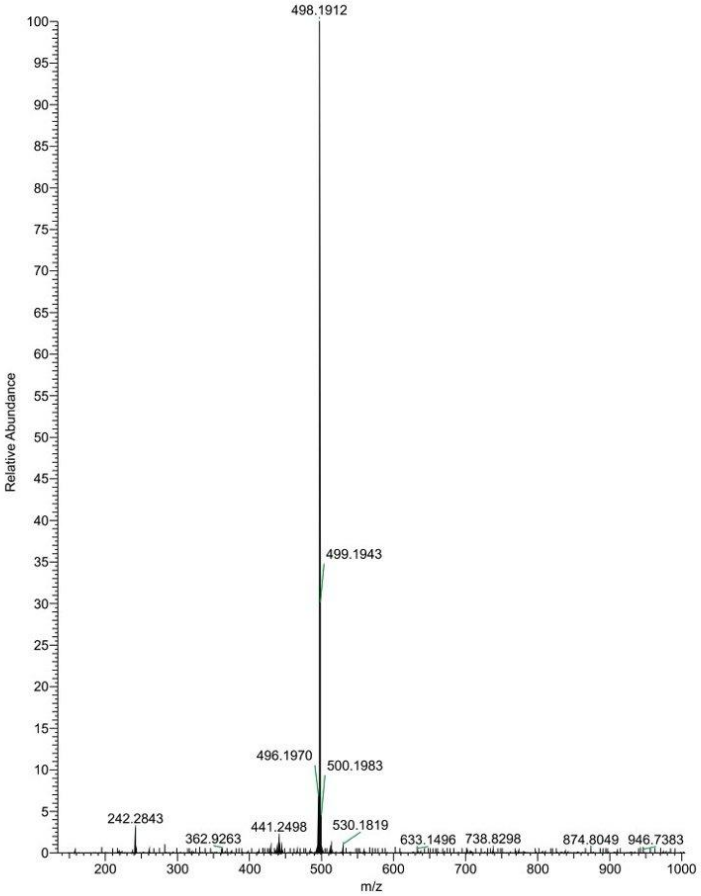

Figure S18. Mass spectrometry (ESI) of the reaction between 10 mM H_2O_2 and **2** in MeCN at RT. The sample was analyzed 30 s after the beginning of the reaction. The 498.1912 m/z feature is assigned to the Fe(III) complex with the doubly protonated form of the H_4qp4 ligand, H_2qp4^{2-}: $[Fe^{III}(H_2qp4)]^+$ (calculated m/z = 498.1929).

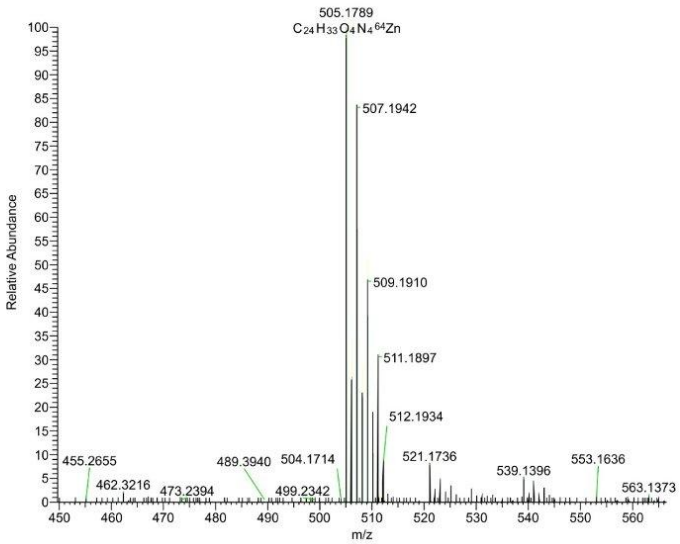

Figure S19. Mass spectrometry (ESI) of the reaction between 10 mM H_2O_2 and **3** in MeCN at RT. The sample was analyzed 30 s after the beginning of the reaction. The 505.1789 m/z feature is assigned to the Zn(II) complex with the singly deprotonated form of the monoquinolate/mono-*para*-quinone H_2qp4 ligand: $[Zn(Hqp4)]^+$ (calculated m/z = 505.1794). The 507.1942 m/z feature is assigned to the Zn(II) with the singly deprotonated form of the diquinol H_4qp4 ligand: $[Zn^{II}(H_3qp4)]^+$ (calculated m/z = 507.1951).

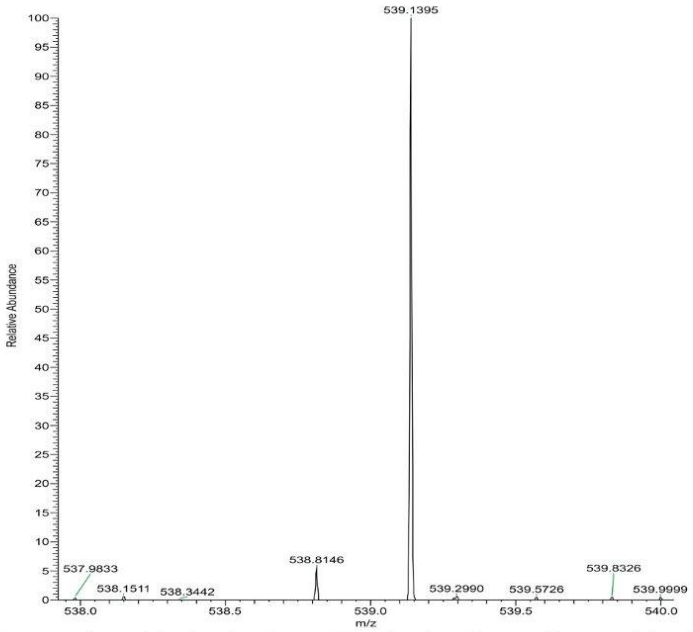

Figure S20. Expansion of the data in **Figure S19**, showing the new feature with m/z = 539.1395, which is consistent with the addition of two O atoms to $[Zn(H_3qp4)]^+$. The m/z may be consistent with $[Zn^{II}(H_2qp4)(OOH)]^+$, where H_2qp4 is the monoquinol/mono-*para*-quinone form of the ligand (calculated m/z = 539.1848).

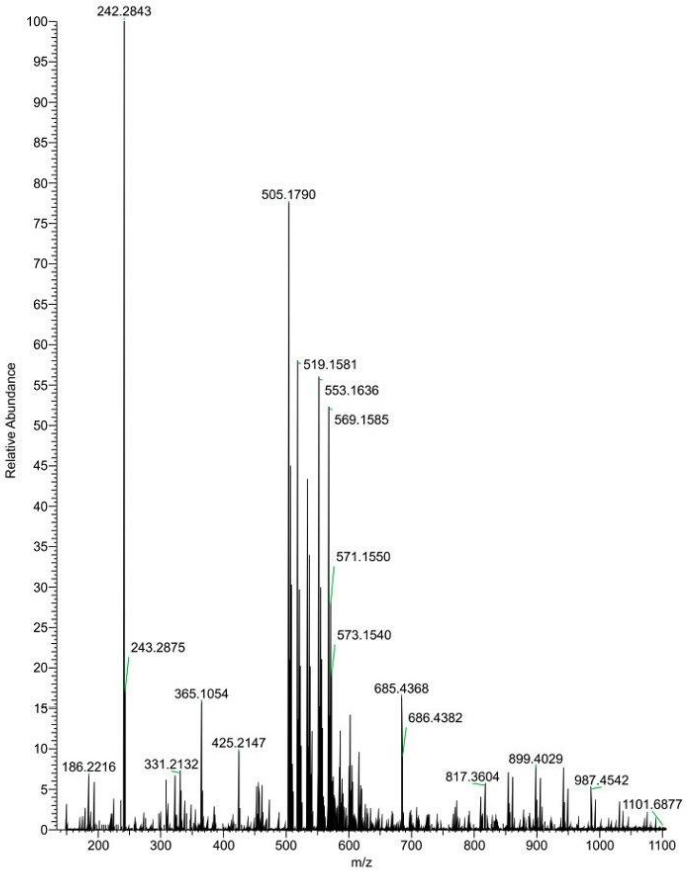

Figure S21. Mass spectrometry (ESI) of the reaction between 10 mM H_2O_2 and **3** in MeCN at RT. The data were acquired 60 s after the beginning of the reaction. Oxygenated products become more prominent.

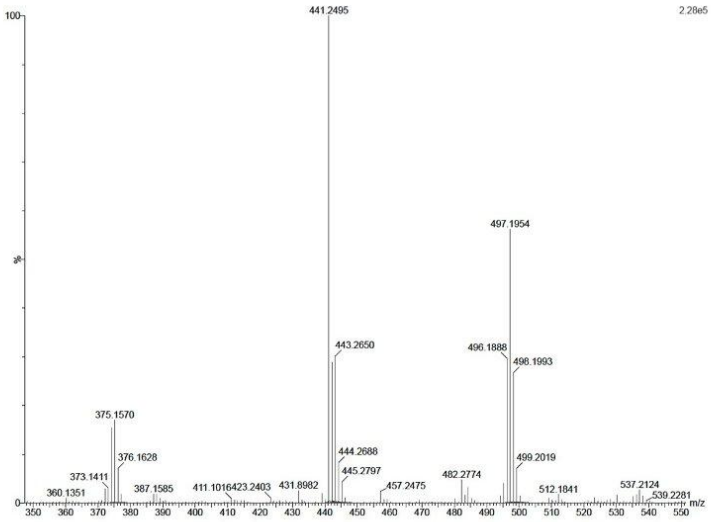

Figure S22. Mass spectrometry (ESI) of the reaction between 300 equivalents of H_2O_2 and **1** in water at RT. The sample was analyzed 60 min after the beginning of the reaction. The 496.1888 m/z feature is assigned to the Mn(II) complex with the singly deprotonated form of the mono-quinolate/mono-*para*-quinone H_2qp4 ligand: $[Mn^{II}(Hqp4)]^+$ (calculated m/z = 496.1882). The 512.1841 m/z peak is assigned to the Mn(II) complex with the singly deprotonated and singly oxygenated form of the mono-quinolate/mono-*para*-quinone form of the ligand: $[Mn^{II}(Hqp4+O)]^+$ (calculated m/z = 512.1832). The 375.1570 m/z feature is assigned to the Mn(II) complex with a mono-quinone ligand missing the other 2,5-dihydroxybenzyl group: $[Mn^{II}(H_2qp4\text{-}C_7H_7O_2+H)$ (calculated m/z =375.1593).

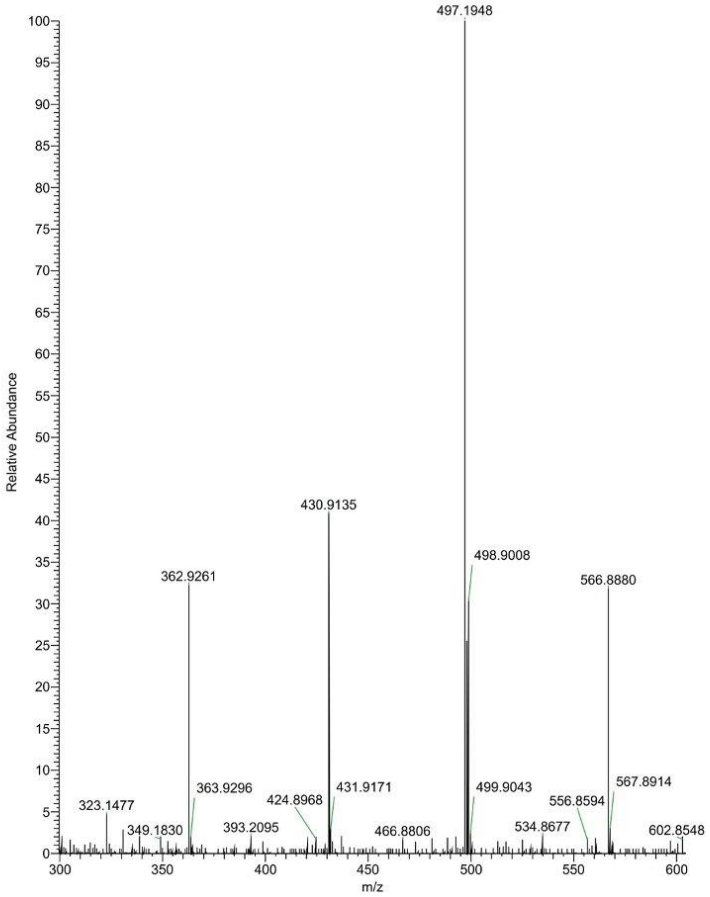

Figure S23. Mass spectrometry (ESI) of the reaction between 300 equivalents of H_2O_2 and **2** in water at RT. The sample was analyzed 60 min after the beginning of the reaction. The 497.1948 m/z feature is assigned to the Fe(III) complex with the singly deprotonated form of the monoquinolate/mono*para*-quinone H_2qp4 ligand: $[Fe(Hqp4)]^+$ (calculated m/z = 497.1851). New prominent m/z peaks are seen at 362.9261, 430.9135, and 566.8880.

References

1. Karbalaei, S.; Knecht, E.; Franke, A.; Zahl, A.; Saunders, A. C.; Pokkuluri, P. R.; Beyers, R. J.; Ivanović-Burmazović, I.; Goldsmith, C. R., A Macrocyclic Ligand Framework That Improves Both the Stability and T_1-Weighted MRI Response of Quinol-Containing H_2O_2 Sensors. *Inorg. Chem.* **2021,** *60* (12), 8368-8379.
2. Karbalaei, S.; Franke, A.; Jordan, A.; Rose, C.; Pokkuluri, P. R.; Beyers, R. J.; Zahl, A.; Ivanović-Burmazović, I.; Goldsmith, C. R., A Highly Water- and Air-Stable Iron-Containing MRI Contrast Agent Sensor for H_2O_2. *Chem. Eur. J.* **2022,** *28*, e202201179.

5 Supporting Information to Chapter 2.2.2

The first reaction system tested with the new high-pressure stopped-flow system was the well-documented iron complex with the biuret tetramido macrocyclic ligand (bTAML) system. Fe(bTAML), is known to stabilize a high valent Fe(V)-oxo species at room temperature and react with organic substrates.[242,243] Consequently, both the reaction of the Fe(III) precursor complex with *meta*-chloroperoxybenzoic acid (*m*-CPBA) as well as the oxidation of substrates were monitored using high-pressure stopped-flow technique. While the primary objective of the high-pressure studies was to investigate C-H activation within the bTAML system, we first examined the formation of the Fe(V)-oxo species (a in Figure 38) to gain further mechanistic insights and assess its stability under high-pressure conditions. The subsequent spontaneous comproportionation between Fe(V) and excess Fe(III) in solution leads to formation of an Fe(IV)-O-Fe(IV) species. (b in Figure 38). This reaction occurs even in the absence of a substrate and was successfully monitored in high-pressure experiments using a two-syringe system.

For all studies, identical experimental conditions were applied. The Fe(bTAML) concentration was set at 0.1 mM, and two equivalents of m-CPBA were used to generate the high-valent Fe(V)-oxo species. Substrate concentrations of xanthene ranged between 10 mM and 23.6 mM. Acetonitrile was used as the solvent, and all measurements were performed at 25 °C. The applied pressure started at 250 atm and was increased in 250 atm increments up to a maximum of 1750 atm. After each pressure increase, a waiting period of 10 minutes ensured that the system had equilibrated before measurement. Additionally, a small volume of solution was flushed through the cuvette to eliminate residual reactants. To rule out irreversible pressure-induced degradation, the pressure was reduced again after reaching the maximum value to verify the reversibility of pressure-dependent effects.

Figure 39 presents the first results from high-pressures studies of the bTAML system, displaying kinetic curves for both Fe(V) formation and decomposition. The calculated activation volumes ($\Delta V^{\#}$) for both processes differ significantly from each other (b and d in Figure 39). The positive ΔV# for the generation of Fe(V) suggests that the O-O bond cleavage is the rate-determining step, whereas the negative ΔV# for comproportionation reflects its nature as an addition reaction.

Even more intriguing is the application of the newly developed three-syringe mixing system for reactions with organic substrates such as xanthene. Figure 40 illustrates the proposed reaction mechanism, in which the rate-determining step involving hydrogen atom abstraction (HAA), ultimately yielding the corresponding alcohol species.[243] Due to the relatively short lifetime of the Fe(V)-oxo species, it must be generated in situ. The three-syringe mixing system enabled us to monitor the reaction of Fe(V)bTAML with xanthene at two different concentrations. The results, including kinetic curves at 330 nm and calculation of activation volumes, are depicted in Figure 41.

The hydrogen atom abstraction (HAA) process from the substrate by the Fe(V) species exhibits a significantly negative $\Delta V^{\#}$, a kinetic parameter that has never previously been determined for this important class of Fe(V)-oxo-mediated reactions. This finding provides strong evidence that the transition state of these reactions involves aggregation and precise spatial alignment of the hydrogen donor and hydrogen abstractor, thereby facilitating efficient hydrogen transfer. Notably, this result is of particular importance, as it clearly differentiates HAA from concerted proton-coupled electron transfer (PCET), which is characterized by a $\Delta V^{\#}$ of zero. These findings establish a fundamental basis for a deeper understanding of chemical processes and reaction mechanisms related to redox transformations and catalysis, paving the way for new mechanistic investigations and advancing core concepts in chemical reactivity.

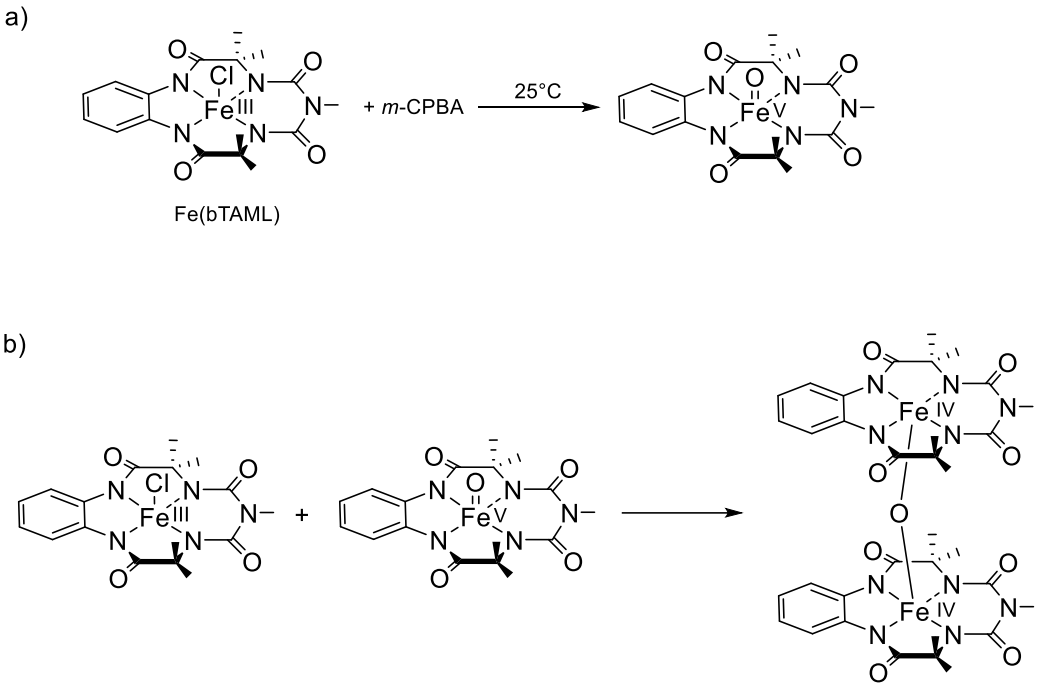

Figure 38: The investigated Fe(bTAML) complex. a) Displays the formation of the high valent Fe(V)-oxo species by reaction of Fe(III)bTAML with *m*-CPBA. In b) the fast comproportionating reaction of the Fe(V)-oxo species with unreacted precursor complex, which results in a Fe(IV) dimer is shown.[243]

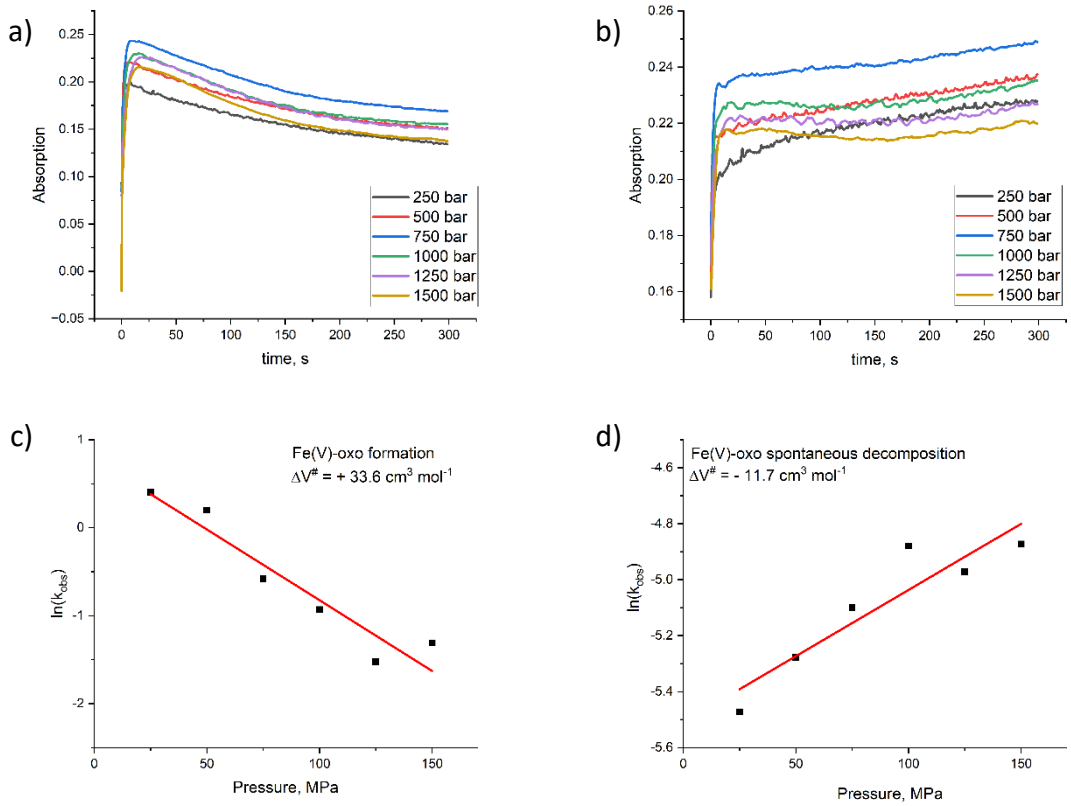

Figure 39: High Pressure Stopped Flow studies of the reaction of Fe(bTAML) and *m*-CPBA. a) Shows the kinetic traces at 445 nm followed to investigate the formation of the Fe(V)-oxo species. In c) the linear dependence resulting in the activation volume ($\Delta V^{\#}$) for the Fe(V)-oxo formation process. Analogous in b) the kinetic traces at 330 nm followed the Fe(V) decomposition and d) shows the activation volume for this reaction

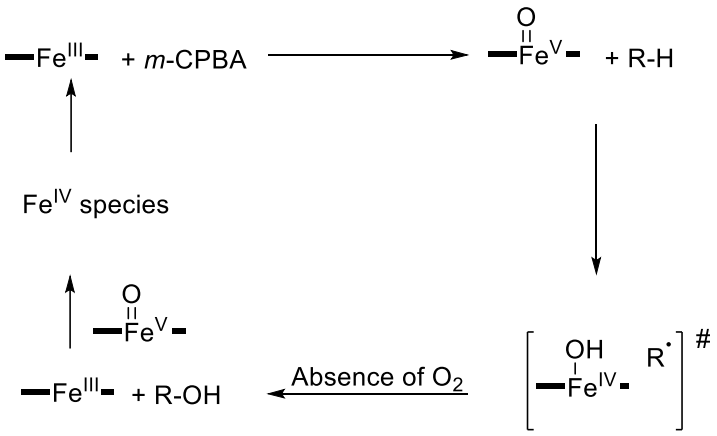

Figure 40: Proposed mechanism for FebTAML with organic substrates.[243]

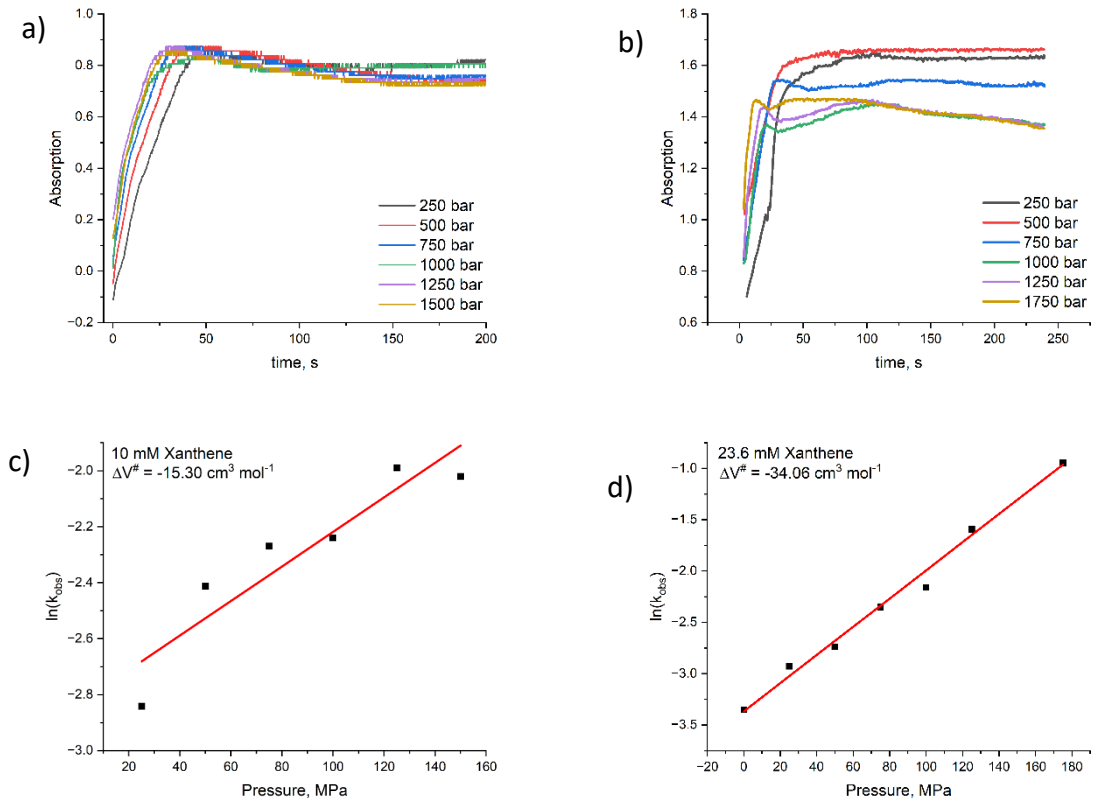

Figure 41: High Pressure Stopped Flow studies of the reaction of Fe(bTAML) and xanthene at different concentrations. a) Shows the kinetic traces at 330 nm followed to investigate the decomposition of the Fe(V)-oxo species while reacting with 10mM xanthene. In c) the linear dependence resulting in the activation volume ($\Delta V^{\#}$) for the reaction of Fe(V)-oxo with 10mM xanthene. Analogous in b) the kinetic traces at 330 nm followed the Fe(V) decomposition with 23.6mM and d) shows the activation volume for the reaction with corresponding concentrations.

6 References

[1] M. E. Ortiz, L. J. N.-V., C. Camargo, and J. A. Squella. *Pharmaceutical Research* **2004**, *21*, 428-435.

[2] Frimer, A. A. In *Peroxides (1983)*, 1983; pp 429-461.

[3] Fridovich, I. *Annu Rev Pharmacol Toxicol* **1983**, *23*, 239-257.

[4] Sawyer, D. T. Electrochemistry for Chemists. **1995**.

[5] Inas M. AlNashef, M. L. L., Matthew C. Kittle; Michael A. Matthews, a. J. W. W. *Electrochemical and Solid-State Letters* **2001**, *11*, 16-18.

[6] Bielski, B. H. J.; Cabelli, D. E.; Arudi, R. L.; Ross, A. *Journal of Physical and Chemical Reference Data* **1985**, *14* (4), 1041-1100.

[7] Hayyan, M. H., M. A.; AlNashef, I. M. *Chem Rev* **2016**, *116* (5), 3029-3085. From NLM Medline.

[8] H.-S. Wong, P.-A. Monternier, M. D. Brand, *Free Radical Biology and Medicine* **2019**, *143*, 545-559.

[9] J. Fang, H.-S. Wong, M. D. Brand, *Redox Biology* **2020**, *37*.

[10] M. Herb, M. Schramm, *Antioxidants (Basel)* **2021**, *10*.

[11] H. Kong, N. S. Chandel, *J Biol Chem* **2018**, *293*, 7499-7507.

[12] V. G. Grivennikova, A. D. Vinogradov, *Biochim Biophys Acta* **2006**, *1757*, 553-561.

[13] S. Drose, U. Brandt, *Adv Exp Med Biol* **2012**, *748*, 145-169.

[14] P. Hernansanz-Agustin, J. A. Enriquez, *Antioxidants (Basel)* **2021**, *10*.

[15] L. Bleier, S. Drose, *Biochim Biophys Acta* **2013**, *1827*, 1320-1331.

[16] P. Lanciano, B. Khalfaoui-Hassani, N. Selamoglu, A. Ghelli, M. Rugolo, F. Daldal, *Biochim Biophys Acta* **2013**, *1827*, 1332-1339.

[17] R. Banerjee, J. Purhonen, J. Kallijarvi, *FEBS J* **2022**, *289*, 6936-6958.

[18] F. Guillaud, S. Drose, A. Kowald, U. Brandt, E. Klipp, *Biochim Biophys Acta* **2014**, *1837*, 1643-1652.

[19] P. Mitchell, *FEBS Letters* **1975,** *59* (2), 137–139.

[20] U. Brandt, B. Trumpower, *Crit Rev Biochem Mol Biol* **1994**, *29*, 165-197.

[21] A. Osyczka, C. C. Moser, P. L. Dutton, *Trends Biochem Sci* **2005**, *30*, 176-182.

[21] M. J. C. Ronald E. White, *Ann. Rev. Biochem.* **1980**, *49*, 315-356.

[22] A. Veith, B. Moorthy, *Curr Opin Toxicol* **2018**, *7*, 44-51.

[23] I. G. Denisov, T. M. Makris, S. G. Sligar, I. Schlichting, *Chemical Reviews* **2005,** *105* (6), 2253–2278.

[24] R. C. Zangar, D. R. Davydov, S. Verma, *Toxicology and Applied Pharmacology* **2004**, *199* 316–331.

[25] L. D. Gorsky, D. R. Koop, M. J. Coon, *Journal of Biological Chemistry* **1984**, *259*, 6812-6817.

[26] J. Blanck, O. Ristau, A. A. Zhukov, A. I. Archakov, H. Rein, K. Ruckpaul, *Xenobiotica* **1991**, *21*, 121-135.

[27] R. C. Bray, G. Palmer, H. Beinert, *Journal of Biological Chemistry* **1964**, *239*, 2667-2676.

[28] H. Ukeda, D. Kawana, S. Maeda, M. Sawamura, *Biosci Biotechnol Biochem* **1999**, *63*, 485-488.

[29] A. van der Vliet, T. J. R. Tuinstra, A. Bast, *Biochemical Pharmacology* **1989**, *38*, 2807-2818.

[30] D. A. W. Jonathan D. Pollock, Mary A. C. Gifford, Ling Lin LP, Xunxiang Du, Jason Fisherman, Stuart H. Orkin, Claire M. Doerschuk & Mary C. Dinauer, *Nature Genetics* **1995**, *9*, 202-209.

[31] A. Gluschko, M. Herb, K. Wiegmann, O. Krut, W. F. Neiss, O. Utermohlen, M. Kronke, M. Schramm, *Cell Host Microbe* **2018**, *23*, 324-337 e325.

[32] M. Herb, M. Schramm, *Antioxidants (Basel)* **2021**, *10*.

[33] A. Bhattacharyya, R. Chattopadhyay, S. Mitra, S. E. Crowe, *Physiol Rev* **2014**, *94*, 329-354.

[34] H. Tong, P. S. J. Lakey, A. M. Arangio, J. Socorro, C. J. Kampf, T. Berkemeier, W. H. Brune, U. Poschl, M. Shiraiwa, *Faraday Discuss* **2017**, *200*, 251-270.

[35] M. Shiraiwa, K. Selzle, U. Poschl, *Free Radic Res* **2012**, *46*, 927-939.

[36] D. W. Dockery, C. A. Pope *Annu. Rev. Public Health.* **1994**, *15*, 107-132.

[37] J. Lelieveld, J. S. Evans, M. Fnais, D. Giannadaki, A. Pozzer, *Nature* **2015**, *525*, 367-371.

[38] Y. S. Seo, J. M. Park, J. H. Kim, M. Y. Lee, *Antioxidants (Basel)* **2023**, *12*.

[39] W. Gehling, B. Dellinger, *Environ Sci Technol* **2013**, *47*, 8172-8178.

[40] P. A. Alpert, J. Dou, P. Corral Arroyo, F. Schneider, J. Xto, B. Luo, T. Peter, T. Huthwelker, C. N. Borca, K. D. Henzler, T. Schaefer, H. Herrmann, J. Raabe, B. Watts, U. K. Krieger, M. Ammann, *Nat Commun* **2021**, *12*, 1769.

[41] P. A. Riley, *Int J Radiat Biol* **1994**, *65*, 27-33.

[42] P. K. Farris, G. Valacchi, *Antioxidants (Basel)* **2022**, *11*.

[43] T. L. de Jager, A. E. Cockrell, S. S. Du Plessis, *Adv Exp Med Biol* **2017**, *996*, 15-23.

[44] B. Halliwell, C. E. Cross, *Environmental Health Perspectives* **1994**, *102*, 5-12.

[45] A. Gorlach, E. Y. Dimova, A. Petry, A. Martinez-Ruiz, P. Hernansanz-Agustin, A. P. Rolo, C. M. Palmeira, T. Kietzmann, *Redox Biol* **2015**, *6*, 372-385.

[46] J. Kanner, *Mol Nutr Food Res* **2007**, *51*, 1094-1101.

[47] J. Kanner, J. Selhub, A. Shpaizer, B. Rabkin, I. Shacham, O. Tirosh, *Redox Biol* **2017**, *12*, 929-936.

[48] B. L. Tan, M. E. Norhaizan, W. P. Liew, *Oxid Med Cell Longev* **2018**, *2018*, 9719584.

[49] G. Egervari, C. A. Siciliano, E. L. Whiteley, D. Ron, *Trends Neurosci* **2021**, *44*, 1004-1015.

[50] D. Wu, A. I. Cederbaum, *Semin Liver Dis* **2009**, *29*, 141-154.

[51] H. Sies, V. V. Belousov, N. S. Chandel, M. J. Davies, D. P. Jones, G. E. Mann, M. P. Murphy, M. Yamamoto, C. Winterbourn, *Nat Rev Mol Cell Biol* **2022**, *23*, 499-515.

[52] M. Schieber, N. S. Chandel, *Curr Biol* **2014**, *24*, R453-462.

[53] Haber, F.; Weiss, J. The Catalytic Decomposition of Hydrogen Peroxide by Iron Salts. *Proc. R. Soc. London, Ser. A* **1934**, *147*.

[54] J. P. Kehrer, *Toxicology* **2000**, *149*, 43-50.

[55] Pattison, D. I., Davies, M. J., and Hawkins, C. L. Reactions and reactivity of myeloperoxidase-derived oxidants: differential biological effects of hypochlorous and hypothiocyanous acids. *Free Radic. Res.* **2012**, *46*, 975-995.

[56] H. D.-R. Esterbauer, M.; Waeg, G.; Striegl, G.; Jürgens, G., *Chemical Research in Toxicology* **1989**, *3*, 77-92.

[57] W. A. P. Pryor, N. A., *Free Radical Biology and Medicine* **1990**, *8*, 541-543.

[58] T. P. A. B. Devasagayam, K. K.; Ramasarma, T., *Indian Jounal of Biochemistry & Biophysics* **2003**, *40*, 300-308.

[59] Y. Park, S. Nam, H. J. Yi, H. J. Hong, M. Lee, *Nutr Res* **2009**, *29*, 812-818.

[60] Nimse, S. B.; Pal, D. Free radicals, natural antioxidants, and their reaction mechanisms. *RSC Advances* **2015**, *5* (35), 27986-28006.

[61] E. Niki, Y. Yoshida, Y. Saito, N. Noguchi, *Biochem Biophys Res Commun* **2005**, *338*, 668-676.

[62] Y. C. Kao, P. C. Ho, Y. K. Tu, I. M. Jou, K. J. Tsai, *Int J Mol Sci* **2020**, *21*.

[63] L. J. Su, J. H. Zhang, H. Gomez, R. Murugan, X. Hong, D. Xu, F. Jiang, Z. Y. Peng, *Oxid Med Cell Longev* **2019**, *2019*, 5080843.

[64] F. Ito, Y. Sono, T. Ito, *Antioxidants (Basel)* **2019**, *8*.

[65] E. E. Farmer, M. J. Mueller, *Annu Rev Plant Biol* **2013**, *64*, 429-450.

[66] C. A. Juan, J. M. Perez de la Lastra, F. J. Plou, E. Perez-Lebena, *Int J Mol Sci* **2021**, *22*.

[67] R. Orru, D. E. Pazmino, M. W. Fraaije, A. Mattevi, *J Biol Chem* **2010**, *285*, 35021-35028.

[68] K. Jomova, R. Raptova, S. Y. Alomar, S. H. Alwasel, E. Nepovimova, K. Kuca, M. Valko, *Arch Toxicol* **2023**, *97*, 2499-2574.

[69] C. L. Hawkins, M. J. Davies, *J Biol Chem* **2019**, *294*, 19683-19708.

[70] P. J. M. Dizdaroglu, M. Birincioglu, H. Rodriguez, *Free Radical Biology & Medicine* **2002**, *32*, 1102-1115.

[71] M. S. Cooke, M. D. Evans, M. Dizdaroglu, J. Lunec, *FASEB J* **2003**, *17*, 1195-1214.

[72] A. Collins, A. Vettorazzi, A. Azqueta, *Toxicol Lett* **2020**, *327*, 58-68.

[73] J. A. M. Anthony P. Breen, *Free Radical Biology & Medicine* **1995**, *18*, 1033-1077.

[74] L. L. J. Tuo, H. E. Poulsen, A. Wemann, O. Svendsen, S. Loft, *Free Radical Biology & Medicine* **2000**, *29*, 147-155.

[75] K. J. Alexander, M. McConville, K. R. Williams, K. V. Luzyanin, I. A. O'Neil, R. Cosstick, *Chemistry* **2018**, *24*, 3013-3020.

[76] M. Dizdaroglu, *Mutation Research* **1992**, *275*, 331-342.

[77] V. J.-P. Leveque, C. K. Vance, H. S. Nick, D. N. Silverman, *Biochemistry* **2001**, *40*, 10586-10591.

[78] T. Mann, D Keilin, *Proc. R. Soc. Lond. B* **1938**, *126*, 303-315.

[79] J. M. McCord, I. Fridovich, *Journal of Biological Chemistry* **1969**, *244*, 6049-6055.

[80] A. Tainer, E. D. Getzoff, K. M. Beem, J. S. Richardson, D. C. Richardson, *J. Mol. Biol.* **1982**, *160*, 181-217.

[81] R. A. Hallewell, H. E. Parge, J. A. Tainer, *Proc. Natl. Acad. Sci. U.S.A.* **1992**, *89*, 6109-6113.

[82] A. F. Miller, *Curr Opin Chem Biol* **2004**, *8*, 162-168.

[83] B. G. Trist, J. B. Hilton, D. J. Hare, P. J. Crouch, K. L. Double, *Angew Chem Int Ed Engl* **2021**, *60*, 9215-9246.

[84] C. S. St. Clair, H. B. Gray, J. S. Valentine, *Inorganic Chemistry* **1991**, *31*, 925-927.

[85] R. J. F. Branco, P. A. Fernandes, M. J. Ramos, *Journal of Molecular Structure: THEOCHEM* **2005**, *729*, 141-146.

[86] H. A. Azab, L. Banci, C. Luchinat, M. Sola, M. S. Viezzoli, *Inorg Chem* **1992**, *31*, 4649-4655.

[87] M. DiDonato, L. Craig, M. E. Huff, M. M. Thayer, R. M. Cardoso, C. J. Kassmann, T. P. Lo, C. K. Bruns, E. T. Powers, J. W. Kelly, E. D. Getzoff, J. A. Tainer, *J Mol Biol* **2003**, *332*, 601-615.

[88] J. J. Perry, D. S. Shin, E. D. Getzoff, J. A. Tainer, *Biochim Biophys Acta* **2010**, *1804*, 245-262.

[89] UCSF ChimeraX: Structure visualization for researchers, educators, and developers. Pettersen EF, Goddard TD, Huang CC, Meng EC, Couch GS, Croll TI, Morris JH, Ferrin TE. *Protein Sci.* **2021**, 3070-3082.

[90] W. F. Beyer, I. Fridovich, G. T. Mullenbach, R. Hallewell, *Journal of Biological Chemistry* **1987**, *262*, 11182-11187.

[91] A. Bafana, S. Dutt, A. Kumar, S. Kumar, P. S. Ahuja, *Journal of Molecular Catalysis B: Enzymatic* **2011**, *68*, 129-138.

[92] T. Kamiya, *J Clin Biochem Nutr* **2024**, *75*, 1-6.

[93] S. B. Chidambaram, N. Anand, S. R. Varma, S. Ramamurthy, C. Vichitra, A. Sharma, A. M. Mahalakshmi, M. M. Essa, *IBRO Neurosci Rep* **2024**, *16*, 373-394.

[94] M. Tajiri, H. Aoki, A. Shintani, K. Sue, S. Akashi, Y. Furukawa, *Free Radic Biol Med* **2022**, *183*, 60 68.

[95] I. N. Zelko, T. J. Mariani, R. J. Folz, *Free Radical Biology & Medicine* **2002**, *33*, 337-349.

[96] S. V. Antonyuk, R. W. Strange, S. L. Marklund, S. S. Hasnain, *J Mol Biol* **2009**, *388*, 310-326.

[97] S. L. Marklund, *Proc. Natl. Acad. Sci.* **1982**, *79*, 7634–7638.

[98] F. J. Yost, I. Fridovich, *Journal of Biological Chemistry* **1973**, *248*, 4905-4908.

[99] G. A. P. D. Ringe, F. Yamakura, K. Suzuki, D. Ohmori, *Proc. Natl. Acad. Sci. USA* **1983**, *80*, 3879 3883.

[100] I. W. Boucher, A. M. Brzozowski, J. A. Brannigan, C. Schnick, D. J. Smith, S. A. Kyes, A. J. Wilkinson, *BMC Struct Biol* **2006**, *6*, 20.

[101] M. G. Caiola, A. Canini, R. Ocampo-Friedmann, *Physiologia* **1996**, *35*, 90-94.

[102] I. G. Munoz, J. F. Moran, M. Becana, G. Montoya, *Protein Sci* **2005**, *14*, 387-394.

[103] M. S. Lah, M. M. Dixon, K. A. Pattridge, W. C. Stallings, J. A. Fee, M. L. Ludwig, *Biochemistry* **1995**, *34*, 1646-1660.

[104] Y. Li, T.-T. Huang, E. J. Carlson, S. Melov, P. C. Ursell, J. L. Olson, L. J. Noble, M. P. Yoshimura, C. Berger P. H. Chan, D. C. Wallace, C. J. Epstein, *Nature Genetics* **1995**, *11*, 376-381.

[105] R. M. Lebovitz, H. Zhang, H. Vogel, J. Cartwright Jr., L. Dionne, N. Lu, S. Huang, M. M. Matzuk, *Proc. Natl. Acad. Sci. USA* **1996**, *93*, 9782-9787.

[106] A. F. Miller, *FEBS Lett* **2012**, *586*, 585-595.

[107] E. J. Dowling, C. L. Chander, A. W. Claxson, C. Lillie, D. R. Blake, *Free Radical Research Communications* **1993**, *18*, 291-298.

[108] D. N. Silverman, H. S. Nick, *Methods in enzymology* **2002**, *349*, 61-74.

[109] A. S. Hearn, M. E. Stroupe, D. E. Cabelli, C. A. Ramilo, J. P. Luba, J. A. Tainer, H. S. Nick, D. N. Silverman, *Biochemistry* **2003**, *42*, 2781-2789.

[110] J. M. Whittaker. M. M. Whittaker, *JBIC* **1997**, *2*, 667-671.

[111] J. M. Whittaker, M. M. Whittaker, *Biochemistry* **1996**, *35*, 6762-6770.

[112] J. Azadmanesh, G. E. O. Borgstahl, *Antioxidants (Basel)* **2018**, *7*.

[113] S. Vathyam, R. A. Byrd, A.-F. Miller, *Magnetic Resonance in Chemistry* **2000**, *38*, 536-542.

[114] R. A. Edward, M. M. Whittaker, J. W. Whittaker, G. B. Jameson, E. N. Baker, *J Am Chem Soc* **1998**, *120*, 9684-9685.

[115] H.-D. Youn, H. Youn, J.-W. Lee, Y.-I. Yim, J. K. Lee, S.-O. K., Y. C. Hah, *Archives of Biochemistry and Biophysics* **1996**, *334*, 341-348.

[116] H.-D. Youn, E.-J. Kim, J.-H. Roe, Y. C. Hah S.-O. Kang, *Biochem J* **1996**, *318*, 889-896.

[117] J. Wuerges, Y.-I. Yim, H.-S. Yim, S.-O. Kang, K. D. Carugo, *PNAS* **2004**, *101*, 8569-8574.

[118] J.-W. Lee, S.-O. Kang, *Methods in enzymology* **2002**, *349*, 90-101.

[119] K. C. Ryan, O. E. Johnson, D. E. Cabelli, T. C. Brunold, M. J. Maroney, *J Biol Inorg Chem* **2010**, *15*, 795-807.

[120] M. Undsemaa, T. Tamm, *J Phys Chem A* **2003**, *107*, 9997-10003.

[121] D. P. Barondeau, C. K. Bruns, J. A. Tainer, E. D. Getzoff, *Biochemistry* **2004**, *43*, 8038-8047.

[122] R. W. Herbst, P. A. Bryngelson, K. A. Higgins, K. C. Ryan, D. E. Cabelli, S. C. Garman, M. J. Maroney, *Biochemistry* **2009**, *48*, 3354-3369.

[123] I. A. Abreu, D. E. Cabelli, *Biochim Biophys Acta* **2010**, *1804*, 263-274.

[124] E. P. Broering, P. T. Truong, E. M. Gale, T. C. Harrop, *Biochemistry* **2013**, *52*, 4-18.

[125] D. Tietze, H. Breitzke, D. Imhof, E. Kothe, J. Weston, G. Buntkowsky, *Chemistry* **2009**, *15*, 517-523.

[126] D. Tietze, M. Tischler, S. Voigt, D. Imhof, O. Ohlenschlager, M. Gorlach, G. Buntkowsky, *Chemistry* **2010**, *16*, 7572-7578.

[127] D. P. Barondeau, C. K. Bruns, J. A. Tainer, E. D. Getzoff, *Biochemistry* **2004**, *43*.

[128] C. B. Castro, M. P. Ferreira, C. G. C. Marques Netto, *Current Research in Chemical Biology* **2021**, *1*.

[129] V. Pelmenschikov, P. E. M. Siegbahn, *J Am Chem Soc* **2006**, *128*, 7466-7475.

[130] R. Prabhakar, K. Morokuma, D. G. Musaev, *J Comput Chem* **2006**, *27*, 1438-1445.

[131] J. Shearer, *Acc Chem Res* **2014**, *47*, 2332-2341.

[132] K. Pong, *Expert Opin Biol Ther* **2003**, *3*, 127-139.

[133] D P. Riley, R. H. Weiss, *Analytical Biochemistry* **1991**, *196*, 344-349.

[134] J. Rabani, D. Klug-Roth, *The Journal of Physical Chemistry* **1976**, *80*, 588-591.

[135] J. Rabani, D. Klug-Roth, J. Lilie, *The Journal of Physical Chemistry* **1973**, *77*, 1169-1175.

[136] L W. Oberley, S. W. C. Leuthauser, R. F. Pasternack, T. D. Oberley, L. Schutt, J. R. J. Soreson, *Agents and Actions* **1984**, *15*.

[137] Q. X. Li, Q. H. Luo, Y. Z. Li, M. C. Shen, *Dalton Trans* **2004**, 2329-2335.

[138] A. Squarcina, A. Santoro, N. Hickey, R. De Zorzi, M. Carraro, S. Geremia, M. Bortolus, M. Di Valentin, M. Bonchio, *ACS Catalysis* **2020**, *10*, 7295-7306.

[139] A. Martinez-Camarena, P. A. Sanchez-Murcia, S. Blasco, L. Gonzalez, E. Garcia-Espana, *Chem Commun (Camb)* **2020**, *56*, 7511-7514.

[140] A. Martinez-Camarena, J. M. Llinares, A. Domenech-Carbo, J. Alarcon, E. Garcia-Espana, *RSC Adv* **2019**, *9*, 41549-41560.

[141] V. A. Daier, E. Riviere, S. Mallet-Ladeira, D. M. Moreno, C. Hureau, S. R. Signorella, *J Inorg Biochem* **2016**, *163*, 162-175.

[142] A. Vincent, J. R. Fores, E. Tauziet, E. Quevrain, A. Dancs, A. Conte-Daban, A. S. Bernard, P. Pelupessy, K. Coulibaly, P. Seksik, C. Hureau, K. Selmeczi, C. Policar, N. Delsuc, *Chem Commun (Camb)* **2020**, *56*, 399-402.

[143] G. Csire, S. Timari, J. Asztalos, J. M. Kiraly, M. Kiss, K. Varnagy, *J Inorg Biochem* **2017**, *177*, 198-210.

[144] Á. Dancs, K. Selmeczi, D. Árus, D. Szunyogh, T. Gajda, *International Journal of Peptide Research and Therapeutics* **2017**, *24*, 571-575.

[145] J. Domergue, P. Guinard, M. Douillard, J. Pecaut, S. Hostachy, O. Proux, C. Lebrun, A. Le Goff, P. Maldivi, C. Duboc, P. Delangle, *Inorg Chem* **2023**, *62*, 8747-8760.

[146] D. Nakane, Y. Wasada-Tsutsui, Y. Funahashi, T. Hatanaka, T. Ozawa, H. Masuda, *Inorg Chem* **2014**, *53*, 6512-6523.

[147] P. Guinard, S. Hostachy, L. Diebold, J. Pecaut, A. Le Goff, C. Duboc, P. Delangle, *Angew Chem Int Ed Engl* **2024**, *63*, e202409343.

[148] H. Y. Ching, I. Kenkel, N. Delsuc, E. Mathieu, I. Ivanovic-Burmazovic, C. Policar, *J Inorg Biochem* **2016**, *160*, 172-179.

[149] M. Baudry, A. Bruce, M. Palucki, E. Jacobsen, B. Malfroy, *Biochem Biophys Res Commun* **1993**, *192*, 964-968.

[150] I. Spasojevic, I. Batinic-Haberle R. D. Stevens, P. Hambright, J. Grodkowski, A. N. Thorpe, P. Neta, I. Fridovich, *Inorg Chem* **2001**, *40*, 726-739.

[151] S. R. Doctrow, K. Huffman, C. Bucay Marcus, G. Tocco, E. Malfroy, H. Kruk, C. A. Adinolfi, K. Baker, N. Lazarowych, J. Mascarenhas, B. Malfroy, *J Med Chem* **2002**, *45*, 4549-4558.

[152] S. Melov, S. R. Doctrow, J. A. Schneider, J. Haberson, M. Patel, P. E. Coskun, K. Huffman, D. C. Wallace, B. Malfroy, *The Journal of Neuroscience* **2001**, *21*, 8348-8353.

[153] R. A. Rosenthal, B. Fish, R. P. Hill, K. D. Huffman, Z. Lazarova, J. Mahmood, M. Medhora, R. Molthen, J. E. Moulder, S. T. Sonis, P. J. Tofilon. S. R. Doctrow, *Anti-Cancer Agents in Medicinal Chemistry* **2011**, *11*, 359-372.

[154] D. Salvemini, D. P. Riley, S. Cuzzocrea, *Nat Rev Drug Discov* **2002**, *1*, 367-374.

[155] D. P. RIley, *Chem Rev* **1999**, *99*, 2573-2587.

[156] D. P. Riley, S. L. Henke, P. J. Lennon, R. H. Weiss, William L. Neumann, W. J. Rivers Jr., K. W. Aston, K. R. Sample, C.-S. Ling, H. Rahman, J.-J. Shieh, D. H. Busch, W. Szulbinski, *Inorg Chem* **1996**, *35*, 5213-5231.

[157] D. P. Riley, S. L. Henke, P. J. Lennon, K. Aston, *Inorg Chem* **1999**, *38*, 1908-1917.

[158] D. P. Riley, P. J. Lennon, W. L. Neumann, R. H. Weiss, *J Am Chem Soc* **1997**, *119*, 6522-6528.

[159] D. Zhang, D. H. Busch, P. L. Lennon, R. H. Weiss, W. L. Neumann, D. P. Riley, *Inorganic Chemistry* **1998,** *37* (5), 956–963.

[160] D. Salvemini, Z.-Q. Wang, J. L. Zweier, A. Samouilov, H. Macarthur, T. P. Misko, M. G. Currie, S. Cuzzocrea, J. A. Sikorski, D. P. Riley, *Science* **1999**, *286*, 304-306.

[161] K. Aston, N. Rath, A. Naik, U. Slomczynska, O. F. Schall, D. P. Riley, *Inorg Chem* **2001**, *40*, 1779-1789.

[162] A. Maroz, G. F. Kelso, R. A. J. Smith, D. C. Ware, R. F. Anderson, *J Phys Chem A* **2008**, *112*, 4929-4935.

[163] D. Lieb, I. Kenkell, J. Miljkovic, D. Moldenhauer, N. Weber, M. R. Filipovic, F. Grohn, I. Ivanović-Burmazović, *Inorg Chem* **2014**, *53*, 1009-1020.

[164] G. F. Kelso, A. Maroz, H. M. Cocheme, A. Logan, T. A. Prime, A. V. Peskin, C. C. Winterbourn, A. M. James, M. F. Ross, S. Brooker, C. M. Porteous, R. F. Anderson, M. P. Murphy, R. A. Smith, *Chem Biol* **2012**, *19*, 1237-1246.

[165] D. Lieb, F. C. Friedel, M. Yawer, A. Zahl, M. M. Khusniyarov, F. W. Heinemann, I. Ivanović-Burmazović, *Inorg Chem* **2013**, *52*, 222-236.

[166] D. Salvemini, D. P. Riley, P. J. Lennon, Z. Q. Wang, M. G. Currie, H. Macarthur, T. P. Misko, *Br J Pharmacol* **1999**, *127*, 685-692.

[167] D. Salvemini, E. Mazzon, L. Dugo, D. P. Riley, I. Serraino, A. P. Caputi, S. Cuzzocrea, *Br J Pharmacol* **2001**, *132*, 815-827.

[168] D. Salvemini, S. Cuzzocrea, *Free Radic Biol Med* **2002**, *33*, 1173-1185.

[169] M. R. Filipović, K. Duerr, M. Mojović, V. Simeunović, R. Zimmerman, V. Niketić, I. Ivanović-Burmazović, *Angew. Chem., Int. Ed.*, **2008**, *47*, 8735-8739.

[170] M. R. Filipović, A. C. W. Koh, S. Arbault, V. Niketic, A. Debus, U. Schleicher, C. Bogdan, M. Guille, F. Lemaitre, C. Amatore, I. Ivanović-Burmazović, *Angew. Chem., Int. Ed.*, **2010**, *49*, 4228-4232.

[171] R. F. Pasternack, B. Halliwell, *Journal of the American Chemical Society* **1979**, *101*, 1026-1031.

[172] R. F. Pasternack, W. R. Skowronek Jr., *Journal of Inorganic Chemistry* **1979**, *11*, 261-267.

[173] K. M. Faulkner, S. I. Liochev, I. Fridovich, *Journal of Biological Chemistry* **1994**, *269*, 23471-23476.

[174] B. J Day, I. Fridovich, J. D Crapo, *Archives of Biochemistry and Biophysics* **1997**, *347*, 256-262.

[175] M. Wolak, R. van Eldik, *Chemistry* **2007**, *13*, 4873-4883.

[176] C. Szabó, J. G. Mabley, S. M. Moeller, R. Shimanovich, P. Pacher, L. Virág, J. H. Van Duzer, W. Williams, A. L. Salzman, J. T. Groves, *Molecular Medicine* **2002**, *8*, 571-580.

[177] I Batinic-Haberle, I. Spasojevic, P. Hambright, L. Benov, I. Fridovich, A. L. Crumbliss, *Inorg Chem* **1999**, *38*, 4011-4022.

[178] I. Spasojevic, I. Batinic-Haberle, J. S. Reboucas, Y. M. Idemori, I. Fridovich, *J Biol Chem* **2003**, *278*, 6831-6837.

[179] J. S. Reboucas, G. DeFreitas-Silva, I. Spasojevic, Y. M. Idemori, L. Benov, I. Batinic-Haberle, *Free Radic Biol Med* **2008**, *45*, 201-210.

[180] S. Shrishrimal, E. A. Kosmacek, A. Chatterjee, M. J. Tyson, R. E. Oberley-Deegan, *Antioxidants (Basel)* **2017**, *6*.

[181] Z. Rajic, A. Tovmasyan, I. Spasojevic, H. Sheng, M. Lu, A. M. Li, E. B. Gralla, D. S. Warner, L. Benov, I. Batinic-Haberle, *Free Radic Biol Med* **2012**, *52*, 1828-1834.

[182] I. Batinic-Haberle, M. E. Tome, *Redox Biol* **2019**, *25*, 101139.

[183] I. Batinic-Haberle, Z. Rajic, A. Tovmasyan, J. S. Reboucas, X. Ye, K. W. Leong, M. W. Dewhirst, Z. Vujaskovic, L. Benov, I. Spasojevic, *Free Radic Biol Med* **2011**, *51*, 1035-1053.

[184] I. Batinic-Haberle, J. S. Reboucas I. Spasojevic, *Antioxidants and Redox Signaling* **2010**, *13*, 877-918.

[185] M. Patriarca, V. Daier, G. Cami, E. Riviere, C. Hureau, S. Signorella, *J Inorg Biochem* **2020**, *207*, 111050.

[186] M. Patriarca, V. Daier, G. Camí, N. Pellegri, E. Rivière, C. Hureau, S. Signorella, *Microporous and Mesoporous Materials* **2019**, *279*, 133-141.

[187] C. Korsvik, S. Patil, S. Seal, W. T. Self, *Chem Commun (Camb)* **2007**, 1056-1058.

[188] E. G. Heckert, A. S. Karakoti, S. Seal, W. T. Self, *Biomaterials* **2008**, *29*, 2705-2709.

[189] J. Colon, L. Herrera, J. Smith, S. Patil, C. Komanski, P. Kupelian, S. Seal, D. W. Jenkins, C. H. Baker, *Nanomedicine* **2009**, *5*, 225-231.

[190] G. Wang, J. Zhang, X. He, Z. Zhang, Y. Zhao, *Chinese Journal of Chemistry* **2017**, *35*, 791-800.

[191] S. L. Schlichte, S. Romanova, K. Katsurada, E. A. Kosmacek, T. K. Bronich, K. P. Patel, R. E. Oberley-Deegan, M. C. Zimmerman, *Redox Biol* **2020**, *36*, 101610.

[192] S. Goldstein, G. Czapski, A. Heller, *Free Radic Biol Med* **2005**, *38*, 839-845.

[193] V. Verma, M. Kaur, S. Sharma, *Bulletin of Materials Science* **2019**, *42*.

[194] J. Kim, M. Takahashi, T. Shimizu, T. Shirasawa, M. Kajita, A. Kanayama, Y. Miyamoto, *Mech Ageing Dev* **2008**, *129*, 322-331.

[195] X. Hu, J. Liu, S. Hou, T. Wen, W. Liu, K. Zhang, W. He, Y. Ji, H. Ren, Q. Wang, X. Wu, *Science China Physics, Mechanics and Astronomy* **2011**, *54*, 1749-1756.

[196] L. Zhang, Y. Zhang, Z. Wang, F. Cao, Y. Sang, K. Dong, F. Pu, J. Ren, X. Qu, *Materials Horizons* **2019**, *6*, 1682-1687.

[197] X. Wang, W. Guo, Y. Hu, J. Wu, H. Wei, in *Nanozymes: Next Wave of Artificial Enzymes*, **2016**, pp. 7-29.

[198] K. Yudoh, K. Shishido, H. Murayama, M. Yano, K. Matsubayashi, H. Takada, H. Nakamura, K. Masuko, T. Kato, K. Nishioka, *Arthritis Rheum* **2007**, *56*, 3307-3318.

[199] P. J. Krustic, E. Wasserman, P. N. Keizer, J. R. Morton, K. F. Preston, *Science* **1991**, *254* 1183-1885.

[200] J. Yao, Y. Cheng, M. Zhou, S. Zhao, S. Lin, X. Wang, J. Wu, S. Li, H. Wei, *Chem Sci* **2018**, *9*, 2927-2933.

[201] N. Singh, M. Geethika, S. M. Eswarappa, G. Mugesh, *Chemistry* **2018**, *24*, 8393-8403.

[202] S. A. B. E. Van Acker, D.-J. Van den Berg, M. N. J. L Tromp, D. H. Griffioen, W. P. Van Bennekom, W. J. F. Van der Vijgh, A. Bast, *Free Radical Biology & Medicine* **1996**, *20*, 331-342.

[203] I. Ciric, D. D. Zagorac, M. Sredojevic, M. F. Aksic, B. Rabrenovic, S. Blagojevic, M. Natic, Pharmaceutics **2024**, 16, 606.

[204] K. B. Pandey, S. I. Rizvi, *Oxidative Medicine and Cellular Longevity* **2009**, *5*, 270-278.

[205] M. Leopoldini, N. Russo, M. Toscano, *Food Chemistry* **2011**, *125*, 288-306.

[206] P.-G. Pietta, *J. Nat. Prod.* **2000**, *63,* 1035-1042.

[207] S. Dikalov, T. Losik, J. L. Arbiser, *Biochem Pharmacol* **2008**, *76*, 589-596.

[208] L. E. Fried, J. L. Arbiser, *Antioxidants and Redox Signaling* **2009**, *11*, 1139-1148.

[209] M. J. Messina, C. L. Loprinzi, *J Nutr* **2001**, *131*, 3095S-3108S.

[210] A. S. Strimpakos, R. A. Sharma, *Antioxid Redox Signal* **2008**, *10*, 511-545.

[211] C. Fiorillo, M. Becatti, A. Pensalfini, C. Cecchi, L. Lanzilao, G. Donzelli, N. Nassi, L. Giannini, E. Borchi, P. Nassi, *Free Radic Biol Med* **2008**, *45*, 839-846.

[212] F. Caruso, S. Incerpi, J. Pedersen, S. Belli, S. Kaur, M. Rossi, *Curr Issues Mol Biol* **2022**, *44*, 5209-5220.

[213] T. M. Monica Leopoldini, Nino Russo, and Marirosa Toscano, *J Phys Chem A* **2004**, *108*, 4916-4922.

[214] Y. Guo, A. Baschieri, F. Mollica, L. Valgimigli, J. Cedrowski, G. Litwinienko, R. Amorati, *Angew Chem Int Ed Engl* **2021**, *60*, 15220-15224.

[215] F. Di Meo, V. Lemaur, J. Cornil, R. Lazzaroni, J. L. Duroux, Y. Olivier, P. Trouillas, *J Phys Chem A* **2013**, *117*, 2082-2092.

[216] G. T. Krayz, S. Bittner, A. Dhiman, J. Y. Becker, *Chem Rec* **2021**, *21*, 2332-2343.

[217] J. Jiang, A. Kappler, *Environ Sci Technol* **2008**, *42*, 3563-3569.

[218] E. J. O'Loughlin, *Environ Sci Technol* **2008**, *42*, 6876-6882.

[219] O. Dangles, *AgroFOOD Industry Hi-tech* **2006** 17, 64–67.

[220] B. Halliwell, *Arch Biochem Biophys* **2008**, *476*, 107-112.

[221] I. Kenkel, A. Franke, M. Durr, A. Zahl, C. Ducker-Benfer, J. Langer, M. R. Filipovic, M. Yu, R. Puchta, S. R. Fiedler, M. P. Shores, C. R. Goldsmith, I. Ivanović-Burmazović, *J Am Chem Soc* **2017**, *139*, 1472-1484.

[222] L. Senft, J. L. Moore, A. Franke, K. R. Fisher, A. Scheitler, A. Zahl, R. Puchta, D. Fehn, S. Ison, S. Sader, I. Ivanović-Burmazović, C. R. Goldsmith, *Chem Sci* **2021**, *12*, 10483-10500.

[223] F. C. Friedel, D. Lieb, I. Ivanović-Burmazović, *J Inorg Biochem* **2012**, *109*, 26-32.

[224] M. B. Ward, A. Scheitler, M. Yu, L. Senft, A. S. Zillmann, J. D. Gorden, D. D. Schwartz, I. Ivanović-Burmazović, C. R. Goldsmith, *Nat Chem* **2018**, *10*, 1207-1212.

[225] J. Butler, W. H. Koppenol, E. Margoliash, *Journal of Biological Chemistry* **1982**, *257*, 10747-10750.

[226] J. Diguiseppi, I. Fridovich, *Arch Biochem Biophys* **1980**, *203*, 145-150.

[227] I. G. Munteanu, C. Apetrei, *Int J Mol Sci* **2021**, *22*.

[228] R. Joshi, *Radiation Physics and Chemistry* **2017**, *139*, 74-82.

[229] K. Kobayashi, *Chem. Rev*. **2019**, *119*, 4413−4462.

[230] S. Goldstein, C. Michel, W. Bors, M. Saran, G. Czapski, *Free Radic Biol Med* **1987**, *4*, 295-303.

[231] D. Klug-Roth, J. Rabani, *The Journal of Physical Chemistry* **1976**, *80*, 588-591.

[232] G. J. McClune, J. A. Fee, *FEBS Lett* **1976**, *67*, 294-298.

[233] D. P. Riley, W. J. Rivers, R. H. Weiss, *analytical Biochemistry* **1991**, *196*, 344-349.

[234] S. Goldstein, G. Czapski, *Free Radic Res Commun* **1991**, *12*, 5-10.

[235] J. S. Reboucas, I. Spasojevic, I. Batinic-Haberle, *Biol Inorg Chem* **2008**, *13*, 289–302.

[236] K. M. Faulkner, S. I. Liochev, I. Fridovich, *The Journal of Biological Chemistry* **1994**, *269*, 23471-23476.

[237] R. H. Weiss, A. G. Flickinger, W. J. Rivers, M. M. Hardy, K. W. Aston, U. S. Ryan, D. P. Riley, *Journal of Biological Chemistry* **1993**, *268*, 23049-23054.

[238] K. Ishihara, S. Funahashi, M. Tanaka, *Rev. Sci. Instrum.* **1982,** *53*, 1231-1234.

[239] K. Heremans, J. Snauwaert, J. Rijkenberg, *Rev. Sci. Instrum.* **1980,** *51*, 806-808.

[240] O. Troeppner, D. Huang, R. H. Holm, I. Ivanović-Burmazović, *Dalton Trans.* **2014,** *43*, 5274-5279.

[241] O. Troeppner, R. Lippert, T. E. Shubina, A. Zahl, N. Jux, I. Ivanović-Burmazović, *Angew. Chem. Int. Ed.* **2014,** *53*, 11452-11457.

[242] S. Pattanayak, A. J. Jasniewski, A. Rana, A. Draksharapu, K. K. Singh, A. Weitz, M. l. Hendrich, L. Que, Jr., A. Dey, S. S. Gupta, *Inorg. Chem.* **2017**, *56*, 6352−6361.

[243] M. Ghosh, K. K. Singh, C. Panda, A. Weitz, M. P. Hendrich, T. J. Collins, B. B. Dhar, and S. S. Gupta, *J. Am. Chem. Soc*. **2014**, *136*, 9524−9527.